STRUCTURE, FUNCTION, AND REGULATION OF THE HUMAN FE-S CLUSTER BIOSYNTHETIC SUBCOMPLEX

A Dissertation

by

SETH A. CORY

Submitted to the Office of Graduate and Professional Studies of
Texas A&M University
in partial fulfillment of the requirements for the degree of

DOCTOR OF PHILOSOPHY

Chair of Committee,	David P. Barondeau
Committee Members,	Frank M. Raushel
	Paul A. Lindahl
	Pingwei Li
Head of Department,	Simon W. North

December 2019

Major Subject: Chemistry

ABSTRACT

Iron-sulfur (Fe-S) clusters are inorganic cofactors found throughout all domains of life. These clusters are often ligated to proteins allowing Fe-S clusters to participate in a variety of essential processes such as oxidative respiration and photosynthesis. In eukaryotes, Fe-S clusters are assembled by a multi-subunit protein complex, and the synthesized clusters are subsequently distributed to target apoproteins. Specifically, in human mitochondria, the cysteine desulfurase, NFS1, catalyzes the conversion of cysteine to alanine and sulfane sulfur, which is transferred as a persulfide intermediate to acceptor proteins. Unexpectedly, NFS1 forms a tight complex with the LYRM adaptor protein (ISD11) and with the mitochondrial acyl-carrier protein (ACP). This complex is responsible for the transfer of persulfide sulfur to ISCU2 where a [2Fe-2S] cluster can be synthesized. Prior to these studies, little was known about the structure of the biosynthetic subcomplex consisting of NFS1, ISD11, and ACP and how structural differences between the eukaryotic and prokaryotic cysteine desulfurases might be linked to the frataxin (FXN) activation requirement in the human system.

A variety of biochemical and biophysical approaches were applied to determine structure-function properties for the human Fe-S cluster biosynthetic subcomplex (NFS1-ISD11-ACP). We found that the human Fe-S cluster biosynthetic subcomplex displays a unique, open cysteine desulfurase architecture that provides a structural explanation for the complex's low activity and demonstrates clear roles for ISD11 and ACP within eukaryotic Fe-S cluster biosynthesis. Additional crystallographic, functional, and mass spectrometry studies suggest the NFS1-ISD11-ACP subcomplex exists as a mixture of forms in solution with distinct quaternary structures. We show that multiple species can be separated by cation exchange chromatography and that all species, including those generated by treatment with the substrate L-cysteine, are in equilibrium with one another. Cation-exchange coupled small-angle X-ray scattering was used to investigate the conformational landscape of the NFS1-ISD11-ACP subcomplex. These studies demonstrated a unique species that has an extended conformation in solution upon treatment with the substrate. Taken together, our studies provide evidence for a morpheein-like regulatory model in which FXN stimulates the cysteine desulfurase and Fe-S cluster assembly activities by driving a subunit rearrangement for the NFS1-ISD11-ACP-ISCU2 complex.

DEDICATION

This dissertation is dedicated to my wife (Corrin), parents (Darrell and Ranee), and brother (Sean) who have supported me throughout my Ph.D. and always kept me motivated to complete my studies.

ACKNOWLEDGMENTS

I would first like to thank Professor David Barondeau for providing me the resources and creative freedom to conduct my research. Additionally, I would like to thank both past and present members of the Barondeau lab for their support and constructive criticism over the years. I would also like to acknowledge my committee members Professor Frank Raushel, Professor Paul Lindahl, and Professor Pingwei Li for their helpful suggestions during my time at Texas A&M.

I would like to especially thank Dr. D.J. Martin for not only being a great friend, but also for being an excellent mentor who taught me to be rigorous and self-reflective in my research. I would also like to specially thank Steven Havens for being a great friend and also a great research associate who helped me prepare protein complexes, setup crystal trays, and troubleshoot complex research challenges.

A special thanks goes to my family who pushed me throughout my graduate career and always supported me. Their support during my academic career has been unmeasurable.

Finally, I would like to thank my wife, Corrin. She has been by my side every step of this journey. Her support on the best and the worst days of research kept my spirits high. She always kept me motived, and I will forever be grateful for that.

For Chapter II, the following acknowledgments were published with the manuscript. The reference can be found here: Cory, S. A., Van Vranken, J. G., Brignole, E. J., Patra, S., Winge, D. R., Drennan, C. L., Rutter, J., and Barondeau, D. P. (2017)

Structure of human Fe-S assembly subcomplex reveals unexpected cysteine desulfurase architecture and acyl-ACP-ISD11 interactions, *Proc. Natl. Acad. Sci. U.S.A. 114*, E5325-E5334. We thank Chris Putnam and Jennifer Bridwell-Rabb for helpful discussions, Chi-Lin Tsai for the initial crystallization conditions, and Pingwei Li and Mark F. Mabanglo for helpful experimental suggestions. We are grateful to Mike Rigney for management of the Electron Microscopy Facility at Brandeis University, where the EM data were collected; James Sacchettini for use of X-ray diffraction equipment; and the TAMU Chemistry Mass Spectrometry facility. This work was supported in part by NIH Grant R01GM110755 (to J.R. and D.R.W.), Robert A. Welch Grant A-1647 (to D.P.B.), NIH Grant R01GM096100 (to D.P.B.), and NSF Grant CHE 1508269 (to D.P.B.). Use of the Stanford Synchrotron Radiation Lightsource, SLAC National Accelerator Laboratory, is supported by the US Department of Energy, Office of Science, Office of Basic Energy Sciences under Contract DE-AC02-76SF00515. The SSRL Structural Molecular Biology Program is supported by the DOE Office of Biological and Environmental Research and by the National Institutes of Health, National Institute of General Medical Sciences (including P41GM103393). C.L.D and J.R. are Howard Hughes Medical Institute Investigators. The contents of this publication are solely the responsibility of the authors and do not necessarily represent the official views of NIGMS or NIH.

For Chapter III, the acknowledgments are as follows. We would like to thank Dr. James Sacchettini for use of the X-ray diffraction equipment. Support for this work was funded by the NIH Grant R01GM096100. This work was conducted at the Advanced Light Source (ALS), a national user facility operated by Lawrence Berkeley National Laboratory

on behalf of the Department of Energy, Office of Basic Energy Sciences, through the Integrated Diffraction Analysis Technologies (IDAT) program, supported by DOE Office of Biological and Environmental Research. Additional support comes from the National Institute of Health project ALS-ENABLE (P30 GM124169) and a High-End Instrumentation Grant S10OD018483.

For Chapter IV, the acknowledgments are as follows. We would like to thank Professor Frank Raushel and Dr. Andrew Begley for the use and training on their BioRad FPLC. This research used resources of the Advanced Photon Source, a U.S. Department of Energy (DOE) Office of Science User Facility operated for the DOE Office of Science by Argonne National Laboratory under Contract No. DE-AC02-06CH11357. This project was supported by grant 9 P41 GM103622 from the National Institute of General Medical Sciences of the National Institutes of Health. Use of the Pilatus 3 1M detector was provided by grant 1S10OD018090-01 from NIGMS. We would like to specially thank Dr. Srinivas Chakravarthy for his help in data collection. In addition, we would like to specially thank Dr. Jesse Hopkins for his help in data processing and analysis, and in particular, for writing the custom python script that made data subtraction facile.

CONTRIBUTORS AND FUNDING SOURCES

The work in this dissertation was supervised by a committee consisting of Professor David Barondeau (advisor), Professor Frank Raushel, Professor Pingwei Li (outside of department), and Professor Paul Lindahl.

Chapter II is a direct re-print of the paper I published in *Proceedings of the National Academy of Sciences of the United States of America* and has been formatted to follow the appropriate dissertation format. I determined the structure of NFS1-ISD11 in complex with *E. coli* acyl carrier protein. I performed many of the experiments featured in this manuscript including complex preparation and purity validation for the negative stain electron microscopy experiments which were performed by Dr. Edward J. Brignole under the supervision of Professor Catherine L. Drennan at Massachusetts Institute of Technology. Gas chromatography – mass spectrometry data was collected by Dr. Bo Wang of the Texas A&M Department of Chemistry Mass Spectrometry Facility. The *in vivo* experiments were conducted and analyzed by Dr. Jonathan G. Vanvranken under the supervision of Professor Jared Rutter and Professor Dennis Winge from the University of Utah. Kinetic parameter determination for $SDA_{ec}U$ and $SDA_{ec}UF$ was conducted by Dr. Shachin Patra under the supervision of Professor David P. Barondeau at Texas A&M University. I wrote the manuscript with the help of Dr. David P. Barondeau and our collaborators. Additionally, I prepared or edited all of the figures for publication.

Most of the experiments presented in Chapter III were conducted or designed by me. Steven Havens aided in protein complex and crystal tray preparation under the supervision of Professor David Barondeau. Cheng-Wei Lin is a co-first author on this manuscript and contributed to the execution of the native ion-mobility mass spectrometry experiments under the supervision of Dr. David Barondeau and Dr. David Russell at Texas A&M University. Dr. Shachin Patra constructed the Δ1-55NFS1(Q64S, P299H, L300Q) variant and conducted the activity and FXN binding experiments for this variant in the presence of ISD11 and ACP_{ec}. Initial activity measurements, small-angle X-ray scattering data analysis, and crystallography experiments were conducted by me. High throughput SAXS measurements were conducted at the SIBYLS beamline 12.3.1 at the Advanced Light Source in Berkeley by Kathryn Burnett. Figures were prepared and edited by me.

A majority of the experiments performed in Chapter IV were conducted by me. The cation-exchange coupled small-angle X-ray scattering experiments were conducted by me with the help of Dr. Srinivas Chakravarthy at the BioCAT (18ID) beamline at the Advanced Photon Source. Data processing was conducted by me. High throughput frame by frame subtractions were conducted using a custom Python script written by Dr. Jesse Hopkins from the BioCAT (18ID) beamline at the Advanced Photon Source. Steven Havens helped prepare protein complexes for experiments, and Cheng-Wei Lin conducted the native ion-mobility mass spectrometry experiments under the supervision of Dr. David Barondeau and Dr. David Russell at Texas A&M University. Figures were prepared or edited by me.

Work presented in this dissertation was supported by the National Institutes of Health/National Institutes of General Medical Sciences R01GM096100, the National Science Foundation CHE 1508269, and the Robert A. Welch Foundation A-1647 grants.

TABLE OF CONTENTS

Page

LIST OF FIGURES

LIST OF TABLES

Page

CHAPTER I

INTRODUCTION AND LITERATURE REVIEW

Iron-Sulfur Clusters: Early Discovery

The first report of a possible iron-sulfur (Fe-S) protein was published in 1949 by Otto Warburg in which the carbon-monoxide (CO) inhibited photoactivation spectrum of hydrogenase was measured.[1, 2] This spectrum had a uniquely lower extinction coefficient (10^5) at 436 nm which was typical of other small molecule Fe-S species and unlike the typically observed extinction coefficient for CO treated heme compounds (10^8).[1, 2] While this work was not immediately pursued, it laid the ground work for the possibility of additional inorganic based protein cofactors. Subsequent reports of unique enzymes which could aid in the reduction of substrates in the absence of heme or flavin cofactors appeared in the late 1950s and early 1960s.[3-5] These reports crucially identified early ferredoxins which provided the foundation for the identification of Fe-S clusters as not only biologically relevant, but also essential protein cofactors that function in a variety of different pathways including photosynthesis and oxidative respiration.[6, 7]

As research progressed in the Fe-S cluster field, the chemistry of Fe-S cluster ligand spheres, geometries, and stoichiometries was defined, and the widespread use of these cofactors in different metabolic and biosynthetic pathways was uncovered. In addition to the roles of these Fe-S proteins, there was great interest in the acquisition of the cofactor itself by the target protein. While Fe-S enzymes can be reconstituted *in vitro* by the addition of inorganic sulfide, ferrous/ferric iron, and free thiols,[6, 8, 9] the concentration of these reagents *in vivo* would be toxic to the host organism and would lead to oxidative stress via Fenton chemistry[10] or inhibition of respiratory complex IV.[11] Therefore, the investigation of a unique biosynthetic system for the synthesis of Fe-S clusters was thoroughly sought-after by many labs starting in the early 1990s.

Here we aim to broadly cover different types of Fe-S clusters and their synthesis. We will cover the three major Fe-S cluster biosynthetic pathways. We will first cover the early discoveries of the nitrogen fixation (NIF) and iron-sulfur cluster (ISC) pathways in prokaryotes. Next, we will address the SUF pathway in prokaryotes. Finally, our primary focus will be on the ISC pathway in eukaryotes with an in-depth discussion on the individual protein components involved in mitochondrial Fe-S cluster biosynthesis.

Forms and Function

Fe-S clusters are protein cofactors formed by iron and inorganic sulfide. These clusters are often ligated to proteins by cysteine or histidine sidechains (Figure I.1). However, there are instances where these clusters can be ligated by other amino acid side-chains such as serine[12] and aspartic acid[13] or even by the protein backbone amide nitrogen.[14] Fe-S clusters are also present in a variety of different iron-to-sulfide stoichiometries. Given the wide range of Fe-S cluster forms and ligation environments, the delocalization of electron density over the iron and sulfide atoms primes these clusters for a wide range of physiological functions such as electron transfer and substrate activation.

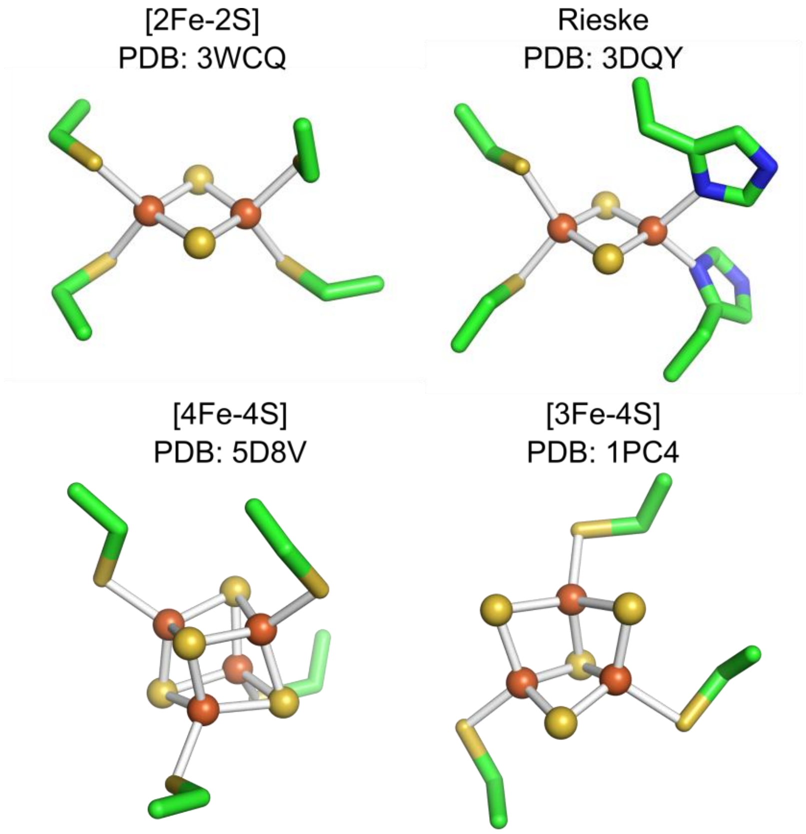

Figure I.1 Structures of classical iron-sulfur clusters. Figures were prepared using PyMOL v 1.3 using the following PDB IDs 3WCQ, 3DQY, 5D8V, and 1PC4. Atoms are colored in the following way: iron (orange), sulfur (yellow), and carbon (green). Coordinate covalent bonds are shown as white sticks, and backbone protein atoms have been removed for clarity.

Classical Iron-Sulfur Clusters

The most common forms of Fe-S clusters are $[2Fe\text{-}2S]^{+/2+}$, $[3Fe\text{-}4S]^{0/+}$, and $[4Fe\text{-}4S]^{+/2+/3+}$ where $Fe^{2+/3+}$ ions are tetrahedrally coordinated by protein sidechains and bridging sulfide ligands (Fig. I.1).[15-18] The variability in geometric form, electronic state, first coordination sphere, and surrounding protein environment tunes the redox and binding properties of the cluster for their physiological purpose. One of the classical examples of Fe-S cluster function is within ferredoxins. Ferredoxins often contain [2Fe-2S], [3Fe-4S], or [4Fe-4S] clusters. Ferredoxins with [2Fe-2S] clusters with redox potentials centered around -320 mV[2, 19, 20] can be found in a variety of different biosynthetic pathways including Fe-S cluster and steroid biosynthesis in humans.[21] These clusters are often ligated by cysteine residues; however, the Rieske type ferredoxin coordinates one of the iron atoms in the cluster with two histidine ligands (Fig. I.1). This shifts the redox potential of the cluster from about -50 to +400 mV[20, 22] where, for example, it is used in the oxidation of ubiquinol and reduction of cytochrome c within respiratory complex III for oxidative phosphorylation.[22, 23] On the other hand, [4Fe-4S] containing ferredoxins have reduction potentials centered around -500 mV for the +2 to +1 couple and +300 mV for the 3+ to 2+ couple.[2, 19, 20, 24] Interestingly, there are also polyferredoxins which can reach redox potentials close to -700 mV.[2, 19, 25] Lastly, there exist unique situations where ferredoxins contain [3Fe-4S] clusters shifting the reduction potential of these clusters towards -100 mV.[2, 19] Although ferredoxin is the prototypical electron transfer example for these cluster types, these cluster forms can also be found within a variety of different enzymes such as hydrogenase,[26] acetyl-CoA synthase carbon monoxide dehydrogenase,[27] sulfite reductase,[28] and respiratory complexes[29] where they function as electron wires to the active site cofactor.

While classical Fe-S clusters can function in electron transfer, they can also function in substrate binding. Aconitase is a prime example where one iron atom in its [4Fe-4S] cluster does not have a cysteine ligand donated from the protein, but instead, directly ligates its substrate citrate for isomerization to isocitrate.[30, 31] In mammals, an additional form of aconitase, otherwise named iron-regulatory protein 1 (IRP1), can be found in the cytosol. Under iron deplete conditions, IRP1 no longer contains an Fe-S cluster and binds to iron regulatory elements on mRNA.[32] This IRP1 binding stabilizes mRNA for receptors involved in cellular iron import and represses translation of mRNA for proteins such as the iron storage protein ferritin.[6, 32]

An additional example of [4Fe-4S] cluster enzymes is the radical S-adenosyl methionine (SAM) superfamily. These enzymes utilize an open coordination position on an iron atom of the cluster to coordinate SAM via the carboxylate and amine moieties of the methionine. Upon reduction of the cluster, the donated electron is injected into SAM causing a homolytic cleavage between the S-C(5’) bond generating a deoxy-adenosyl radical, which can act as a powerful oxidant and commonly functions in hydrogen atom abstraction either on the parent protein or the target substrate.[33] Fascinatingly, some members of the radical SAM family, biotin synthase (BioB)[34] and lipoyl synthase (LipA),[12] have been shown to use an additional auxiliary Fe-S cluster as a sulfur donor to the substrate after hydrogen atom abstraction by the deoxy-adenosyl radical. The radical

SAM family of enzymes is a clear example of the richness in chemistry that can be achieved by utilizing Fe-S clusters.

Finally, classical Fe-S clusters can function in regulation and structure stabilization. Proteins such as SoxR and IscR utilize [2Fe-2S] clusters as sensors for regulatory purposes. For example, under oxidative stress, the cluster on SoxR becomes oxidized, a conformational change occurs, and the transcription of SoxS follows.[35] SoxS is a transcriptional activator of the superoxide response regulon in *Escherichia coli*.[36] The function of IscR will be discussed later in the text. Another intriguing form of regulation occurs within fumarate nitrate reduction regulator (FNR) in which reversible degradation of its [4Fe-4S] cluster under oxygen-rich conditions generates both the [2Fe-2S] and apo-forms of the enzyme. The active form of the enzyme contains a $[4Fe\text{-}4S]^{2+}$ cluster which binds to DNA and turns on the expression of anaerobic metabolic genes. Degradation of this cluster causes the loss of FNR activity and subsequent activation of aerobic metabolic genes.[37-39] In reference to structural based regulation, endonuclease III and MutY utilize a [4Fe-4S] cluster to place a specific set of basic residues for their interaction with the negatively charged phosphate backbone of DNA.[40, 41] While initial work suggested that the cluster undergoes no oxidation or reduction and serves no catalytic role in these cases, work by the Barton lab has suggested that these types of enzymes utilize the Fe-S cluster to localize and repair DNA damage via a charge transport mechanism that is dependent on the redox state of the cluster.[42]

Clearly, classical Fe-S clusters serve a variety of catalytic purposes from electron transfer to substrate binding and activation. In addition, these clusters can use their redox properties to activate or inactivate the parent proteins' regulatory purposes. Lastly, enzymes can also use Fe-S clusters as structural motifs to facilitate binding interactions. Therefore, these clusters are valuable cofactors in the context of their host organisms.

Unique Iron-Sulfur Clusters

Fe-S clusters also come in more complex stoichiometric and geometric forms. Sulfite reductase (Fig. I.2A)[7] utilizes a [4Fe-4S] cluster to transfer electrons directly to a siroheme for the six electron reduction of sulfite to hydrogen sulfide.[28] Carbon monoxide dehydrogenase (Fig. I.2B, figure generated prior to structural determinations)[7] utilizes a [3Fe-4S-Ni] cluster coupled to a dangling iron atom to achieve the oxidation of carbon monoxide to carbon dioxide.[27, 43, 44] Lastly, nitrogenase uses two multi-nuclear Fe-S clusters for the reduction of nitrogen to ammonia (Fig. I.2C,D).[7, 14] While these complex reactions all require the presence of complex Fe-S clusters, how these clusters are synthesized and delivered to targets *in vivo* generated a large amount of interest within the bioinorganic community. The remainder of this chapter will discuss Fe-S cluster biosynthetic pathways.

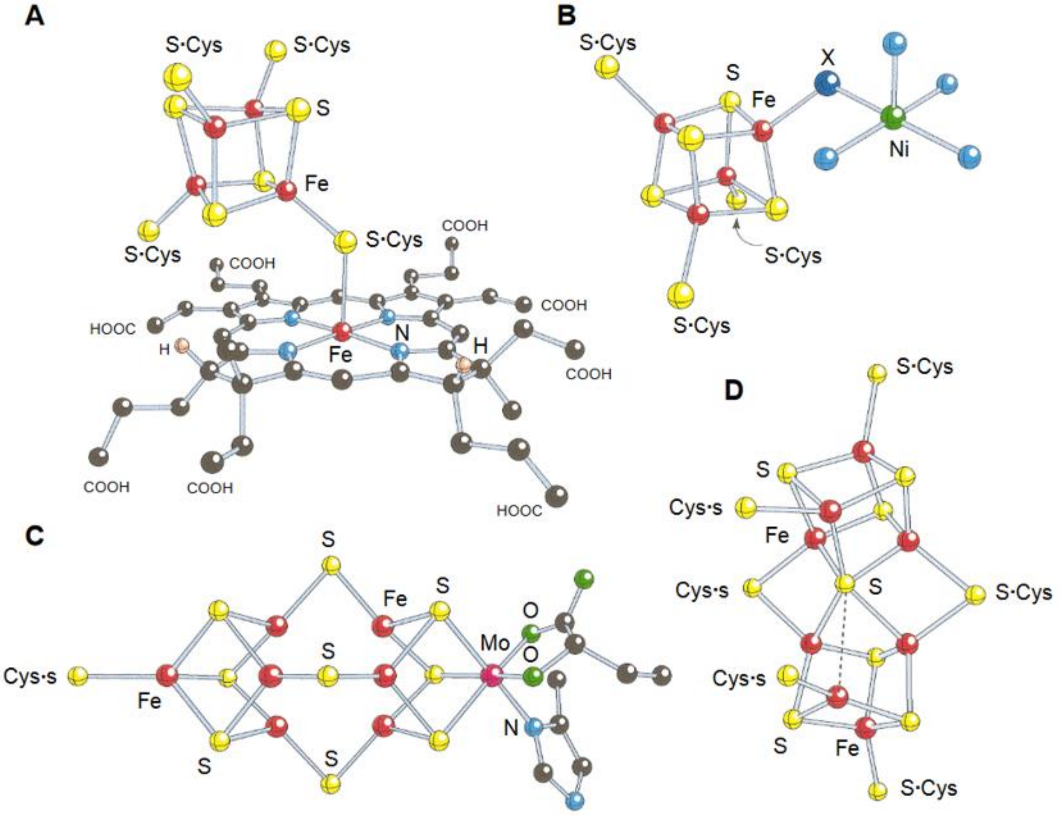

Figure I.2 Structures of unique iron-sulfur cluster active sites. Cofactor structures are represented by ball and stick for the following enzymes (A) sulfite reductase (B) carbon monoxide dehydrogenase (C-cluster) prior to structure determinations (C) nitrogenase (Mo-Fe cofactor), and (D) nitrogenase (P-cluster). From "Iron-Sulfur Clusters: Nature's Modular, Multipurpose Structures" by Beinert, H., Holm, R. H., and Munck, E., 1997. *Science*, *277*, 653-659. Reprinted with permission from The American Association for the Advancement of Science. Copyright 1997 by The American Association for the Advancement of Science.

Nitrogen Fixation (NIF) Iron-Sulfur Cluster Biosynthetic Pathway

The first discovery of an Fe-S cluster biosynthetic pathway was reported in 1989 by Dennis Dean and co-workers when attempting to elucidate the maturation of nitrogenase cofactors. Key sequencing experiments and genetic knockouts in *Azotobacter vinelandii* revealed fifteen genes specific to the *nif* operon that could play a potential role in the maturation process.[45] The first indication that these genes were involved in Fe-S cluster biosynthesis and maturation of nitrogenase came from genetic knockouts of *nif* specific genes, *nifS* and *nifU*, which generated iron (Fe) and molybdenum-iron (MoFe) nitrogenase proteins containing lower levels of activity.[46, 47] Recombinant production of NifS revealed a homodimeric enzyme that contained a pyridoxal 5'-phosphate (PLP) cofactor and was capable of converting L-cysteine to L-alanine and hydrogen sulfide in the presence of the reductant dithiothreitol (DTT).[48] Further enzymology, including inactivation studies by alkylating agents, and structural studies demonstrated that NifS contains a catalytic mobile-loop cysteine that is required for the desulfurization of cysteine and generation of a persulfide intermediate.[48-50]

In order to achieve maturation of the Fe and Mo-Fe proteins in nitrogenase, the persulfide sulfur from NifS would need to be delivered to a downstream acceptor protein where an Fe-S cluster could ultimately be synthesized. The idea that NifU could be an Fe-S cluster scaffold was plausible as it had already been shown that the MoFe-cofactor was synthesized separately from the target polypeptide.[51, 52] Subsequent robust spectroscopic and functional characterization of NifU demonstrated that it was capable of forming a [2Fe-2S][53, 54] and that the NifS persulfide sulfur was the source of the inorganic sulfide.[55]

In fact, when in the presence of NifS and NifU, the Fe-protein of nitrogenase could be activated thereby demonstrating the potential implications of an Fe-S cluster assembly system and intermediate scaffold.[56]

Iron-Sulfur Cluster (ISC) Biosynthetic Pathway in Prokaryotes

Biochemical studies on *A. vinelandii* cells grown under conditions not requiring nitrogen fixation (*nifS* deletion) and small sequencing efforts revealed the presence of an additional cysteine desulfurase that could participate in Fe-S cluster biosynthesis.[57] These genes were proposed to be the general house-keeping proteins involved in the biosynthesis and delivery of Fe-S clusters to targets not involved in nitrogen fixation. Significant breakthroughs in genome sequencing then allowed for the further identification of these house-keeping genes in *E. coli*,[58] *Hemophilus influenza*,[59] *Saccharomyces cerevisiae*,[60] and *Homo sapiens*.[57, 61] There are eight genes (Fig. I.3)[62] within the *isc* operon of *E. coli*, many of which have been thoroughly characterized.

The first gene in the operon encodes for the transcriptional regulator IscR which binds a [2Fe-2S] cluster and represses the *isc* operon. However, under oxidative stress or iron limiting conditions, the apo form of IscR transcriptionally activates the *suf* Fe-S biosynthetic operon to protect Fe-S assembly under high O_2 conditions (to be discussed below).[63-65] The second gene in the *isc* operon encodes for the PLP dependent cysteine desulfurase IscS.[66] IscS is a group I cysteine desulfurase and shares high sequence similarity with NifS.[57, 67] Like NifS, IscS delivers persulfide sulfur to the next gene product IscU where [2Fe-2S] cluster assembly occurs.[68, 69] An additional gene product from this operon, ferredoxin (Fdx), has been proposed to be the electron donor for this process.[70-72]

Interestingly, this operon contains two additional gene products with relatively unknown functions, IscA and IscX. IscA has been proposed to be an iron donor[73-75] and an intermediate scaffold which can functionally reconstitute ferredoxin's [2Fe-2S] cluster.[76-78] On the other hand, IscX has been proposed to be an iron donor.[79, 80] Additionally, this operon features two chaperones HscB and HscA which play a role in cluster transfer from IscU to target proteins via an unknown structural perturbation mechanism.[81-83] An additional gene, CyaY, which does not appear in the *isc* operon, has been shown to interact with IscS[84, 85] and act as an inhibitor of Fe-S cluster biosynthesis *in vitro*.[80, 86, 87] Additionally, CyaY has also been suggested to be an iron donor.[74, 84]

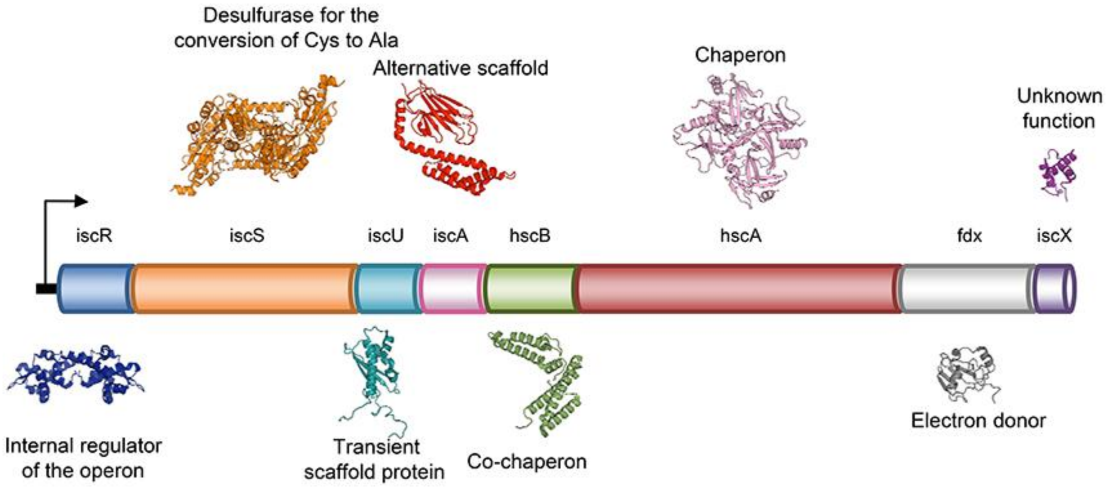

Figure I.3 Depiction of the *isc* operon of *E. coli* including x-ray crystal structures. Reprinted from "Hybrid Methods in Iron-Sulfur Cluster Biogenesis" by Prischi, F., and Pastore, A., 2017. *Front. Mol. Biosci. 4,* 1-13. Copyright 2017 by Prischi and Pastore which is covered under the open-access terms of the Creative Commons Attribution License (CC BY 4.0). The original work can be found here: https://www.frontiersin.org/articles/10.3389/fmolb.2017.00012/full#h11.

Sulfur Assimilation (SUF) Iron-Sulfur Cluster Biosynthetic Pathway

While some [2Fe-2S] clusters are oxygen stable undergoing a single oxidation event, [4Fe-4S] clusters tend to degrade rapidly in the presence of oxygen. Some prokaryotic organisms utilize a specialized Fe-S cluster biosynthetic pathway to generate clusters in these instances. An additional Fe-S cluster biosynthetic pathway in *E. coli* was discovered upon mutation of the *sufD* and *sufS* genes.[88] SufS is a group II cysteine desulfurase featuring a shorter mobile loop and an additional β-hairpin at the dimer interface of the functional homo dimer.[89, 90] These mutants showed defects in the ferric iron reductase FhuF which is a [2Fe-2S] cluster containing protein.[88] Unlike the *isc* operon, the *suf* operon is not essential under normal growth conditions and serves as a redundant method for the generation of Fe-S clusters.[91] The operon is activated under oxidative stress conditions[92] and features a unique Fe-S cluster assembly scaffold in which persulfide sulfur on SufS is transferred to an intermediate persulfide scaffold, SufE,[93, 94] and then to the assembly complex composed of SufB, SufC, and SufD.[95, 96] SufA has been proposed as an intermediate cluster scaffold/transfer protein.[96] Mechanistic work focused on the SUF system will not be described in detail here.

Iron-Sulfur Cluster (ISC) Biosynthetic Pathway in Eukaryotes

Preface to Eukaryotic Fe-S Cluster Biosynthesis

A large amount of research conducted on the eukaryotic ISC pathway was supplemented by early experiments conducted on the prokaryotic system. Here we will describe in detail the specific functions of each of the proteins within the eukaryotic [2Fe-2S] cluster assembly pathway. Given the high homology between the eukaryotic and prokaryotic ISC systems, we will also describe key experiments pertaining to the prokaryotic systems that have provided valuable insights into the difference in functions of the respective proteins in the pathways.

Eukaryotic Fe-S Cluster Biosynthetic Subcomplex

In the late 1990s, work by the Culotta, Dancis, and Lill groups identified and characterized genes involved in the synthesis of Fe-S clusters in *Saccharomyces cerevesia*.[97-99] Eukaryotic Fe-S cluster biosynthesis occurs within the mitochondria matrix (Fig. I.4)[100] and is an essential process.[99, 101] Clusters are synthesized by a multi-protein complex and are transferred downstream to [2Fe-2S] targets using a scaffold-glutaredoxin-chaperone coupled system or to a potential [4Fe-4S] biosynthetic machinery consisting of ISA1, ISA2, and IBA57.[102, 103] These clusters are then transferred to their destination using NFU and BOL targeting factors.[100] This discussion will be restricted to the [2Fe-2S] cluster biosynthetic machinery. In addition, nomenclature between yeast and humans is different, and a legend has been provided in Figure I.4 to clarify the differences. The human nomenclature will be utilized throughout the remainder of the text.

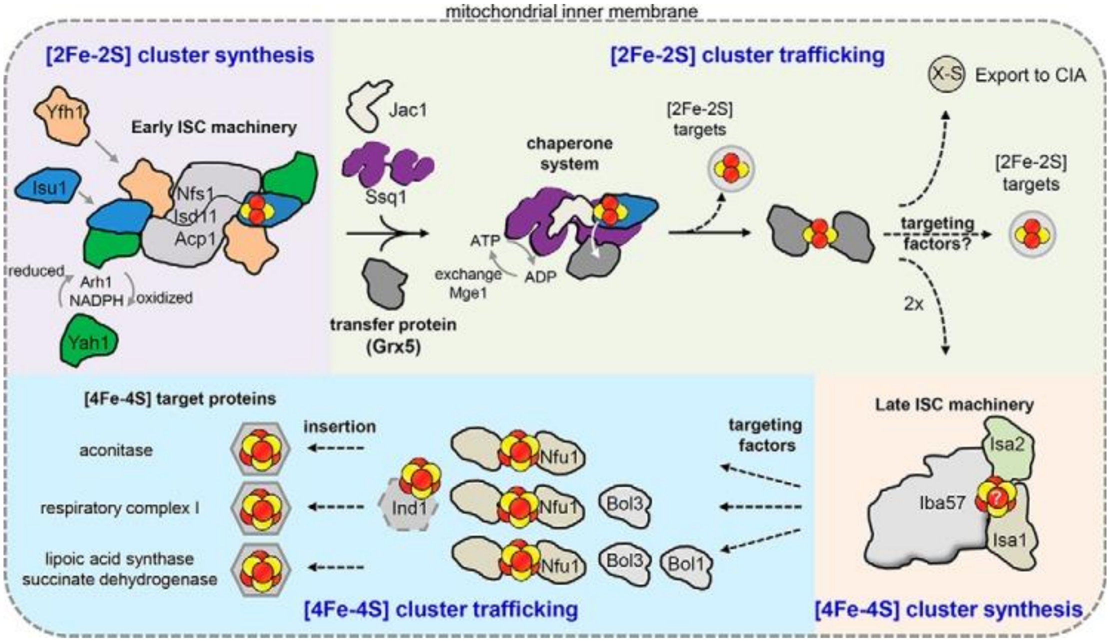

Figure I.4 Cartoon schematic representation of mitochondrial Fe-S cluster biosynthesis and transfer. Here the nomenclature for *S. cerevisiae* is used where the following are all equivalent in humans: Nfs1 (NFS1), Isd11 (ISD11), Acp1 (NDUFAB1 or ACP), Isu1 (ISCU2), Yfh1 (FXN), Yah1 (FDX2), Arh1 (FDXR), Isa1 (ISCA1), Isa2 (ISCA2), and Iba57 (IBA57). *Journal of Biological Chemistry* by American Society for Biochemistry and Molecular Biology Inc. Reproduced with permission of American Society for Biochemistry and Molecular Biology Inc. in the format Thesis/Dissertation via Copyright Clearance Center. Reprinted with permission from “Iron-sulfur cluster biogenesis and trafficking in mitochondria” by Braymer, J. J. and Lill, R., 2017, *J. Biol. Chem.*, 292, 12754-12763. Copyright 2017 by American Society for Biochemistry and Molecular Biology.

At the center of this biosynthetic pathway is the group I PLP-dependent cysteine desulfurase, NFS1. This enzyme is essential to eukaryotic organisms and is localized in both the cytosol and mitochondria,[104] but its primary function appears to be in the mitochondria.[105] NFS1 catalyzes the conversion of L-cysteine to L-alanine and persulfide sulfur on a mobile loop cysteine. The mechanism of PLP dependent conversion of cysteine to alanine has been well established by the Dean and Bollinger groups using both group I and group II cysteine desulfurases (Fig. I.5).[106] In this mechanism, the amine of cysteine nucleophilically attacks the Schiff base formed between the enzyme's lysine and PLP to generate a Cys-aldimine species. A base of unknown origin deprotonates the Cα carbon of cysteine and electrons are then cycled down into the PLP to generate a Cys-quinonoid species. Electrons are then recycled through the PLP ring, and deprotonation of the mobile loop cysteine occurs to generate a nucleophilically activated cysteine residue and the Cys-ketimine intermediate. The mobile loop cysteine then participates in C-S bond cleavage to generate a mobile loop-based persulfide. Acid-base chemistry follows to generate the product alanine. Much of this mechanism has been validated by functional studies of site-directed mutants, X-ray crystallographic structures, hydrogen-deuterium exchange, and stopped-flow ultraviolet-visible spectroscopy experiments.[48-50, 89, 106, 107]

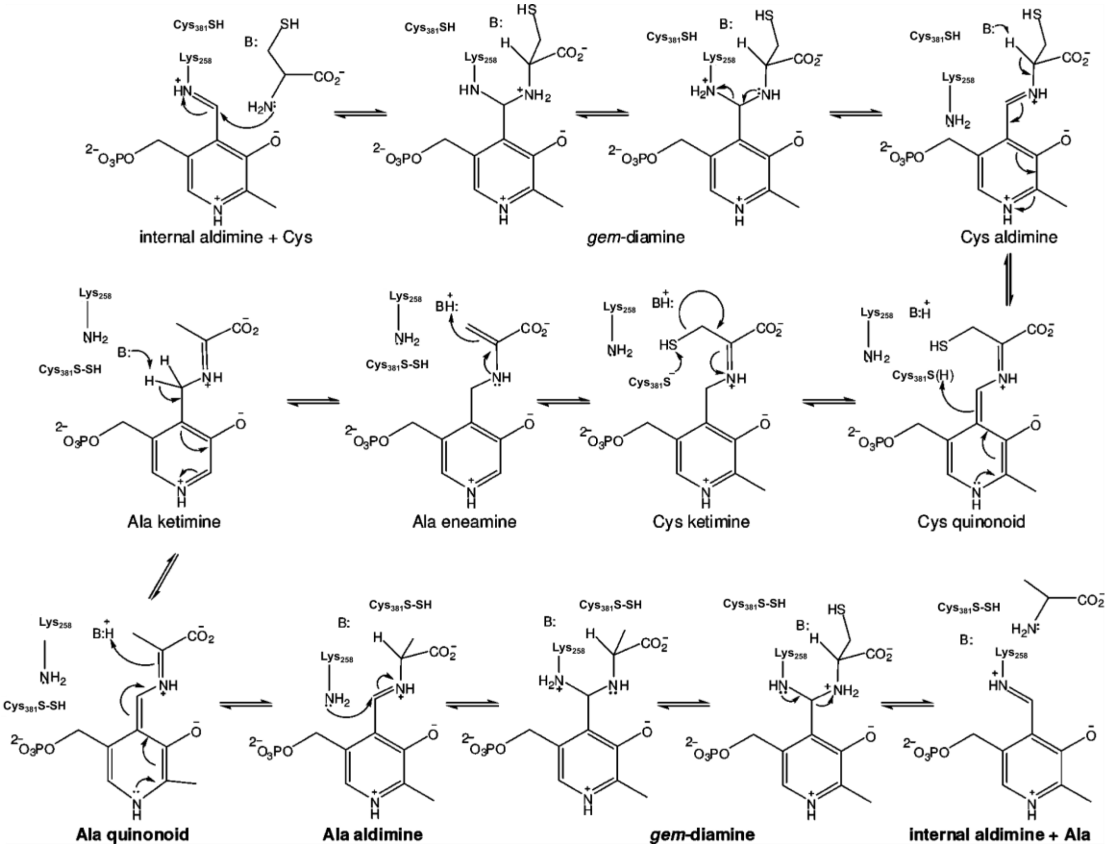

Figure I.5 Cysteine desulfurase mechanism. Reprinted (adapted, numbering changed to NFS1 residues) with permission from “Kinetic Analysis of Cysteine Desulfurase CD0387 from *Synechocystis sp*. PCC 6803: Formation of the Persulfide Intermediate” by Behshad, E. and Bollinger, M. J., 2009. *Biochemistry*, 48, 12014-12023. Copyright 2009 American Chemical Society. This figure was adapted from Zheng et al. and requires additional permission. Reprinted (adapted) with permission from “Mechanism of the Desulfurization of L-Cysteine Catalyzed by the nifS Gene Product” by Zheng, L., White, W. H., Cash, C. L., and Dean, D. R., 1994. *Biochemistry*, 33, 4714-4720. Copyright 1994 American Chemical Society.

While the basic principles of this mechanism are universal for cysteine desulfurases, there are substantial differences between NFS1 and previously characterized group I cysteine desulfurases. A prime example is a direct comparison between the *E. coli* IscS and human NFS1, which exhibit a 60 % sequence identity. *E. coli* IscS is a strong homodimer[108, 109] for which the structure has been determined (Fig. I.6).[85, 110] Although early analytical size exclusion chromatography experiments described NFS1 as a homodimer,[111] experiments conducted on NFS1 isolated from *S. cerevisiae* and more recent experiments characterizing human NFS1 suggest that there is also a monomeric fraction,[112-114] which has not been reported for *E. coli* IscS. In addition to the oligomeric state, the activity profiles of these enzymes are vastly different. Activities of cysteine desulfurases are typically measured using the methylene blue assay in which an external reductant, often DTT, is used to cleave the persulfide on the cysteine desulfurase to generate free sulfide. The reaction is then quenched with acid. *N*,*N*-dimethyl-*p*-phenylenediamine and ferric chloride are added to synthesize methylene blue, which can be quantified by its absorbance at 670 nm. *E. coli* IscS exhibits a k_{cat} of 7.5 ± 0.1 min^{-1} and a K_{M} for cysteine of 17 ± 2 µM.[87] Whereas, human NFS1 was reported to be only capable of performing a single turnover and is unstable often resulting in precipitation of the enzyme.[111]

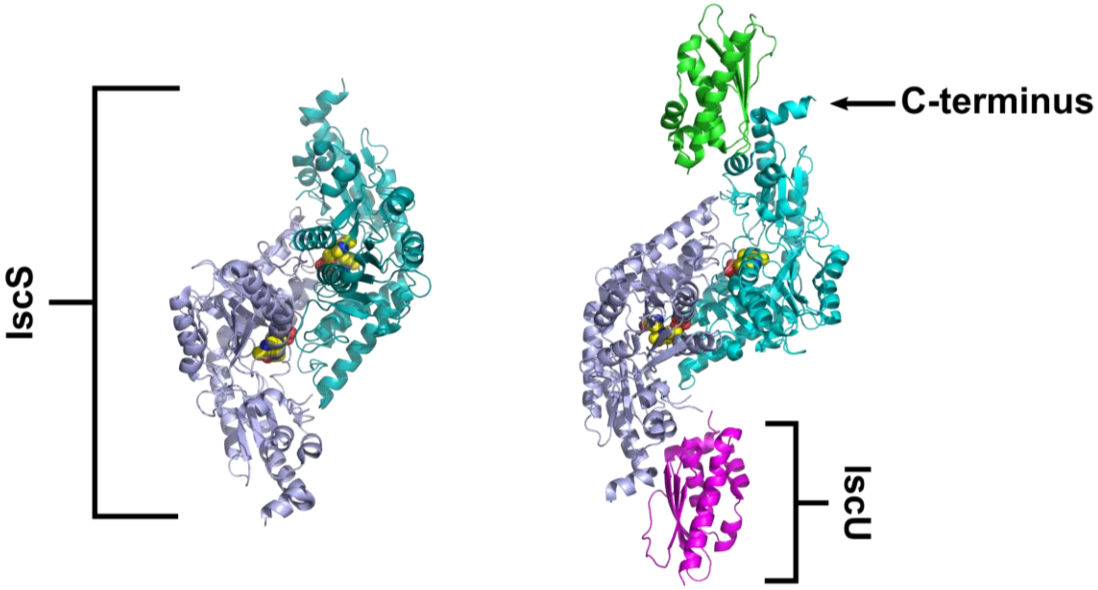

Figure I.6 X-ray crystal structures of *E. coli* IscS and IscS-IscU. The IscS dimer (1P3W.pdb) is colored teal and light blue. The PLP cofactor is show in yellow spheres with heteroatoms colored by common notation. The IscU subunits (3LVL.pdb) are colored green and pink.

Clearly, there exist distinct differences between NFS1 and IscS with regard to oligomeric state and activity. However, an additional difference is the presence of the eukaryotic-specific adaptor protein ISD11 which was discovered in the mid to late 2000s. ISD11 appears to trace back to an α-proteobacteria endosymbiotic event consistent with the acquisition and presence of Fe-S cluster assembly proteins within the mitochondria.[115] Knockout of ISD11 in *S. cerevisiae* and suppression of ISD11 using siRNA in human cells resulted in growth defects and loss of activity for classical Fe-S cluster containing enzymes such as aconitase.[112, 116, 117] Pull-down experiments and size-exclusion chromatography demonstrated that ISD11 tightly interacts with NFS1 and generates an $\alpha_2\beta_2$ complex with drastically improved stability.[111, 112, 117] However, the cysteine desulfurase activity of NFS1 is still quite low in the NF$\underline{\text{S}}$1-IS$\underline{\text{D}}$11 complex, called SD, compared to IscS. SD exhibits a k_{cat} of 1.9 ± 0.1 min^{-1} and a K_{M} for cysteine of 340 ± 60 µM.[111, 118] Specific residues on ISD11 have been targeted to show their importance, including the N-terminus.[114, 119] In fact, one clinical mutation, R68L, results in oxidative phosphorylation deficiency and a loss of in vitro activity for the SD complex. This mutant still forms a complex with NFS1 clearly demonstrating there are critical interactions between ISD11 and NFS1 that are required for cysteine desulfurase activity.[113, 119] This is consistent with the notion that NFS1 in *S. cerevisiae* is incapable of forming a persulfide in the absence of ISD11 as demonstrated by experiments using [^{35}S]-cysteine.[120] The structure-function relationship between NFS1 and ISD11 was only recently discovered when structures of NFS1 in complex with ISD11 were determined.[121, 122] These structures will be discussed in depth in later chapters.

The next protein involved in Fe-S cluster biosynthesis was recently discovered to be the mitochondrial acyl-carrier protein (ACP). Mitochondrial ACP is involved in the generation of an octanoyl-ACP species in which an eight-carbon long acyl-chain is tethered to its 4'-phosphopantetheine (4'-PPT) cofactor via a thioester bond, which is used as a substrate for lipoic acid biosynthesis.[123, 124] The substrate for fatty acid synthesis is acetyl-CoA. Knockdowns of mitochondrial ACP in mammals results in a decrease in lipoic acid content on proteins requiring the cofactor and loss of function in respiratory complex I.[125] Defects in other respiratory complexes which utilize ACP for assembly are also observed.[126] Interestingly, *in vitro* assays utilizing human β-ketoacyl synthase showed the efficient synthesis of mitochondrial ACP containing acyl chains up to fourteen carbons long,[127] and additional *in vivo* biochemistry studies suggest that these species are essential for mitochondrial biogenesis.[128]

Remarkably designed experiments by the Winge and Rutter groups used *S. cerevisiae* to narrow down its function in 2016. Due to the non-essential nature of lipoic acid biosynthetic genes in this organism, the essential function of mitochondrial ACP in *S. cerevisiae* was directly investigated. Using ACP knockdowns, the group demonstrated depletion of the NFS1-ISD11 complex and loss of aconitase activity, which suggests the mitochondrial ACP plays a direct role in Fe-S cluster biosynthesis. In fact, mitochondrial ACP interacts directly with the NFS1-ISD11 complex, called SDA, and improves its stability.[129]

Intriguingly, ISD11 is a member of the LYRM superfamily that contain a conserved Leu-Tyr-Arg motif. At least eleven LYRM proteins have been identified in human cells with primary localization in mitochondria.[130] Structural[131-133] and interaction studies suggest all of these LYRM proteins interact with ACP.[126, 134-136] A recently published cryo-electron microscopy (cryoEM) structure of respiratory complex I from *Ovis aries* showed discrete interactions between mitochondrial ACP and the two LYRM proteins of the complex. In this structure, ACP threads its lipid, often 3-hydroxymyristoyl,[137-139] bound cofactor into the three-helix bundle of the LYRM proteins.[133] Mutations in the LYRM protein's LYR-motif, which directly interact with ACP, or mutation of an invariant phenylalanine that stabilizes the acyl 4'-PPT cofactor result in the loss of the ACP association and complex I activity.[132] This appears to be the same case for the NFS1-ISD11 complex where acyl-ACPs ranging from eight to fourteen carbons long with variable modification have been observed in isolation with the SDA complex from *Neurospora crassa*.[139] Additionally, upon the construction of *S. cerevisiae* strains incapable of generating acyl- or holo-ACP, by mutation of the invariant serine that covalently links 4'-PPT, loss of the NFS1-ISD11 complex and aconitase activity were observed.[129] It is expected that these interactions between ACP and LYRM proteins are similar in different complexes. Recent papers have utilized *E. coli* Acp as a functional replacement for recombinant studies using human NFS1-ISD11.[109, 121, 122] There appears to be no functional difference in the complex using human ACP.[140] This was shown to be true in structures of NFS1 in complex with ISD11 which will be discussed in depth in Chapter II and III. Additionally, while Acp has been shown to be associated with IscS in *E. coli* this interaction was reversible in the presence of an external reductant. The interaction appeared to be a disulfide linkage between the mobile loop cysteine on IscS and the 4’-PPT thiolate on Acp and was likely an artifact of aerobic isolation.[141] The physiological relevance of this interaction is still unknown.

Fe-S Cluster Biosynthesis on the Scaffold ISCU2

In order to synthesize an Fe-S cluster *in vivo*, a scaffold protein is required. This process requires two cysteine substrates, two ferrous iron atoms, and two electrons. The scaffold protein in human Fe-S cluster biosynthesis is ISCU2. In *E. coli*, the bacterial homolog of ISCU2, IscU, binds to the C-terminal α-helix of IscS and is capable of directly accepting the persulfide sulfur (Fig. I.6).[85] Given the high degree of homology between the prokaryotic and eukaryotic ISC systems, the function of ISCU2 and its interaction interface with NFS1 were hypothesized to be the same. ISCU2 forms a stable complex with the SDA complex that has been named SDAU.[109] The predicted interaction interface was independently validated by the Craig group in 2012 by the construction of a C-terminal truncation of *S. cerevisiae* NFS1. Upon co-immunoprecipitation a substantial loss of binding to the scaffold protein, ISCU2, was observed in addition to increased instability *in vivo* due to a regulatory protease called Pim1.[142] Additionally, recent x-ray crystal and cryoEM structures of the human enzymes have demonstrated the interaction interface between the C-terminus of NFS1 and ISCU2.[122, 143]

The mechanism by which clusters are synthesized on ISCU2 is poorly understood. ISCU2 has three conserved cysteines, and significant evidence exists for persulfide or polypersulfide formation on these residues in both prokaryotes and eukaryotes.[69, 144-146] However, the question of the order in which substrates are incorporated, sulfur first or iron first mechanisms, still exists. Extended X-ray absorption fine structure (EXAFS) spectroscopy data from the Stemmler group demonstrated iron binding to primarily oxygen and nitrogen ligands on ISCU2; however, upon initiation of [2Fe-2S] cluster formation, sulfur-based ligands to iron were observed.[147] Additionally, it has been shown that persulfide can be generated on ISCU2 in the absence of iron.[144, 145] Neither the iron bound or persulfide bound scaffold protein have been shown to be kinetically competent intermediates in Fe-S cluster biosynthesis. Additionally, for many years, the external reductant, DTT, has been used in Fe-S cluster biosynthesis assays which plays a role in persulfide cleavage,[111, 118] thiol-exchange reactions,[145] and off-path Fe-S mineral assembly as shown by low-temperature Mössbauer spectroscopic studies.[148] Based on work in prokaryotes, it was postulated that the human system could synthesize [4Fe-4S] clusters via a reductive coupling mechanism.[149] However, this was demonstrated to not be the case in studies that avoided the use of DTT in Fe-S cluster assembly assays. In this study, $[2Fe\text{-}2S]^{2+}$ clusters were shown to be transiently synthesized by the SDU complex and transferred to ferredoxin (FDX1), and [4Fe-4S] cluster synthesis could be observed in the presence of DTT.[150]

Another question surrounding the synthesis of clusters on ISCU2 is the electron donor. While DTT has been used in the past, evidence from prokaryotes suggests a ferredoxin (Fdx) – ferredoxin reductase system is the physiological electron donor.[71, 72] However, since two of the electrons required for cluster synthesis come from ferrous iron, an additional two electrons must come from ferredoxin. This presents a mechanistic problem as ferredoxin is a single electron donor, and no evidence has been presented that the ferredoxin reductase system interacts with the entire complex. It has been proposed in the prokaryotic system that a radical persulfide anion intermediate is generated on IscS.[71, 80] However, no direct evidence for this species exists. In humans, there are two mitochondrial ferredoxins, FDX1 and FDX2.[21, 151] Experimental evidence suggests that both forms can cleave the persulfide on NFS1 and potentially participate in Fe-S cluster biosynthesis.[152-154] FDX1 has an additional role in steroid biosynthesis.[21, 154] Assays which utilize ferredoxins have yet to correlate the amounts or rates of NADPH consumption with Fe-S cluster synthesis. In addition, these experiments have used UV-visible spectroscopic methods to detect cluster synthesis by following the formation of oxidized [2Fe-2S]-ISCU2.[152, 155] However, oxidized [2Fe-2S]-FDX has the same absorbance features. A better detection assay would be to use circular dichroism (CD) spectroscopy as the [2Fe-2S] cluster bound to these different proteins have distinct spectral features.

Allosteric Activator Frataxin

Frataxin (FXN) is a 210 amino acid protein which localizes to the mitochondria.[156, 157] It was initially identified in 1996 as the protein responsible for the onset of Friedreich's ataxia. Identified on chromosome 9q13, patients with point mutations or unstable GAA triplet nucleotide expansions in the first intron produce lower levels of the protein.[158] As a result of this, defects in iron metabolism and iron overload in the mitochondria were observed.[159] This lead to the early hypothesis that FXN functions as an iron storage protein. However, this hypothesis was later challenged by a strain of *S. cerevisiae* featuring the deletion of a mitochondrial iron transporter and overexpression of FXN.[160] In this strain, the deletion results in iron accumulation in the mitochondria with similar phenotypes to FXN knockouts.[160] Based on the hypothesis that FXN could sequester and store iron, overexpression of *S. cerevisiae* FXN was predicted to alleviate the iron accumulation phenotype. However, upon a 4.5 times overexpression of FXN, in comparison to wild-type, no alleviation of iron accumulation in the mitochondria was observed.[160] Given the prevalence of this disease, a large amount of research has been conducted to understand the function of FXN.

Upon import into the mitochondria, the mitochondrial targeting peptide is cleaved, and an additional post-processing event occurs to form the functional form of FXN(81-210).[161, 162] The function of this processed protein was validated by the rescuing of a lethal frataxin deletion in murine fibroblasts by complementation with a form of human FXN only capable of generating FXN(81-210) in the mitochondria.[163] While FXN(42-210) does exist in the mitochondria, it does not appear to be essential and possibly functions in mitochondrial import.[163] Therefore we will limit the discussion to FXN(81-210).

Early studies focused primarily on the iron-binding properties of FXN. Like its structural homolog in *E. coli* (CyaY),[74] monomeric FXN has been shown to bind up to seven iron atoms per monomer with K_D values ranging from 10 to 55 μM[164] and oligomerize in the presence of ferric iron.[165] These results may be an artifact of the acidic patch on FXN that has been recently shown to form discrete interactions with an arginine-rich region at the dimer interface of NFS1 that is far from the cluster synthesis site of ISCU2.[143, 166]

While FXN is capable of binding iron, genetic studies suggest that FXN has a direct role in Fe-S cluster biosynthesis.[167, 168] In fact, FXN has a unique effect on the activity of the SDAU complex. In 2010, a report from the Barondeau group demonstrated the capability of FXN to form a complex with SDU, called SDUF, and to activate the cysteine desulfurase activity of SDU and accelerate Fe-S cluster biosynthesis. Here the group demonstrated a k_{cat} increase from 0.89 ± 0.04 min^{-1} to 5.2 ± 0.4 min^{-1} and a K_{M} decrease from 590 ± 50 μM to 11 ± 3 μM for cysteine when analyzing the SDU complex in the context of FXN.[118] Follow-up studies have further validated an increases in cysteine desulfurase activity, persulfide formation and transfer, and Fe-S cluster formation on ISCU2.[144, 145, 148, 149, 154, 166, 169-171] These results all appear to be consistent with the hypothesis that frataxin plays a role in the early stages of Fe-S cluster biosynthesis in humans.[168] In fact, Friedreich's ataxia mutants either result in the reduction in the binding of FXN to the biosynthetic complex or in its ability to stimulate the cysteine desulfurase activity.[172, 173]

Interestingly, there are some unique features of FXN when compared to the prokaryotic ISC system. For example, the structural homolog of FXN, CyaY, has been shown to be an inhibitor of *in vitro* Fe-S cluster assembly assays that include IscS and IscU.[86, 87] Unexpectedly, CyaY can be used as an activator of the human SDU complex in Fe-S cluster assembly assays, which suggests the primary functional differences between the two systems existed at the cysteine desulfurase level.[87] In addition, CyaY and Fdx compete for binding on IscS;[70, 71] whereas, FXN and FDX2 appear to bind to the SDU complex simultaneously.[154] These functional differences have strongly enforced the need for atomic resolution structures of the SDA, SDAU, and SDAUF complexes in order to establish the mechanism of FXN-based activation.

Cytosolic Fe-S Cluster Assembly

In humans, NFS1 and ISCU1 can be found in the cytosol. NFS1 appears to act as a player in molybdopterin biosynthesis.[111] Recent evidence suggests that ISCU1 is a component of cytosolic Fe-S cluster biosynthesis in humans.[174] However localization of these components to the cytosol in *S. cerevisiae* has yet to be observed and suggests differences in their assembly pathways. In fact, radiolabeling experiments from the Dancis and Pain labs have shown that both Fe-S and sulfur-based intermediates are exported from *S. cerevisiae* mitochondria through the use of the Atm1 transporter and used in cytosolic Fe-S cluster assembly.[175, 176] A discrete set of assembly proteins in a very different Fe-S cluster biosynthetic pathway also operates in the cytosol but is outside the scope of this discussion.[177]

Regulation of the Eukaryotic Fe-S Cluster Assembly Complex

Along with FXN being an allosteric activator, evidence suggests that ACP may also play a crucial role in regulating the activity of the Fe-S cluster assembly complex.[129] The requirement for long-chain acyl-ACP species for respiratory complex maturation suggests the use of ACP and the mitochondrial fatty acid synthesis pathway for acetyl-CoA level sensing.[128, 178] At high concentrations of acetyl-CoA, the TCA cycle can be used to generate reducing equivalents in the form of $FADH_2$ and NADH for oxidative respiration. Simultaneously, long-chain acyl-ACP species would be synthesized turning on both Fe-S cluster biosynthesis and respiratory complex assembly. An additional report has provided evidence for post-translational modifications in the form of phosphorylation which can regulate NFS1 activity in *S. cerevisiae*.[179]

Comments Regarding the Structures of the Eukaryotic Fe-S Cluster Assembly Complex

Up until 2017, there were no atomic resolution structures of the SDA, SDAU, or SDAUF. The Barondeau, Cygler, Yue, and Han groups have made significant advancements in these areas. In 2017, two different structures of the SDA complex[121, 122] were published along with additional structures of SDAU.[122] Advancements in cryoEM have also made it possible to determine the structure of the SDAUF complex.[143] The results of these findings and their implications will be discussed in chapter II and III of this dissertation.

CHAPTER II

STRUCTURE OF HUMAN FE-S ASSEMBLY SUBCOMPLEX REVEALS UNEXPECTED CYSTEINE DESULFURASE ARCHITECTURE AND ACYL-ACP-ISD11 INTERACTIONS[*]

Overview

In eukaryotes, sulfur is mobilized for incorporation into multiple biosynthetic pathways by a cysteine desulfurase complex that consists of a catalytic subunit (NFS1), LYR protein (ISD11), and acyl carrier protein (ACP). This NFS1-ISD11-ACP (SDA) complex forms the core of the iron-sulfur (Fe-S) assembly complex and associates with assembly proteins ISCU2, frataxin (FXN), and ferredoxin to synthesize Fe-S clusters. Here we present crystallographic and electron microscopic structures of the SDA complex coupled to enzyme kinetic and cell-based studies to provide structure-function properties of a mitochondrial cysteine desulfurase. Unlike prokaryotic cysteine desulfurases, the SDA structure adopts an unexpected architecture in which a pair of ISD11 subunits form the dimeric core of the SDA complex, which clarifies the critical role of ISD11 in eukaryotic assemblies. The different quaternary structure results in an incompletely formed substrate channel and solvent-exposed pyridoxal 5′-phosphate cofactor and provides a rationale for the allosteric activator function of FXN in eukaryotic systems. The

---

[*] Reprinted with permission from “Structure of human Fe-S assembly subcomplex reveals unexpected cysteine desulfurase architecture and acyl-ACP-ISD11 interactions” by Cory, S. A., Van Vranken, J. G., Brignole, E. J., Patra, S., Winge, D. R., Drennan, C. L., Rutter, J., and Barondeau, D. P., 2017, *Proc. Natl. Acad. Sci. U.S.A.*, 114, E5325-E5334, For the individual article: Copyright 2017 by the authors listed above.

structure also reveals the 4′-phosphopantetheine-conjugated acyl-group of ACP occupies the hydrophobic core of ISD11, explaining the basis of ACP stabilization. The unexpected architecture for the SDA complex provides a framework for understanding interactions with acceptor proteins for sulfur-containing biosynthetic pathways, elucidating mechanistic details of eukaryotic Fe-S cluster biosynthesis, and clarifying how defects in Fe-S cluster assembly lead to diseases such as Friedreich's ataxia. Moreover, our results support a lock-and-key model in which LYR proteins associate with acyl-ACP as a mechanism for fatty acid biosynthesis to coordinate the expression, Fe-S cofactor maturation, and activity of the respiratory complexes.

Significance Statement

Prokaryotic and eukaryotic organisms use analogous pathways to synthesize protein cofactors called iron-sulfur clusters. An unexplained difference between pathways is the functional requirements of the respective cysteine desulfurases. In eukaryotes, the cysteine desulfurase NFS1 requires additional accessory subunits for function. The lack of structural information has limited mechanistic insight into the role of these accessory proteins in mitochondrial Fe-S cluster biosynthesis. Here we determined crystallographic and electron microscopic structures of the NFS1-ISD11-ACP subcomplex. These results reveal an unexpected cysteine desulfurase architecture that reconciles mechanistic differences between the prokaryotic and eukaryotic systems, reveals the basis of control of iron-sulfur cluster assembly through fatty acid synthesis, and serves as a structural foundation for investigating human diseases related to iron–sulfur cluster assembly.

Introduction

Iron-sulfur (Fe-S) clusters are protein cofactors and are required for critical biological processes such as oxidative respiration, nitrogen fixation, and photosynthesis. The iron-sulfur cluster (ISC) biosynthetic pathway, which is found in most prokaryotes and in the mitochondrial matrix of eukaryotes, is responsible for the synthesis of Fe-S clusters and distribution of these cofactors to the appropriate target proteins. Despite the homology between analogous components of the prokaryotic and eukaryotic ISC pathways, there are key unexplained differences, such as the requirement of the LYR protein ISD11 and acyl carrier protein (ACP) for function in eukaryotic but not prokaryotic ISC systems.[129, 180]

Mitochondrial LYR proteins are members of a recently identified superfamily that are characterized by their small size (10-22 kDa), high positive charge, invariant Phe residue, and eponymous Leu-Tyr-Arg (LYR) motif near their N terminus.[130] LYR proteins function as subunits or assembly factors for respiratory complexes I, II, III, and V. Human LYRM4, also known as ISD11, is critical for the function of the Fe–S assembly complex,[112, 116, 117, 119, 120, 181] whereas LYRM8, a key maturation factor for mitochondrial complex II, interacts with the HSC20 chaperone,[182] which is important for Fe–S cluster delivery to apo targets. Despite their vital roles in Fe–S cluster cofactor biogenesis and oxidative respiration, structure-function details for these LYR proteins are poorly understood.

An emerging theme for LYR proteins is their interaction with ACP.[130, 183] ACP operates in the mitochondrial fatty acid synthesis (mtFAS) pathway to synthesize fatty acids using a 4′-phosphopantetheine (4′-PPT) prosthetic group covalently attached to a serine residue on ACP. Acyl intermediates are linked by a thioester bond and shuttled between fatty acid biosynthetic enzymes to generate medium and long-chain fatty acids.[123, 124, 128, 184] One of the best known functions of the mtFAS pathway is to generate octanoyl-ACP, which is required for lipoic acid biosynthesis. However, mitochondrial ACP also functions as a required subunit for respiratory complex I and is predominately associated with the long-chain fatty acid 3-hydroxytetradecanoate.[131-133, 137, 138, 185-187] More recently, ACP has been identified as an essential functional component of the eukaryotic Fe-S cluster biosynthetic complex.[129] Currently, there are no X-ray crystal structures that detail interactions between ACP and LYR proteins that provide insight into the eukaryotic adaption of ACP for these moonlighting functions.

In eukaryotes, Fe-S clusters are synthesized by a multicomponent assembly complex.[118, 163, 188] At the center of the complex, the pyridoxal 5′-phosphate (PLP)-dependent cysteine desulfurase NFS1 forms a tight complex with ISD11.[111, 112, 116, 117] The NFS1-ISD11 complex catalyzes the conversion of L-cysteine to L-alanine and generates a persulfide intermediate on a cysteine of the mobile S-transfer loop of NFS1 (S-loop).[188, 189] The terminal sulfur of this intermediate is transferred to the scaffold protein ISCU2, where it is combined with ferrous iron and electrons, from a ferredoxin,[151, 154] to form Fe-S clusters. In humans, a low-activity Fe-S assembly complex consisting of NFS1-ISD11 and the catalytic subunit ISCU2 can be activated by binding of the allosteric activator frataxin (FXN).[118] NFS1 also provides sulfur for other processes including tRNA synthesis[190] and molybdenum cofactor biosynthesis.[111] Importantly, clinical mutations of

NFS1 (R72Q)[191] and *ISD11* (R68L)[113] result in deficiencies in multiple oxidative respiratory complexes, whereas mutations of *ISCU* and *FXN* result in myopathy with exercise intolerance[192] and Friedreich's ataxia[158], respectively. The lack of structural data for eukaryotic cysteine desulfurase and Fe-S assembly complexes has limited the mechanistic understanding of these critical biosynthetic processes, the role of the essential proteins ISD11 and ACP, and insight into how clinical mutants compromise function.

Results

Structure of the Cysteine Desulfurase Subcomplex for Eukaryotic Fe–S Cluster Biosynthesis

We identified recombinant coexpression conditions that allowed the purification of a complex between human NFS1-ISD11 and native *Escherichia coli* ACP (ACP_{ec}, 44% identical to human mitochondrial ACP) (Fig. II.1), consistent with a recent report.[109] An X-ray crystal structure of the NFS1-ISD11-ACP_{ec} (SDA_{ec}) complex was determined using molecular replacement-single wavelength anomalous dispersion (MR-SAD) and refined to a resolution of 3.09 Å (R_{work}/R_{free} of 21.2/25.9 %) with excellent geometry (Table II.1). The SDA_{ec} structure exhibited an overall $\alpha_2\beta_2\gamma_2$ assembly (Fig. II.2A) with two $\alpha_2\beta_2\gamma_2$ assemblies in the asymmetric unit. The NFS1 fold is highly similar to *E. coli* IscS (Fig. II.2B)[110] and shares 60% sequence identity (Fig. II.3). NFS1, like IscS, contains a larger domain that includes a PLP active site and a smaller domain that likely interacts with ISCU2. The primary differences between NFS1 and IscS include a small extension in NFS1 α-helix 2 (Nα2), larger disordered region for the mobile S-loop, and disorder in a triple glycine-containing segment (GGG motif; see Subunit Orientation and Assembly of SDA_{ec}). In addition, some subunits display a different conformation for the equivalent C-terminal α-helix that is used by IscS (Sα13) to interact with IscU.[85, 193] Surprisingly, this mitochondrial cysteine desulfurase crystal structure also revealed an ACP-lipid-ISD11 motif and a fundamentally different oligomeric architecture for NFS1 compared with its bacterial orthologs.

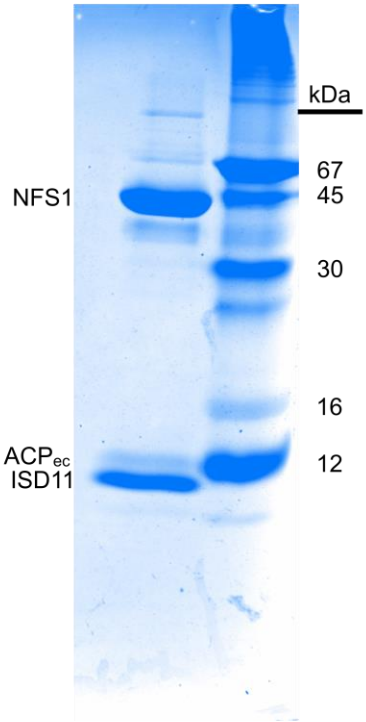

Figure II.1 Human NFS1-ISD11 co-purifies with *E. coli* ACP. A 14% SDS-PAGE gel shows the presence of NFS1, ISD11, and *E. coli* ACP (ACP$_{ec}$). ACP$_{ec}$(apo-MW = 8.6 kDa with pI = 4, 4'-PPT MW = 358 Da) stains poorly with Coomassie Blue and migrates to a position larger than its predicted molecular weight.

Table II.1 Crystallographic data collection and refinement statistics.

	NFS1-ISD11-ACP$_{ec}$ (Se-met)[a]	**NFS1-ISD11-ACP$_{ec}$ (Native)**
PDB code		5USR
Data collection	SSRL 7-1	SSRL 7-1
Space group	$P2_12_12_1$	$P2_12_12_1$
Cell dimensions		
a, b, c (Å)	125.53, 147.69, 168.09	125.48, 147.78, 168.45
α, β, γ (^{o})	90, 90, 90	90, 90, 90
Wavelength (Å)	0.9776	1.12709
Resolution (Å)[b]	50.00 - 3.68 (3.74 - 3.68)	50.00 - 3.09 (3.14 - 3.09)
R_{sym} (%)[b]	14.1 (>100)[c]	6.7 (>100)[c]
R_{meas} (%)[b]	14.4 (>100)[c]	6.9 (>100)[c]
$CC_{1/2}$ (%)[b,d]	N.A. (85.7)	N.A. (61.9)
$<I/\sigma(I)>$[b]	39 (3.4)	40 (2.0)
Completeness (%)[b]	99.9 (99.0)	99.4 (88.6)
Redundancy[b]	28.9 (26.9)	8.0 (7.4)
Refinement		
Resolution (Å)		47.83-3.09
Total reflections		58013
R_{work}/R_{free}		0.212/0.259
No. atoms		
all		15666
N'-pyridoxyl-lysine-5'-monophosphate (LLP)		96
S-dodecanoyl-4'-phosphopantetheine (8Q1)		136
B-factors		
average		127.2
LLP		107.7
8Q1		109.3
R.m.s deviations		
Bond lengths (Å)		0.002
Bond angles (^{o})		0.547
Ramachandran outliers (%)		
Favored		95.2
Outliers		0.4
Rotamer outliers (%)		1.2
Clash Score		7.2

[a] Bijvoet pairs were kept separate during data processing

[b] Values in parentheses reflect the highest resolution bin

[c] Values greater than 100% were reported as 0.000 by the version of HKL200/Scalepack used.

[d] Average $CC_{1/2}$ was not reported by the version of HKL2000/Scalepack used.

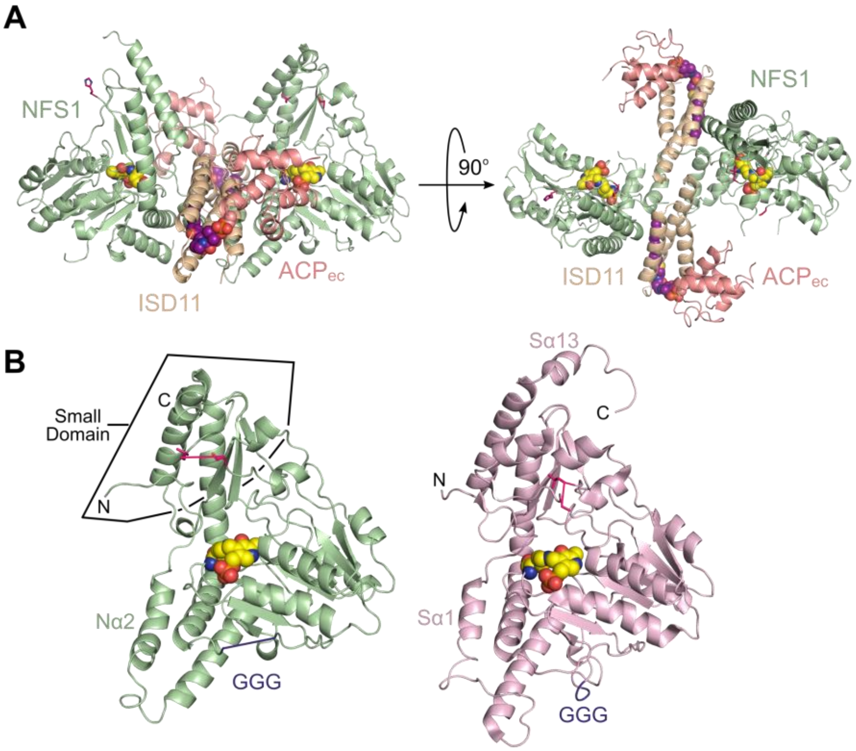

Figure II.2 The architecture of a mitochondrial cysteine desulfurase. (A) Ribbon diagram of the SDA$_{ec}$ structural architecture displayed with NFS1 (light green), ISD11 (wheat), and ACP$_{ec}$ (salmon) in two orthogonal orientations. The K258-PLP (yellow) and lipid-bound 4'-PPT (magenta) cofactors are shown as spheres. (B) NFS1 and IscS (light pink; PDB ID code 3LVM) subunits displayed in similar orientations. Residues connecting disordered mobile S loop are shown in hot pink, whereas those connecting the GGG loop are in plum. The rmsd for 277 NFS1 (chain A) and IscS (chain A) Cα atoms is 0.84 Å.

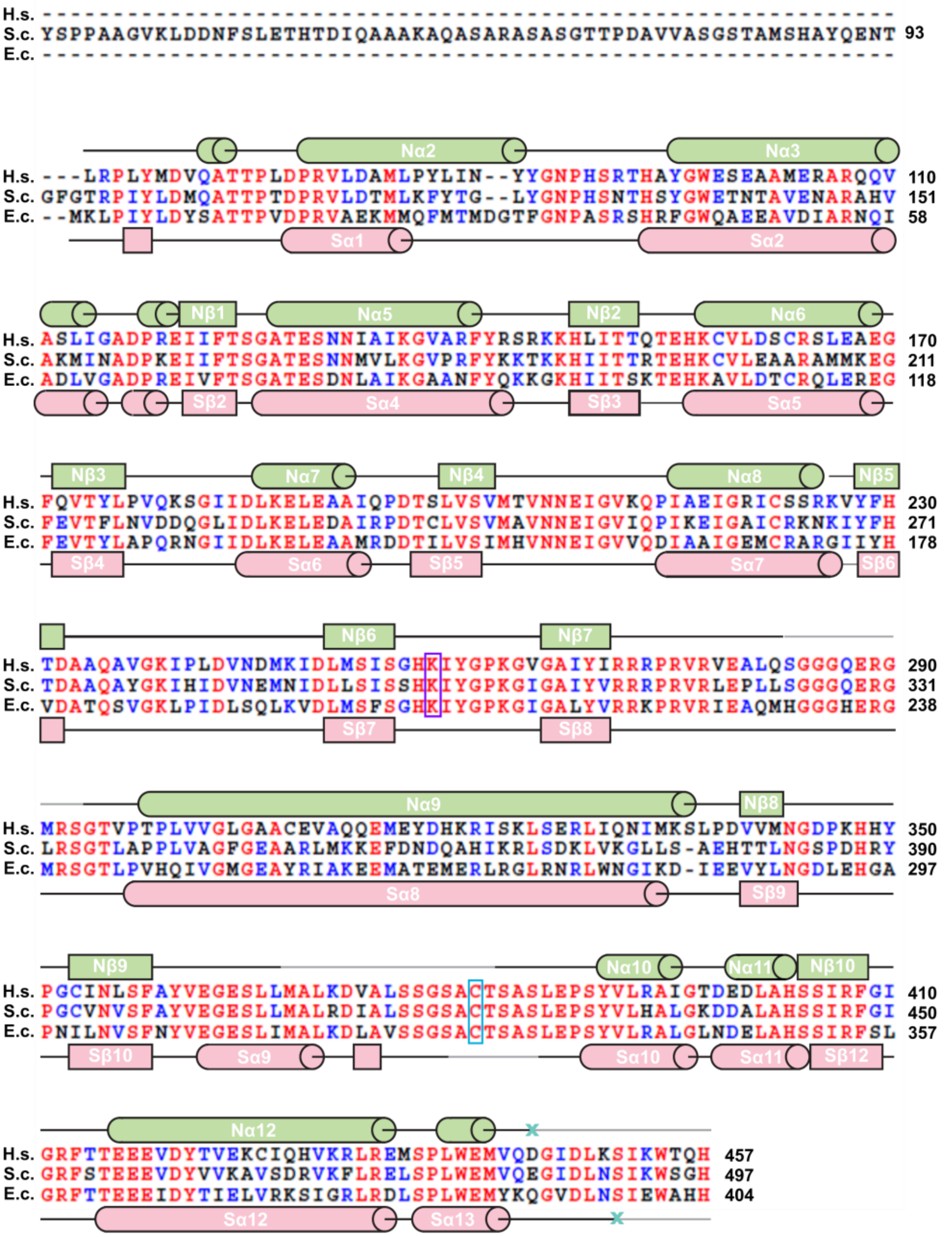

Figure II.3 Secondary structure and sequence alignment for NFS1. Aligned sequences are displayed for *Homo sapiens* (H.s.) NFS1, *S. cerevisiae* (S.c.) Nfs1, and *E. coli* (E.c.) IscS. Secondary structure elements for NFS1 (light green) were determined by removing helix and sheet records provided by Phenix and allowing Pymol to provide the assignment. Secondary structure elements for IscS (light pink) were assigned based on the PDB header. Blue X's indicate the position of the last residues built into the most complete chain for the NFS1 and IscS (PDB code: 3LVM) structures. Light grey sections between secondary structure elements indicate disordered regions. The Lys that covalently attached to the PLP (K258 in NFS1) and the Cys in the mobile S-loop (C381 in NFS1) are highlighted in violet and sky blue boxes, respectively. Amino acid labels in red are fully conserved, while those in blue are conserved in at least 50% of the compared organisms.

Identification of the ACP-Lipid-ISD11 Motif

The electron density revealed a 3-helix bundle fold for ISD11 that included most of the highly conserved residues (Fig. II.4 and Table II.2). ACP_{ec} displays a conformation similar to both uncomplexed bacterial ACP[194] and human ACP structures (Fig. II.5) with large B-factors (Table II.2), consistent with the reported high flexibility and dynamic properties of ACP.[195] ACP_{ec} interacts with ISD11 through two distinct interfaces. The first interface is mediated by a 4′-PPT-conjugated fatty acid covalently attached to ACP_{ec}, which is threaded into a groove on ISD11 (Fig. II.6A). To generate this groove and accommodate the fatty acid, ISD11 adopts an unusual 3-helix bundle conformation in the SDA_{ec} structure that lacks a traditional hydrophobic core and contains remarkably few side-chain interactions between ISD11 α-helices Iα2 and Iα3. At least 12 carbons in the acyl-chain (dodecyl-ACP) were evident in the electron density (Fig. II.6A), but longer acyl-chains could also be accommodated in the ISD11 core. In fact, we determined recombinant SDA_{ec} contains primarily a 16-carbon acyl-chain by performing gas chromatography-mass spectrometry (GC-MS) on isolated fatty-acid methyl esters (FAMEs) that were obtained from SDA_{ec} through a transesterification procedure (Fig. II.7). The aliphatic portion of the 4′-PPT cofactor is stabilized by hydrophobic interactions contributed by invariant residues on ISD11 including F40, which packs against the lipid cofactor, and F23, which is near the tip of the acyl-chain (Fig. II.6A). The functional importance of F40 was verified using a chromosomally *ISD11*-depleted *Saccharomyces cerevisiae* strain covered with an *ISD11* plasmid to test mutants. *S. cerevisiae* mitochondria with Isd11 containing the F43A variant (equivalent to human F40A) showed comparable expression levels to native Isd11 but decreased amounts of the Nfs1-Isd11 complex (Fig. II.6C,E). A similar result is observed for mitochondria either depleted in Acp1 (yeast ACP homolog) or with an Acp1 variant incapable of attaching the 4′-PPT prosthetic group.[129]

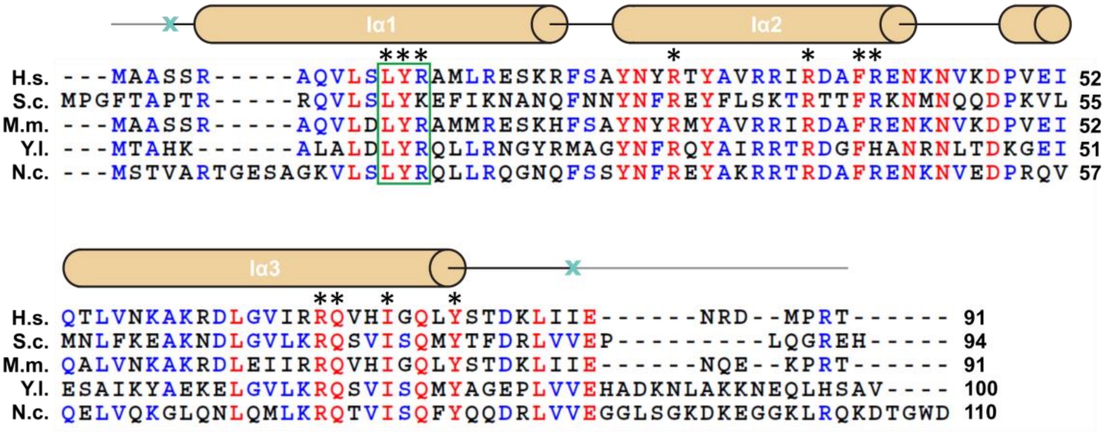

```
                         ***              *       *  **
H.s.  ---MAASSR-----AQVLSLYRAMLRESKRFSAYNYRTYAVRRIRDAFRENKNVKDPVEI 52
S.c.  MPGFTAPTR-----RQVLSLYKEFIKNANQFNNYNFREYFLSKTRTTFRKNMNQQDPKVL 55
M.m.  ---MAASSR-----AQVLDLYRAMMRESKHFSAYNYRMYAVRRIRDAFRENKNVKDPVEI 52
Y.l.  ---MTAHK------ALALDLYRQLLRNGYRMAGYNFRQYAIRRTRDGFHANRNLTDKGEI 51
N.c.  ---MSTVARTGESAGKVLSLYRQLLRQGNQFSSYNFREYAKRRTRDAFRENKNVEDPRQV 57

                     **  *   *
H.s.  QTLVNKAKRDLGVIRRQVHIGQLYSTDKLIIE------NRD--MPRT------ 91
S.c.  MNLFKEAKNDLGVLKRQSVISQMYTFDRLVVEP---------LQGREH----- 94
M.m.  QALVNKAKRDLEIIRRQVHIGQLYSTDKLIIE------NQE--KPRT------ 91
Y.l.  ESAIKYAEKELGVLKRQSVISQMYAGEPLVVEHADKNLAKKNEQLHSAV---- 100
N.c.  QELVQKGLQNLQMLKRQTVISQFYQQDRLVVEGGLSGKDKEGGKLRQKDTGWD 110
```

Figure II.4 Secondary structure and sequence alignment for ISD11. Secondary structure elements for ISD11 were mapped (similar to Fig. II.3) to a sequence alignment containing *H. sapiens* (H.s.), *S. cerevisiae* (S.c.), *Mus musculus* (M.m.), *Yarrowia lipolytica* (Y.l.), and *Neurospora crassa* (N.c.). Asterisks indicate residues targeted by mutagenesis studies. The LYR-motif is highlighted with a green box. Blue X's indicate the position of the last residues built into the most complete chain for ISD11. Amino acid labels indicate conservation level (red is fully conserved, blue is >50% conserved).

Table II.2 Residues modeled in the X-ray crystal structure of SDA_{ec}.

Chain	Protein	SDA_{ec} residues	Residues not modeled	Average B-factor ($Å^2$)
A	NFS1	56-457	283-293, 368-384, 446-457	112.2
B	ISD11	1-91	1-3, 80-91	110.4
C	NFS1	56-457	87-95, 283-294, 373-388, 445-457	149.7
D	ISD11	1-91	1-3, 84-91	113.5
E	NFS1	56-457	87-94, 276-294, 360-401,437-457	99.1
F	ISD11	1-91	1-3, 79-91	97.1
G	NFS1	56-457	61-65, 87-97, 276-294, 367-402, 441-457	111.7
H	ISD11	1-91	1-2, 80-91	110.9
I	ACP_{ec}	1-78	1, 78	153.6
J	ACP_{ec}	1-78	1-2, 78	193.7
K	ACP_{ec}	1-78	1-4, 74-78	202.4
L	ACP_{ec}	1-78	1-2, 74-78	211.1

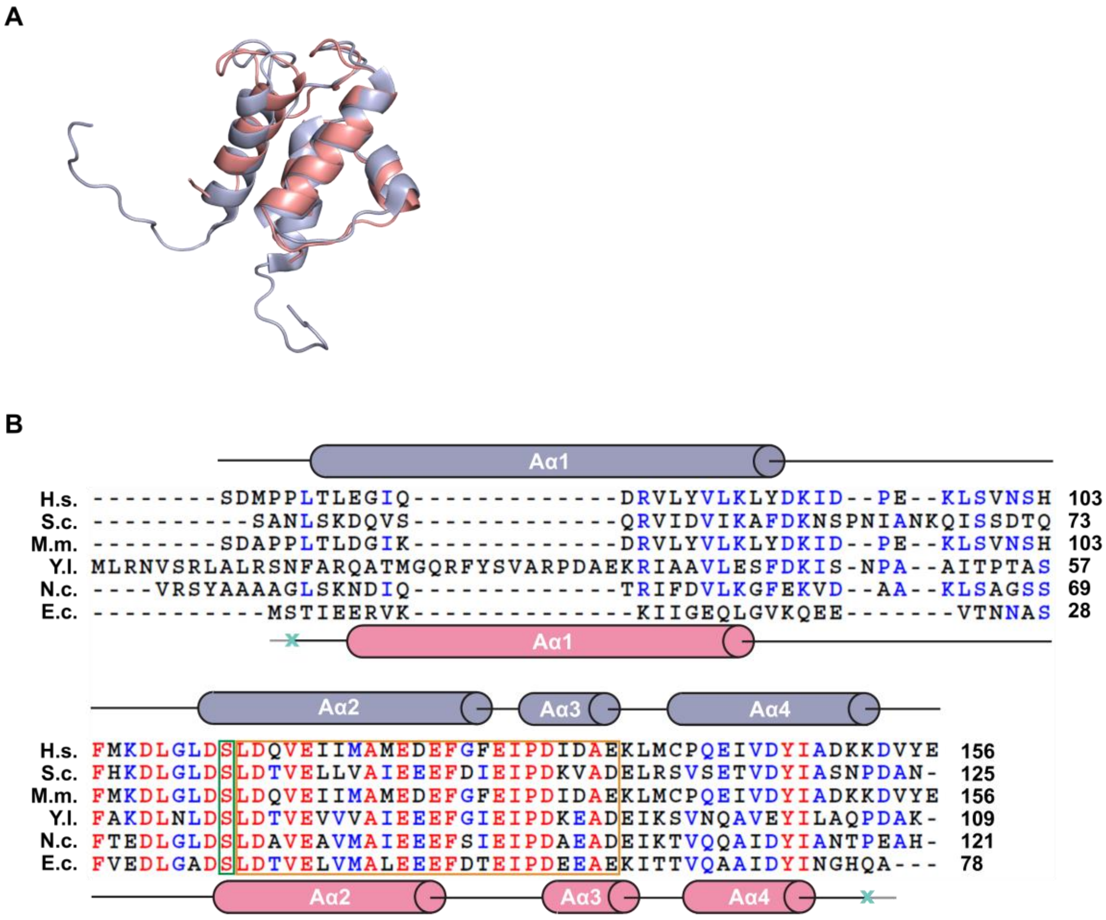

Figure II.5 Structural and sequence comparison of ACP$_{ec}$ with eukaryotic homologs. (A) Structural overlay of ACP$_{ec}$ (chain L, salmon) with human mitochondrial ACP (plum; PDB code: 2DNW), which have a Cα rmsd of 1.3 Å for 66 atoms. (B) Secondary structures for human and *E. coli* ACP were mapped to sequence alignments similar to Figs. II.3 and II.4. The conserved serine that covalently attaches to the 4'-PPT is highlighted with a green box, and the ISD11 interacting region is highlighted with an orange box. Blue X's indicate the position of the last residues built into the most complete chain for ACP$_{ec}$. Amino acid labels show conservation level (red is fully conserved, blue is >50% conserved).

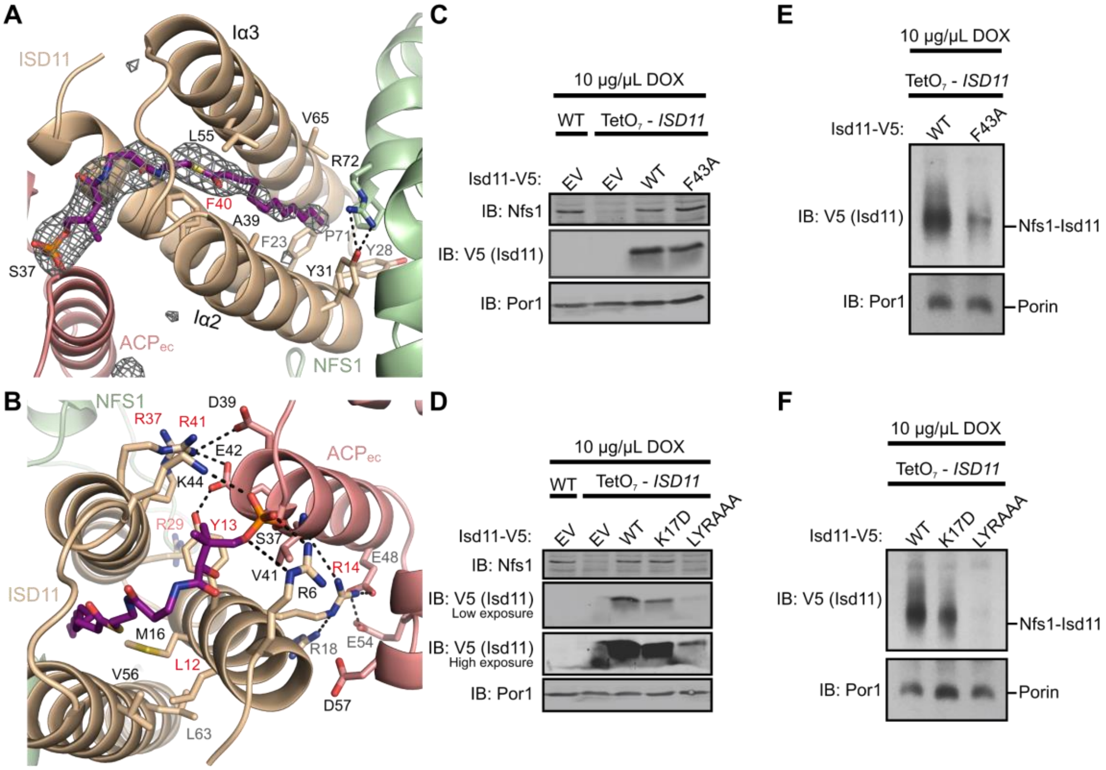

Figure II.6 ISD11-acyl-ACP interactions are critical for the formation of the SDA$_{ec}$ complex. (A) Simulated annealing-omit mF_o - DF_c map (gray mesh) contoured to 3.0σ revealed a lipid-bound 4′-PPT inserted into the hydrophobic core of ISD11. The map was displayed with a 5 Å region padding. (B) ACP$_{ec}$ interacts with ISD11 using electrostatic contacts and interactions with the LYR motif. Residues labeled in red in *A* and *B* were targeted for mutagenesis experiments in *S. cerevisiae*. Purified mitochondria from the indicated strains (WT or TetO$_7$-*ISD11*) were either resolved by SDS/PAGE (*C* and *D*) or solubilized in 1% digitonin and resolved by BN-PAGE (*E* and *F*). Cells were grown for 18 h in the presence 10 μg/mL DOX. The indicated proteins and protein complexes were assessed by immunoblot. Low and high exposure indicates the intensity of light used to scan the blot. LYRAAA is the triple alanine variant (L15A Y16A K17A) of the LYR motif. EV is empty vector control. Porin is included as a loading control. IB, immunoblot.

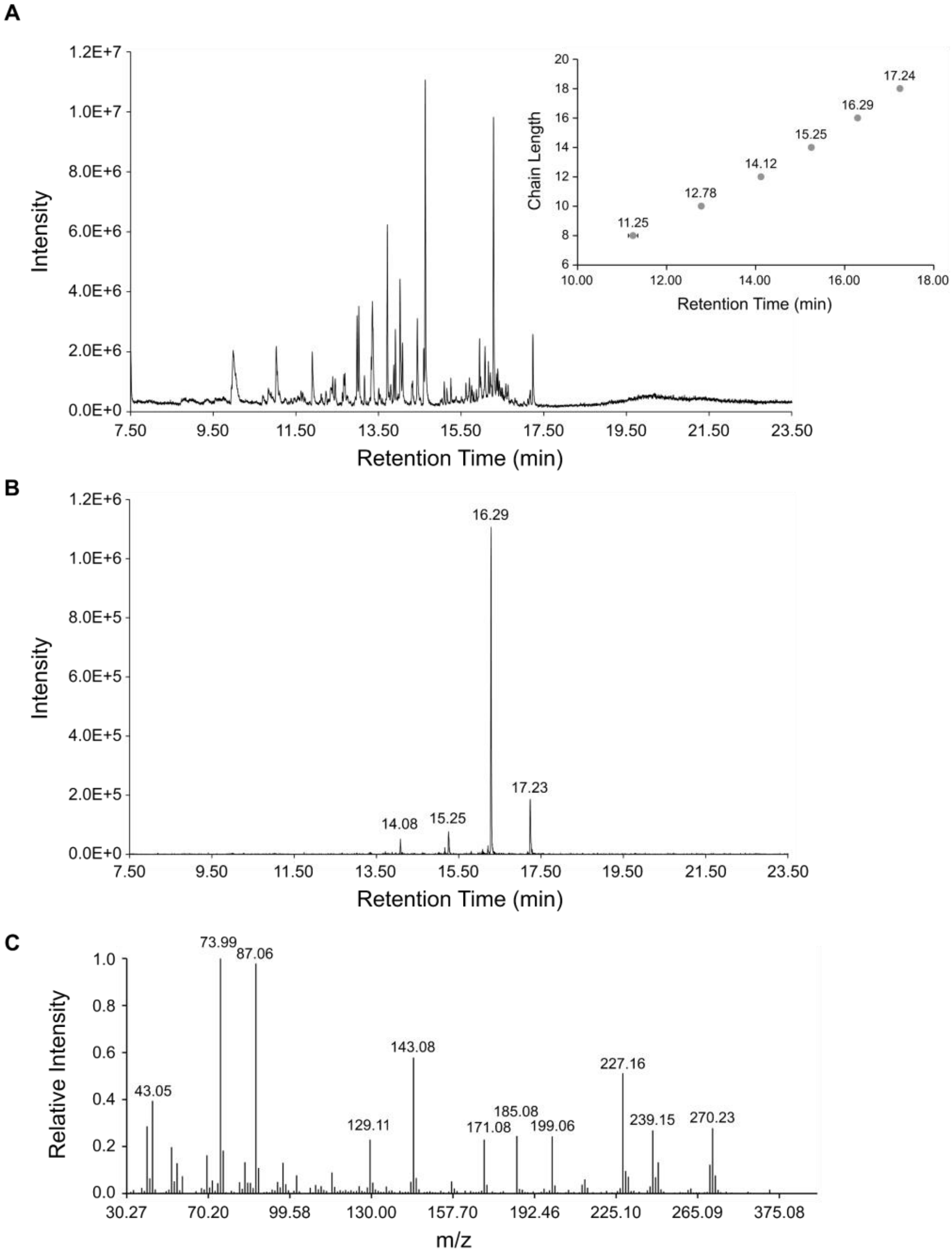

Figure II.7 Identification of 4'-PPT conjugated fatty acids associated with the SDA$_{ec}$ complex. (A) Representative raw total ion chromatogram (TIC) for isolated FAMEs from a transesterified sample of SDA$_{ec}$. Inset displays the retention time of standard FAMEs (n = 2). (B) Representative TIC filtered by m/z = 73.5-74.5, a high probability fragment from electron ionization (EI) of FAMEs. (C) A representative EI fragmentation pattern of the peak at t = 16.29 min (corresponding to a chain length of 16 carbons). Analysis of unknown transesterified SDA$_{ec}$ samples were conducted in triplicate.

Conserved residues on ISD11 have key roles in stabilizing the 3-helix bundle by providing a second, primarily electrostatic, interface with ACP$_{ec}$. The phosphate linker of the 4′-PPT is stabilized in the SDA$_{ec}$ structure through interactions with side chains of conserved R6 and K44 residues on ISD11 (Fig. II.6B). R29 interacts with backbone carbonyls of the F23-containing loop of ISD11 (Fig. II.8A), whereas R37 and R41 form salt bridges with ACP$_{ec}$ residues E42 and D39, respectively (Fig. II.6B). The residues of the characteristic ISD11 LYR motif contribute L12 hydrophobic interactions to an interface between ISD11 helices, Y13 forms a hydrogen bond to ACP$_{ec}$ E42, and R14 forms a salt bridge with ACP$_{ec}$ E48 (Fig. II.6B). *S. cerevisiae* mitochondria containing R32D, R40D, and R44D *ISD11* point mutations (equivalent to human ISD11 R29D, R37D, and R41D, respectively) or substitution of the LYR motif had decreased levels of Isd11 and loss of the Nfs1–Isd11 complex (Figs. II.6D, II.6F, II.8B, and II.8C). These results are consistent with a role for these residues in Isd11 stability and/or association with Acp1.[129] The residues on ACP$_{ec}$ that interact with ISD11 in the SDA$_{ec}$ structure are also conserved between *E. coli* and human mitochondrial ACP (Fig. II.5B) and suggest similar interactions will likely contribute to the interface between NFS1-ISD11 and human ACP. Together, these results provide insight into the unexpected role of ACP in eukaryotic Fe-S cluster biosynthesis by identifying ACP-lipid interactions that promote the stability of ISD11 and function of the Fe-S assembly complex.

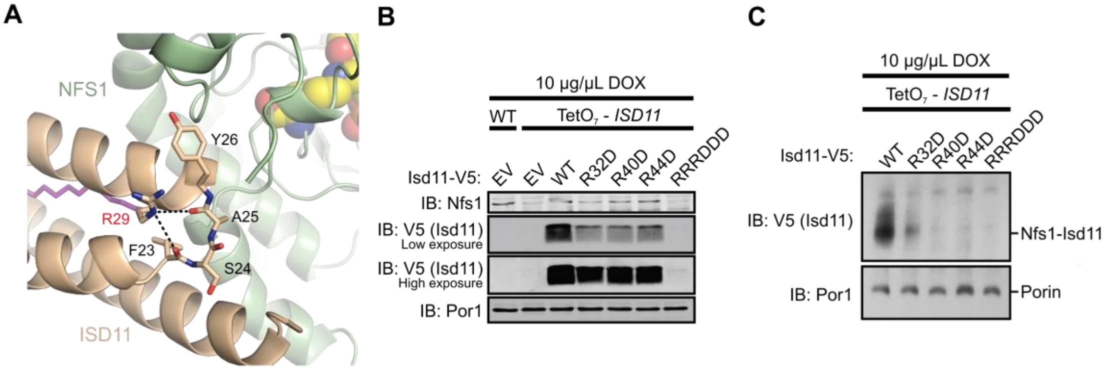

Figure II.8 Arg residues are important for ISD11 stability and interactions with ACP$_{ec}$. (A) R29 forms hydrogen bonds to the backbone carbonyl oxygen atoms of the F23-containing loop. NFS1 and ISD11 are displayed in light green and wheat, respectively. The PLP is displayed as spheres and the acyl-chain is shown in purple. Residues targeted by mutagenesis experiments are highlighted in red. Purified mitochondria from the indicated *S. cerevisiae* strains were either resolved by SDS-PAGE (B) or solubilized in 1% digitonin and resolved by BN-PAGE (C). Cells were grown for 18 h in the presence 10 µg/mL doxycycline. The indicated proteins and protein complexes were assessed by immunoblot. The R32D R40D R44D variant (equivalent to human R29D R37D R41D) is labeled RRRDDD.

Subunit Orientation and Assembly of SDA_{ec}

ISD11 forms two different interfaces with NFS1 that stabilize the SDA_{ec} subcomplex. In the first and larger interface, the Iα2 helix and acyl-chain are positioned in a pocket that is formed between the Nα2, Nα9, and Nα12 helices of NFS1 (Fig. II.9A). The NFS1 residues in this ISD11-binding pocket are highly conserved in eukaryotes; whereas the analogous residues for bacterial IscS are more variable (Fig. II.10). Notable interactions in this interface include NFS1 residue R72, which forms a hydrogen bond with invariant Y31 on ISD11, as well as the highly conserved NFS1 P71 and ISD11 F23, and appear to cap the end of the acyl-chain (Fig. II.9B). Interestingly, the R72Q NFS1 variant is associated with a Fe–S cluster disease, infantile mitochondrial complex II/III deficiency,[191] suggesting that these interactions are functionally important. In the second, smaller, interface, the adjacent Iα3 helix of ISD11 lays across the Nα2 helix in an antiparallel orientation (Fig. II.9C). In contrast to IscS, the NFS1 residues in this second interface with ISD11 are often conserved (Fig. II.10). A hydrophobic pocket is generated by residues L75 and I72 of ISD11 and L74, M77, L78, L81, and I82 of NFS1 (Fig. II.9D). This pocket is bridged by hydrogen bonding residues on ISD11 to residues and backbone carbonyls on a loop between NFS1 Nα2 and Nα3.

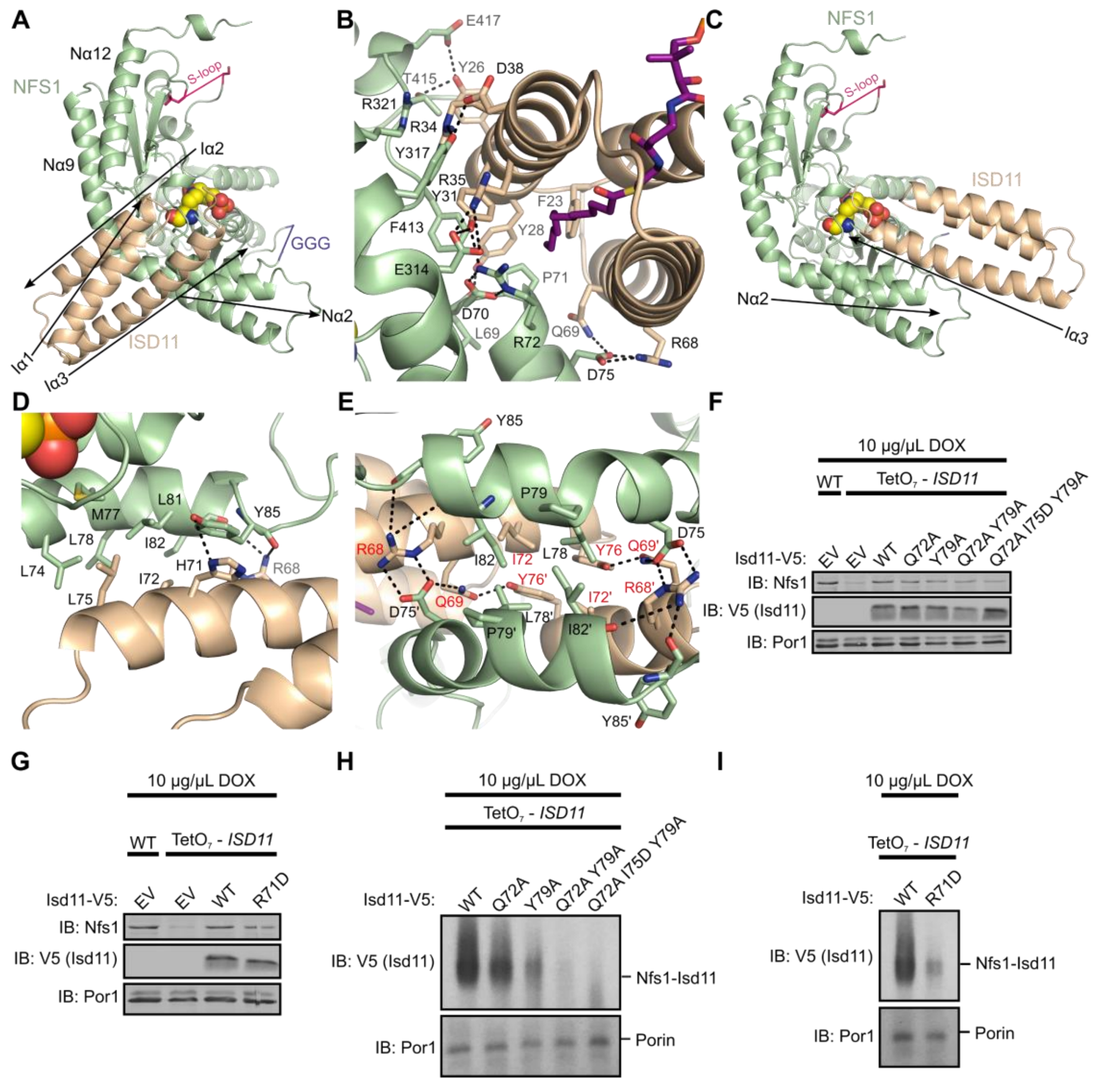

Figure II.9 Two distinct NFS1-ISD11 interfaces are important for forming the SDA$_{ec}$ architecture. (A) Global overview of the primary NFS1-ISD11 interface (ACP and lipid are omitted for clarity). ISD11 packs against Nα9, Nα12, and Nα2 helices of NFS1. (B) Specific interactions of the primary NFS1-ISD11 interface (ACP omitted for clarity). The acylated 4′-PPT is shown in purple. (C) Global overview of the secondary NFS1-ISD11 interface. ISD11 Iα3 has an antiparallel orientation compared with NFS1 Nα2. (D) Specific interactions of the second NFS1-ISD11 interface. The PLP is shown in spheres. (E) The 4-helix bundle core of the SDA$_{ec}$ complex. Residues labeled in red were tested in vivo using analogous substitution in *S. cerevisiae*. Arrows show the polypeptide direction for the α-helices. Purified mitochondria from the indicated strains were solubilized from cells similar to Fig. II.6 and resolved by SDS/PAGE (F and G) and BN-PAGE (H and I). EV, empty vector; IB, immunoblot.

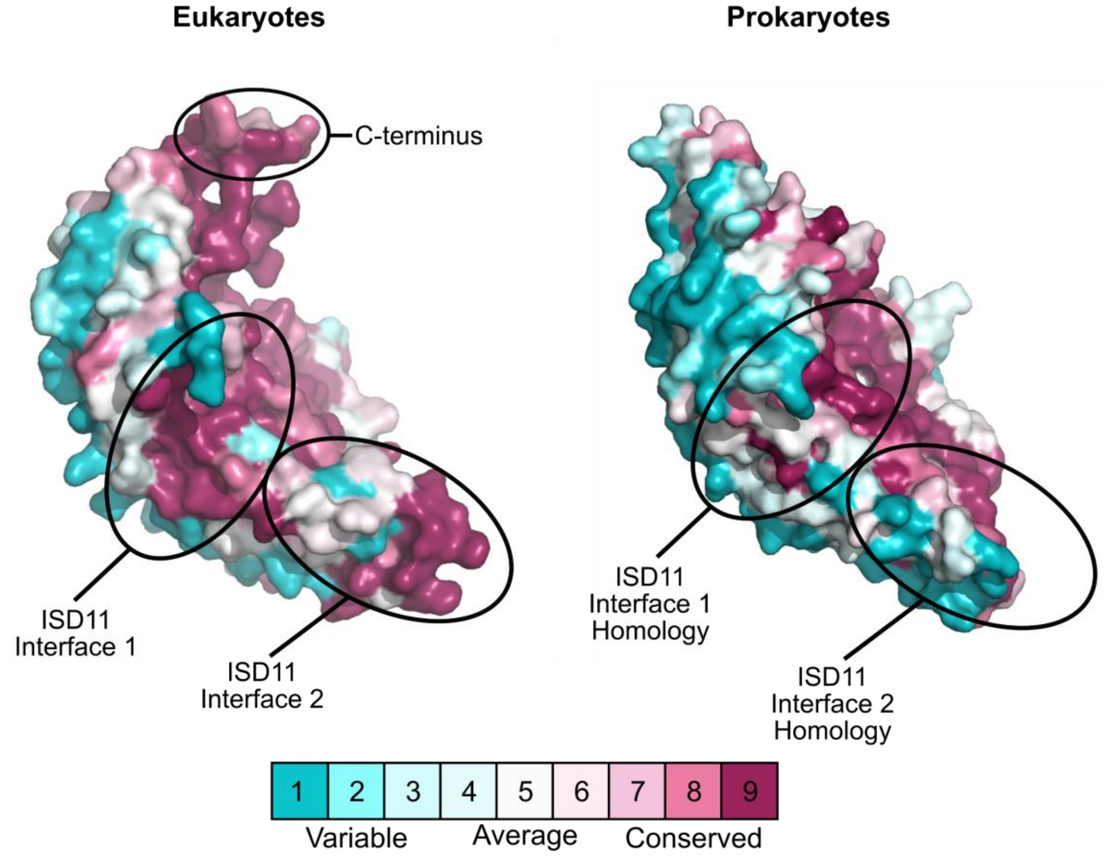

Figure II.10 Eukaryotic cysteine desulfurases have conserved interfaces for binding ISD11. Eukaryotic (n = 64) and prokaryotic (n = 45) group I cysteine desulfurase sequences were aligned separately and sequence conservation was mapped onto NFS1 for eukaryotes and onto IscS (PDB code: 3LVM) for prokaryotes. The C-terminal region of NFS1, which likely interacts with ISCU2, is also highly conserved. The equivalent highly conserved C-terminal region for IscS is in a different conformation that is not visible in this orientation. Consurf scores, indicating relative conservation, are displayed in the scale bar.

Interestingly, when two SDA_{ec} $\alpha_1\beta_1\gamma_1$ assemblies come together to form the $\alpha_2\beta_2\gamma_2$ architecture (Fig. II.2A), the NFS1-ISD11 interfaces generate an unusual, interlocking 4-helix bundle core made up of two copies of the ISD11 Iα3 helices and two copies of the NFS1 Nα2 helices (Fig. II.9E). A cluster of hydrophobic residues consisting of ISD11 (I72) and NFS1 (L78 and I82) from each of the two $\alpha_1\beta_1\gamma_1$ assemblies stabilizes the 4-helix bundle. The interactions between the four subunits appear to be facilitated by an extension of Nα2 (compared with Sα1 of IscS; Fig. II.2B and Fig. II.3) and a kink induced by conserved P79. Moreover, hydrogen bonds across the ISD11-ISD11 interface between side chains of Q69 and Y76, and salt bridge interactions between ISD11 R68 and NFS1 D75 appear to further stabilize the SDA_{ec} complex (Fig. II.9E). The importance of these interactions was tested through the introduction of single Y79A, double Q72A Y79A, and triple Q72A I75D Y79A (equivalent to human Q69A I72D Y76A) *ISD11* point mutants along with the R71D *ISD11* substitution (equivalent to human R68D) into *S. cerevisiae*. Isolated mitochondria showed Isd11 variants exhibit comparable expression levels to native Isd11 but decreased amounts of Nfs1-Isd11 complex (Fig. II.9F–I). These cell-based results coupled to the sequence conservation for interfacial residues (Fig. II.3 and Fig. II.4), previous pull-down experiments,[119] and involvement of variant ISD11 (R68L) with a mitochondrial genetic disorder[113] support the functional importance of these core SDA_{ec} interactions and explain the requirement of ISD11 for eukaryotic Fe–S cluster biosynthesis.[112, 116, 117]

The positions of the two NFS1 subunits in the SDA_{ec} complex are fundamentally different compared with previous cysteine desulfurase structures. The limited, hydrophobic interactions between the Nα2 helices are the only contacts between NFS1 subunits (122 Å^2 of buried surface area) in the SDA$_{ec}$ complex. This observation is in stark contrast to all previously determined structures of cysteine desulfurases, which exhibit common homodimeric architectures (Fig. II.11) and extensive buried surface area (2,351 Å^2 for *E. coli* IscS).[50, 110] The first NFS1-ISD11 interface in the SDA$_{ec}$ complex would not exclude a bacterial-like dimer, possibly explaining the recent discovery that ISD11 can interact but not influence the activity of bacterial IscS.[108] However, the second NFS1-ISD11 interface in the SDA$_{ec}$ complex is not compatible with the IscS dimer. Overlay of an IscS molecule from the bacterial dimer with a NFS1 subunit reveals the second IscS molecule would spatially overlap with ISD11 (Fig. II.11). Interestingly, NFS1 and IscS use interactions on orthogonal faces of the equivalent helices (Nα2, Sα1) to generate the different oligomeric arrangements.

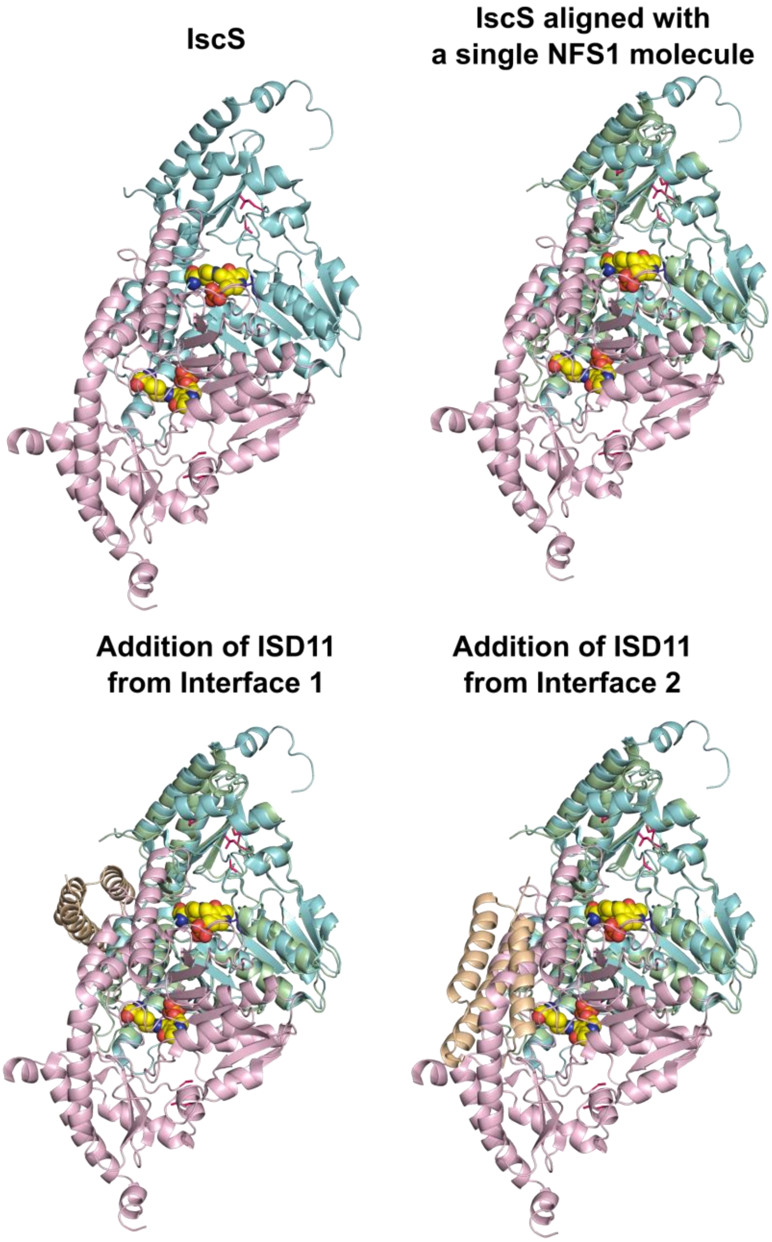

Figure II.11 IscS and NFS1 have different quaternary structures. Ribbon diagram for the IscS structure (top left, PDB code: 3LVM) with subunits displayed in pink and cyan. The PLP cofactors are displayed as spheres. NFS1 (green) aligned with the cyan subunit of IscS is shown on the top right. ISD11 (wheat) added to NFS1 interface 1 does not overlap with IscS (bottom left). In contrast, the addition of ISD11 to NFS1 interface 2 is sterically precluded by the second subunit (pink) of the IscS dimer (bottom right).

To further evaluate the protein assembly architecture of the complex, we used negative stain electron microscopy (EM) (Fig. II.12 and Fig. II.13A). A total of 128 class averages were generated from the data (Fig. II.13B), 36 of which were used in an ab initio reconstruction (Fig. II.13C). This reconstruction was refined using 11,481 particles to yield a structure of the SDA_{ec} complex to ∼15 Å resolution (Fig. II.13C–E). This reconstruction matched well with the overall arrangement of the SDA_{ec} crystal structure (correlation coefficient, 0.70) (Fig. II.12A and Fig. II.13F). On the other hand, the 3D EM reconstruction was incompatible with the canonical *E. coli* IscS dimer (Fig. II.12B and Fig. II.13G; correlation coefficient, 0.56). Overall, the crystal and EM structures for the SDA_{ec} complex reveal a rare situation in which orthologs with high sequence identity and the same protein fold exhibit distinct oligomeric architectures that result in dramatically different functional properties (see Biophysical and Functional Properties of SDA_{ec} Complex).

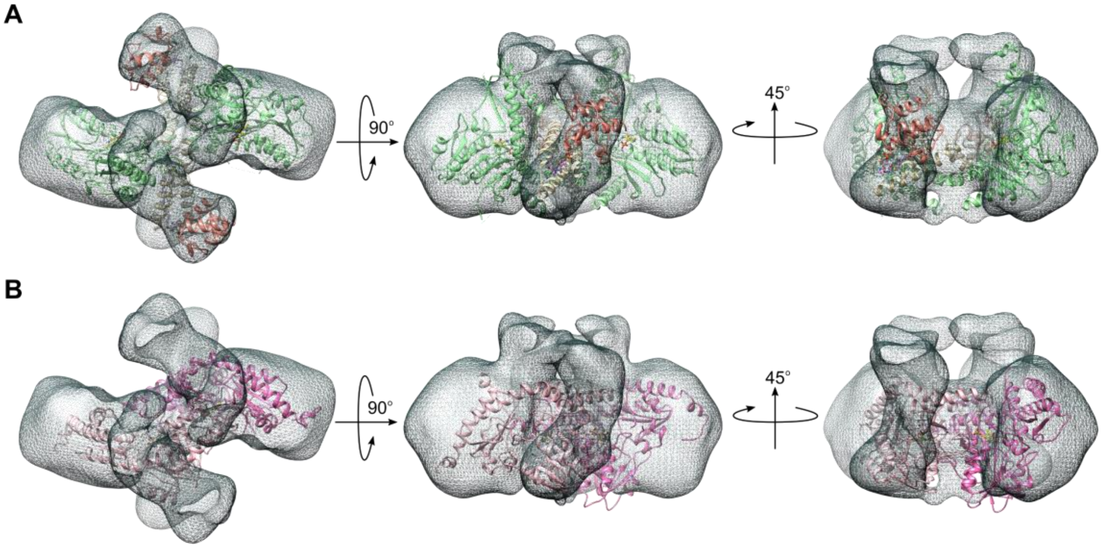

Figure II.12 Single particle reconstruction of the SDA$_{ec}$ complex with EM supports the crystallographic architecture. (A) SDA$_{ec}$ was reconstructed from EM images of negatively stained specimens (isosurface contoured with dark gray mesh). The SDA$_{ec}$ crystal structure (chains C, D, E, F, I, and L) fit well into the EM density map. Subunits are colored as in Fig. II.2. (B) The 3D EM reconstruction does not match well with the architecture of the *E. coli* IscS structure (subunits shown in light and dark pink).

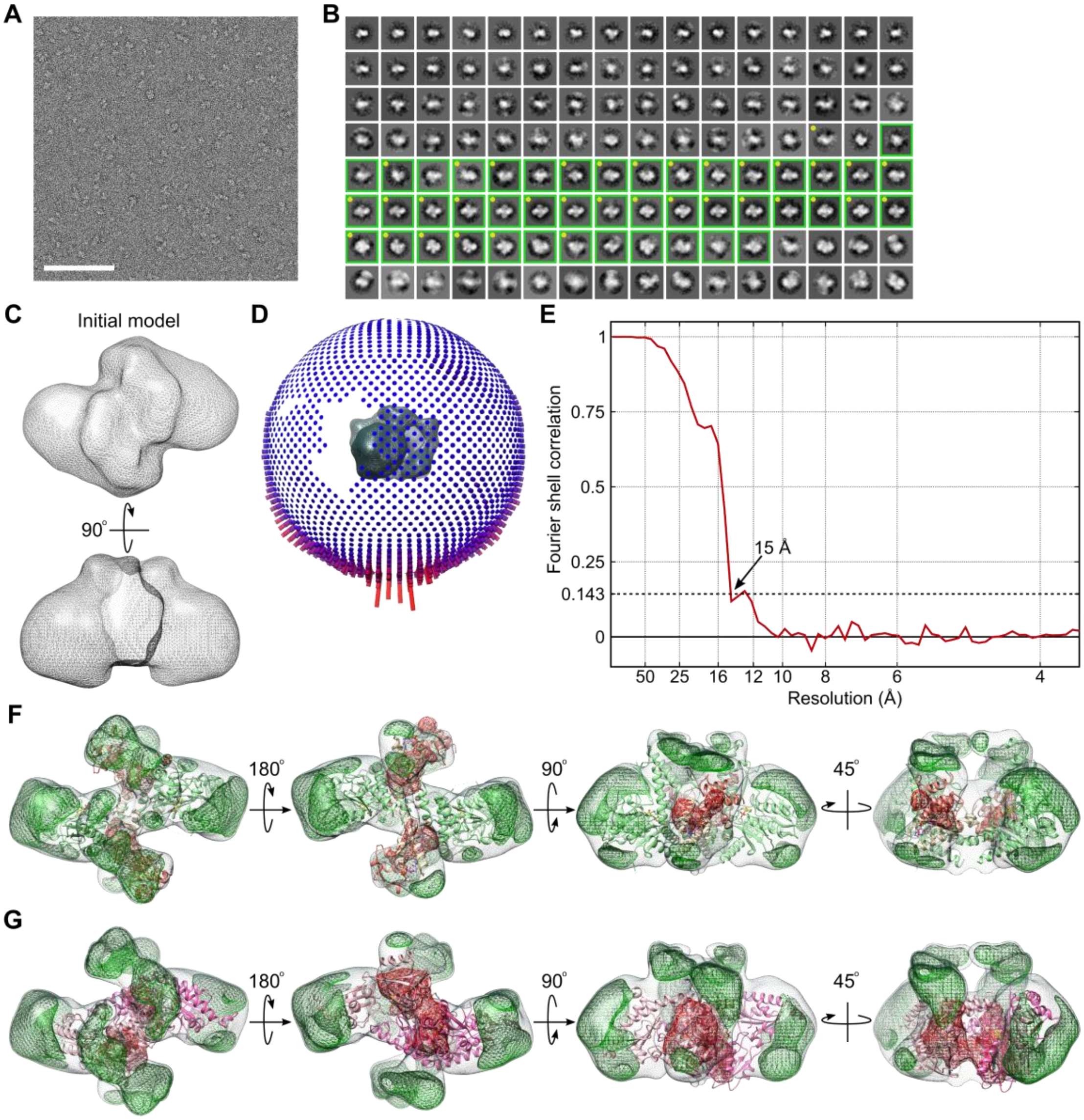

Figure II.13 EM images of a negative stained specimen of $\mathrm{SDA_{ec}}$ were of sufficient quality to produce a reliable 3D reconstruction of the complex. (A) A representative area from a micrograph showing suitable particle distribution and contrast of the negative stained specimen. Scale bar represents 100 nm. (B) 2D class averages from all windowed particles. Each average panel is 235 Å wide. Comprised of more than half of the total windowed particles, the 45 well-defined classes that were retained for further image analysis are highlighted in green. (C) Initial model (isosurface contoured with gray mesh) generated from a subset of the class averages marked with yellow dots in panel B. (D) Particles show a preferred orientation but are sufficiently distributed to produce a complete reconstruction. Height and color of the bars indicates number of particles assigned to a particular view relative to reconstruction (dark gray mesh, also shown in Fig. II.12). (E) Plot of Fourier shell correlation (FSC) between reconstructions that were calculated from independently refined half-sets of particles suggests a nominal resolution of approximately 15 Å. (F) Difference maps (positive in green mesh, negative in red mesh) calculated by subtracting the fit $\mathrm{SDA_{ec}}$ structure (subunits colored as in Fig. II.2) from the EM density map (gray transparent mesh). (G) Difference maps after subtracting the fit *E. coli* IscS (PDB code: 3LVM) from the EM map. Note the substantial negative difference density in the center of the IscS dimer indicating a poor match with the EM density, whereas the $\mathrm{SDA_{ec}}$ has only minor patches of negative density.

Biophysical and Functional Properties of SDA$_{ec}$ Complex

Crystallographic and EM structural analysis revealed that adaptor proteins (ISD11 and ACP) incorporated into the eukaryotic system support an unprecedented structural framework for the cysteine desulfurase reaction and Fe-S cluster biosynthesis. Incorporation of ISD11-ACP$_{ec}$ generates a SDA$_{ec}$ complex less prone to aggregation with increased solubility compared with the NFS1-ISD11 complex, consistent with the recently discovered Acp1 requirement for Nfs1-Isd11 stability and function in *S. cerevisiae*.[129] In fact, the SDA$_{ec}$ complex elutes from an analytical size-exclusion column with a mass consistent with a (SDA$_{ec}$)$_2$ stoichiometry with no evidence of monomeric or oligomeric species at the concentration analyzed (Fig. II.14). Steady-state kinetic analysis on SDA$_{ec}$ revealed a significantly lower K_M for L-cysteine (Table II.3) in comparison with the previously characterized complex that evidently lacked ACP$_{ec}$[111, 113, 118] and exhibited similar FXN binding and k_{cat} activation phenomena (Table II.3) that are hallmarks of mitochondrial cysteine desulfurases.[118] Moreover, we found that SDA$_{ec}$ variants reproduce the kinetic profiles of previously identified NFS1 (RRR/AAA is analogous to human R272A R275A R277A)[166] and ISD11 (R68L)[113] substitutions that lack FXN-based activation (Fig II.15). Interestingly, these results indicate that NFS1 requires the association of four additional functional proteins (ISD11, ACP$_{ec}$, ISCU2, and FXN) to mimic the stability and steady-state kinetic parameters of the bacterial cysteine desulfurase ortholog IscS.

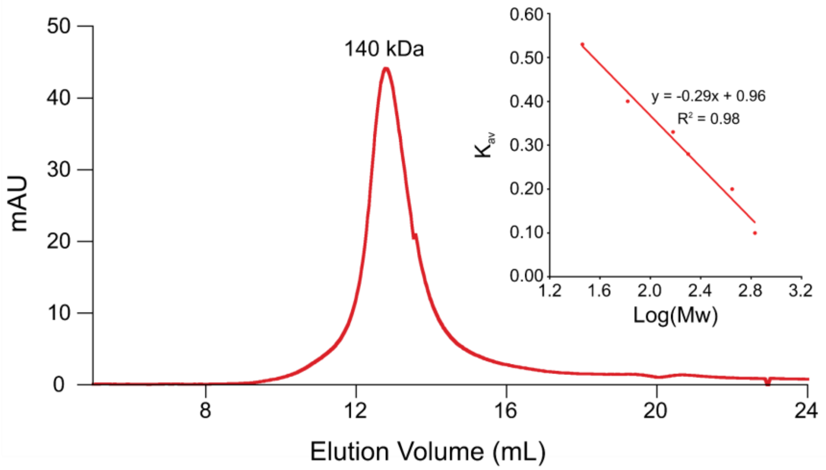

Figure II.14 The SDA$_{ec}$ complex is a dimer in solution. Representative data for S200 size exclusion analysis of the SDA$_{ec}$ complex (10 µM, 500 µL injection). Inset shows the average K_{av} for standards (thyroglobulin 669 kDa, apoferritin 443 kDa, β-amylase 200 kDa, alcohol dehydrogenase 150 kDa, albumin 66 kDa, carbonic anhydrase 29 kDa) run in triplicate. Duplicate runs of blue dextran were used to determine the void volume.

Table II.3 Michaelis-Menten kinetic parameters for cysteine turnover by Fe-S cluster assembly complexes.

Complex	K_M (µM)	k_{cat} (min^{-1})	k_{cat}/K_M (M^{-1} s^{-1})	Reference
NFS1-ISD11 (SD)	340 ± 60	1.9 ± 0.1	93 ± 20	118
SD + FXN (SDF)	330 ± 60	1.7 ± 0.1	86 ± 20	118
SD + ISCU2 (SDU)	590 ± 50	0.89 ± 0.04	25 ± 2	118
NFS1-ISD11-ACP_{ec} (SDA_{ec})	*1.3 ± 0.3	0.60 ± 0.04	8000 ± 2000	This work
SDA_{ec} + ISCU2 ($SDA_{ec}U$)	*0.82 ± 0.3	0.62 ± 0.11	13000 ± 5000	This work
SDUF	11 ± 3	5.2 ± 0.4	7900 ± 2000	118
$SDA_{ec}UF$	10.1 ± 0.2	11.6 ± 0.9	19100 ± 2000	This work
IscS	17 ± 2	7.5 ± 0.1	7400 ± 900	87

*Due to the insensitivity of the methylene blue assay at these concentrations of sulfide production, K_M parameters should observed as estimates rather than exact values.

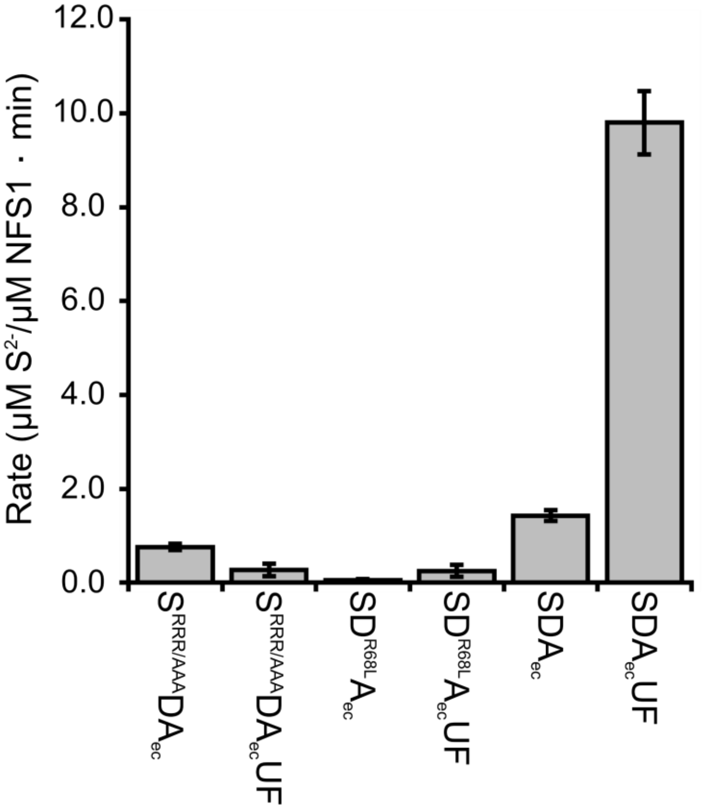

Figure II.15 NFS1-ISD11 variants result in the loss of FXN-based stimulation for the cysteine desulfurase activity. The methylene blue assay was conducted for cysteine desulfurase activity in the presence of 100 μM cysteine, 0.5 μM SDA$_{ec}$ (or corresponding variant), 4 mM D,L-DTT, 10 μM PLP, and 1.5 μM ISCU2 and FXN (when included). Reactions were quenched after 6 min, sulfide was quantified, and initial rates were determined. Standard deviations represent the error in triplicate measurement. SDA$_{ec}$UF corresponds to the SDA$_{ec}$ complex that also includes ISCU2 and FXN.

The active sites were compared to understand the lower cysteine turnover rates for eukaryotic NFS1 complexes compared with prokaryotic IscS. Inspection of the NFS1 active site revealed that most of the interactions with PLP are similar to IscS (Fig. II.16). One notable difference between the NFS1 and IscS active sites is the substrate channel; NFS1 has a shallow substrate-binding pocket and solvent-exposed PLP (Fig. II.17). In contrast, one subunit of the IscS dimer contributes to the active site of the other subunit via interactions from the N35-S40 loop and a second loop that contains the GGG motif and T243, which forms a hydrogen bond to the phosphate of the PLP cofactor (Fig. II.16 and Fig. II.17B,C). These contributions to the active site are precluded by the different oligomeric architecture for the eukaryotic complex and may explain the low activity for the SDA_{ec} complex as well as the activator requirement in the eukaryotic system.

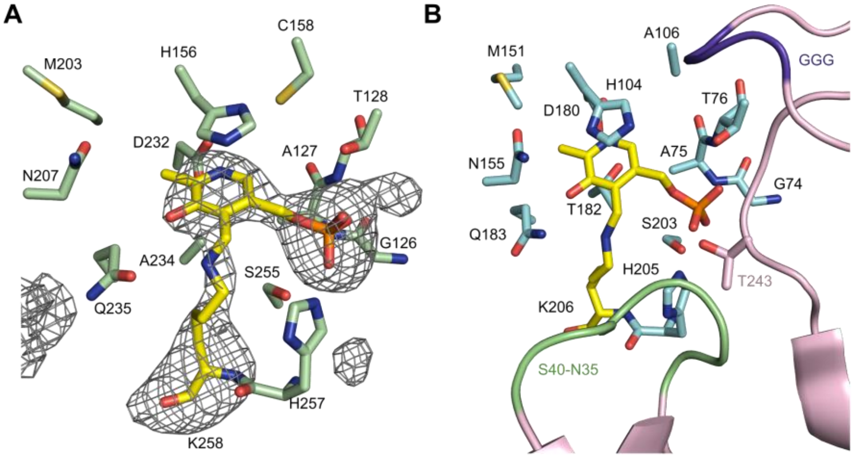

Figure II.16 Comparison of the active sites for NFS1 and IscS. The NFS1 (A) and IscS (B) active sites displayed in a similar orientation reveals comparable intrasubunit interactions with the PLP. Intersubunit interactions (S40-N35 loop, green; GGG motif purple, other residues from second subunit including T243, magenta) also contribute to the active site for IscS (PDB code: 3LVM) that are not present in NFS1. Simulated annealing - omit mF_o-DF_c map contoured to 3.0σ (grey mesh) is shown for the PLP-K258 of NFS1. The map was displayed with a 5 Å region padding.

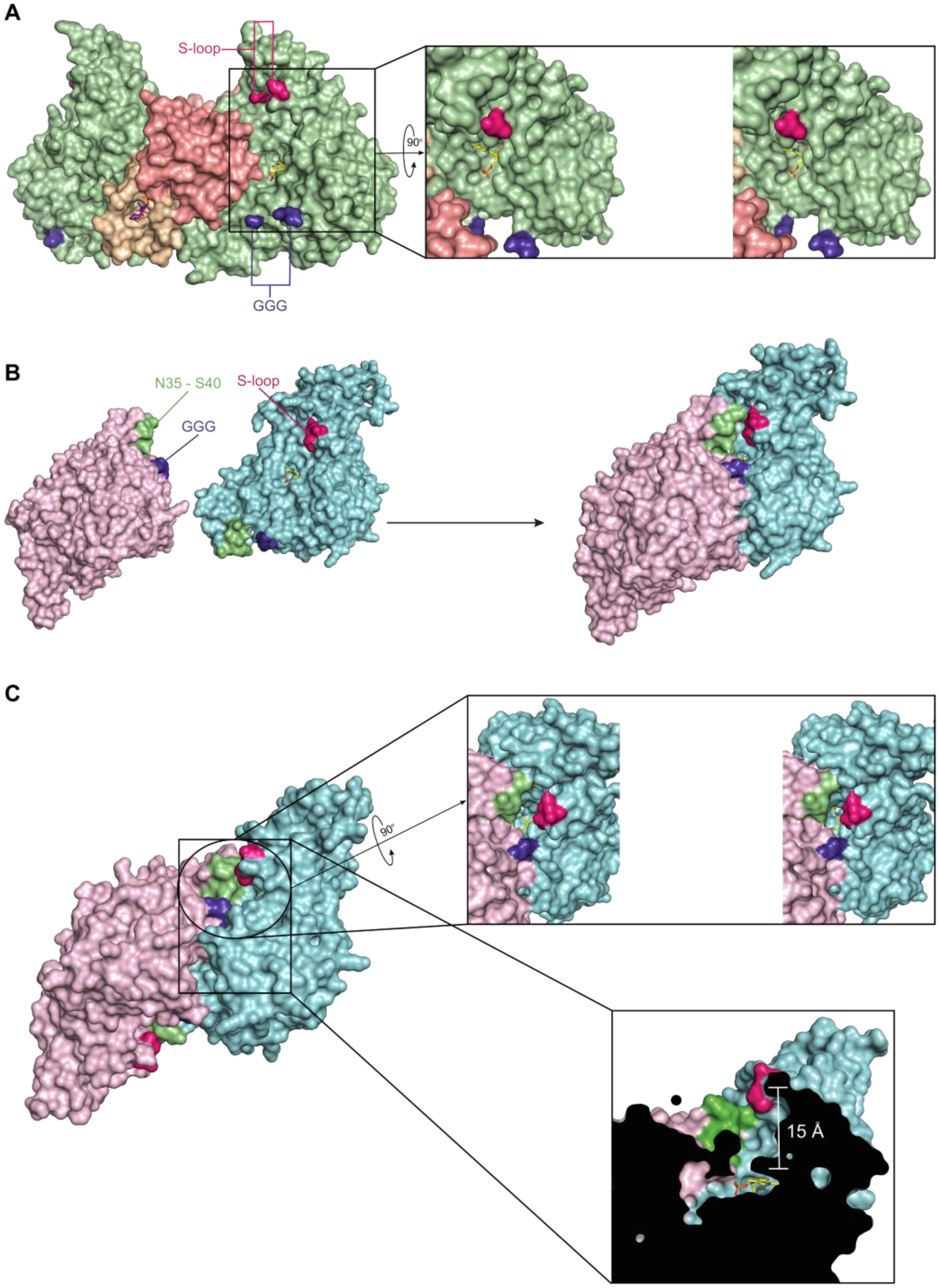

Figure II.17 The PLP is solvent exposed in the SDA$_{ec}$ complex and buried in the IscS structure. (A) Surface view of NFS1 active site reveals that it is shallow and solvent exposed. Inset shows a stereo view of the active site with the PLP (yellow). (B) The formation of the IscS dimer buries the PLP between the monomeric units. (C) Stereo view of the IscS substrate tunnel (top right), and a surface clip of the dimer interface displaying the depth of the substrate tunnel (bottom right).

The SDA_{ec} crystal structure reveals a connection between the acylated 4′-PPT and PLP cofactors in which changes in the ACP cofactor could propagate to the NFS1 active site. Although ACP_{ec} does not directly interact with NFS1, the acyl-chain attached to 4′-PPT is threaded into the ISD11 hydrophobic core and is ~18 Å from the PLP (Fig. II.18). The PLP is covalently attached to K258 and anchored by interactions between the phosphate moiety and the backbone amides and side chains of T128, S255, and H257, which are invariant residues in eukaryotic cysteine desulfurases. Interestingly, the backbone carbonyl of H257 forms a hydrogen bond to the side chain of T67 of the N-terminal loop that, in turn, packs against ISD11. The N terminus and additional adjacent hydrogen-bonding residues appear to function as a relay between the acyl-chain and PLP. Moreover, NFS1 residue R412, which is downstream of the presumed cysteine interacting residue R407, forms backbone interactions with ISD11 R34 and NFS1 Y260 and participates in a salt bridge network with NFS1 residues D70 and the clinical mutant R72. These invariant residues provide a possible link between the substrate-binding site and the acyl-chain that may contribute to the altered K_M for cysteine in the presence of ACP_{ec} (Table II.3).

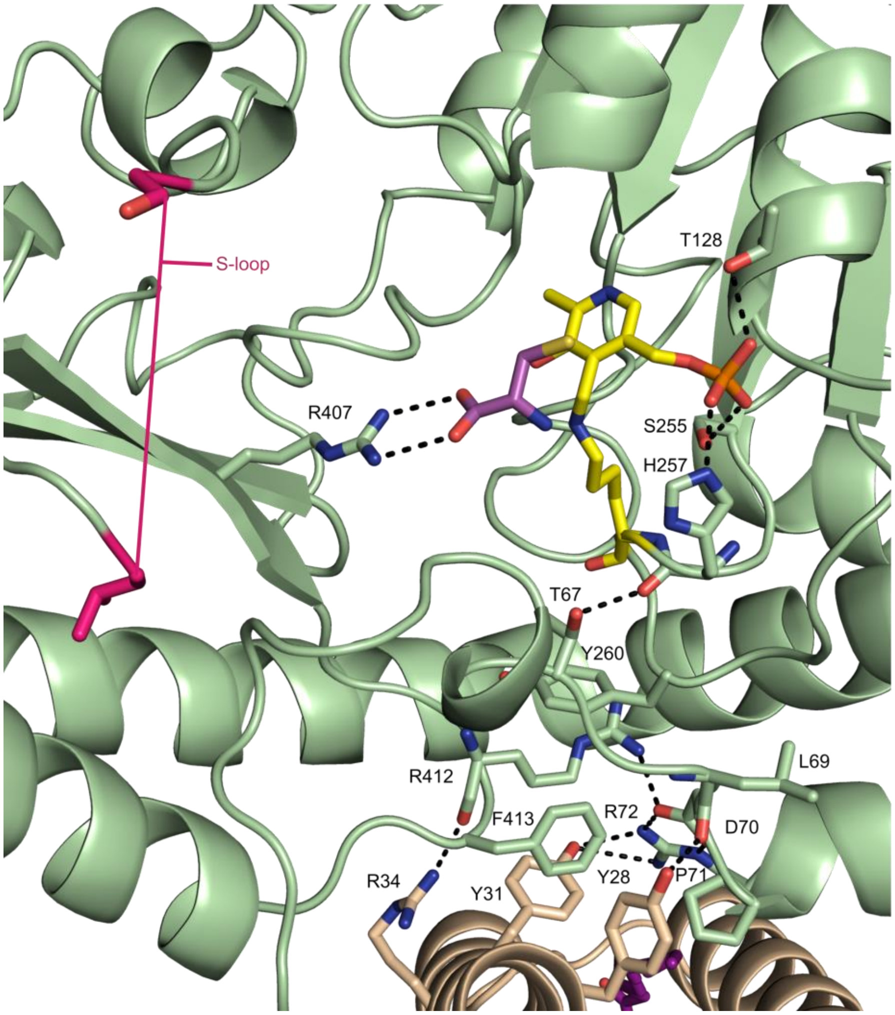

Figure II.18 Hydrogen bonding network between the acyl-chain and PLP active site for the SDA$_{ec}$ complex. Conserved residues on NFS1 provide a relay of hydrogen bonds that propagate between the Lys-bound PLP cofactor (carbons in yellow) and the acyl-chain of the 4'-PPT (magenta). The cysteine substrate (carbons in magenta) was modeled into the active site based on a substrate bound SufS structure (PDB code: 5DB5). Residues connecting disordered mobile S-loop are shown in hot pink.

Discussion

Eukaryotes synthesize Fe-S clusters in the mitochondrial matrix using a biosynthetic pathway that contains the same basic components as the prokaryotic ISC system. However, key, unexplained functional differences exist for the Fe-S assembly complexes that center on the respective cysteine desulfurases. First, two additional proteins, ISD11 and ACP, are required for the stabilization and function of NFS1 in the eukaryotic system.[111, 112, 116, 117, 119, 129] In contrast, there is no evidence for a role of ACP in prokaryotic Fe-S cluster assembly, and the ACP interactions appear limited to a disulfide bond that would inactivate IscS.[66, 141] Second, despite sharing 60% sequence identity with IscS, NFS1 is inactive on its own.[111, 113] Third, in vitro assays reveal that FXN stimulates the cysteine desulfurase and Fe-S cluster biosynthetic activities in the eukaryotic system,[87, 113, 118, 144, 145, 148, 166, 169] whereas the prokaryotic FXN homolog CyaY inhibits Fe-S cluster assembly on the scaffold protein IscU.[86, 87] Unexpectedly, the cysteine desulfurases and not the FXN homolog control the mode of activation/inhibition in these assays for the respective systems.[87] Despite these functional differences, analogous residues for the eukaryotic (Fig II.15)[166] and prokaryotic[85] cysteine desulfurases appear to contribute to the binding of FXN homologs. Lastly, the electron donor for cluster assembly, ferredoxin (FDX2), appears to bind simultaneously with the FXN homolog in yeast[154] but to compete for binding with CyaY in the prokaryotic system.[70, 71] To help explain these functional differences, we determined crystallographic and EM structures of the SDA_{ec} complex and demonstrated that the SDA_{ec} complex has a fundamentally different architecture compared with all previously determined cysteine desulfurase structures.

The unexpected architecture and incompletely formed substrate-binding channel for the SDA_{ec} complex provide a rationale for the differences in prokaryotic and eukaryotic cysteine desulfurase function and their interactions with accessory proteins for Fe-S cluster biosynthesis. Although the residues that interact directly with and tune the chemistry of the PLP cofactor are largely the same (Fig. II.16), the different quaternary structure of SDA_{ec} results in the loss of intersubunit interactions that line a tunnel to the active site in IscS (Fig. II.17). We hypothesize that FXN functions as an allosteric activator by promoting a conformation that replaces these interactions. In doing so, FXN guides the NFS1 sulfur-transfer loop trajectory, increasing the efficiency and rate of sulfur transfer chemistry, which results in the observed FXN-based stimulation in the cysteine desulfurase, interprotein sulfur transfer, and Fe-S cluster assembly kinetics.[118, 144, 145, 148, 149, 154, 166, 169, 170] Moreover, the cup-like architecture for the SDA_{ec} complex, in contrast to the prokaryotic system, results in the two active sites facing one another and opens up the prospect of subunit interactions across the dimeric interface. A model (Fig. II.19) positions the ISCU2 subunits adjacent to one another in the complex and suggests the possibility that [2Fe-2S]-ISCU2 units may be able to reductively couple their clusters to form a [4Fe-4S]-ISCU2 species, consistent with uncomplexed bacterial IscU[196] and a previous report on the mammalian Fe–S assembly complex.[149] Overall, the SDA_{ec} complex provides a framework for comprehending the differences in function compared with the prokaryotic system and understanding the binding of accessory proteins to the eukaryotic cysteine desulfurase.

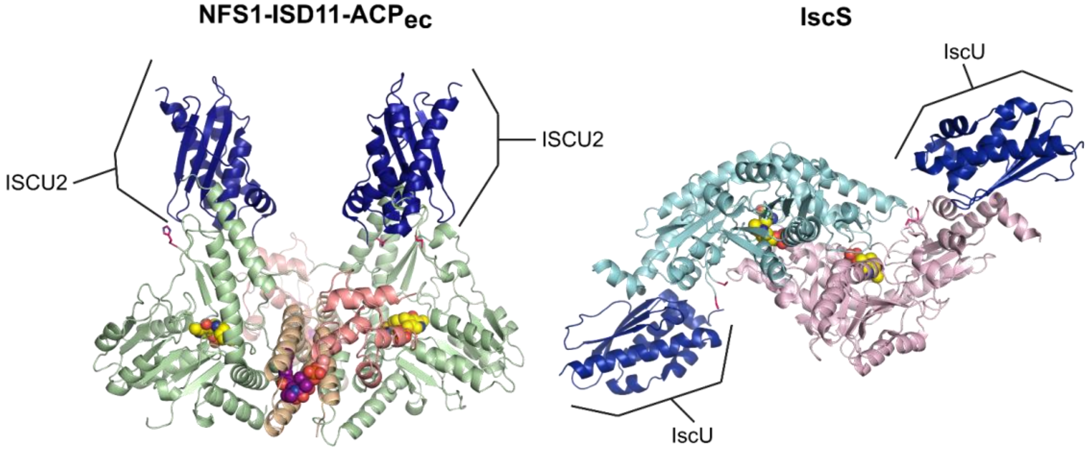

Figure II.19 Modeling suggests the relative positions of the scaffold subunits are different in the NFS1-ISD11-ACP$_{ec}$-ISCU2 and IscS-IscU structures. The interactions between the NFS1 subunit of the SDA$_{ec}$ complex and ISCU2 were modeled (left) based on the analogous interactions in the IscS-IscU structure (PDB code: 3LVL, right).

We propose the cysteine desulfurase architecture provides a mechanism to integrate activity control elements into the eukaryotic system. In our monomer-based association model (Fig. II.20), a heterotrimeric SDA species is first formed from interactions of monomeric NFS1 with ISD11-ACP. In the second stage, the heterotrimeric SDA species dimerize to form the stable 4-helix bundle core of the SDA_{ec} architecture. Consistent with this model, NFS1-NFS1 interactions appear to be significantly weaker than IscS-IscS interactions and result in a population of monomeric NFS1,[112-114] which has a tendency to aggregate in the absence of either member of the ISD11-ACP pair.[112, 129] In contrast, the SDA_{ec} dimeric architecture is the predominant species that elutes from a size exclusion column (Fig. II.14) and is the major species present in EM samples (Fig. II.12 and Fig. II.13), which are conducted at submicromolar concentrations similar to Fe-S assembly protein levels measured in mitochondria.[197-199] Additional EM studies of a much larger and functionally distinct oligomeric form of the eukaryotic Fe-S assembly complex are also consistent with an NFS1 quaternary structure different from IscS.[200] Another PLP-containing enzyme, ornithine decarboxylase, also uses quaternary structure differences to modulate activity.[201] Overall, we propose that eukaryotes have adopted a cysteine desulfurase architecture that allows FXN and ACP to control Fe-S cluster biosynthesis.

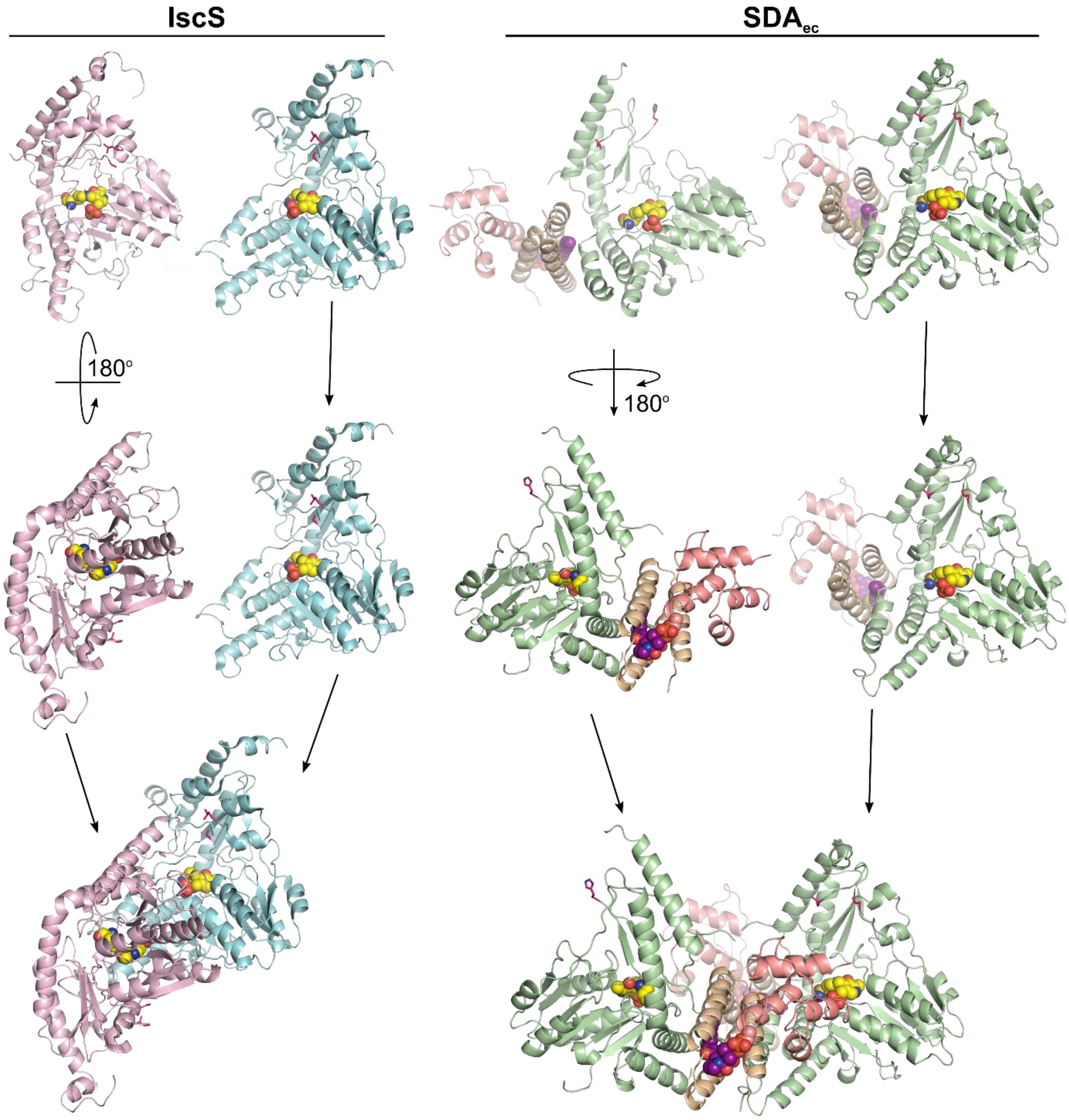

Figure II.20 Proposed assembly pathways for generation of the IscS and NFS1-ISD11-ACP$_{ec}$ architectures. IscS (PDB code: 3LVM) assembles as a tight homodimer (left). NFS1-ISD11-ACP$_{ec}$ assembles via a monomeric pathway utilizing two NFS1-ISD11-ACP$_{ec}$ units to produce the final complex (right).

In addition, the SDA_{ec} structure provides another portrait of LYR-ACP interactions. Although the incorporation of ACP is a recently discovered component for the eukaryotic Fe-S cluster assembly machinery, its inclusion follows an emerging paradigm for interactions between mitochondrial ACP and LYR proteins.[132] Previous studies demonstrate that ACP, in addition to its central role in mtFAS, forms a complex with LYRM3 and LYRM6 of Respiratory Complex I.[131, 133, 185-187] Similar to the SDA_{ec} complex, the LYR motif and invariant Phe residue are required to anchor ACP to LYRM6 and to produce a functional complex.[132] Overlay of ISD11-ACP with previously determined LYR-ACP structures reveals that all three LYR proteins have the same relative orientation to ACP (Fig. II.21A). Mapping the sequence conservation of all 11 human LYR proteins, which include components implicated in Fe-S cluster insertion[182] and assembly factors of respiratory complexes II,[202] III,[203] and V,[204] onto ISD11 reveals a common interface and invariant Phe that could be used to interact with ACP (Fig. II.21B). Recent affinity capture MS studies further support this hypothesis by providing evidence that ACP interacts with at least 7 of the 11 human LYR proteins,[135, 136] including LYR proteins that also interact with HSC20 and are implicated in the Fe-S cluster delivery mechanism.[182, 205] These results suggest that the LYR superfamily forms lock-and-key interactions with ACP-associated 4′-PPT-conjugated fatty acids that influence or control their maturation and function.

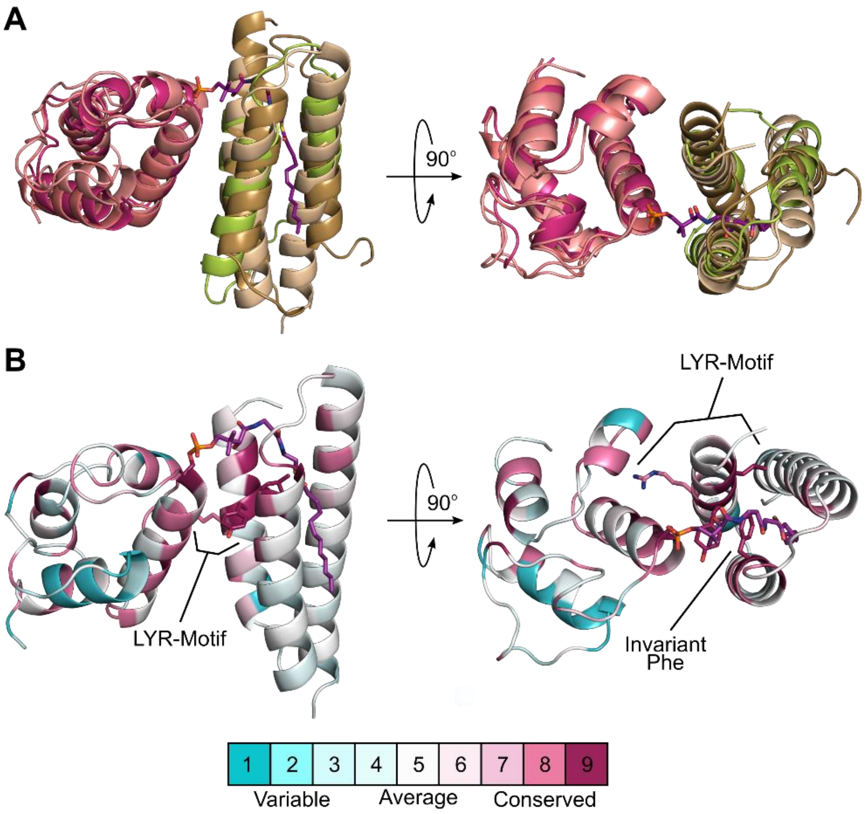

Figure II.21 LYR-ACP interactions identified in the SDA$_{ec}$ complex appear conserved for the LYR superfamily of proteins. (A) Structural overlay of ISD11-ACP(wheat and salmon) with LYRM3-ACP (limon and deep salmon) and LYRM6-ACP (sand and warm pink) from bovine complex I (PDB ID code 4UQ8).(B) Sequence conservation of the 11 human LYR proteins mapped onto ISD11-ACP of the SDA$_{ec}$ structure. Similar sequence conservation of ACP$_{ec}$ and human mitochondrial ACP is also mapped to ISD11-ACP. Consurf scores, indicating relative conservation, are displayed in the scale bar.

The connection between ACP and Fe-S cluster biosynthesis is consistent with a previously proposed model in which mtFAS plays a regulatory role in oxidative respiration.[123, 128] Experimental evidence supports a role of ACP-associated fatty acids in the processing of mitochondrial RNA and expression of the respiratory complexes,[128, 206] synthesis of Fe–S cluster cofactors,[129] and achieving the mature protein assembly and active conformation for the respiratory complexes.[130, 133] Thus, it appears from our results and the work of others that the evolutionarily conserved pathways of Fe-S cluster biosynthesis, oxidative phosphorylation, and mtFAS have been connected by LYR proteins and their respective acyl-ACP associations. The mechanistic role for the acyl-chain is still unclear; however, it is possible that acyl-ACP acts as a metabolic sensor for the mitochondria by reporting the abundance of acetyl-CoA, as proposed previously,[123] and allowing mtFAS to coordinate the expression, Fe-S cofactor assembly, and activity of the respiratory complexes. Overall, the cross-communication between biosynthetic and primary metabolic pathways through the utilization of LYR-acyl-ACP interactions is a potential and exciting avenue of regulation that warrants further investigation.

Materials and Methods

Protein Expression and Purification

Plasmids containing the genes for *NFS1* (pET-15b) and the natural S11A variant[207] of *ISD11* (pACYDuet-1) were transformed into BL21(DE3) cells[118] and expressed using autoinduction media.[208] Cultures were grown to an OD_{600} of 1-2 at 37 °C, the temperature was reduced to 18 °C, and the cells were collected after overnight growth. The cell pellet was resuspended in buffer A [50 mM Hepes, 500 mM NaCl, 5 mM imidazole, and 5% (vol/vol) glycerol, pH 7.8], and the cells were ruptured with six rounds of sonication. The cell lysate was combined with a buffered PLP solution (final concentration, 100 μM) and brought into an anaerobic Mbraun glovebox (∼12 °C, <1 ppm O2 monitored by a Teledyne model 310 analyzer). The lysate was loaded onto a 5 mL Ni-NTA (GE Healthcare Life Sciences) column and eluted using a linear gradient of buffer A and buffer B [50 mM Hepes, 250 mM NaCl, 500 mM imidazole, and 5% (vol/vol) glycerol, pH 7.8]. The resulting yellow fractions were pooled, diluted with buffer C (50 mM Hepes and 10% glycerol, pH 7.5), and combined with EDTA, DTT, and PLP at final concentrations of 2 mM, 5 mM, and 100 μM, respectively. The sample was loaded onto a 27-mL cation exchange (POROS 50HS, Applied Biosystems) column and eluted using a linear gradient of buffers C and D [50 mM Hepes, 1 M NaCl, and 10% (vol/vol) glycerol, pH 7.5]. Yellow fractions were pooled and combined with 2 mM EDTA, 5 mM DTT, and 100 μM PLP (final concentrations). The sample was then concentrated under argon using an amicon (10 kDa cutoff) and loaded onto a HiPrep 26/60 Sephacryl S300 HR (GE Healthcare Life Sciences) column equilibrated in buffer E [50 mM Hepes, 250 mM NaCl, and 10% (vol/vol) glycerol, pH 7.5]. The $\mathrm{SDA_{ec}}$ fractions were pooled, concentrated using the amicon to 280 μM (λ_{max} = 420 nm, ε = 10.9 $\mathrm{mM^{-1}\cdot cm^{-1}}$), frozen in liquid nitrogen, and stored at –80 °C. For selenomethionine (SeMet)-labeled protein, proteins were expressed using a PASM-5052 medium as described by Studier,[208] and the same purification strategy described above was used. SeMet containing proteins were concentrated to 215 μM, frozen in liquid nitrogen, and stored in a –80 °C freezer until further use. Site-directed mutants of NFS1 and ISD11 were constructed following the

QuikChange protocol (Agilent). The resulting variants were expressed and purified as described above except that the cation column was skipped for the RRR/AAA variant. ISCU2 and FXN were expressed and purified as previously described.[118] ISCU2 and FXN concentrations were determined using extinction coefficients at 280 nm of 8,250 and 26,030 $M^{-1}\cdot cm^{-1}$, respectively.

Crystallization and X-Ray Data Collection

SDA$_{ec}$ aliquots, which were stored in buffer E, were thawed and diluted to 177 μM with 50 mM Hepes, 150 mM NaCl, pH 8.0, for crystallization. Optimized crystallization conditions were identified using the hanging drop vapor diffusion method in which 2 μL of 177 μM SDA$_{ec}$ was combined with 2 μL of a well solution produced by mixing a 450-μL crystallization solution of 0.1 M Citrate BIS-Tris propane (CBTP), pH 6.4, 0.3 M CsCl, 0.2 M allylglycine, 5 mM Tris(2-carboxyethyl)phosphine (TCEP), and 8% (wt/vol) PEG 3350 with 50 μL of 40% (vol/vol) acetone. Single crystals grew within 1 week at 22 °C. SeMet-labeled SDAec crystals were grown under similar conditions with a modified crystallization solution [0.1 M CBTP, pH 6.4, 0.3 M CsCl, 0.2 M allylglycine, 6 mM TCEP, and 4% (wt/vol) PEG 3350], which was also mixed with a 40% (vol/vol) acetone solution to provide a final well solution containing 4% (vol/vol) acetone. Crystals were harvested and cryoprotected by removing most of the liquor surrounding the crystal and gradually increasing the PEG 400 concentration in 5% (vol/vol) increments (30-s soaks) until the final concentration reached 25% (vol/vol). Crystals were then removed from the mother liquor/cryoprotection mixture using 0.3-0.4 mm loops (Hampton Research) and plunged into liquid nitrogen. All data sets were collected at SSRL beamline 7-1 (ADSC

Q315R) at 100 K. A wavelength of 1.12709 Å was used for native data collection, and a wavelength of 0.9776 Å was used for SeMet data collection. The selenium peak for the SeMet containing crystals was determined by an X-ray fluorescence scan. Diffraction data were integrated, scaled, and merged using HKL2000.[209] Statistics are in Table II.1.

Crystallographic Structure Determination and Refinement

Initial phases were determined by the MR-SAD method using Phaser-EP[210] in Phenix[211] using a monomer of IscS [Protein Data Bank (PDB) ID code 3LVM][85] as a search model. A total of 46 SeMet sites were found with an initial figure-of-merit (FOM) of 0.47 at a resolution of 3.72 Å. Phenix fast chain tracing was used to build an initial model that was improved by the Phenix autobuild GUI. Phases were then extended to the native resolution using RESOLVE[212] for further model building and refinement. Phenix.refine[213] was used to randomly select the Rfree set, which corresponded to 3.4% of the total reflections and perform initial rounds of rigid body and xyz-coordinate refinement using 3LVM as a reference model to generate dihedral restraints.[214] A partially sequenced NFS1-ISD11 pair was built using Coot[215] and subsequently used for MR in Phaser against the native dataset to generate four partially sequenced NFS1-ISD11 pairs in the asymmetric unit. Iterative rounds of model building and refinement were performed in Coot[215] and phenix.refine, respectively. Anomalous difference maps were used to aid in the sequencing of ISD11 and ACP (Fig. II.22). Due to high B factors in ACP regions, a high resolution model of apo-ACP (1T8K.pdb)[194] was docked into the electron density for refinement. Ligand restraints from the Phenix library for the lys-PLP (LLP.pdb) cofactor were used during refinement. The acylated 4′-PPT cofactor was built using

JLigand,[216] and restraints were generated using ReadySet and eLBOW.[217] The initial Rfree reflections selected included reflections between 3.09 Å and 3.07 Å corresponding to the edges of the detector. Thus, the Rfree set was truncated to 3.09 Å, and 26 reflections were added to the set using Phenix to generate a set corresponding to 2,000 reflections (3.4%) within refinement resolution. The B factors were reset to 103 Å^2 (Wilson B factor calculated by Xtriage), and several rounds of Cartesian-simulated annealing were used to remove bias from the addition of these reflections by refining to convergence.[218] The final model was refined by applying xyz-coordinate, group B factor (one per residue), TLS (one group per chain), and individual B-factor refinement. Stereochemistry, secondary structure, ADP, and torsion angle NCS restraints were applied. Figures were generated in PyMOL.[219] Data refinement statistics are listed in Table II.1. Chain details are listed in Table II.2. The final model was evaluated using Molprobity.[220]

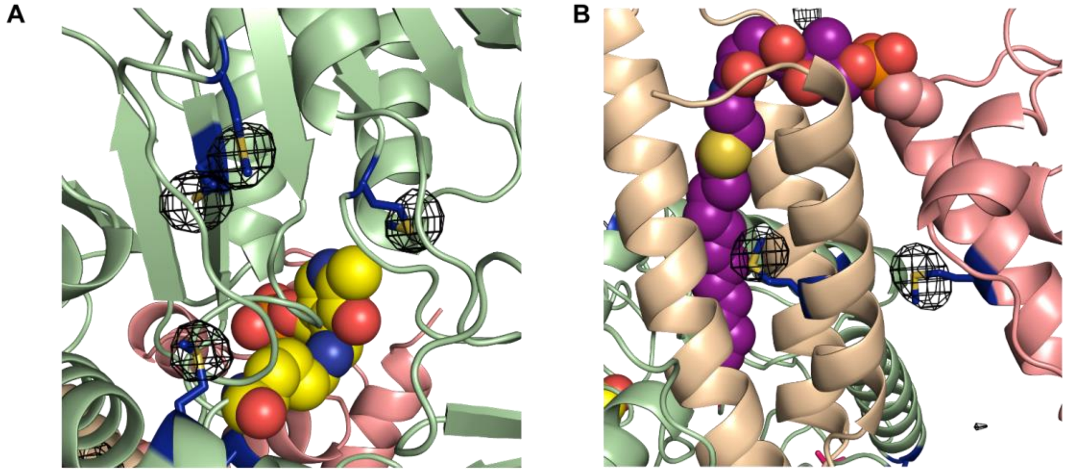

Figure II.22 Anomalous data identifies positions of selenium atoms in the structure of NFS1. Regions near the (A) PLP (yellow spheres) and (B) 4'-PPT (purple spheres) are displayed for the SDA_{ec} complex. Ribbon diagrams for NFS1 (light green), ISD11 (wheat), and ACP_{ec} (salmon) are displayed with anomalous difference electron density contoured at 6.0σ (black mesh).

Acyl-Chain Isolation

The acyl-chain associated with ACP in SDA_{ec} recombinant material was identified by transesterification to FAMEs[221] and GC-MS. Briefly, 1 mL of 110-150 μM SDA_{ec} was prepared by thawing frozen aliquots and diluting them with anhydrous methanol. A 10-mL solution of 10% (vol/vol) H_2SO_4 in anhydrous methanol was added to the 1 mL protein sample in a 25 mL screw cap vial. The sample was mixed vigorously and brought to reflux in a water bath (70–80 °C). Anhydrous sodium sulfate (1-1.5 g) was added to the mixture, incubated under reflux conditions for 2 h, and then cooled to room temperature. A small amount of anhydrous methanol was added to resuspend the white precipitate. Approximately 15 mL of hexane (mixture of isomers; Sigma-Aldrich) was added to this suspension. For best results and to maximize FAME extraction, the phases were allowed to mix vigorously on a shaker at 37 °C overnight. The organic phase was then extracted the following morning, transferred to a 15-mL glass screw cap vial, and evaporated under N_2. Two additional 15-mL extractions with hexane were conducted with vigorous mixing at 37 °C for 1 h each. After all of the hexane had been evaporated, small portions of hexane were used to rinse the vial for transfer of the isolated product to a small 1-mL screw cap vial. The solvent was completely evaporated from the 1-mL vial under N_2, and finally, 100 μL of hexane was added to the vial to prepare the sample for GC-MS analysis.

GC-MS Analysis of FAMEs

GC-MS was performed on an Ultra GC/DSQ (ThermoElectron) using electron impact ionization (EI). An injection volume of 1 μL, inlet temperature of 225 °C, and Rxi-5ms (60 m length, 0.25 mm i.d., 0.25 μm film thickness; Restek) column were used.

Helium was used as the carrier gas at a constant flow of 1.5 mL/min. For sample analysis, the oven temperature was initially held at 50 °C for 5 min, increased to 320 °C at a rate of 20 °C/min, and then held at 320 °C for 5 min. All standards were prepared at a concentration of 1 mg/mL in hexanes. Identification of standards and samples were based on both retention time and EI fragmentation.

Yeast Strains and Growth Conditions

S. cerevisiae R1158 (BY4741 derivative; *MATa*, URA3::CMV-tTA, *his3Δ1 leu2Δ0 met15Δ0*) was used as the wild-type strain. Mutants were generated using standard methods by homologous recombination of PCR-amplified fragments. Yeast transformations were performed by the standard lithium acetate method, and transformed cells were recovered and grown in synthetic complete glucose (SD) medium lacking the appropriate amino acid(s) for selection purposes. *S. cerevisiae* cells were grown in YPA (rich media containing yeast extract, peptone, and adenine) or synthetic minimal medium supplemented with 2% glucose, 2% raffinose, or 2% glycerol. *ISD11* mutants were tested with an *ISD11* knockdown strain (R1158 plus *isd11::Kan*$_R$*TetO*$_7$*-CYC1TATA-ISD11*) and a plasmid (*ISD11-V5*) previously constructed.[129] To suppress *ISD11* expression from the TetO$_7$-*ISD11* allele, overnight cultures were used to inoculate synthetic media containing either 2% glucose or 2% raffinose and 10 μg/mL doxycycline (DOX) to an approximate OD$_{600}$ of 0.05 and were incubated for 16-24 hours as indicated.

Isolation of Yeast Mitochondria and Analysis of Steady-State Protein Levels

Cell pellets were washed once with ddH$_2$O and incubated in TD buffer (100 mM Tris-SO$_4$, pH 9.4 and 100 mM DTT) for 15 min at 30 °C. Spheroplasts were obtained by incubating cells in SP buffer (1.2 M sorbitol and 20 mM potassium phosphate, pH 7.4) supplemented with 0.3 mg/mL lyticase for 1 h at 30 °C to remove the cell wall. Spheroplasts were gently washed once and homogenized in ice-cold SEH buffer (0.6 M sorbitol, 20 mM Hepes-KOH, pH 7.4, 2 mM $MgCl_2$, 1 mM EGTA) using a Dounce homogenizer applied with 30-40 strokes. Crude mitochondria were then isolated by differential centrifugation (1,500 × g for 5 min, 4,500 × g for 5 min, 10,000 × g for 10 min). Yeast mitochondria were solubilized in Laemmli buffer. Samples were resolved by SDS/PAGE and assessed by immunoblot. Blue native polyacrylamide gel electrophoresis (BN-PAGE) was performed as described previously.[222] Mitochondria were resuspended in lysis buffer (Invitrogen) and solubilized with 1% digitonin. Lysates were resolved on a 4-16% gradient native gel (Invitrogen). The steady-state levels of each indicated complex was assessed by immunoblot. Porin was used as a loading control.

Single-Particle EM of the SDA_{ec} Complex

The SDA_{ec} complex (5.0 μg/μL) was diluted to 15 ng/μL in 50 mM Hepes, pH 7.2, 200 mM NaCl, and 1 mM TCEP. A 5-μL sample was applied to a freshly glow-discharged carbon film supported by a 300 mesh copper EM grid (Electron Microscopy Sciences). After ∼1 min the protein solution was blotted from the grid and replaced with 5 μL 1% uranyl acetate. The blot and stain wash were repeated two more times. The final drop of stain was allowed to stand on the grid for ∼1 min before blotting slowly from the grid, leaving a thin film of stain that was air-dried.

SerialEM[223] was used to operate a Tecnai F30 microscope (FEI) at 300 kV equipped with a Falcon II direct electron detector (FEI) at a magnification of 59,000×, resulting in a pixel size of 1.833 Å at the specimen level, and acquire 109 images of the specimen with exposures of 42 $e^-/Å^2$ (Fig. II.13A). Defocus of each image was estimated with CTFFIND4.[224] In RELION-1.4,[225] an initial set of 4,167 particles were manually selected and windowed from 17 images, and a preliminary set of class averages were generated. Three averages with well-defined but dissimilar features were used to automatically select particles from all 109 images in RELION, the selections were visually assessed, and 21,973 particles were windowed. After an initial sorting procedure in RELION,[226] 21,276 particles remained and these were further cleaned by 2D classification, yielding 128 class averages (Fig. II.13B). Sixty-three classes of incomplete complexes roughly the size of an NFS1 monomer and 20 classes of poorly defined aggregates or particles with encroaching neighbors were removed with 11,822 particles remaining (Fig. II.13B). In total, 36 class averages were input to e2initialmodel.py (EMAN2 version 2.12) to generate initial reconstructions with imposed C2 symmetry (Fig. II.13C).[227] Among the resulting initial models, a 3D map with projections that matched well with the averages was selected to initiate 3D refinement with 11,481 particles that remained following an additional round of 2D classification. The 3D classification within RELION into four classes failed to further separate the particles into meaningfully different groups, and therefore, the 11,481 particles were considered to be structurally homogenous and without further cleaning were used for refinement of the initial reconstruction in RELION with a strict high-resolution cutoff of 12 Å to prevent overfitting (Fig. II.13D). Fourier shell correlation calculated within RELION from independently refined maps of half of the data indicates that the final resolution of the map is ~15 Å (Fig. II.13E). The final reconstruction was fit with atomic models of the SDA_{ec} crystal structure or an *E. coli* IscS dimer (PDB ID code 3LVM)[85] and was rendered with UCSF Chimera.[228] Difference maps (Fig. II.13F,G) and correlation coefficients were calculated with the "measure correlation" and "vop subtract" commands in Chimera.

Analytical Size Exclusion Chromatography

Standards (Sigma Aldrich) including albumin (2.5 mg, 66 kDa), apoferritin (2.5 mg, 440 kDa), thyroglobulin (2 mg, 669 kDa), alcohol dehydrogenase (1.25 mg, 150 kDa), β-amylase (1 mg, 200 kDa), and carbonic anhydrase (1.25 mg, 29 kDa) were dissolved in 500 µL of 50 mM Hepes, 250 mM NaCl, pH 7.2. Approximately 250 µL of this standard mixture was loaded into a 500-µL sample loop that contained the same buffer as mentioned above. The entire sample loop (500 µL) was injected onto a Superdex 200 10/300 GL (S200, GE Healthcare Life Sciences) analytical size exclusion column. This procedure was conducted in triplicate. To determine the void volume of the column, 1 mg of blue dextran (Sigma Aldrich) was dissolved in 500 µL of 50 mM Hepes, 250 mM NaCl, pH 7.2. The entire sample was loaded into the sample loop and injected onto the S200 column. This experiment was conducted in duplicate providing a void volume (V_o) of 7.26 ± 0.10 mL. The factory provided column volume was 24 mL. The K_{av} for each standard was then determined using the following equation: $K_{av} = \frac{V_{elution}-V_o}{V_{column}-V_o}$. Samples of 4-10 µM SDA_{ec} were prepared by diluting frozen protein stock in the same buffer as mentioned above. Volumes of 500 µL were loaded into a 500-µL sample loop and the entire sample loop injected onto the S200 column. The K_{av} for the elution peak was determined as described above, and the molecular mass was estimated using a plot of the K_{av} for the standards versus log of molecular mass. An average of five runs provided a molecular mass of 123 ± 7 kDa. Protein was monitored at 280 nm.

Cysteine Desulfurase Activity Measurements

The methylene blue assay for cysteine turnover was conducted as previously described[118] with minor modifications. Briefly, 800-µL reactions containing 0.5 µM SDA, 4 mM D,L-DTT, and 10 µM PLP in 50 mM Hepes, 250 mM NaCl, pH 7.5, were incubated for 15 min at 37 °C with and without three equivalents of the designated accessory subunit/subunits (Table II.3). Reactions were initiated with up to 600 µM L-cysteine and were quenched as previously described after 6 min. The absorbance at 670 nm was converted to the concentration of sulfide using a standard curve generated from a sodium sulfide standard. Kinetic experiments were conducted in at least triplicate and fit to the Michaelis-Menten equation with KaleidaGraph (Synergy software). The errors in Table II.3 represent errors in the fit.

Supplemental Description of Activity Measurements

For the activity assays described within this chapter, sulfide standards of 800 µL ranging from 5 to 60 µM were quenched with 200 µL of a 1:1 mixture of 20 mM *N*,*N*-dimethyl-p-phenylenediamine in 7.2 N HCl and 30 mM $FeCl_3$ in 1.2 N HCl. The synthesis of methylene blue was allowed to proceed for 20 minutes at 37 ^{o}C prior to removal of the samples from the glovebox, centrifugation, and analysis at 670 nm. The absorbance at 670 nm was plotted against sulfide concentration in order to produce a standard curve for quantification of sulfide produced in cysteine desulfurase activity measurements. For SDA_{ec} activity measurements, concentrations of L-cysteine ranging from 0.5 to 32 µM were used to initiate the reaction. The amount of sulfide produced within these assays was less than the lowest concentration of our standard curve, which we assumed to be linear within this range. Measurements were conducted in at least triplicate. Due to the insensitivity of this assay, the reaction time of 6 minutes was chosen in order to remain within the linear region of sulfide production at saturating amounts of cysteine while simultaneously generating sufficient sulfide for detection within these assays. The DTT concentration was chosen based on previously conducted experiments in our lab, which have shown this concentration of DTT to be saturating at saturating amounts of L-cysteine.[87, 118, 172, 173]

Sequence and Structural Alignments

The cysteine desulfurases, ISD11, and ACP were aligned using Clustal Omega default parameters[229] and displayed with Boxshade. Mitochondrial targeting sequences were truncated based on the Uniprot database. Alignments of human mitochondrial ACP and ACP_{ec} were conducted in Clustal Omega using default alignment parameters.[229] All 11 human LYR proteins were aligned in a similar fashion. The sequence of LYRM6 was manually shifted, as previously described,[130] using MEGA6.[230] The results of the alignment were visualized using the ConSurf server with default parameters.[231] For the alignment of human and *E. coli* ACP (Fig. II.21B), identical residues are shaded magenta and different residues are shaded based on the similarity of the amino acids. Structures were aligned in Pymol.

CHAPTER III

ARCHITECTURE-SWAPPING OF THE HUMAN FE-S CLUSTER BIOSYNTHETIC SUBCOMPLEX: A NEW MORPHEEIN

Overview

Iron-sulfur (Fe-S) cluster assembly is a complex process requiring a myriad of protein subunits for the synthesis of a single [2Fe-2S] cluster. Due to the toxic nature of substrates, S^{2-} and Fe^{2+}, but the essential requirement of clusters for processes such as oxidative respiration and DNA replication and repair, the Fe-S cluster biosynthetic subcomplex appears to be highly regulated both at the activity level by frataxin (FXN) and metabolic level by acyl-carrier protein (ACP). Interestingly, recent structures of the subcomplex, consisting of NFS1, ISD11, and ACP, suggest that multiple assembly states exist in solution opening a new avenue for regulatory features in this pathway. These open and closed forms of the subcomplex have the same mass but different quaternary structures. Here we use activity measurements, small-angle X-ray scattering, X-ray crystallography, and native ion-mobility mass spectrometry to demonstrate that both the closed and open architectures of the NFS1-ISD11-ACP complex are present in solution. In addition, isolated crystals of both architectures can be activated by FXN. These results suggest a new morpheein-like regulatory mechanism for the Fe-S assembly complex in which architectural rearrangements facilitate FXN-based activation.

Introduction

Iron-sulfur (Fe-S) clusters are essential inorganic cofactors found in proteins and enzymes amongst all domains of life. These cofactors function in a variety of processes such as oxidative respiration, DNA replication and repair, and catalytic transformations of substrates. Pathways for Fe-S cluster synthesis are often found in the cytosol of prokaryotic cells and mitochondria of eukaryotes.[100, 180] Although these cofactors are essential, the substrates required for their synthesis, S^{2-} and Fe^{2+}, contribute to oxidative stress through inhibition of respiratory complex IV[11] and Fenton chemistry,[10] respectively. Therefore, the synthesis of clusters must be highly regulated. Examples of regulation within the eukaryotic Fe-S cluster biosynthetic pathway include the use of the allosteric activator protein frataxin (FXN),[118, 144, 145] the metabolite sensing acyl-carrier protein,[121, 122, 129, 178] and post-translational modifications.[179] However, the mechanisms of these modes of regulation are poorly understood.

Fe-S cluster synthesis within the eukaryotic mitochondria matrix is facilitated by a large multi-protein assembly complex. The sulfur-hub of the assembly complex exists as a stable subcomplex consisting of the cysteine desulfurase (NFS1),[98, 99, 190] LYR protein (ISD11),[112, 116, 117] and acyl-carrier protein (ACP).[121, 122, 129] This subcomplex provides persulfide sulfur to the scaffold protein, ISCU2, where Fe^{2+} and 2 electrons, from FDX2 or FDX1,[152-154] can be combined to synthesize a $[2Fe\text{-}2S]^{2+}$ cluster.[150] These processes can be accelerated by FXN.[118, 144, 145, 148] Unfortunately, mutations in many of the genes involved in Fe-S cluster biosynthesis result in debilitating diseases that lead to cardiomyopathy and neurodegenerative ataxia (Friedreich's ataxia).[232] A central theme in studies involving eukaryotic Fe-S cluster biosynthetic genes involves determining the mechanisms by which FXN accelerates persulfide formation and sulfur transfer[118, 144, 145] and Fe-S cluster biosynthesis[87, 148] from both functional and structural perspectives.

However, the structural mechanism by which FXN facilitates the activation of Fe-S cluster biosynthesis remains unclear.

Recently, X-ray crystal structures of the human Fe-S cluster assembly sub-complex consisting of NFS1-ISD11 in complex with *E. coli* ACP (ACP_{ec}) were determined.[121, 122] Interestingly, both structures featured identical NFS1-ISD11-ACP_{ec} (SDA_{ec}) interaction interfaces amongst a single αβγ assembly (Fig. III.1A) with a Cα RMSD of 0.65 Å (351 atoms). However, the dimeric architectures ($\alpha_2\beta_2\gamma_2$) of the NFS1-ISD11-ACP_{ec} complex are extraordinarily different (Fig. III.1B,C). In fact, overlay of both architectures clearly display clashes amongst subunits demonstrating that the architectures are unique assemblies (Fig. III.1D). One dimeric architecture features an open state where the active site is completely exposed to solvent and was supported by negative stain electron microscopy reconstructions of the complex at near physiological concentrations (Fig. III.1B).[121] The second dimer architecture features a closed state similar to previously determined crystal structures of prokaryotic cysteine desulfurases with support provided by additional crystal structures in the presence of ISCU2 and small-angle x-ray scattering (SAXS) (Fig. III.1C).[122] In addition, recent chemical crosslinking, SAXS, and cryo-electron microscopy (cryoEM) data have provided additional evidence for the presence of a closed architecture in solution.[143, 233]

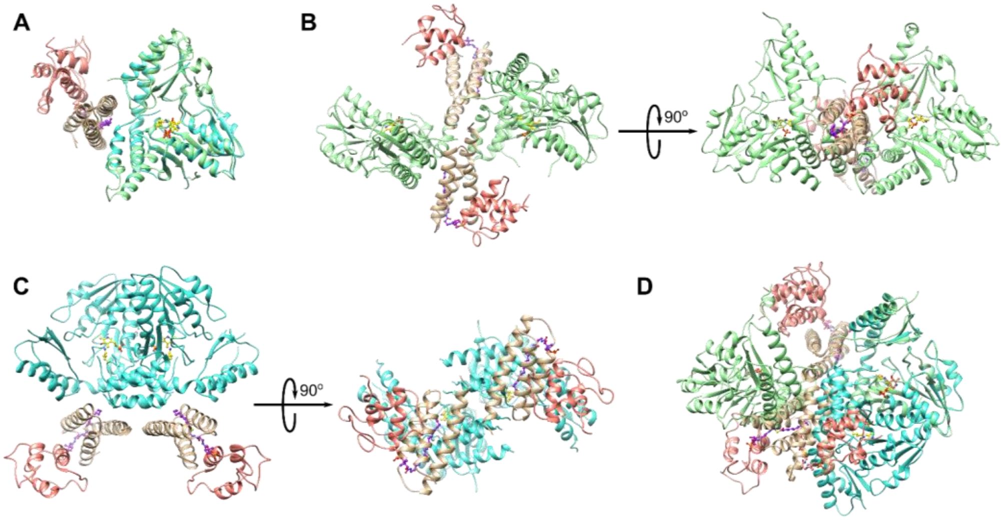

Figure III.1 Comparison of open (5USR.pdb) and closed (5WGB.pdb) architectures of NFS1-ISD11-ACP$_{ec}$. (A) Monomeric assemblies of 5USR.pdb and 5WGB.pdb were aligned in Chimera using MatchMaker. The following colors were used for specific subunits: ISD11 (tan), ACP (salmon), NFS1 (5USR.pdb, light green), and NFS1 (5WGB.pdb, turquoise). Cofactors were colored as follows: pyridoxal 5'-phosphate (yellow) and S-dodecanoyl-4'-phosphopantheine (purple). (B) Display of the open architecture (5USR.pdb). (C) Display of the closed architecture (5WGB.pdb). (D) The two dimeric architectures from *B* and *C* were aligned in Chimera using MatchMaker to demonstrate clear clashes amongst subunits of the overlaid structures.

Due to these recent discoveries, questions regarding the physiological relevance of individual architectural assemblies have surfaced. While structures of the NFS1-ISD11-ACP_{ec} complex in the closed form with and without its adaptor proteins, ISCU2 and FXN,[122, 143] resemble prokaryotic cysteine desulfurase structures of IscS with and without its scaffold,[85, 122, 193] functional differences between the eukaryotic and prokaryotic systems lack sufficient explanation. For example, the *Escherichia coli* FXN homolog, CyaY, suppresses *in vitro* Fe-S cluster biosynthetic assays using IscS and IscU,[86, 87] which is the opposite effect of adding FXN to the eukaryotic system.[87, 148] Interestingly, CyaY can be used to activate the NFS1-ISD11-ISCU2 complex.[87] This suggests that the functional difference in the systems arises not from FXN/CyaY but from the differences in the cysteine desulfurases NFS1 and IscS[87] and may be linked to the distinct subunit interactions of the NFS1-ISD11-ACP_{ec} open architecture (Fig. III.1B).[121] Additionally, evidence suggests FDX2 binds to NFS1 in a different position in comparison to Fdx with IscS.[70, 71, 154] This leads to competition between Fdx and CyaY[70, 71] in prokaryotes but simultaneous binding of FDX2 and FXN in eukaryotes.[154] While these differences may offer an explanation for the presence of an open subcomplex, the high homology amongst subunits between the two systems provides support for a functional closed architecture leaving the physiological significance of both structures unclear.

More recently, a single ^{19}F NMR spectrum of [^{19}F-Trp] NFS1-ISD11-ACP_{ec} was published suggesting multiple conformations in solution; however, it was unclear how many conformations the resulting spectrum contained.[233] The lack of understanding in the conformational landscape of the NFS1-ISD11-ACP_{ec} dimer warrants additional studies to determine the functional significance of both the open and closed architectures. In order to provide a clearer picture for accessory protein interactions and mechanistic steps in Fe-S cluster biosynthesis, the relationship between open and closed architectures must be elucidated. Here we use a variety of functional and biophysical approaches to interrogate solution states of the NFS1-ISD11-$\mathrm{ACP_{ec}}$ complex and provide key results contributing to the potential of architecture swapping control mechanisms in human Fe-S cluster biosynthesis.

Results

Method of $\mathrm{SDA_{ec}}$ Preparation Does Not Affect FXN-based Activation

Our initial goal with this study was to reproduce the expression and purification of the NF$\underline{\mathrm{S}}$1-IS$\underline{\mathrm{D}}$11-$\underline{\mathrm{A}}\mathrm{CP_{ec}}$ ($\mathrm{SDA_{ec}}$) complex as described by the manuscripts featuring the X-ray crystal structure determinations of the open and closed forms of the complex. The expression constructs for the two studies were identical, but there were differences in expression conditions. The open form was generated using a rich, auto-induction media which maximizes $\mathrm{ACP_{ec}}$ association and stability of the $\mathrm{SDA_{ec}}$ complex.[121] The closed form was generated using a rich media, Terrific broth, to obtain a similar result.[122] In addition, the preparations of the open form of the $\mathrm{SDA_{ec}}$ complex featured additional purification steps. Although these differences may seem minute, preparation methods seemed like a plausible explanation for the differences in assembly. However, activity measurements of the $\mathrm{SDA_{ec}}$ complex prepared by these different methods did not suggest major differences in the activity of the complex in the presence of adaptor proteins and $\mathrm{Fe^{2+}}$ (Fig. III.2A,B). $\mathrm{SDA_{ec}}$ prepared under the Barondeau conditions displayed a k_{cat} of

$9.3 \pm 0.5\ \text{min}^{-1}$ and a K_M for cysteine of 22 ± 5 μM. Additionally, SDA_{ec} prepared under the Cygler conditions displayed a k_{cat} of $11 \pm 0.4\ \text{min}^{-1}$ and a K_M for cysteine of 20 ± 3 μM. In fact, these activities are similar to those we have reported in the past when examining the activation feature of FXN in S^{2-} detection assays.[87, 118, 121]

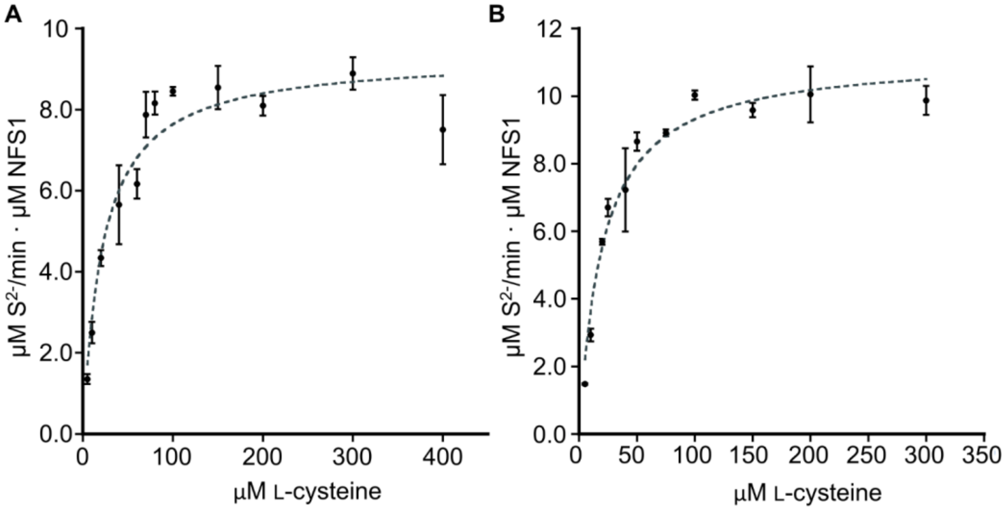

Figure III.2 Michaelis-Menten kinetic plots for cysteine turnover by different preparations of SDA_{ec} in the presence of ISCU2, FXN, and Fe^{2+}. (A) SDA_{ec} prepared by the Barondeau method. (B) SDA_{ec} prepared by the Cygler method. All assays were conducted at pH = 7.5 and 37 ºC using 0.5 µM SDA_{ec}, 1.5 µM ISCU2, 1.5 µM FXN, and 5 µM Fe^{2+}.

Small-angle X-ray Scattering Suggests Multiple Conformations in Solution

Although small-angle x-ray scattering (SAXS) data has been published on this system previously, these studies either ignored one of the architectures, suffered from inconsistent fitting methods, or utilized incomplete models.[122, 233] In particular, we were interested in whether or not the scattering curves generated from our preparations were consistent with the scattering curves of $\mathrm{SDA_{ec}}$ presented in other publications. To do so, we screened several buffer conditions in order to identify a composition which maximized stability and reduced concentration-dependent oligomerization. We found that a high ionic strength buffer achieved this best. Averaged frames of multiple buffer wells with identical composition to our target sample were subtracted from sample frames (Fig. III.3A) prior to sample averaging. We then identified time points at which radiation damage set in and decided where to establish a sample average (Fig. III.3B). The resulting samples were fully folded (Fig. III.3C) but suffered from minor concentration-dependent oligomerization as can be seen from the low q region of the scattering curve (Fig. III.3B, inset), the Guinier analysis (Fig. III.3C, inset), and pair distribution functions (Fig. III.3D). Due to these observations, we chose to continue our analyses with the lowest concentration sample, which provided a smooth pair distribution function and a molecular weight within error[234] of the expected molecular weight (Table III.1).

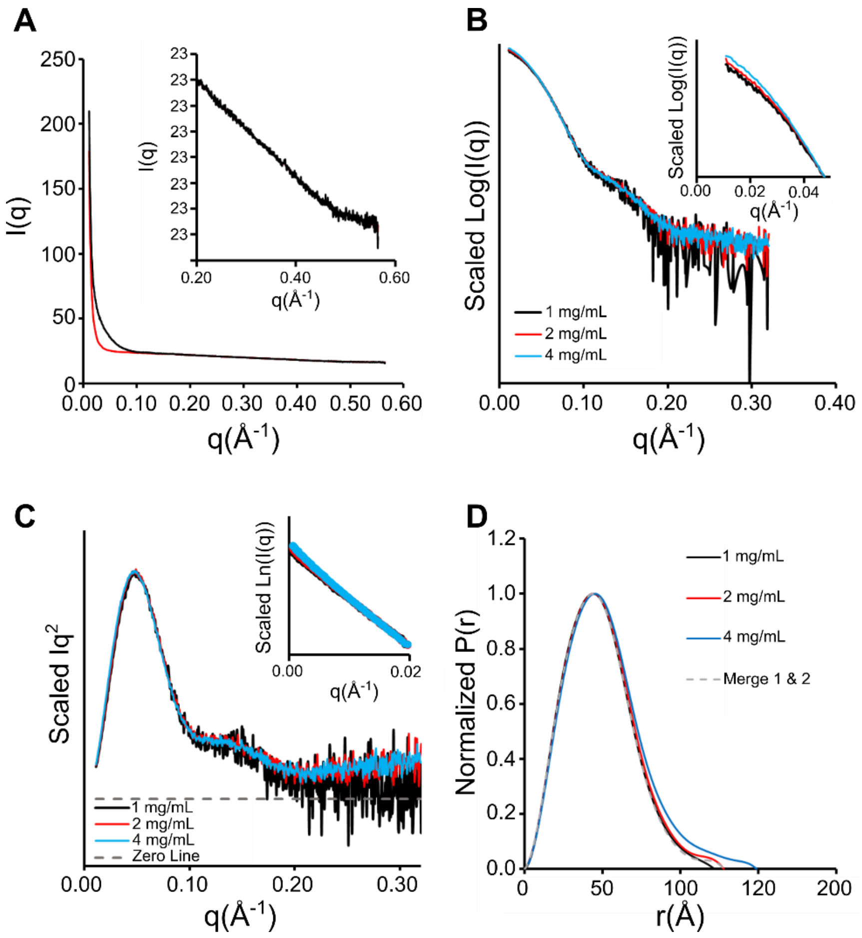

Figure III.3 Small-angle X-ray scattering data processing for SDA$_{ec}$. (A) Overlay of average buffer (100 mM sodium phosphate, 500 mM NaCl, 2 % glycerol, 2 mM TCEP, pH = 8.0) and a single frame from a 1 mg/mL SDA$_{ec}$ in the corresponding buffer. Inset demonstrates overlap of buffer and sample at high q. (B) Overlay of subtracted scattering curves. Inset demonstrates concentration dependent oligomerization. Negative intensities are not shown. (C) Kratky plots for SDA$_{ec}$ at multiple concentrations. Inset displays Guinier plots demonstrating concentration dependent oligomerization. (D) Pair distribution functions for SDA$_{ec}$ samples. Low q region was truncated based on Guinier analysis, and the high q region was truncated to 8/Rg prior to pair distribution analysis.

Table III.1 Small-angle X-ray scattering derived parameters.

	SDA_{ec}	SDA_{ec}	SDA_{ec}	SDA_{ec}	SDA_{ec}
Data source	This manuscript	This manuscript	This manuscript	This manuscript	Markley
Sample concentration (mg/mL)	1	2	4	Merged	N/A
Exposure time (sec)	1.5	1.5	0.6	N/A	N/A
Merged regions				1:(0.0109 - 0.07), 2: (0.1001 - 0.3202)	
Guinier analysis:					
I(0)	31.4 ± 0.2	82.1 ± 0.2	194.0 ± 0.4	81.0 ± 0.4	904.6 ± 8.9
q range ($Å^{-1}$)	0.015-0.035	0.018 - 0.034	0.014 - 0.033	0.015-0.035	0.017 - 0.036
R_g (Å)	36.88 ± 0.25	37.71 ± 0.14	39.69 ± 0.12	36.88 ± 0.25	36.27 ± 0.47
$q R_g$ range	0.565 - 1.285	0.662 - 1.293	0.542 - 1.294	0.565 - 1.285	0.619 - 1.290
R^2	0.993	0.998	0.999	0.993	0.995
P(r) analysis:					
I(0)	31.3 ± 0.1	82.0 ± 0.1	194.5 ± 0.4	80.8 ± 0.32	912.3 ± 5.6
R_g (Å)	36.94 ± 0.12	37.90 ± 0.07	40.54 ± 0.12	37.07 ± 0.16	36.82 ± 0.17
d_{max} (Å)	122	128	149	128	112
q range ($Å^{-1}$)	0.0153 - 0.2171	0.0176-0.2121	0.0137-0.2015	0.0153 - 0.2171	0.0171 - 0.2200
χ^2 (total estimate from GNOM)	1.10	1.11	1.16	0.99	0.8241
Mw analysis (Vc method, kDa)[†]	134	129	149	126	131

[†] The high-angle data was truncated to 0.320 $Å^{-1}$ to maintain a consistent integration area. Low angle data was truncated based on gunier analysis.

N/A = not applicable

Our first analysis of the SAXS data included a comparison of our data to published results that were publicly available on SASBDB[233, 235] and generously provided from Cygler et al.[122] We treated and processed data in a similar fashion to our scattering curves. Specifically, we truncated data within the Guinier region which featured significant aggregation[122] or interference from the beamstop.[233] It appears that data collected by Cygler et al. features a large population of a concentration-dependent oligomer as can be seen by the increase in scattering at low q (data not shown for permission reasons). This conclusion was further confirmed by inspecting Supplementary Figure 5D within Cygler et al's 2017 manuscript, which shows a poor fit of the crystal structure to the low q portion of the scattering curve. Additionally, our analysis of the data (data not shown for permission reasons) closely resembles the reported Rg of 54.7 Å and D_{max} of approximately 180 Å.[122] In fact, data collected on our purified complex in conditions similar to Cygler et al. provided scattering curves nearly identical to those presented by Cygler et al. (data not shown for permission reasons). Alternatively, data collected by Markley et al.[233] closely resembles the data we collected under high ionic strength conditions (Fig. III.4). Given the similarities amongst scattering curves (Fig. III.4), we believe that the solution samples are quite similar in conformation. The differences observed between datasets are primarily due to concentration dependent oligomerization. Additionally, we suspect this may be the reason the published SAXS parameters by Markley et al. on SDA_{ec} in a 2017[109] manuscript are substantially different from the manuscript published in 2018.[233]

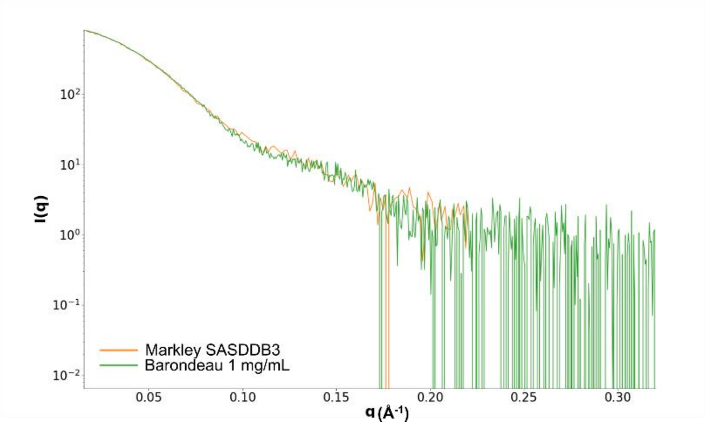

Figure III.4 Comparison amongst published scattering curves. Intensities are plotted on a logarithmic scale. Comparison between the scattering curve published by Markley et al and our preparation SDA$_{ec}$ in 100 mM sodium phosphate, 500 mM NaCl, 2 % glycerol, 2 mM TCEP, pH = 8.0.

For further analyses, the remainder of the data was truncated at high q of 8/Rg. Scattering above 8/Rg is specific to internal scatterers and is background in the measurements analyzed here. Given our previous determination of the negative stain electron microscopy structure of SDA_{ec}, we used the electron microscopy map to generate a dummy atom model to evaluate whether our previous low resolution structural determinations from EM match our solution scattering profile from SAXS. We used EM2DAM[236] to screen for threshold levels which provided a dummy atom model that fit the experimental scattering curve in FoXS.[237] A threshold of 0.07 provided a reasonable fit to the experimental data (X^2 = 2.93); however, the resulting low resolution envelope did not provide any discriminatory information regarding the architecture type present (Fig. III5A-C and Table III.2).

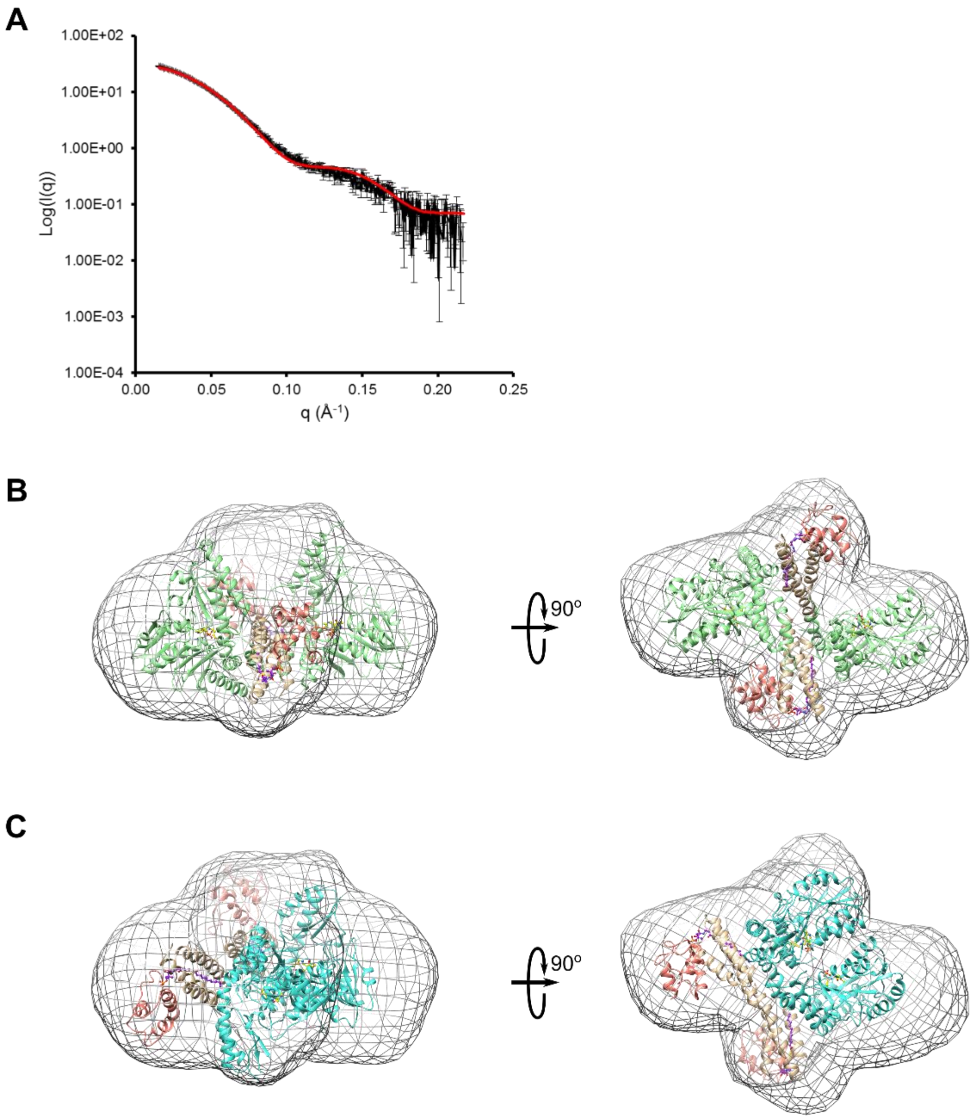

Figure III.5 Comparison of previously determined negative stain electron microscopy envelope to the scattering curve of SDA$_{ec}$. (A) Theoretical scattering curve (red) derived from EM2DAM by varying threshold level of map with following refinement in DAMMIN. Fit of the refined dummy atom model to the experimental scattering curve (black, $X^2 = 2.93$, $q_{range} = 0.0153 – 0.217$). Negative intensities are not shown. (B) Fit of 5USR.pdb to the refined dummy atom model contoured to 20 Å in Chimera. Model is colored as described in Fig. III.1. (C) Fit of 5WGB.pdb to the refined dummy atom model contoured to 20 Å in Chimera. Model is colored as described in Fig. III.1.

Table III.2. Threshold levels and their respective fits to the experimental scattering curve of SDA_{ec}.

Threshold Level	Dummy Atoms	c_1	c_2	X^2
0.1	36737	1.04	3.93	21.33
0.09	42681	1.00	2.57	8.67
0.08	48301	1.00	3.30	3.55
0.07	53938	1.00	3.50	2.93
0.06	59269	1.00	3.96	5.60

Additionally, upon conducting *ab initio* shape analysis, it was clear multiple shapes could be fit to this scattering curve. In fact, AMBIMETER[238] suggested 10 compatible shape categories, and after 20 independent shape reconstructions using DAMMIF[239] and averaging in DAMAVER[240] the reported normalized spatial discrepancy (NSD) was 1.308 ± 0.266 suggesting several different classes of shapes. The resulting shape was refined in DAMMIN,[241] and the available crystal structures were superimposed (Fig. III.6A). We then utilized DAMCLUST[242] to identify groups of shapes that were most similar. Using this strategy, DAMCLUST identified 2 clusters. The structures within the clusters were then averaged in DAMAVER. The averaged model from Cluster 1 contained 15 models (NSD = 0.912) from the DAMCLUST analysis, and the averaged model from Cluster 2 contained 5 models (NSD = 0.753). These averages were then subjected to DAMSTART to produce models with fixed cores which were then refined in DAMMIN (Fig. III.6B). While neither the open nor the closed dimer structures provide a satisfactory fit to either cluster, this analysis does demonstrate the ambiguity in shape analysis for this system (Fig. III.6B). We also performed an identical analysis on the pair distribution function published by Markley et al. AMBETER suggested 25 classes of shapes and clustering analysis generated 5 clusters (Data not shown). Therefore *ab initio* shape reconstruction is not the best method to confirm architecture state in solution in this system.

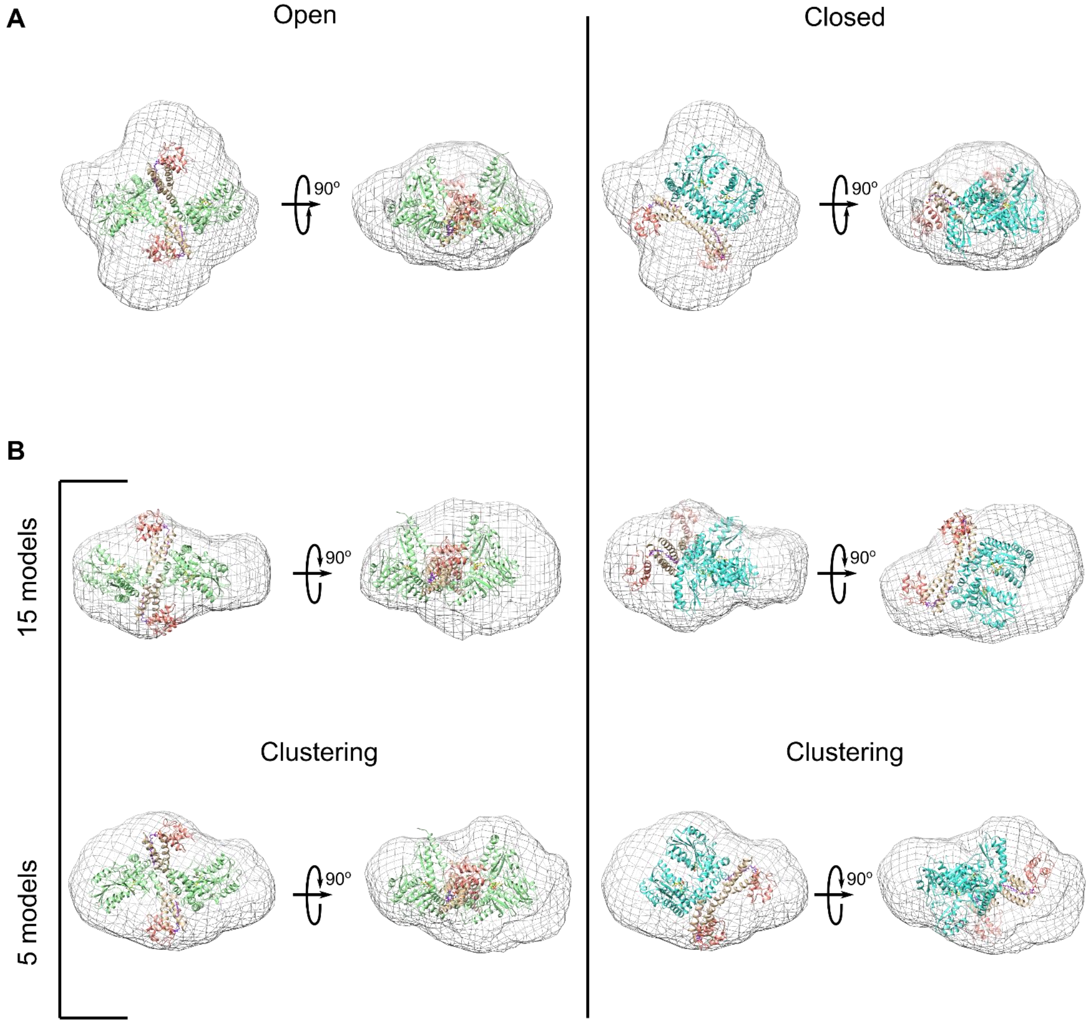

Figure III.6 3D ab initio reconstructions from experimental SAXS data. Models for open (5USR.pdb) and closed (5WGB.pdb) were superimposed with the map (contoured to 20 Å) using Chimera with the fit in map command. (A) Overall reconstructions using 20 models provided a normalized spatial discrepancy of 1.308 implying significant differences amongst models. (B) Overall reconstructions using a clustering approach. When 15 models were averaged a normalized spatial discrepancy of 0.912 was achieved. The remaining 5 models were also averaged providing a normalized spatial discrepancy of 0.753. The fits are ambiguous. Models are colored as described in Fig. III.1.

The final analysis which demonstrated the possibility of a mixture of architectures in solution was atomic modeling. We started our analysis by a simple comparison of the scattering curves to the published crystal structures of the open and closed architectures including the closed SDA_{ec} subcomplex from the $SDA_{ec}U$ crystal structure (5WKP.pdb) which contains a completely closed dimeric conformation.[122] Initially, it appeared that the SDA_{ec} unit from 5WKP.pdb fit the data best (Fig. III.7A and Table III.3); however, all models are lacking a significant number of total scatterers (protein, non-H atoms): 5USR (17.2 %), 5WGB (31.6 %), and 5WKP (12.6 %). This made comparing the quality and accuracy of the fits difficult as these missing scatterers, and their conformations have a significant effect on the theoretical scattering curve. A simple demonstration of this was done by generating an open architecture (5USR.pdb) using the available cryoEM structure of $SDA_{ec}UF$ (6NZU.pdb)[143] by mapping the NFS1 subunits using a Cα alignment method in PyMOL on the open architecture dimer. The newly constructed open dimer was only missing 6.5 % of the total scatters. Fits for the open architecture reconstructed from SDA_{ec} subunits of 6NZU.pdb generated a $X^2 = 3.13$ while the closed SDA_{ec} sub-complex of 6NZU.pdb generated a $X^2 = 1.43$ (Fig. III.7B). Each of these fits was an improvement from the original crystal structure inputs (Table III.3). Because of the effect of these scatters we sought more complete methods for evaluating the crystal structures as solution scatterers. To do this, we utilized the AllosMod-FoXS[237, 243] webserver which uses MODELLER[244] to generate complete models. In addition, the large amount of flexibility that has been observed in the available crystal structures[121, 122] suggests a highly dynamic complex; therefore, we applied molecular dynamics simulations to the generated

MODELLER structures at 300 K which were restrained to be close to the input structure. This methodology was used on all models used in previous fitting analyses (Fig. III.7A,B). This resulted in improved models in all cases (Fig. III.7C,D and Table III.3) that were almost indistinguishable in the context of the error of the experimental SAXS curve. Ultimately, it appears SAXS may not be the best biophysical method for resolving the two architectures primarily due to its low resolution, and in this case, the available models are missing a number of flexible scatters which directly affects atomistic modeling results.

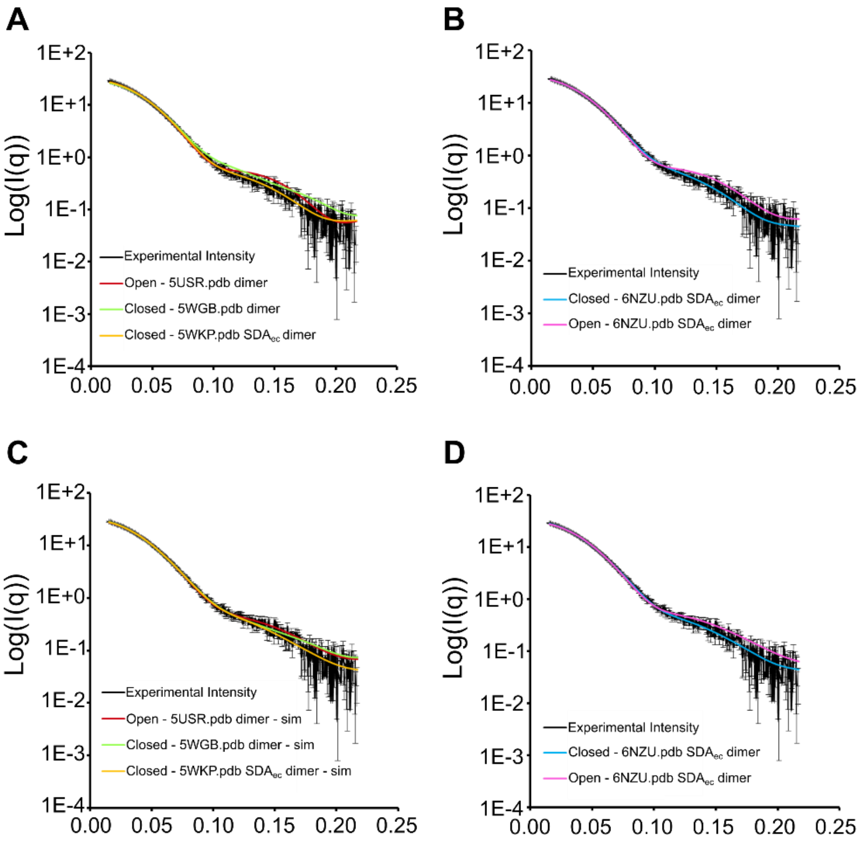

Figure III.7 Atomic modeling of SDA$_{ec}$ SAXS data using FoXS. (A) Fits of SDA$_{ec}$ dimers from available crystal structures to the experimental data. (B) Fits of SDA$_{ec}$ dimers from the available cryoEM structure of SDA$_{ec}$UF. Open SDA$_{ec}$ was generated by Cα alignment of the two NFS1 subunits available in the cryoEM model to the two NFS1 subunits in SDA$_{ec}$ dimer available in 5USR.pdb. (C,D) AllosMOD-FoXS simulations at 300K that remain close to the input to the structure.

Table III.3 Atomic modelling fitting parameters.

						AllosMod-FoXS (10 simulations close to input structure, 300 K)				
Model	5USR.pdb	5WGB.pdb	5WKP.pdb (SDA_{ec})	6NZU.pdb (SDA_{ec} - open)	6NZU.pdb (SDA_{ec} - closed)	5USR.pdb	5WGB.pdb	5WKP.pdb (SDA_{ec})	6NZU.pdb (SDA_{ec} - open)	6NZU.pdb (SDA_{ec} - closed)
q range (Å^{-1})	0.0153 - 0.2171	0.0153 - 0.2171	0.0153 - 0.2171	0.0153 - 0.2171	0.0153 - 0.2171	0.0153 - 0.2171	0.0153 - 0.2171	0.0153 - 0.2171	0.0153 - 0.2171	0.0153 - 0.2171
X^2	3.54	5.86	1.62	3.13	1.43	1.53	1.41	1.18	2.37	1.12
c_1, c_2	1.05, 1.13	1.05, 4.00	1.04, 4.00	1.05, -0.39	1.00, 4.00	1.04, -0.88	1.01, -1.35	0.99. 1.08	1.02, -1.31	0.99, 0.33
Cα RMSD to 5USR.pdb dimer (Å)	NC	NC	NC	0.855	NC	1.584	NC	NC	1.660	NC
Cα RMSD to 5WGB.pdb dimer (Å)	NC	NC	5.384	NC	5.267	NC	0.913	5.729	NC	5.253
Cα RMSD to 5WKP.pdb (-ISCU2) dimer (Å)	NC	5.384	NC	NC	0.627	NC	5.655	1.049	NC	1.176

Crystallization of SDA_{ec} Prepared by Different Methods

Our previous activity and SAXS measurements lead us to the hypothesis that different preparation methods generate a mixture of both open and closed architectures of SDA_{ec}. We tested this hypothesis by buffer exchanging different preparations of the SDA_{ec} complex into opposing crystallization buffers and crystallizing the complex in the alternate crystal forms (Fig. III.8). We further verified the presence of the different crystal forms by screening the crystals on a home-source X-ray diffractometer. After indexing the screened images (Table III.4), it was clear that regardless of the preparation method, a mixture of open and closed architectures are present in solution and can be crystallized.

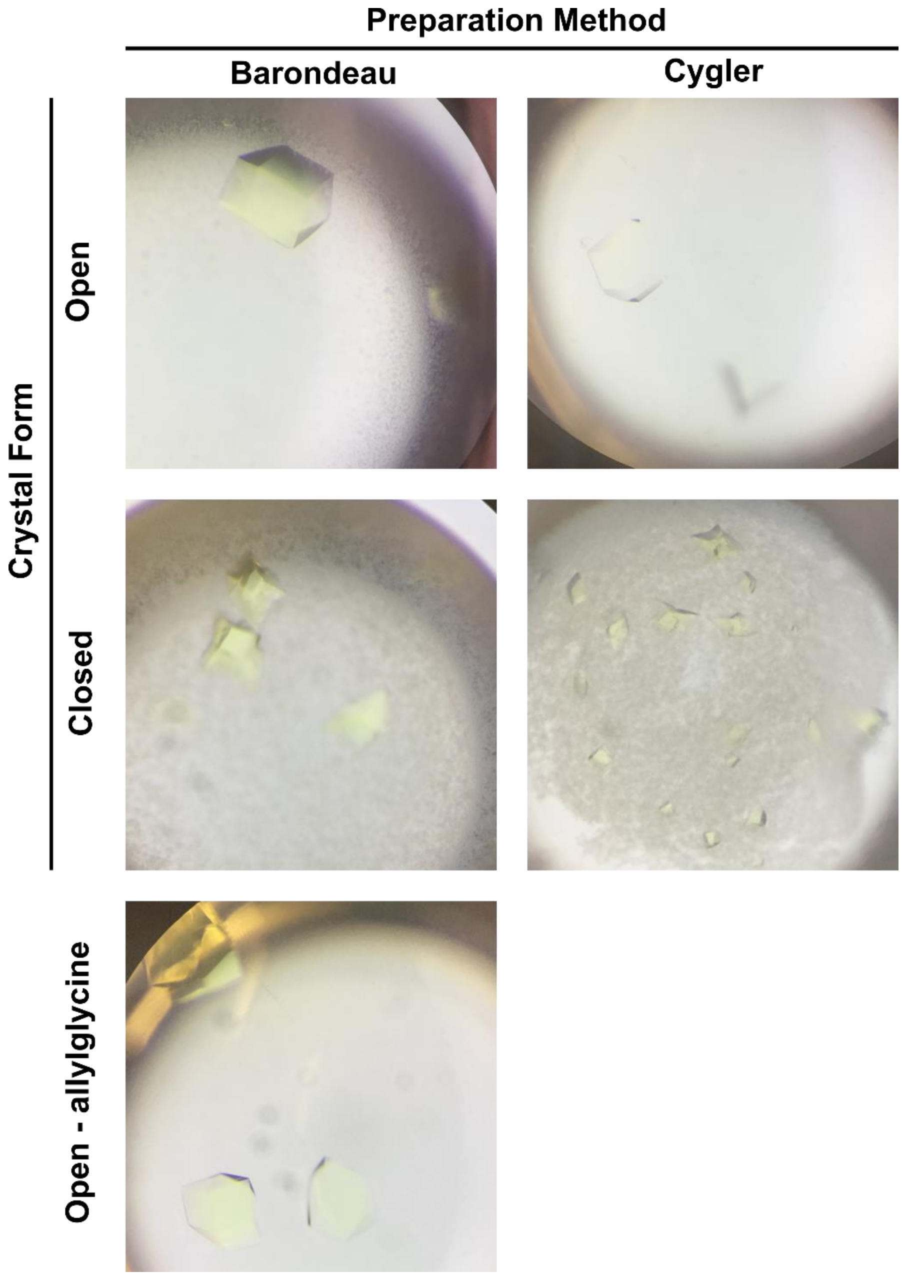

Figure III.8 Various crystal forms of SDA$_{ec}$ prepared by different methods.

Table III.4 Indexing results from the different crystal forms of SDA_{ec} prepared by different methods.

		Unit Cell Parameters					
Preparation Method	**Crystal Form**	**a (Å)**	**b (Å)**	**c (Å)**	**α (°)**	**β (°)**	**γ (°)**
Barondeau	Open	125.8	147.9	168.1	90	90	90
Barondeau	Open (-allylglycine)	122.1	144.1	163.6	90	90	90
Barondeau	Closed	139.2	139.2	200.5	90	90	120
Cygler	Open	125.2	146.8	166.7	90	90	90
Cygler	Closed	139.8	139.8	200.6	90	90	120
Preparation Method	**Crystal Form**	**Published Unit Cell Parameters**					
Barondeau	Open (5USR.pdb)	125.5	147.8	168.5	90	90	90
Cygler	Closed (5WGB.pdb)	140.8	140.8	203.3	90	90	120

Both Closed and Open SDA$_{ec}$ Crystals Can Be Activated by FXN

Based on our SAXS and crystallographic results, both SDA$_{ec}$ architectures appear to be in-solution simultaneously regardless of preparation method. Therefore, we sought a method to "freeze-out" individual architectures and test their activity. In order to do so, we picked single crystals of each architecture and separately measured their activity with and without the activator subunit FXN. Interestingly, both open and closed crystals could be activated by FXN (Fig. III.9), which suggests two possible hypotheses. Both forms of SDA$_{ec}$, open and closed, can be activated, or the presence of FXN and possibly, in concert with substrate causes a subunit rearrangement to a single activated architecture. Interestingly, SAXS measurements and chemical-crosslinking mass spectrometry results on SDA$_{ec}$U and SDA$_{ec}$UF from Markley et al. support the presence of the closed architecture bound to ISCU2 and FXN in solution.[233] However, the study did not attempt to generate additional open SDA$_{ec}$U models for SAXS analysis and utilized a crosslinking reagent that was unable to screen for the presence of the open architecture. The maximum Cα-Cα distance for the crosslinker was 27.4 Å; whereas, the shortest lys-lys, Cα-Cα inter-subunit NFS1 distance in the open form of 5USR.pdb is 32.2 Å. Clearly, specially designed structural and biophysical assays need to be utilized in order to test these hypotheses.

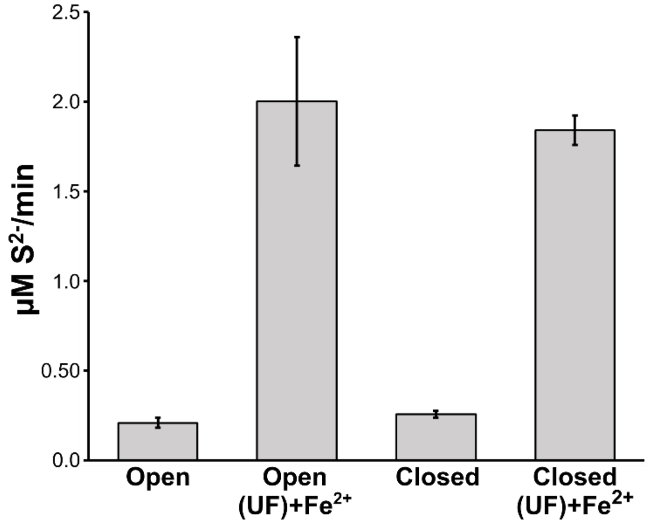

Figure III.9 Cysteine desulfurase activities from isolate crystals in the open and closed forms. Single crystals of both open and closed architectures were isolated. The ability of the isolated crystals to turnover cysteine was evaluated both in the presence and absence of ISCU2, FXN, and Fe^{2+}.

SDA$_{ec}$ Dimers Can Freely Exchange in Solution

To test the above hypotheses, we generated ^{15}N labeled SDA$_{ec}$ for exchange reactions. If ^{15}N labeled complex were capable of exchanging with unlabeled complex, this would suggest that the SDA$_{ec}$ $\alpha_2\beta_2\gamma_2$ species was capable of readily disassociating to to αβγ units which could then re-associate to form the open and closed forms of the complex. Native mass spectrometry was used to monitor the exchange. Interestingly, upon mixing equimolar amounts of labeled and unlabeled SDA$_{ec}$ a clear exchange (83.3 %) was observed over 120 minutes between SDA$_{ec}$ units to generate a $^{15}N^{14}N$-SDA$_{ec}$ mixed species (Fig. III.10A and Table III.5). Addition of ISCU2 or FXN to SDA$_{ec}$ under saturating conditions prior the initiation of the exchange reaction resulted in an inhibition of this exchange process (Table III.5). Interestingly, mixing of tagged IscS with un-tagged IscS resulted in 31.1 % exchange over 120 minutes. Inhibition of this exchange was observed in the presence of IscU (Table III.5). The exchange reaction for un-tagged SDA$_{ec}$ was slower than the tagged material and required 24 hours 78.7 % exchange (Table III.5). We then tested whether un-tagged SDA$_{ec}$ can also be activated by FXN in the presence of 1 mM L-cysteine and Fe^{2+} and found similar activation (1.3 ± 0.01 μM S^{2-}/min · μM NFS1 unactivated, 7.88 ± 0.34 μM S^{2-}/min · μM NFS1 activated) to the tagged SDA$_{ec}$[121] suggesting that while the exchange process is slow the activation remains the same regardless of the presence of the tag. These results indicate that a dissociative and reassembly process for the SDA$_{ec}$ complex occurs in solution that may lead to interconversion between the open and closed forms of the complex.

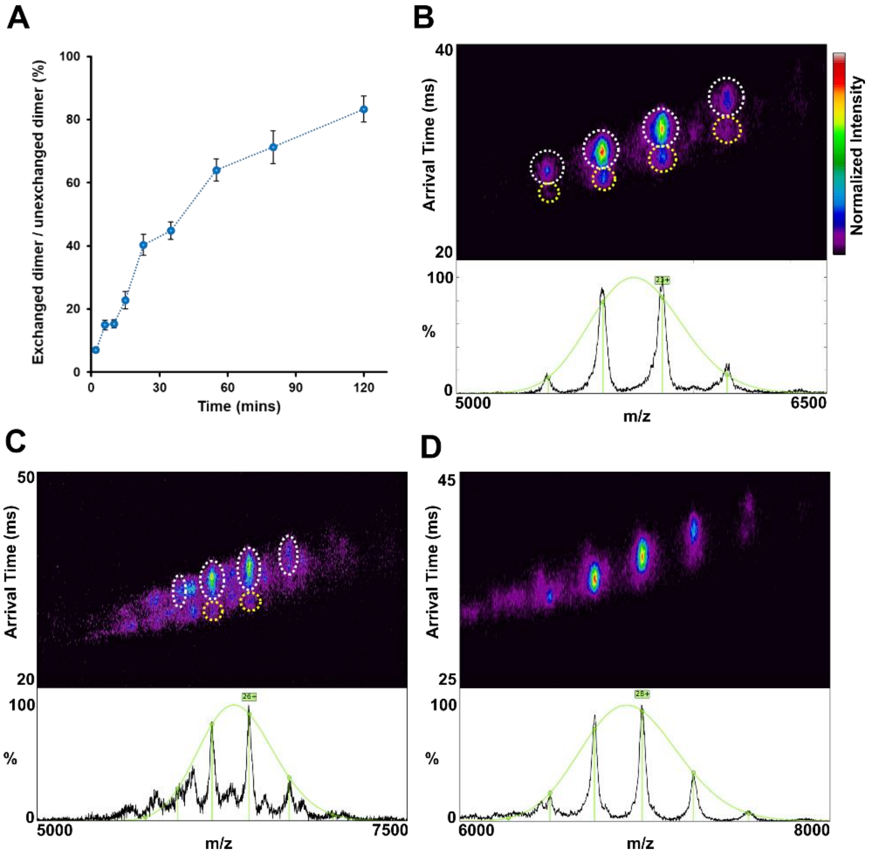

Figure III.10 Native ion-mobility mass spectrometry analysis of SDA$_{ec}$. (A) Kinetic exchange of tagged ^{14}N-SDA$_{ec}$ dimer (^{14}N^{14}N) and ^{15}N-SDA$_{ec}$ (^{15}N^{15}N) dimer using a 1:1 ratio. The Y axis is shown as the amount of exchanged dimer (^{15}N^{14}N) divided by the sum of unexchanged dimer (^{14}N^{14}N and ^{15}N^{15}N). (B) Native IM-MS spectrum of SDA$_{ec}$ shows two major species. The high/low arrival time (extended/compact) species are circled by white/yellow dashed lines respectively. (C) Native IM-MS spectrum of SDA$_{ec}$U shows two major species. The high/low arrival time (extended/compact) species are circled by white/yellow dashed lines respectively. (D) Native IM-MS spectrum of SDA$_{ec}$UF shows single major species.

Table III.5 Kinetic exchange of $^{15}N/^{14}N$-SDA$_{ec}$ or tagged/untagged IscS dimer species at a 1:1 ratio. The values in the table are shown as the amount of exchanged dimer ($^{15}N^{14}N$) divided by unexchanged dimer ($^{14}N^{14}N$ and $^{15}N^{15}N$) in percentage or as the amount of exchanged IscS divided by the unexchanged dimer (tagged and untagged).

Time	**2 mins**	**6 mins**	**10 mins**	**15 mins**	**23 mins**
tagged SDA$_{ec}$	7.0 ± 0.8	14.9 ± 1.6	15.3 ± 1.3	22.8 ± 2.8	40.4 ± 3.3
tagged SDA$_{ec}$U	0.0	0.0	0.0	0.0	0.0
tagged SDA$_{ec}$UF	0.0	0.0	0.0	0.0	0.0
untagged SDA$_{ec}$	0.0	0.0	0.0	0.4 ± 0.4	0.3 ± 0.5
untagged SDA$_{ec}$U	0.0	N/A	N/A	N/A	N/A
untagged SDA$_{ec}$UF	0.0	N/A	N/A	N/A	N/A
IscS	1.6 ± 0.0	N/A	N/A	N/A	N/A
IscS-IscU	0.0	N/A	N/A	N/A	N/A

Time	**35 mins**	**55 mins**	**80 mins**	**120 mins**	**24 hrs**
tagged SDA$_{ec}$	44.8 ± 2.8	64.0 ± 3.4	71.3 ± 5.2	83.3 ± 4.1	N/A
tagged SDA$_{ec}$U	0.0	0.0	0.0	0.0	N/A
tagged SDA$_{ec}$UF	0.0	0.0	0.0	0.0	N/A
untagged SDA$_{ec}$	1.1 ± 0.8	1.5 ± 1.1	2.5 ± 0.9	3.9 ± 0.7	78.7 ± 0.6
untagged SDA$_{ec}$U	0.0	N/A	0.0	0.0	N/A
untagged SDA$_{ec}$UF	0.0	N/A	0.0	0.0	N/A
IscS	7.8 ± 1.2	14.1 ± 0.2	N/A	31.1 ± 0.7	N/A
IscS-IscU	0.0	0.0	N/A	0.0	N/A

N/A = not applicable

The SDA$_{ec}$ Dimer Exists in Two Conformations in Solution and Can Be Driven to a Single Conformation in the Presence of Additional Subunits

In order to investigate the conformational landscape of the SDA$_{ec}$ dimer with and without its accessory subunits, we utilized native ion-mobility mass spectrometry (IM-MS). Upon analyzing SDA$_{ec}$ by itself, we could clearly identify two major species with different collisional cross-sections corresponding to the SDA$_{ec}$ dimer (Fig. III.10B, Fig. III.11A,B, and Table III.6). We preliminarily assigned the larger collisional cross-section to the open conformation and the smaller collision cross section to the closed conformation based on the approximated collisional cross-sections provided by projection superposition approximation calculations (Table III.6). Upon further inspection of the ion mobility mass spectra, it was clear that in the tagged and un-tagged SDA$_{ec}$ analysis the dominant species was the open architecture in solution (Fig. III.11A,B) consistent with previous negative stain electron microscopy experiments.[121] To further validate the presence of these two conformers, we performed a charge reduction analysis in triethylammonium acetate which also showed two clear conformations (Fig. III.12A,B).

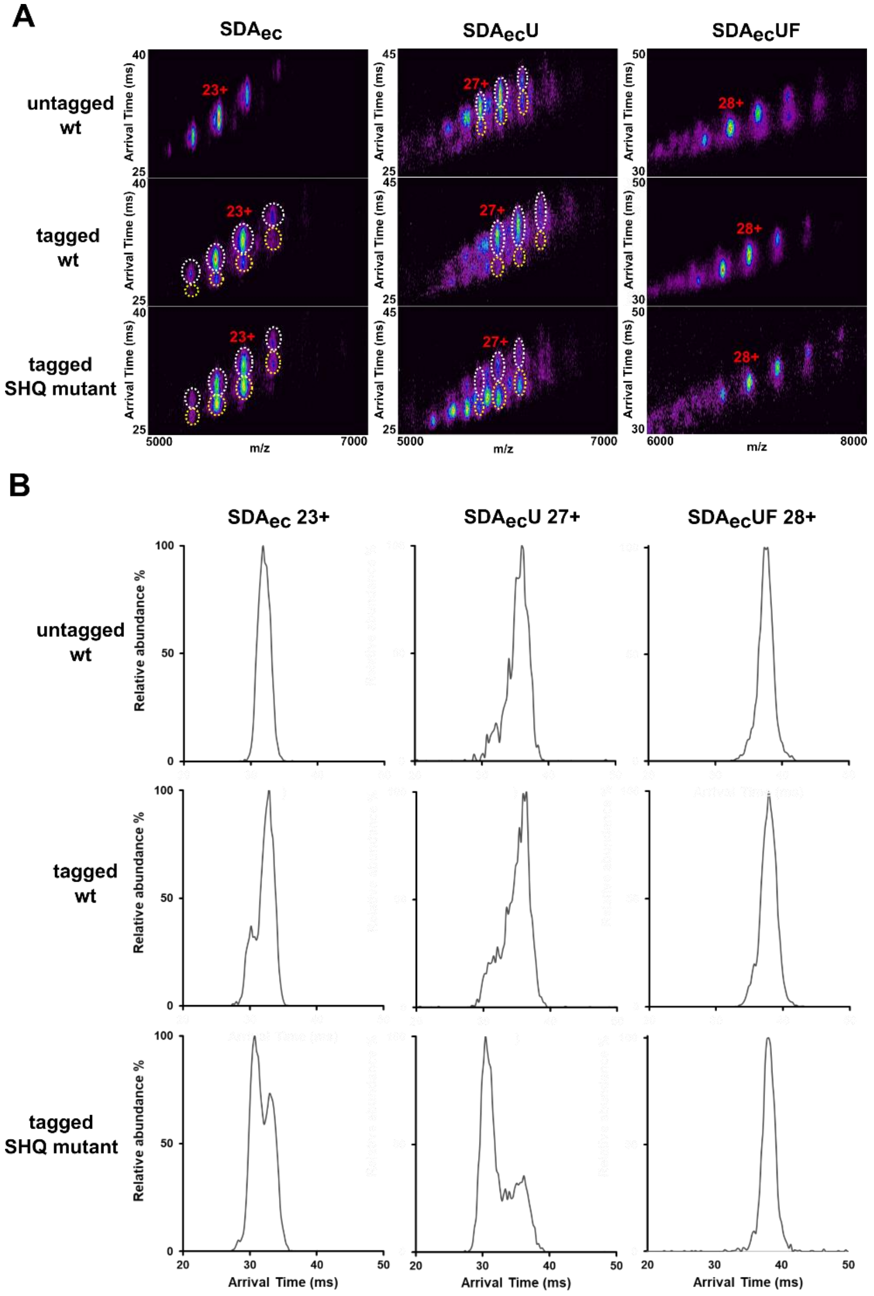

Figure III.11 Ion mobility of all SDA$_{ec}$/SDA$_{ec}$U/SDA$_{ec}$UF species. (A) IM plot of all species. The high/low arrival time (extended/compact) species are circled by white/yellow dashed lines respectively. (B) IM spectra of all species. SDA$_{ec}$ shows two major species (untagged SDA$_{ec}$ shows only extended/high arrival time species); SDA$_{ec}$U shows two major species, with potential intermediates not resolvable. SDA$_{ec}$UF shows a single dominant species.

Table III.6 Collision cross section (Ω) of tagged SDA_{ec} species. Measured Ω using synapt G2 and calculated Ω using the projected superposition approximation method. Experimental and calculated Ω show the same overall trend.

	m / Da	**z**	**Ω_{Exp} (Å^2)**	**Ω_{PSA} (Å^2)**		**Relative error (%)**	
				Models from 6NZU	**Allosmod**	**CCS_{Exp} – CCS_{PSA}**	
Closed tagged SDA_{ec}	134 k	22	6835 ± 135	7598 ± 51	Unable to calculate	-10	N/A
		23	6928 ± 109			-9	N/A
Open tagged SDA_{ec}	134 k	22	7088 ± 155	8161 ± 38	8982 ± 34	-13	-21
		23	7203 ± 159			-12	-20
Closed tagged $SDA_{ec}U$	165 k	26	8194 ± 140	8921 ± 54		-8	
		27	8390 ± 81			-6	
Open tagged $SDA_{ec}U$	165 k	26	8737 ± 48	9086 ± 42		-4	
		27	8802 ± 21			-3	
Closed tagged $SDA_{ec}UF$	193 k	27	9333 ± 22	9684 ± 79		-4	
		28	9370 ± 52			-3	
Open tagged $SDA_{ec}UF$	193 k	27	N/A	10070 ± 64		N/A	
		28	N/A			N/A	

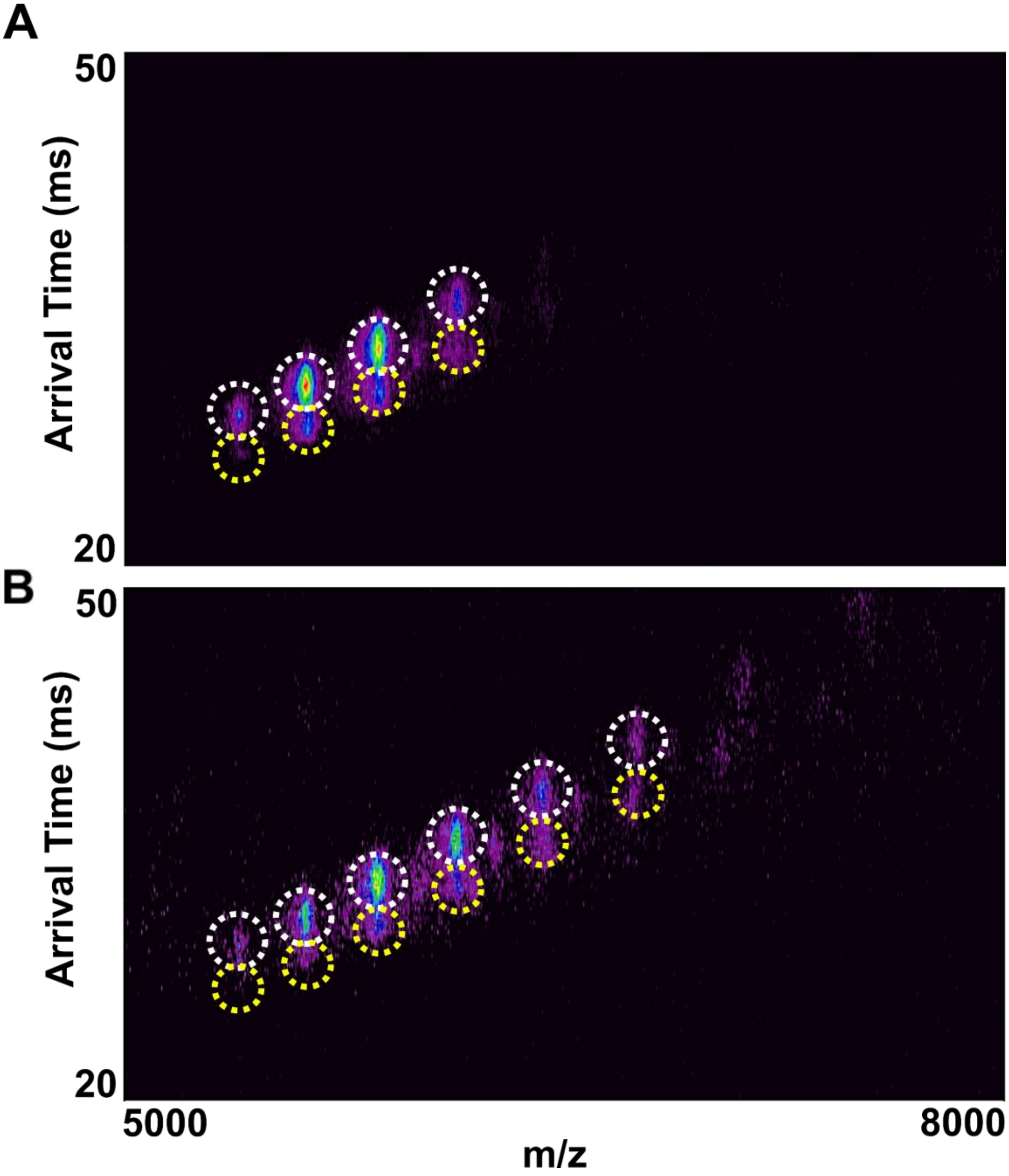

Figure III.12 Two conformations of SDA$_{ec}$ exist after charge reduction. IM-MS spectrum of tagged SDA$_{ec}$ in (A) 200 mM ammonium acetate, pH = 8.5 (B) 200 mM ammonium acetate, 20 mM triethylammonium acetate, pH = 8.5 are shown. The charge reduced (high m/z) species in (B) still retains two conformations. The high/low arrival time (extended/compact) species are circled by white/yellow dashed lines respectively.

To supplement our architecture assignments in the ion-mobility experiments, we designed NFS1(Q64S, P299H, L300Q)-ISD11-ACP$_{ec}$ which is predicted to have an enhanced presence of a closed architecture by the reduction of clashes generated by the N-terminus and inclusion of hydrogen bonding residues at the dimer interface (Fig. III.13A-C and Fig. III.14A,B). These residues are conserved in prokaryotic cysteine desulfurases and provide stabilizing interactions at the dimer interface. In fact, this variant, called SHQ, had enhanced cysteine desulfurase activity in the absence of FXN (Fig. III.15A-C). This variant still activates by FXN but has a reduced FXN binding affinity (Fig. III.15D) potentially due to the restriction of beneficial conformations at the NFS1 dimer interface as a result of the inclusion of the new hydrogen-bonding interactions. As expected, the SHQ variant had an enhancement in the smaller collisional cross-section species consistent with its assignment as a closed architecture (Figure III.11 and Table III.6).

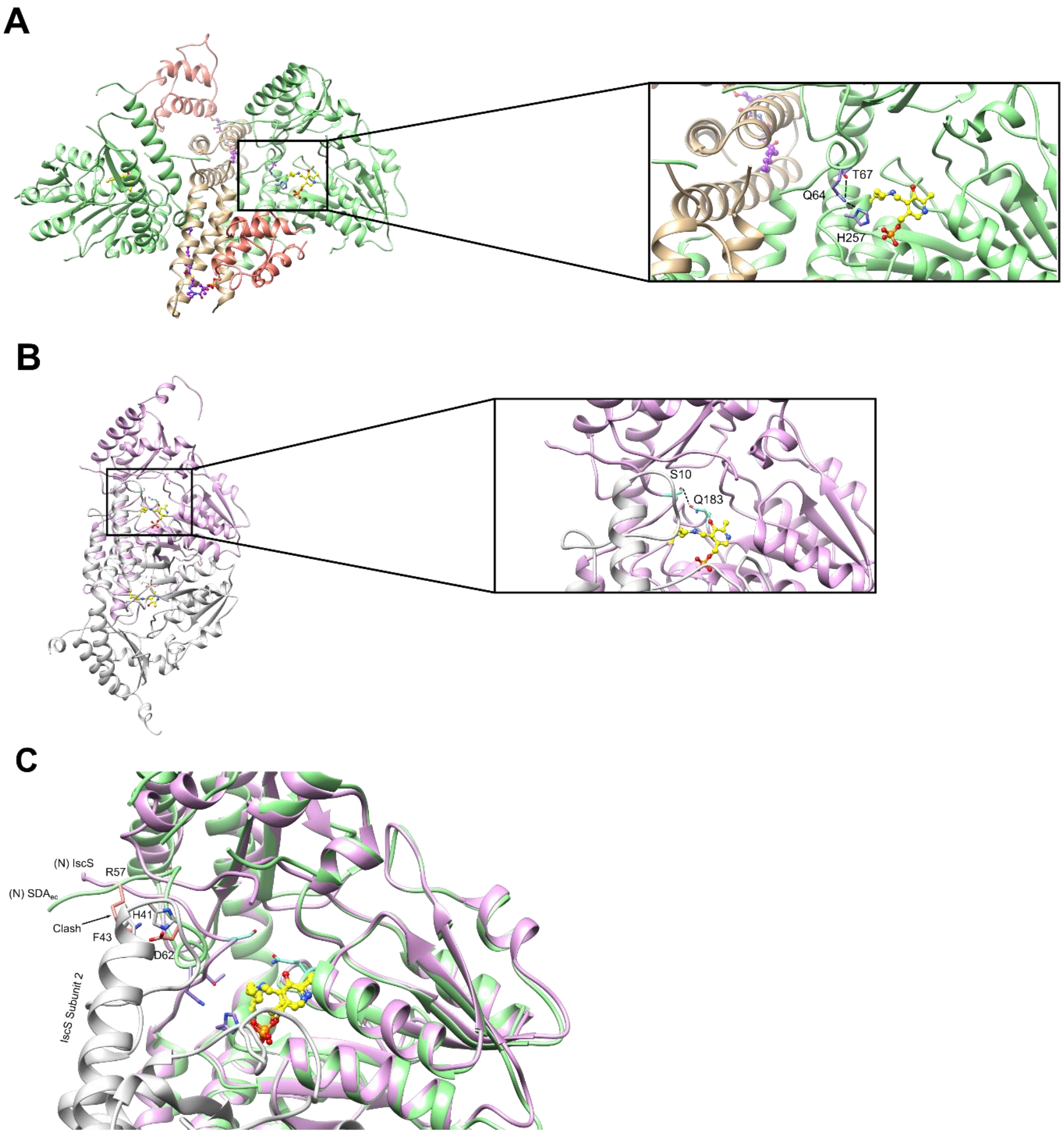

Figure III.13 Part 1 of engineering of an enhanced closed SDA$_{ec}$ dimer. (A) Q64 on subunit A of 5USR.pdb (open SDA$_{ec}$) participates in a hydrogen bonding network which produces a unique N-terminus conformation. (B) S10 participates in a hydrogen bond with Q183 of IscS (3LVM.pdb) to generate a compact N-terminus conformation. (C) The unique N-terminus conformation in the open SDA$_{ec}$ generates clashes with the second subunit of IscS (white) in an overlay of the two structures in A and B. Residues NFS1 (light green) are shown in salmon that would participate in the clash with an IscS (white) like dimer. NFS1(Q64S) is predicted to alleviate the clash present at the N-terminus of a closed (IscS-like) architecture.

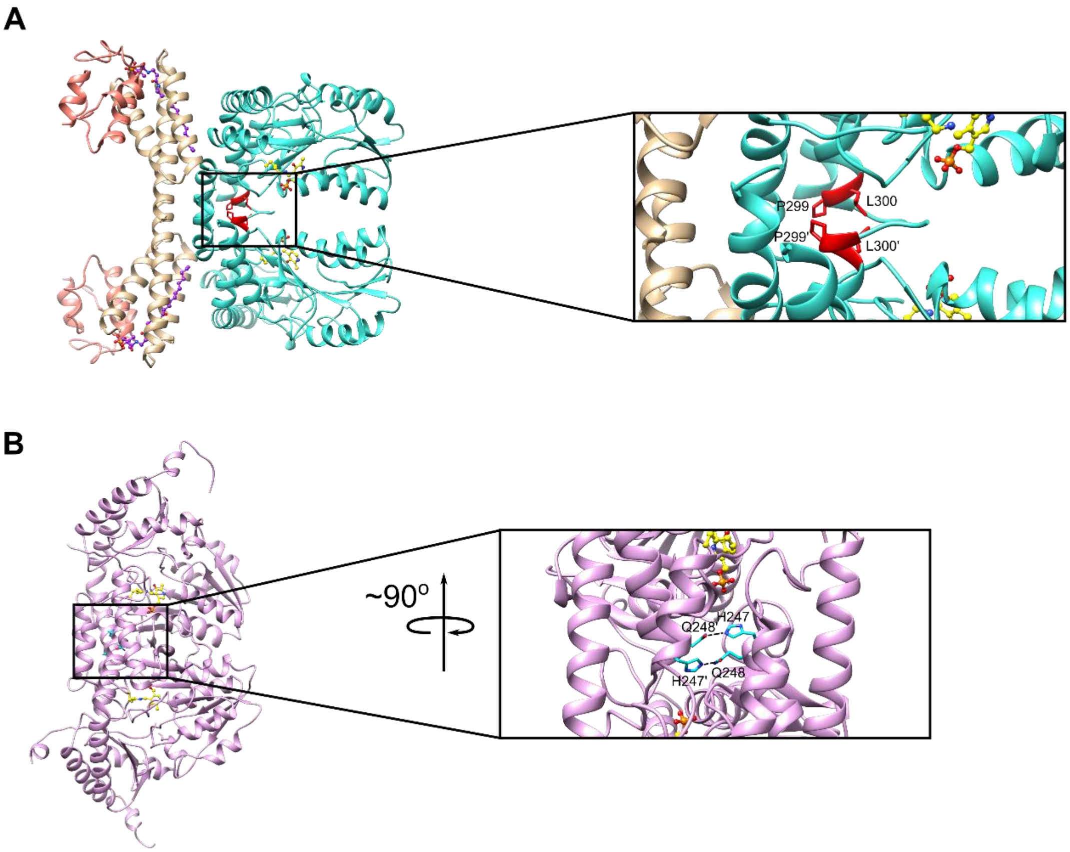

Figure III.14 Part 2 of engineering of an enhanced closed SDA_{ec} dimer. (D) In the closed SDA_{ec} structure (5WGB.pdb), P299 and L300 form vanderwaals interactions at the dimer interface. (E) In the IscS structure (3LVM.pdb), H247 and Q248 form strong hydrogen bonding interactions at the dimer interface. NFS1(P299H, L300Q) is predicted to stabilize a closed architecture.

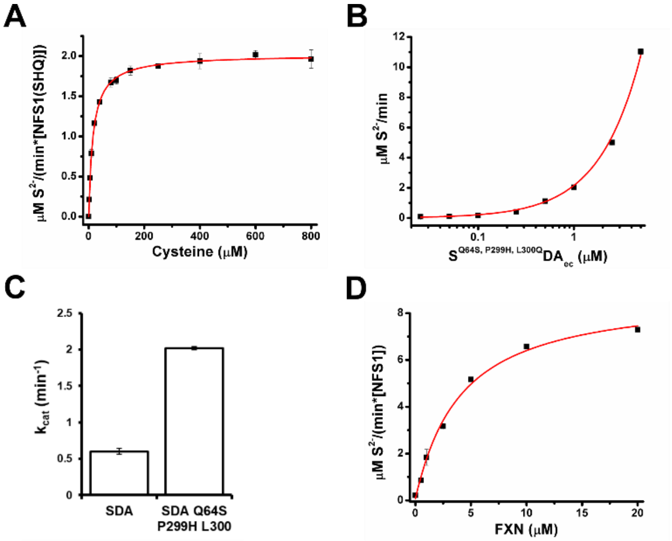

Figure III.15 S(Q64S, P299H, L300Q)DA$_{ec}$ (SHQ) variant has inherently higher activity than SDA$_{ec}$. (A) Michaelis-Menten kinetics (K_M = 15.9 ± 0.6 μM, k_{cat} = 2.02 ± 0.02 min^{-1}) of the SHQ variant. (B) Variation of the concentration of SHQ while keeping cysteine concentration at 1 mM leads to a linear increase (R^2 - 0.9977) of the activity with a slope of 2.16 ± 0.03. The plot is shown on a lin-log scale in order to provide an even distribution of SHQ concentration points within the visual. The determined slope is consistent with the determined k_{cat} value (2.02 ± 0.02). (C) Comparison of k_{cat} of SDA$_{ec}$ and the SHQ variant. (D) FXN in the presence of ISCU2 activates the SHQ variant to the SDA$_{ec}$UF level but FXN binds weakly to the SHQ variant (K_D = 3.8 ± 0.6 compared to 0.22 ± 0.05).

However, upon addition of ISCU2, two species, regardless of tag, are observed in the ion mobility analysis suggesting the presence of an open $SDA_{ec}U$ architecture that has not been captured in high resolution structures (Fig. III.10C and Fig. III.11). For the SHQ variant, in the presence of ISCU2, this variant displayed a higher population of closed $SDA_{ec}U$ (Fig. III.11) further supporting our architecture assignments of these species. Conversely, ion mobility analysis of IscS and IscU showed only a single conformation (Fig. III.16A,B). Interestingly, under saturating ISCU2 and FXN conditions, only a single species is identified (Fig. III.10D and Fig. III.11). Based on SAXS and cryoEM data,[143, 233] this species is likely a closed, fully activated $SDA_{ec}UF$ species. These results in combination with the crystal activation and exchange assays suggest a dynamic exchange between open and closed cysteine desulfurase architectures, which drives the FXN activation phenomenon.

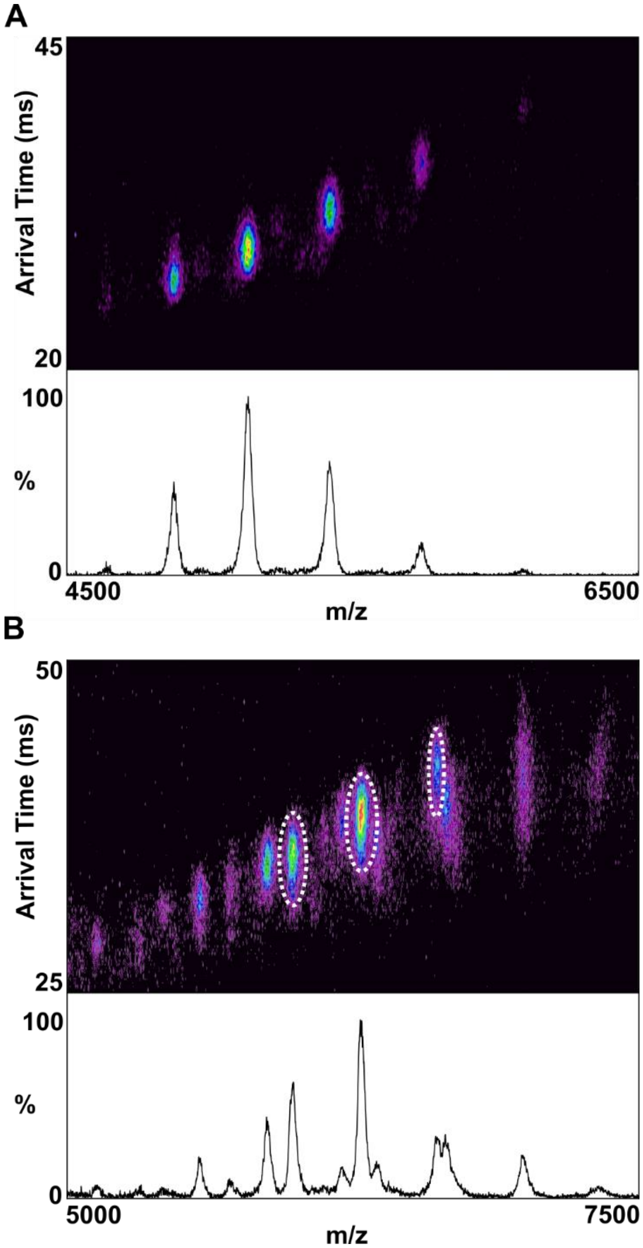

Figure III.16 IscS and (IscS-IscU)$_2$ have single conformation. Single major species of (A) IscS (B) (IscS-IscU)$_2$ (circled by white dash line) are observed using native IM-MS.

Discussion

The atomic level details of FXN-based activation of the eukaryotic Fe-S assembly subcomplex have remained highly sought after but have been difficult to obtain. *In vitro* assays have suggested that the basis for FXN activation relies on the cysteine desulfurase. This was explicitly demonstrated through the activation of SDU by both FXN and its bacterial homolog CyaY. However, the NFS1 homolog, IscS, was inhibited by both CyaY and FXN.[87] Although these cysteine desulfurases are 60 % identical, they appear to act differently in the presence of their adaptor proteins. The first evidence for the differences between eukaryotic and prokaryotic cysteine desulfurases was revealed by the determination of the SDA_{ec} crystal structure in the open architecture.[121] Interestingly, different structures of SDA_{ec}, $SDA_{ec}U$, and $SDA_{ec}UF$ followed shortly which closely resembled structures of the prokaryotic cysteine desulfurases.[122, 143] This posed the question of physiological relevance regarding the structures. While the open structure seemed to clearly demonstrate the essential nature of ISD11 and to provide a rationale for FXN-based activation within the eukaryotic system, the precedent for closed cysteine desulfurase architectures within ISC pathways had already been firmly established.[50, 85, 110, 193]

Some of these studies and those that followed attempted to utilize solution techniques to evaluate the architecture in solution. However, these studies either completely disregarded the open architecture[122] or did not utilize the appropriate probes to test for both open and closed architectures in solution.[233] We have shown here that our complex has a nearly identical conformation to the complex prepared by other laboratories

(Fig. III.4). In addition, we clearly demonstrate that both open and closed architectures are present in solution through crystallographic trapping studies (Fig. III.8 and Table III.4).

Because FXN can activate both crystal forms (Fig. III.9), this generates two models. Either both architectures can be activated to the same extent, or the architectures are in equilibrium, and a single, activated form is generated in the presence of all adaptor proteins. We tested these hypotheses with native ion-mobility mass spectrometry which lead to an equilibrium model (Fig. III.17). In this model, the SDA_{ec} architectures are in equilibrium with one another, and FXN, in combination with ISCU2, drives the formation of an activated cysteine desulfurase species (Fig. III.17). Exchange experiments with tagged SDA_{ec} demonstrated that interconversion could occur through a monomeric disassembly proceses; however, the exchange between un-tagged SDA_{ec} is slow (Table III.5). Interestingly, the un-tagged SDA_{ec} also displays only a single conformation for $SDA_{ec}UF$ suggesting the possibility of an open to closed tethered dimer transition that is unexchangable (Fig. III.11). Additionally, the ion-mobility data suggested that ISCU2 can bind to both the closed and open SDA_{ec} forms, and only in the presence of FXN, does a single conformational state form (Fig. III.10D and Fig. III.11A, B). This observation is consistent with low activity properties of $SDA_{ec}U$ and activation only occurring within the $SDA_{ec}UF$ complex.[121]

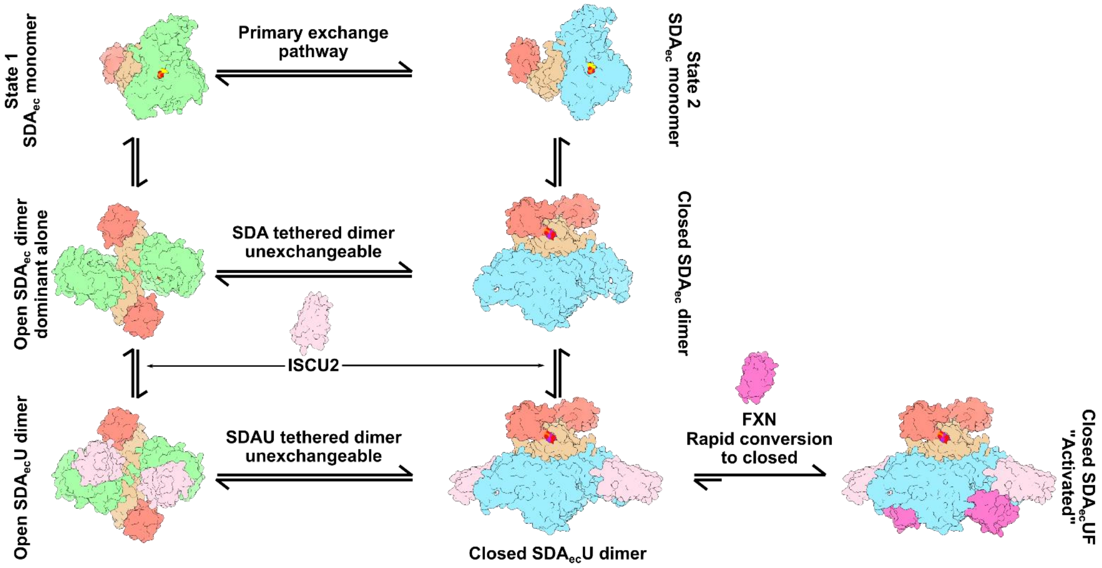

Figure III.17 Morpheein model for the Fe-S cluster biosynthetic subcomplex.

These data in combination with the crystal activation experiments support a global rearrangement of $\mathrm{SDA_{ec}}$ in the presence of ISCU2 and FXN with a low activity open architecture being the dominant species in solution in the absence of these additional subunits. While the recent cryo-EM structure suggested that the mechanism of FXN activation is driven by the loss of the NFS1 mobile loop cysteine (C381) coordination to zinc bound ISCU2 which alleviates inhibition,[143] this model does not explain why the cysteine desulfurase activity of $\mathrm{SDA_{ec}}$ by itself is low. Therefore, we hypothesize that driving the equilibrium towards a fully closed cysteine desulfurase is the primary structural basis for FXN based activation of the human Fe-S assembly subcomplex.

This type of global re-arrangement is, to our knowledge, uncommon. The closest model that describes this situation is the morpheein model. Morpheeins are enzymatic systems that are in a dynamic equilibrium with a variety of different oligomeric or architectural states. The equilibrium between states is allosterically regulated, and in order for one oligomer or architecture to convert to the other, the system must dissociate, undergo a conformational change, and then re-associate,[245] which is also described in our model with the designation of State 1 and State 2 of the $\mathrm{SDA_{ec}}$ monomer (Fig. III.17).[245] Examples of human morpheeins are phenylalanine hydroxylase,[246] porphobilinogen synthase,[247] and cystathionine β-synthase.[248] Typically, these systems are regulated by small molecule effectors; however, in Fe-S cluster biosynthesis, this regulation appears to occur via a protein (FXN) dependent regulation mechanism. Interestingly, clinical mutations can have an effect on these systems' oligomeric distributions and activities.[246, 248, 249] Therefore, it is not out of the question that the human Fe-S cluster assembly subcomplex could be regulated in a similar manner. Further studies will require thoughtfully designed biochemical probes and high resolution structural analysis to determine the mechanistic relationship between the open and closed architectures of SDA_{ec}. In fact, these studies will provide key information on the basis of FXN activation.

Materials and Methods

Protein Expression and Purification

Glutathione S-transferase (GST) was subcloned using the MEGAWHOP protocol[250] into a pET-30a(+) vector containing ISCU2(Δ1-35) to generate a C-terminally tagged construct designated ISCU2-tev-GST with or without a His_6 tag following the GST tag. The resulting vector was transformed into BL21(DE3) for expression. Cells were grown at 37 ^{o}C to an OD_{600} of 0.5. Protein expression was induced with 0.1 mM isopropyl β-D-1-thiogalactopyranoside (IPTG) at 18 ^{o}C. Cells were grown overnight, harvested by centrifugation the following morning, and stored in a -80 ^{o}C freezer until use. The cell pellet from a 9 L culture was thawed and re-suspended in GST A buffer (50 mM Hepes, 150 mM NaCl, pH = 7.8). Lysozyme (20 mg, Sigma-Aldrich) and protease inhibitor cocktail (20 mg, Sigma-Aldrich) were added to the suspension. The cells were lysed by 2 cycles of French press as 18,500 psi. Cell debris was cleared by centrifugation at 10,000 rpm for 30 minutes. The clarified lysate was loaded onto a manually packed GST-column (Prometheus) at 4 ^{o}C. Bound protein was eluted with GST buffer B (50 mM Hepes, 150 mM NaCl, 10 mM glutathione (GSH), pH = 7.8). A tobacco etch virus (TEV) protease digest was conducted overnight at 4 ^{o}C. The digested product was loaded onto a 5 mL Ni-NTA column (GE Healthcare) in order to remove TEV. The flow-through from the Ni column was concentrated to 20 mL, diluted to 150 mL with Cation A buffer (50 mM Hepes, pH = 7.8), and loaded onto a 27-mL cation exchange (POROS 50HS, Applied Biosystems) column and eluted with a linear gradient of NaCl (0 – 1 M). In the case of the His_6 tagged construct, the cation exchange step was skipped. The fractions containing ISCU2 were concentrated, brought into an anaerobic Mbraun glovebox (~ 12 ^oC, <1 ppm O_2 as monitored by a Teledyne model 310 analyzer), and supplemented with 5 mM D,L-dithiothreitol (DTT) prior to loading onto a HiPrep 26/60 Sephacryl S100 HR (GE Healthcare Life Sciences) column equilibrated in size exclusion buffer (50 mM Hepes, 150 mM NaCl, pH = 7.5). The fractions corresponding to monomeric ISCU2 were collected, concentrated, and flash frozen in liquid nitrogen for storage at -80 ^oC until use. Concentration was determined using an extinction co-efficient of 9970 M^{-1} cm^{-1} at 280 nm as estimated by ExPASy ProtParam.[251]

FXN(Δ1-81) was subcloned into a pET-28a(+) vector containing His_6-GST-tev-CyaY[87] using the MEGAWHOP[250] protocol to generate a His_6-GST-tev-FXN construct. Protein expression was conducted in a similar fashion to ISCU2-tev-GST. The cell pellet from a 3 L culture was thawed and re-suspended in GST A buffer (50 mM Hepes, 150 mM NaCl, pH = 7.8). Lysozyme (10 mg) and protease inhibitor cocktail (10 mg) were added to the suspension. The cells were lysed by 2 cycles of French press as 18,500 psi. Cell debris was cleared by centrifugation at 10,000 rpm for 30 minutes. The initial GST column, TEV cleavage, and Ni column clean-up steps were performed similarly to the ISCU2-tev-GST preparation. The flow-through fractions were collected, concentrated, and loaded onto a HiPrep 26/60 Sephacryl S100 HR column equilibrated in size exclusion buffer (50 mM Hepes, 150 mM NaCl, pH = 7.5). Fractions containing FXN were pooled, concentrated, frozen in liquid nitrogen, and stored at -80 ^{o}C until use. Concentration was determined using an extinction co-efficient of 26930 M^{-1} cm^{-1} at 280 nm as estimated by ExPASy ProtParam.[251]

The NFS1(Δ1-55)-ISD11(S11A)-ACP_{ec} (SDA_{ec}) was prepared by two methods. The methods, including construct design, expression media, and purification protocols, of Barondeau (open)[121] and Cygler (closed)[122] were followed as described in the previous manuscripts. Concentration was determined using an extinction co-efficient of 10.9 mM^{-1} cm^{-1} at 420 nm. Cleavage of the N-terminal His_6 tag on NFS1 was performed by introducing a TEV cleavage site by mutagenesis of the original NFS1 plasmid. After cleavage, NFS1 contains a single glycine residue prior to residue 56 in the construct. Purification of the cleaved NFS1(Δ1-55)-ISD11(S11A)-ACP_{ec} was conducted as previously described[121] with a TEV cleavage step after a cation exchange column and a follow-up Ni-NTA column to remove cleaved tag and TEV.

E. coli proteins IscU and IscS were expressed and purified as previously described.[87] The extinction coefficient of 6.6 mM^{-1} cm^{-1} at 388 nm was used to estimate the concentration of PLP cofactor, which represented the concentration of active IscS, in 0.1 M NaOH. The extinction coefficient of 11460 M^{-1} cm^{-1} at 280 nm was used to estimate the concentration of IscU.

Expression and Purification of ^{15}N Labelled SDA_{ec}

Proteins containing ^{15}N were expressed by inoculating 2 – 6 liters of N-5052 auto induction media[208] with 8 mL of overnight LB starter culture. The complexes were purified as previously described in the section above. However, the purified complexes were never supplemented with external pyridoxal 5'-phosphate throughout the preparation.

Activity Measurements of Purified Complexes

The methylene blue assay was conducted as previously described in assay buffer (50 mM Hepes, 250 mM NaCl, pH = 7.5).[121] Reaction mixtures of 800 µL containing the following components: 0.5 µM SDA$_{ec}$, 1.5 µM ISCU2, 1.5 µM FXN, 4 mM D,L-DTT, and 5 µM $(NH_4)_2Fe(SO_4)_2 \cdot 6H_2O$ were incubated at 37 °C for 15 minutes prior to addition of varying amounts of L-cysteine. Reactions were quenched as previously described after 6 minutes. Sulfide quantification was conducted as previously described. The rate for each L-cysteine concentration was measured at least in triplicate. Data was fit using KaleidaGraph (Synergy Software) to a traditional Michaelis-Menten equation. The errors in the Michaelis-Menten parameters represent errors in the fit to the experimental data. FXN binding was evaluated as previously described.[172]

Preparation of the SDA$_{ec}$ Complex for Small-angle X-ray Scattering

Purified SDA$_{ec}$ was injected onto a Superdex 200 10/300 GL (S200, GE Healthcare Life Sciences) equilibrated in 50 mM Hepes, 250 mM NaCl, pH = 7.2 to remove any aggregates from the freeze/thaw cycle of the sample. Yellow fractions were collected, pooled, and concentrated to approximately 10 mg/mL. Dialysis buttons (Hampton Research) were loaded with 50 µL of sample and sealed with a 3.5 kDa dialysis membrane disc (Hampton Research, Spectrum) that had been washed thoroughly with Milli-Q H_2O. Samples were then dialyzed in a variety of buffers within 50 mL falcon tubes overnight at

4 ^{o}C prior to dilution within a 96-well plate. The 96-well plate containing samples was sealed and shipped wrapped in ice packs to the SIBYLS beamline (12.3.1) at the Advanced Light Source (ALS). The plate was stored at 4 ^{o}C and was centrifuged at 3700 rpm for 10 minutes prior to data collection. Data collection parameters can be found in Table III.7.

Table III.7. Small-angle X-ray scattering data collection parameters.

	SDA_{ec}
Organism	*H. sapiens* , *E* . coli
Source	Recombinant
Source of Data	This work
Theoretical Mw, excluding cofactors (kDa)	133 kDa
Sample concentrations (mg/mL)	1, 2, 4
Sample buffer	100 mM phosphate 500 mM NaCl 2% glycerol 2 mM TCEP pH = 8.0
Instrument/data processing	SIBYLS ALS 12.3.1
q range ($Å^{-1}$)	0.011-0.565
Wavelength (Å)	1.27
Cell thickness (mm)	1.5
Sample to detector distance (m)	1.5
Temperature (^{o}C)	10
Exposure time (sec)	10
Delta/time slicing	Every 0.3 seconds
Total frames	32

Small-angle X-ray Scattering Data Analysis

Individual buffers and frames were analyzed for consistency. Buffers with the same composition and scattering profile were averaged using the ATSAS 2.8.4[236] package to generate an average buffer scattering curve. Sample frames were then individually subtracted from the averaged buffer in the RAW 1.5.1 package.[252, 253] Subtracted frames were then averaged in RAW at different time points in order to determine the onset of radiation damage. Exposure times which included the least amount of radiation damage were used for further analysis. Additional information regarding Guinier analysis, pair-distribution function analysis, and curve fitting can be found in Table III.1. A list of software used can be found in Table III.8.

Table III.8 Small-angle X-ray scattering analysis software.

SAXS data reduction	ATSAS 2.8.4/RAW 1.5.1
Basic analyses: Guinier, P(r), Mw	ATSAS 2.8.4/RAW 1.5.1 - GNOM
Shape/bead modelling	ATSAS Online/ATSAS 2.8.4/RAW 1.5.1 - DAMMIF, DAMCLUST, DAMAVER, DAMSTART, DAMMIN EM2DAM
Reconstruction settings	Slow, P2, 20 reconstructions
Refinement settings	Slow, P2
Atomic struture modelling	FoXS
Missing sequence modelling	AllosMod-FoXS Webserver, 10 simulations 300 K

Crystallization of Alternate Crystal Forms from Different Preparation Methods

Crystallization of the open and closed forms of SDA_{ec} were performed as previously described[121, 122] using the Barondeau and Cygler preparation methods respectively. All screens were setup using the hanging-drop vapor diffusion method with 500 µL crystallization solution in the well and a 4 µL drop (2µL protein : 2µL crystallization solution) on the coverslip. To crystallize SDA_{ec} prepared by the Barondeau method in the closed form, the protein complex was buffer exchanged into 10 mM BIS-TRIS (pH 5.5), 200 mM NaCl, 20mM KCl, 2 mM NaH_2PO_4, 2 mM Na_2HPO_4, 5 % (vol/vol) glycerol, 1 mM D,L-DTT, and 75 mM imidazole by multiple rounds of concentration and dilution using a Vivaspin 500 100 kDa spin concentrator (GE Healthcare). To crystallize SDA_{ec} prepared by the Cygler method in the open form, the protein complex was either buffer exchanged into 50 mM Hepes, 250 mM NaCl, 10 % glycerol, pH = 7.5 or injected onto a Superdex 200 10/300 GL (S200, GE Healthcare Life Sciences) equilibrated in 50 mM Hepes, 250 mM NaCl, 10 % glycerol, pH = 7.5. Final crystallization conditions and protein concentrations can be found in Table III.9.

Table III.9 Crystallization conditions for various preparations of SDA$_{ec}$

Preparation Method	Crystal Form	Crystallization Condition	Protein Concentration (μM)	Well Volume (μL)	Drop Ratio (μL : μL)	Temperature (°C)
Barondeau	Open	5 mL of 40% acetone added to 11.25 mL of 0.1 M CBTP (pH = 6.4), 0.3 M CsCl, 0.2 M D,L-allylglycine 5 mM TCEP, 8% PEG 3350 (bulk crystallization soluti	See reference #121	500	2 : 2	22
Barondeau	Open (-allylglycine)	1.25 mL of 40% acetone added to 11.25 mL of 0.1 M CBTP (pH = 6.4), 0.3 M CsCl, 5 mM TCEP, 8% PEG 3350 (bulk crystallization solution)	See reference # 121	500	2 : 2	22
Barondeau	Closed	0.1M MES, pH = 6.5, 0.3 M ammonium acetate, 0.02 M calcium acetate hydrate, 0.02 M calcium chloride dihydrate, and 15% isopropanol	220	500	2 : 2	12
Cygler	Open	0.1 M CBTP (pH = 6.4), 0.2 M CsCl, 0.2 M D,L-allylglycine 5 mM TCEP, 10% PEG 3350, 4 % acetone	See reference # 121	500	2 : 2	22
Cygler	Closed	0.1M MES, pH = 6.5, 0.3 M ammonium acetate, 0.02 M calcium acetate hydrate, 0.02 M calcium chloride dihydrate, and 15% isopropanol	226	500	2 : 2	12

X-ray Data Collection, Indexing, and Unit Cell Determinations

Single crystals of SDA_{ec} in the open architecture were harvested and cryo-protected as previously described[121] using a final concentration of 20 % (vol/vol) PEG 400. Crystal trays of SDA_{ec} in the closed architecture were transferred to a 17 ^{o}C room where single crystals were harvested and cryo-protected as previously described.[122] Diffraction data was collected using a rotating anode Cu K-α source and a Rigaku R-AXIS IV detector. Specifically, two images for each crystal form were collected at $2\Theta = 0^{o}$ and 90^{o} at a temperature of 120 K with an exposure time of 6 minutes, detector distance ranging from 200 to 250 mm, and an oscillation angle ranging from 0.5^{o} to 0.2^{o} depending on the diffraction quality. Indexing was performed with iMosflm[254] version 7.2.2 from the CCP4[255] package. The unit cell parameters were automatically chosen by iMosflm.

Activity Analysis of Single Crystals

The methylene blue assay was conducted in a similar manner as described above. Crystals of SDA_{ec}, in either form, were harvested from four separate drops. Each drop had an individual 10 µL wash drop containing assay buffer before the crystal was transferred to a 200 µL drop of assay buffer. The 200 µL drop containing single crystals was transferred to a seeding tool where they were crushed to generate a slurry. The slurry was brought into an anaerobic glovebox where the activity measurements were conducted. A total of six alternating reactions (150 µL) with and without the additional subunits and Fe^{2+} were performed by mixing 20 µL of crystal slurry, additional subunits (3 µM), Fe^{2+} (10 µM), and D,L-DTT (4 mM) together and incubating at 37 ^{o}C for 15 minutes. The reactions were initiated by addition of L-cysteine to a final concentration of 1 mM. A quench solution of 37.5 µL of a 1:1 mixture of 20 mM *N*,*N*-dimethyl-p-phenylenediamine in 7.2 N HCl and 30 mM $FeCl_3$ in 1.2 N HCl was added to the mixture after 10 minutes. Sulfide concentration was determined as described previously in the manuscript. A total of two independent triplicate runs were conducted totaling six measurements for each sample.

Native Mass Spectrometry Experiments

Native mass spectrometry (Native MS) was performed on two instruments for different purposes: an Exactive Plus with extended mass range (EMR) Orbitrap MS (Thermo Fisher Scientific, San Jose, CA) for high resolution measurements or a Synapt G2 instrument (Waters Corporation, U.K.) equipped with a 8k RF generator for ion mobility measurements. Gold-coated tips prepared using a Sutter 1000 were used for nano-electrospray ionization experiments.[256] Fresh protein samples including SDA_{ec}, ISCU2, FXN, IscS, and IscU were buffer exchanged into 200 mM ammonium acetate (pH = 8.5) using Micro Bio-Spin 6 Columns (Bio-Rad). Experimental and expected masses can be found in Table III.10.

Table III.10 Calculated and measured masses for SDA$_{ec}$ species used in this study. All calculated masses excluding the N-terminal methionine (if present in the sequence). The calculated masses of SDA$_{ec}$ and SDA$_{ec}$ complexes included the mass of the covalently attached PLP and the assumed mass of the acyl-4'PPT ACP$_{ec}$ was 523 Da. Masses of SDA$_{ec}$/SDA$_{ec}$U/SDA$_{ec}$UF/ISCU2/FXN were measured under native condition (200 mM ammonium acetate, pH = 8.5). Masses of SDA$_{ec}$ subunits were also measured under denaturing conditions (1% formic acid). All masses are measured using EMR.

Speices		Calculated Mass (Da)	Measured Mass (Da)	Measured Mass range
14N-untagged SDA$_{ec}$		129097	129265 ± 64	129201−129329
15N-untagged SDA$_{ec}$		130693	130838 ± 70	130768−130908
14N-untagged SDAecU		159521	159708 ± 99	159609−159807
15N-untagged SDA$_{ec}$U		161117	161285 ± 130	161155−161415
14N-untagged SDAecUF		187997	188175 ± 97	188078−188272
15N-untagged SDA$_{ec}$UF		189593	189770 ± 124	189646−189894
14N-tagged SDAec		134135	134235 ± 76	134159−134311
15N-tagged SDA$_{ec}$		135809	135892 ± 72	135820−135964
14N-tagged SDAecU		164559	164880 ± 193	164687−165073
15N-tagged SDA$_{ec}$U		166233	166596 ± 181	166415−166777
14N-tagged SDAecUF		193035	193329 ± 212	193117−193541
15N-tagged SDA$_{ec}$UF		194709	195004 ± 155	194849−195159
SHQ		134149	134259 ± 69	15203−15219
ISCU2 + Zn		15212	15211 ± 8	14231−14245
FXN		14238	14238 ± 7	134190−134328
Speices	**Subunit**			
14N-untagged SDA$_{ec}$	S	44717	44716 ± 17	44700−44734
	D	10611	10610 ± 12	10599−10623
15N-untagged SDA$_{ec}$	S	45273	45262 ± 18	45255−45291
	D	10760	10757 ± 11	10749−10771
14N-tagged SDA$_{ec}$	S	47197	47194 ± 18	47179−47215
	D	10611	10610 ± 12	10599−10623
15N-tagged SDA$_{ec}$	S	47792	47785 ± 18	47774−47810
	D	10760	10758 ± 11	10749−10771
SHQ	S	47211	47208 ± 28	47183−47239
	D	10611	10611 ± 13	10598−10624

Subunit Exchange of SDA$_{ec}$/SDA$_{ec}$U/SDA$_{ec}$UF/IscS/IscS-IscU Using Native Mass Spectrometry

Subunit exchange experiments were performed on an EMR Orbitrap MS. The high resolution of EMR gives resolved peaks between subunit mixtures for quantification purpose. Instrument parameters were tuned to minimize collisional activation, while retaining reasonable signal to noise. The mass spectrometer parameters used were set as: m/z range 3000-10000, capillary temperature 200-300 °C, S-Lens RF level 200, source DC offset 25 V, injection flatapole DC 16 V, inter flatapole lens DC 12 V, bent flatapole DC 7-12 V, transfer multipole DC offset 7-10 V, C-trap entrance lens tune offset 0 V, trapping gas pressure setting 7, in-source dissociation voltage 0 eV, HCD collision energy 10 eV, FT resolution 8750–35000, positive ion mode, and ion maximum injection time 50–200 ms. For SDA$_{ec}$ dimer exchange experiments, the dimer concentration was determined based on the relative abundance of the dimer in the mass spectrum. The protein concentration was scaled to achieve a final dimer concentration of 10 µM. To initiate exchange of ^{15}N and ^{14}N-SDA$_{ec}$ a 1:1 ratio of ^{15}N-SDA$_{ec}$ and ^{14}N-SDA$_{ec}$ dimer concentration (10 µM) were mixed. For subunit exchange of SDA$_{ec}$U, ^{15}N-SDA$_{ec}$ and ^{14}N-SDA$_{ec}$ were mixed with ISCU2 separately using a 1:3 ratio, and incubated for 30 minutes to get ^{15}N-SDA$_{ec}$U and ^{14}N-SDA$_{ec}$U complexes ($\alpha_2\beta_2\gamma_2\delta_2$). These complexes were mixed at room temperature to initiate exchange. For exchange of SDA$_{ec}$UF, ^{15}N-SDA$_{ec}$ and ^{14}N-SDA$_{ec}$ were mixed with ISCU2 and FXN separately using a 1:3:3 ratio and incubated for 30 minutes to get ^{15}N-SDA$_{ec}$UF and ^{14}N-SDA$_{ec}$UF complexes ($\alpha_2\beta_2\gamma_2\delta_2\varepsilon_2$). ^{15}N-SDA$_{ec}$UF and ^{14}N-SDA$_{ec}$UF were mixed using a 1:1 ratio at room temperature to initiate exchange.

Exchange of tagged IscS and untagged IscS was investigated using a 1:1 dimer ratio at room temperature. Dimer concentration was determined in a similar fashion as described for the SDA_{ec} exchange experiments. For subunit exchange of IscS-IscU, tagged IscS and untagged IscS were mixed with IscU separately using a 1:3 ratio and incubated for 30 minutes to get holo untagged IscS-IscU and tagged IscS-IscU complexes ($\alpha_2\beta_2$). Exchange was initated by mixing untagged IscS-IscU and tagged IscS-IscU complexes at a 1:1 ratio at room temperature. At various time points, aliquots (4 uL) were taken for native MS analysis. Each spectrum was taken for 20 seconds. The initial MS data was collected using the Thermo Exactive software under the RAW format. The RAW data files were converted into text files using a custom Python script making use of the Python library multiplierz. The protein species were deconvoluted and converted into mole fractions by processing the text files with the software program UniDec.[257] Percent exchanged for a random distribution is defined as (abundance of exchanged species having two different subunits)/(sum of abundance of unexchanged species). For a complete random exchange, the expected percent exchange is 2/(1+1) x 100 = 100%.

Ion-mobility Mass Spectrometry of SDA_{ec}/$SDA_{ec}U$/$SDA_{ec}UF$

Native ion-mobility mass spectrometry (Native IM-MS) was performed on a Synapt G2 instrument. The instrument was set to a capillary voltage of 1 kV, source temperature of 30 °C, sampling cone voltage of 10 V, extraction cone voltage of 1 V, trap and transfer collision energy off, and backing pressure (5.07 mbar), trap flow rate at 8 ml/min (4.36×10^{-2} mbar), He cell flow rate at 200 ml/min (1.37×10^{3} mbar), IMS flow rate at 50 ml/min (6.82 mbar). The T-wave settings for trap (310 ms^{-1}/6.0 V), IMS (250

ms^{-1}/9-12 V) and transfer (65 ms^{-}1/2 V), and trap bias (25.0 V). MassLynx 4.1 (Waters) and Pulsar were used to deconvolute all recorded mass spectra.[258] These parameters were chosen in order maximize the intensity of detected ions and retain the native-state of the folded protein. A sodium iodide solution was used to externally calibrate mass spectra. Experimental collisional cross section (CCS) of ^{14}N tagged SDA_{ec} (134.2 kDa), ^{14}N untagged SDA_{ec} (129.3 kDa), $SDA_{ec}U$ (using ^{14}N tagged SDA_{ec}, 164.9 kDa), $SDA_{ec}UF$ (using ^{14}N tagged SDA_{ec}, 193.3 kDa) were calibrated using solutions of transthyretin (55.6 kDa), concanavalin A (103.0 kDa), and pyruvate kinase (237 kDa) as previously described.[259, 260] Parameters for calculating the CCS using the online projected superposition approximation (PSA) webserver (psa.chem.fsu.edu) were set as follows: buffer gas of nitrogen, temperature of 298 K, projection accuracy of 0.01, projection integration accuracy as 0.009, shape accuracy as 0.01, shape maxiter as 25, and shape meshfactor as 1.[261-263] The models used for calculating CCS were generated as described in the main text for atomistic modeling of the SAXS data.

Additional Software and Figure Generation

Plots were generated in either Excel (Microsoft) or Kaliedegraph (Synergy Software). Structural figures were generated using Chimera 1.11.2.[264] Cα RMSD calculations were conducted in PyMOL 1.3.[219] High resolution artboards and figures were developed using Inkscape (https://inkscape.org/) and GIMP (https://www.gimp.org/).

CHAPTER IV

CATION-EXCHANGE COUPLED SMALL-ANGLE X-RAY SCATTERING ANALYSIS OF SUBSTRATE TREATED HUMAN FE-S CLUSTER ASSEMBLY SUBCOMPLEX

Overview

Iron-sulfur clusters are synthesized by a multi-subunit protein complex in eukaryotic mitochondria. The subcomplex containing the cysteine desulfurase (NFS1), ISD11, and acyl-carrier protein (ACP) provides sulfur for this process. In chapter III, we described a morpheein model for this subcomplex. However, this model did not include the effects of substrate addition. Here we describe a methodology for isolating specific conformations of the subcomplex which are generated upon L-cysteine addition by cation exchange chromatography. We investigated the clinical variant ISD11(R68L) and enhanced closed dimer variant NFS1(Q64S, P299H, L300Q) in the context of the subcomplex using cation exchange chromatography and native ion-mobility mass spectrometry. Lastly, we preliminarily characterize the species eluted from a cation exchange column using in-line small-angle X-ray scattering.

Introduction

Iron-sulfur (Fe-S) cluster biosynthesis is an essential process which occurs in the mitochondria of eukaryotic organisms. In fact, a specific protein complex is required for the synthesis and distribution of [2Fe-2S] clusters to their downstream targets such as respiratory complexes.[100] At the center of this complex is the functional sulfur mobilization subcomplex consisting of the cysteine desulfurase (NFS1),[98, 99, 111] eukaryotic specific adaptor protein (ISD11),[112, 116, 117] and acyl-carrier protein (ACP).[109, 121, 122, 129, 140] This complex binds additional adaptor proteins such as the electron donor (FDX1 or FDX2),[21, 151-154] the [2Fe-2S] scaffold (ISCU2),[148, 150] and allosteric activator (FXN).[87, 118, 144, 145, 148, 150, 172, 173] Mutations in many of these proteins result in debilitating diseases such as oxidative phosphorylation deficiency, ISCU2 myopathy, and Freidrich's ataxia.[113, 232] In chapter III, we described a unique situation for this sulfur mobilization subcomplex, in which the architecture of the subcomplex changes in the presence of ISCU2 and FXN to generate a fully closed, activated cysteine desulfurase. This type of transition has never been described before and most closely resembles morpheeins.

Morpheeins are a subset of proteins which undergo oligomeric or architectural transitions in the presence of effector molecules.[265] In fact, there are several human proteins which have been described to feature morpheein behavior. Examples include cystathionine β-synthase,[248, 266-268] farnesyltransferase,[269, 270] mitochondrial malate dehydrogenase,[271, 272] phenylalanine hydroxylase,[246, 273-280] pyruvate kinase,[281, 282] β-tryptase,[283] tumor necrosis factor-α,[284] and porphobilinogen synthase.[247, 249, 285-287] The most well characterized morpheeins which are conserved across several species are phenylalanine hydroxylase and porphobilinogen synthase.

Phenylalanine hydroxylase is a monooxygenase which uses tetrahydrobiopterin (BH_4) to catalyze the hydroxylation of L-phenylalanine to L-tyrosine. This enzyme contains three domains: a regulatory N-terminal domain, a catalytic domain, and a C-terminal domain which plays a role in tetramer stabilization.[246, 278, 279] In this system, L-phenylalanine binding, at a site distinct from the active site, induces tetramerization, activity, and cooperative behavior.[246, 273, 275, 277] Interestingly, in the absence of substrate, there exists a dimer to tetramer equilibrium, and the conformation of this tetramer is distinctly different from the conformation of the substrate activated tetramer which has been demonstrated by size-exclusion coupled small-angle x-ray scattering (SAXS).[278, 279]

Porphobilinogen synthase catalyzes the condensation of two 5-aminolevulinic acid molecules in the second step of porphyrin biosynthesis. This system features two distinct dimer conformations. One dimer leads to hexamer formation, and the other leads to octamer formation.[249, 285-287] In order to convert from hexamer to octamer, the larger oligomeric species must first dissociate to a dimer species, and the dimer requires a distinct conformational switch at the N-terminus in order to participate in hexamer formation.[247, 287] The octamer is the high activity species.[287]

The situation described for porphobilinogen synthase closely resembles the morpheein model we described in Chapter III (Fig. III.17) for the human Fe-S cluster assembly subcomplex. In this situation, the open NFS1-ISD11-ACP$_{ec}$ (SDA$_{ec}$) $\alpha_2\beta_2\gamma_2$ species is the low activity form and must disassociate to $\alpha\beta\gamma$ unit and undergo a conformational switch in order to reassemble into the high activity closed SDA$_{ec}$ $\alpha_2\beta_2\gamma_2$ species. The process appears to also occur through a dimer tethering processes based on slow exchange rates for untagged SDA$_{ec}$. Furthermore, we showed that this transition does not occur completely unless ISCU2 and FXN are present which drives the FXN-based activation phenomena.

Here we utilize cation-exchange chromatography, native ion-mobility mass spectrometry, and cation-exchange coupled SAXS to isolate and characterize conformationally distinct populations of species of purified SDA_{ec} with and without substrate. We first show that there is a distribution of species with different charge densities based on cation-exchange chromatography. The distribution of these species changes upon substrate, L-cysteine, addition, and these species appear to be in equilibrium with one another. We then use native ion-mobility mass spectrometry to correlate these species with the open and closed architectures. Lastly, we characterize the conformation of these species with cation-exchange coupled SAXS measurements.

Results

Species Isolation by Cation-Exchange Chromatography

Based on our previous observations of morpheein like behavior of the SDA_{ec} complex, we were particularly interested in the effect of substrate treatment. Studies on porphobilinogen synthase have shown that distinct oligomeric states can be isolated on an anion exchange resin and can interconvert between hexamer and octamer upon dialysis in the presence of substrate. Upon treatment with substrate there appears to be an observable exchange going from hexamer to octamer in this system.[285, 288] We utilized a similar approach for SDA_{ec} in which we injected wild-type onto a high resolution cation exchange resin and were capable of separating three species. Species 1 is likely the result of the premature elution of peak 2 due to the inability remove all salt from the injected sample for stability purposes (Fig. IV.1A). Upon isolation of the major species (peak 3), concentration, re-dilution with buffer A, and re-injection onto the column, all three peaks re-appear suggesting a dynamic equilibrium amongst all three species (Fig. IV.1B). Interestingly, after addition of 10 mM L-cysteine and a 10 minute incubation period, peak

3 decreases in intensity, and peak 1 and 2 increase in intensity. However, the primary absorbance in peak 1 comes from generated cysteine persulfides flowing through the column which absorb at 280 nm (Fig. IV.1C). This suggested a conformational change occurring within the species that alters its chromatographic behavior. We then re-isolated peak 2, concentrated the peak, and diluted it with buffer A prior to re-injection. Elution of this sample revealed all three peaks once again suggesting that even the substrate treated sample is in equilibrium with the original species observed in the non-substrate treated wild-type sample (Fig. IV.1D). Peak 2 in the substrate treated sample is likely substrate bound, and upon re-equilibration of this peak in buffer A, substrate dissociates from the SDA_{ec} complex resulting in the re-population of the original peaks (Fig. IV.1D).

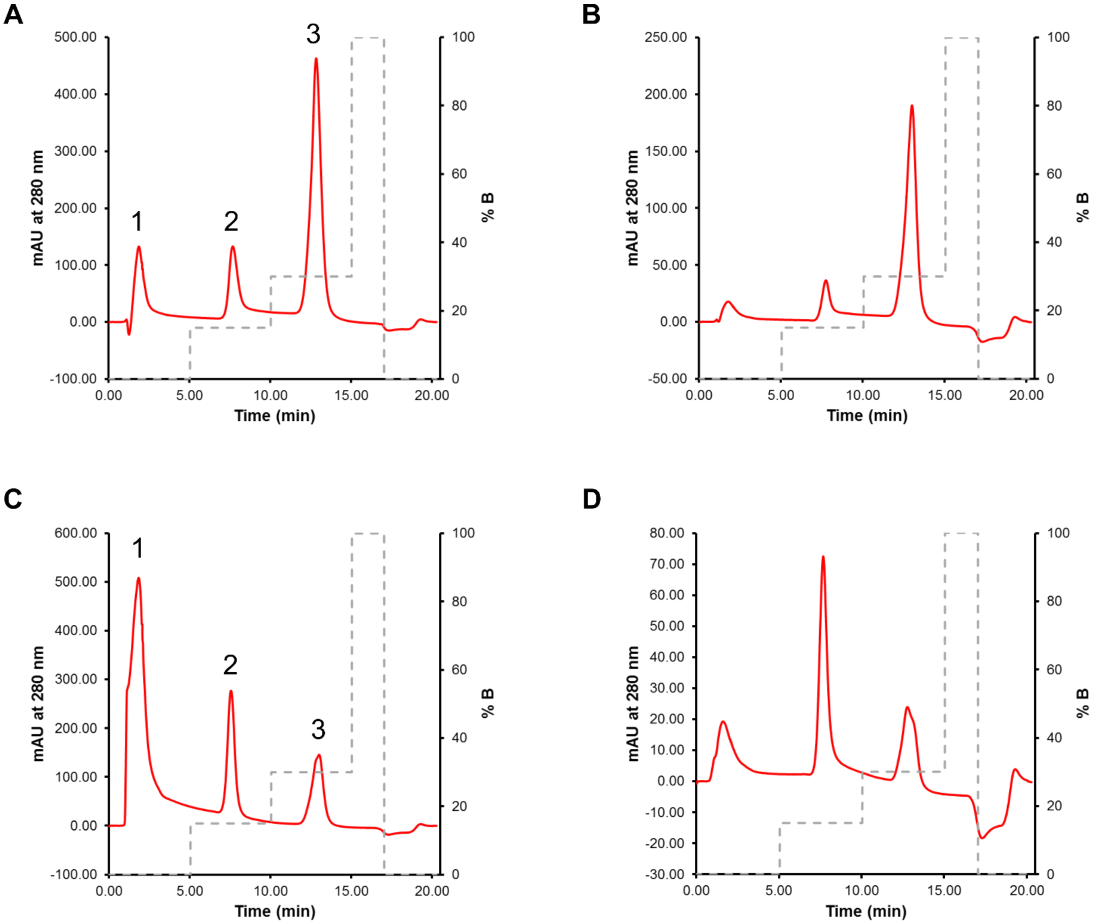

Figure IV.1 Cation exchange chromatography of SDA_{ec} in the absence and presence of L-cysteine. All 280 nm traces are show in red. Buffer B gradient is displayed in grey dashed lines. (A) 30 µM injection of SDA_{ec} onto a Mono S 5/50 GL column and elution by step gradient identifies three speceis. (B) Peak 3 in panel A was isolated and concentrated to approximately 400 µL and diluted to 1 mL with buffer A prior to re-injection. All species identified in panel A re-appear. (C) 30 µM injection of SDA_{ec} in the presence of 10 mM L-cysteine shows a re-distribution of peaks in comparison to panel A. (D) Peak 2 in panel C was isolated and concentrated to approximately 400 µL and diluted to 1 mL with buffer A prior to re-injection. All species identified in panel C re-appear.

Cation-Exchange Chromatography and Ion-mobility Mass Spectrometry of SDA$_{ec}$ Variants

To gain additional conformation information on these species, we turned to site-directed variants, native ion-mobility mass spectrometry, and cation-exchange coupled SAXS. We first compared the chromatographic behavior of wild-type to Δ1-55NFS1(Q64S, P299H, L300Q)-ISD11-ACP$_{ec}$, called SHQ, and Δ1-55NFS1-ISD11(R68L)-ACP$_{ec}$, called R68L. Using the cation-exchange coupled SAXS setup, we were capable of monitoring both the absorbance due to the pyridoxal 5'phosphate cofactor of NFS1 and the integrated scattering intensity of the peaks coming off of the column. We were capable of observing an identical peak behavior with wild-type as described in our original experiments (Fig. IV.1A,C and Fig. IV.2A). However, upon analysis of R68L which is an inactive form,[113, 121] only a single species is observed in the absence and presence of L-cysteine (Fig. IV.2B). This is consistent with the observation that R68L is inactive, and the observed chromatographic change in wild-type is required for activity. When analyzing SHQ, we observed identical chromatographic behavior in comparison to wild-type in the absence and presence of L-cysteine (Fig. IV.2C). However, we did observe an enhancement in peak 2 without substrate (Fig. IV.2D). Based on previous prediction and observation that SHQ is enhanced in the closed architecture (see Chapter III), we preliminarily assigned peak 2 to the closed architecture.

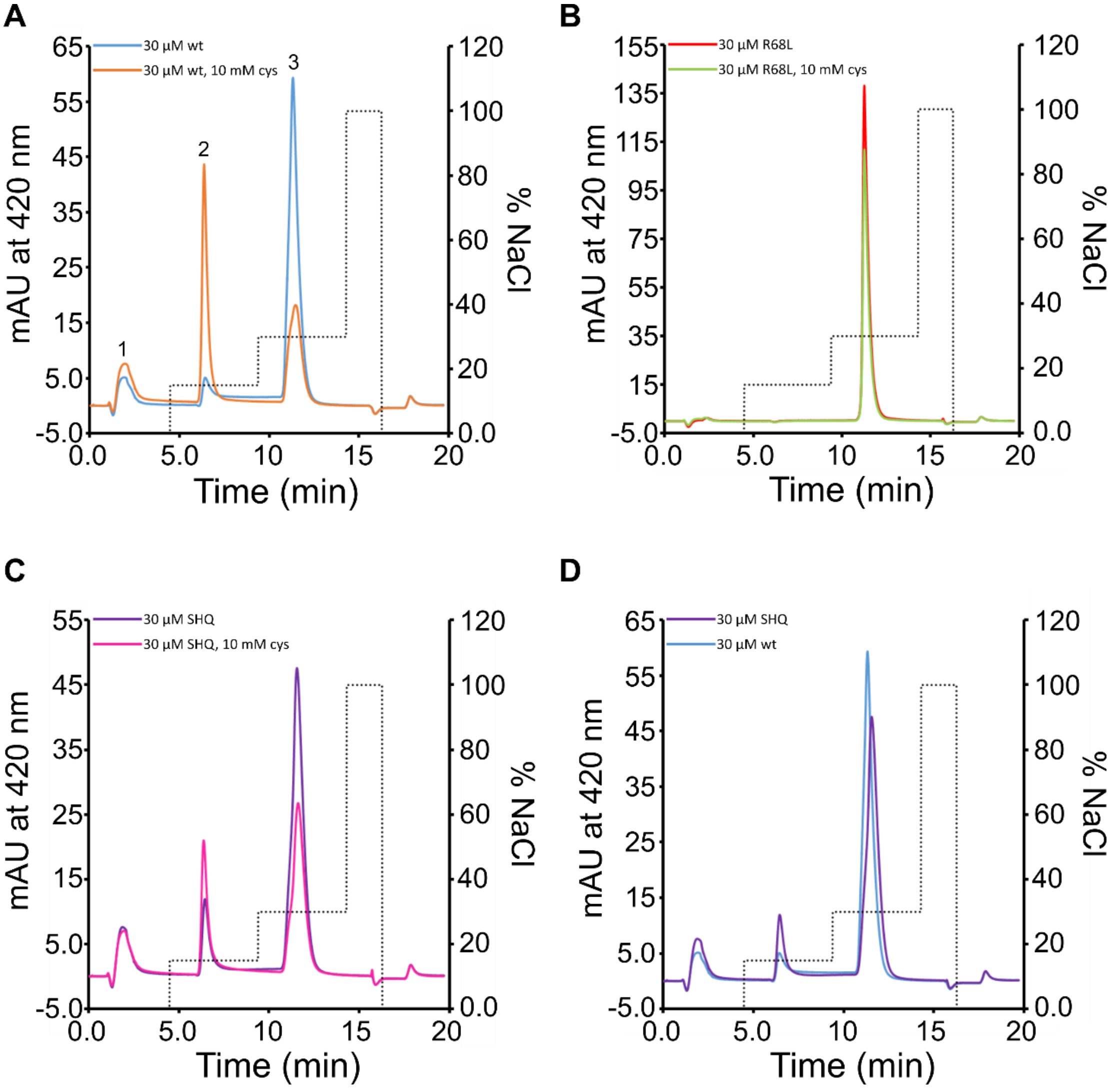

Figure IV.2 Cation exchange chromotagraphy of various SDA$_{ec}$ variants on the beamline setup. Buffer B gradient is shown in grey dotted line. (A) Injection of 1 mL, 30 µM SDA$_{ec}$ in the absence and presence of L-cysteine shows identical distribution observed in Figure IV.1. (B) Injection of 1 mL, 30 µM R68L in the absence and presence of L-cysteine displays a single species and no population re-distribution in the presence of L-cysteine. (C) Injection of 1 mL, 30 µM SHQ in the absence and presence of L-cysteine shows similar behavior to wild-type in panel A. (D) Comparison of wild-type and SHQ in the absence of substrate shows an enhancement in peak 2 and depletion in peak 3 suggesting a population change in the SHQ variant.

To further support this assignment, we utilized native ion mobility mass spectrometry to investigate the different variants used in this study. For wild-type, we observed two distinct species as described in Chapter III (Fig. IV.3A). For SHQ, we observed an enhancement in the population of the lower arrival time species previously assigned as the closed architecture (Fig. IV.3B) consistent with our experiments in Chapter III. Additionally, this is consistent with the population shifts observed in the cation-exchange chromatography experiments when comparing wild-type to SHQ (Fig. IV.2D). Lastly, for R68L, we observed a single species (Fig. IV.3C), albeit at a lower arrival time in comparison to the observed species in wild-type and SHQ experiments, but this observation is consistent with the chromatographic behavior of this variant (Fig. IV.2B). This suggests that R68L has a more compact conformation in solution, and this conformation is non-productive for cysteine turnover.

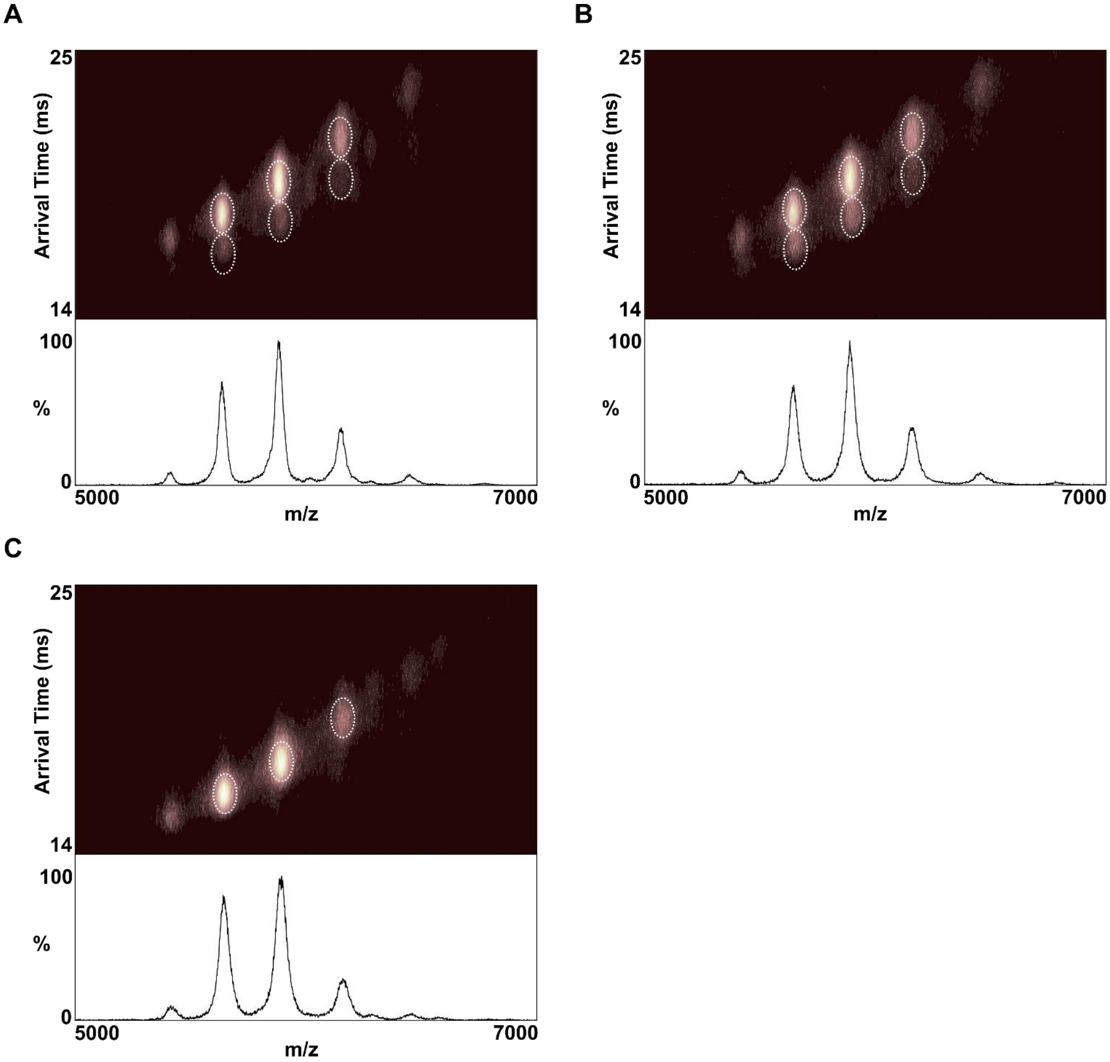

Figure IV.3 Ion-mobility mass spectra of SDA$_{ec}$ and corresponding variants used in this study. (A) Spectra of 10 µM wild-type shows two clear species. (B) Spectra of 10 µM SHQ shows two clear species with an enhancement in the species with smaller arrival time in comparison to wild-type. (C) Spectra of 10 µM R68L shows one species.

Cation-Exchange Coupled Small-angle X-ray Scattering of SDA_{ec} and Functionally Distinct Variants

To further analyze the conformation of these species which feature unique chromatographic behavior, we coupled the experiments conducted in Figure IV.2 to in-line SAXS. SAXS measurements require an accurate buffer subtraction from the sample. It has been demonstrated previously that ion-exchange coupled SAXS experiments can be conducted using either a linear gradient or a step-wise gradient and that buffer subtraction can be achieved either by measurement of background before and after peak elution with following background interpolation through the eluted peak, frame by frame background subtraction from an independent buffer run, or by generation of sufficient mixing ratios of buffers to provide a satisfactory background subtraction to individual frames.[289] Due to the equilibrium present between the individual peaks, we were unable to generate sufficient separation of these species using a shallow, linear gradient of NaCl (data not shown), and instead utilized a step gradient (Fig. IV.2). In order to effectively conduct this experiment, we utilized blank injections prior to and after sample injection and performed a frame by frame subtraction. Because, NaCl is a contrast agent in SAXS, the background scattering increases as the NaCl concentration changes. This can be observed in blank injection runs (Fig. IV.4). The integrated intensity of non-background subtracted frames was consistent with the chromatrographic peak population distributions (Fig. IV.2 and Fig. IV.4).

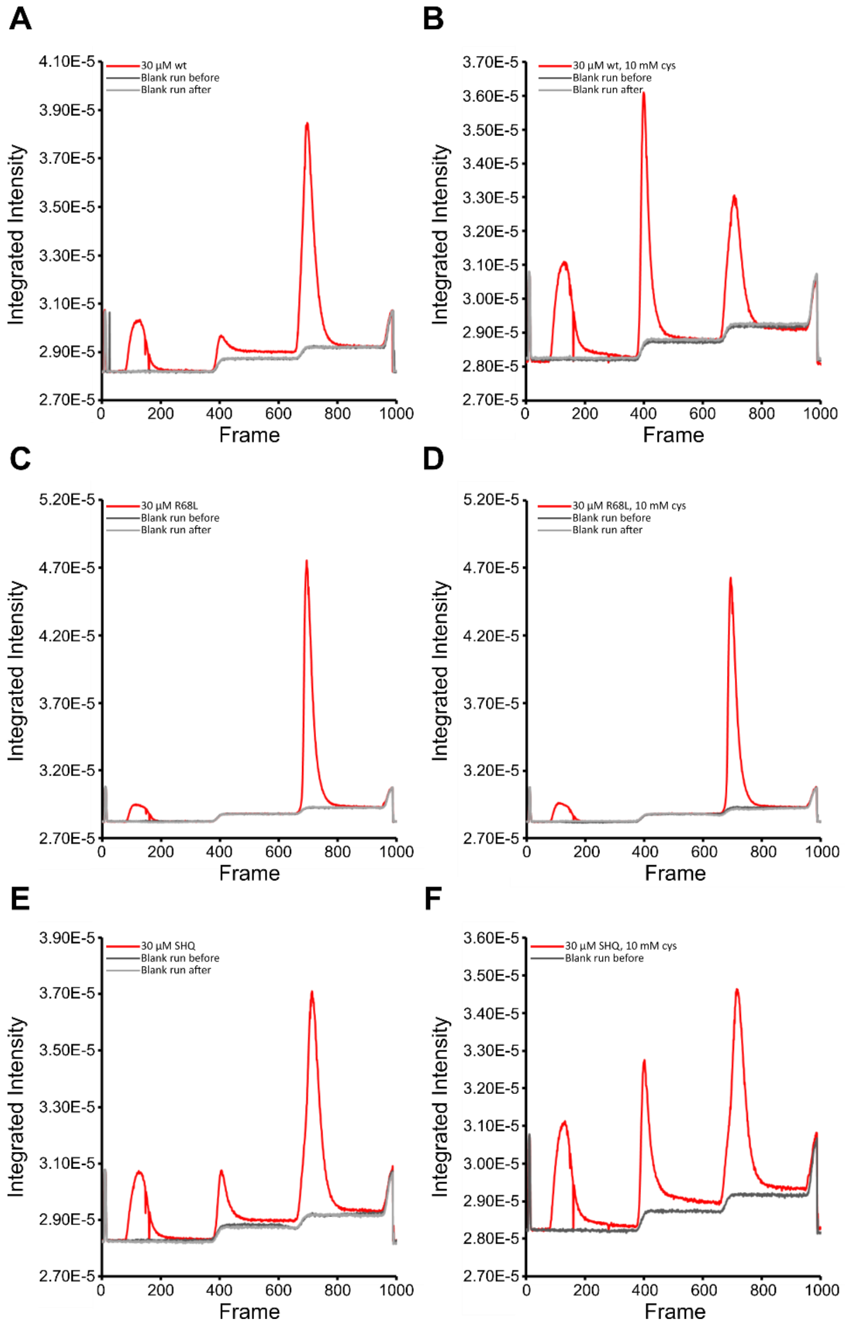

Figure IV.4 Integrated intensity versus frame for the cation exchange coupled small-angle X-ray scattering setup prior to blank subtraction show identical distribution of species eluting from the column with respect to UV-visible tracking in Figure IV.2. (A) Comparison of wild-type to blank runs before and after sample run. (B) Comparison of wild-type in the presence of 10 mM L-cysteine to blank runs before and after sample run. (C) Comparison of R68L to blank runs before and after sample run. (D) Comparison of R68L in the presence of 10 mM L-cysteine to blank runs before and after sample run. (E) Comparison of SHQ to blank runs before and after sample run. (F) Comparison of SHQ in the presence of 10 mM L-cysteine to blank runs before the sample run.

Blank runs were evaluated against sample runs, and blank runs with consistent baseline within the comparison were used for a frame by frame background subtraction against the sample runs. All profiles provided a flat baseline except for wild-type in the presence of cysteine in which a linear baseline correction was applied to account for a slight over subtraction (Fig. IV.4B, Fig. IV.5B, Fig. IV.6B). Given the baseline consistency we moved forward with the analysis. Automated Guinier (Fig. IV.5) and molecular weight analysis (Fig. IV.6) was applied to the subtracted frames in order to investigate the eluted species.

Based on inspection of the automated Guinier (Fig. IV.5) and molecular weight analysis (Fig. IV.6), it was obvious that more than one species was present in each isolated peak. For example, in the Guinier analysis of wild-type of peak 3, the radius of gyration (Rg) ranges from approximately 38 to 43 Å (Fig. IV.5A). In addition, the molecular weight of this peak varies from approximately 122 to 156 kDa with up to a 10 % error in this measurement based on the volume of correlation method[234] (Fig. IV.6A). This type of behavior is observed in almost all peaks analyzed both in the absence and presence of substrate. We attempted singular value decomposition and evolving factor analysis to isolate specific scattering curves; however, evolving factor analysis appeared to be unstable and did not provide reliable scattering curves.[278]

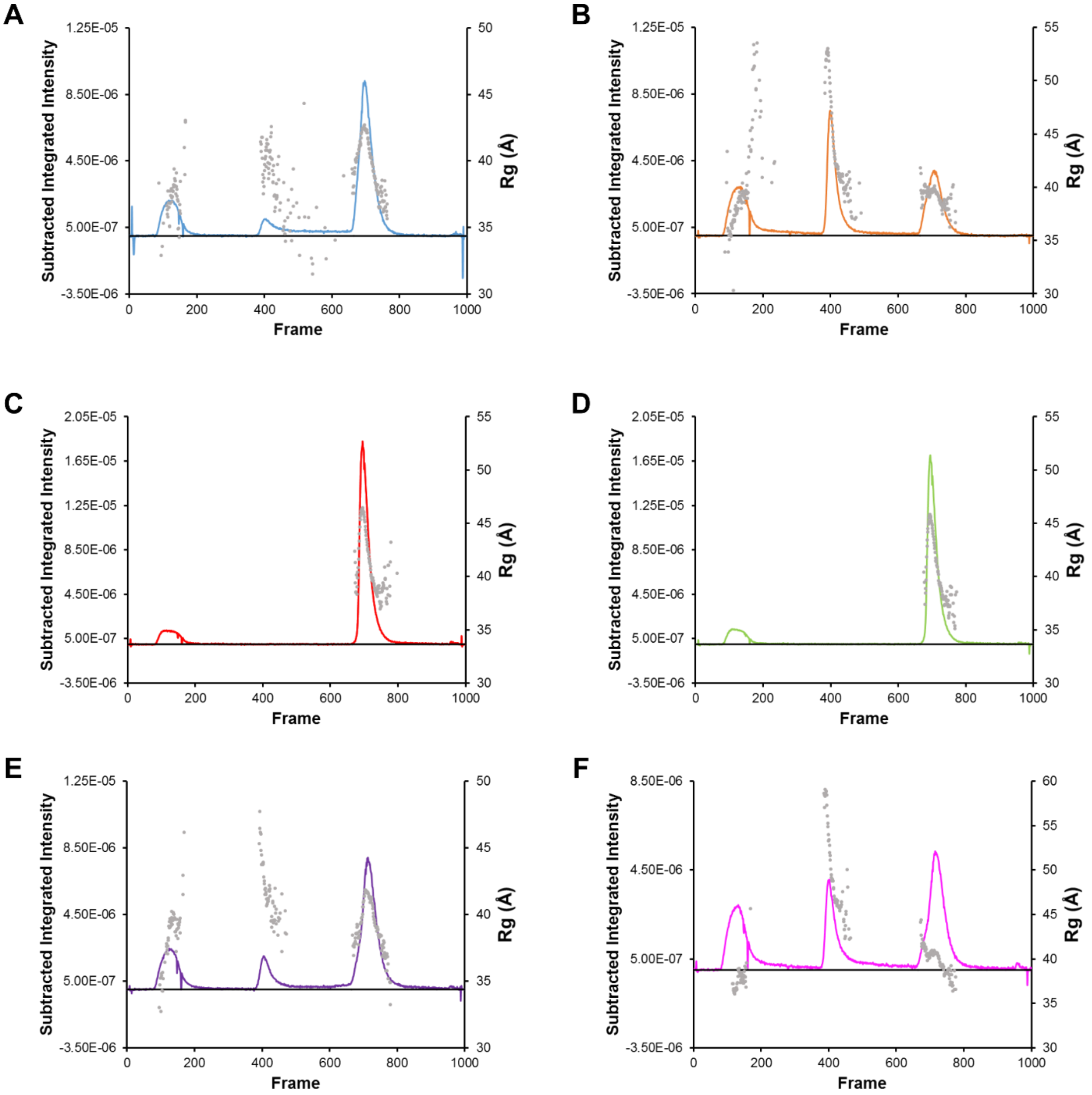

Figure IV.5 Subtracted integrated intensity versus frame featuring an automated radius of gyration (Rg) analysis. Rg is displayed in grey dots. (A) Wild-type. (B) Wild-type in the presence of L-cysteine. (C) R68L (D) R68L in the presence of L-cysteine (E) SHQ (F) SHQ in the presence of L-cysteine.

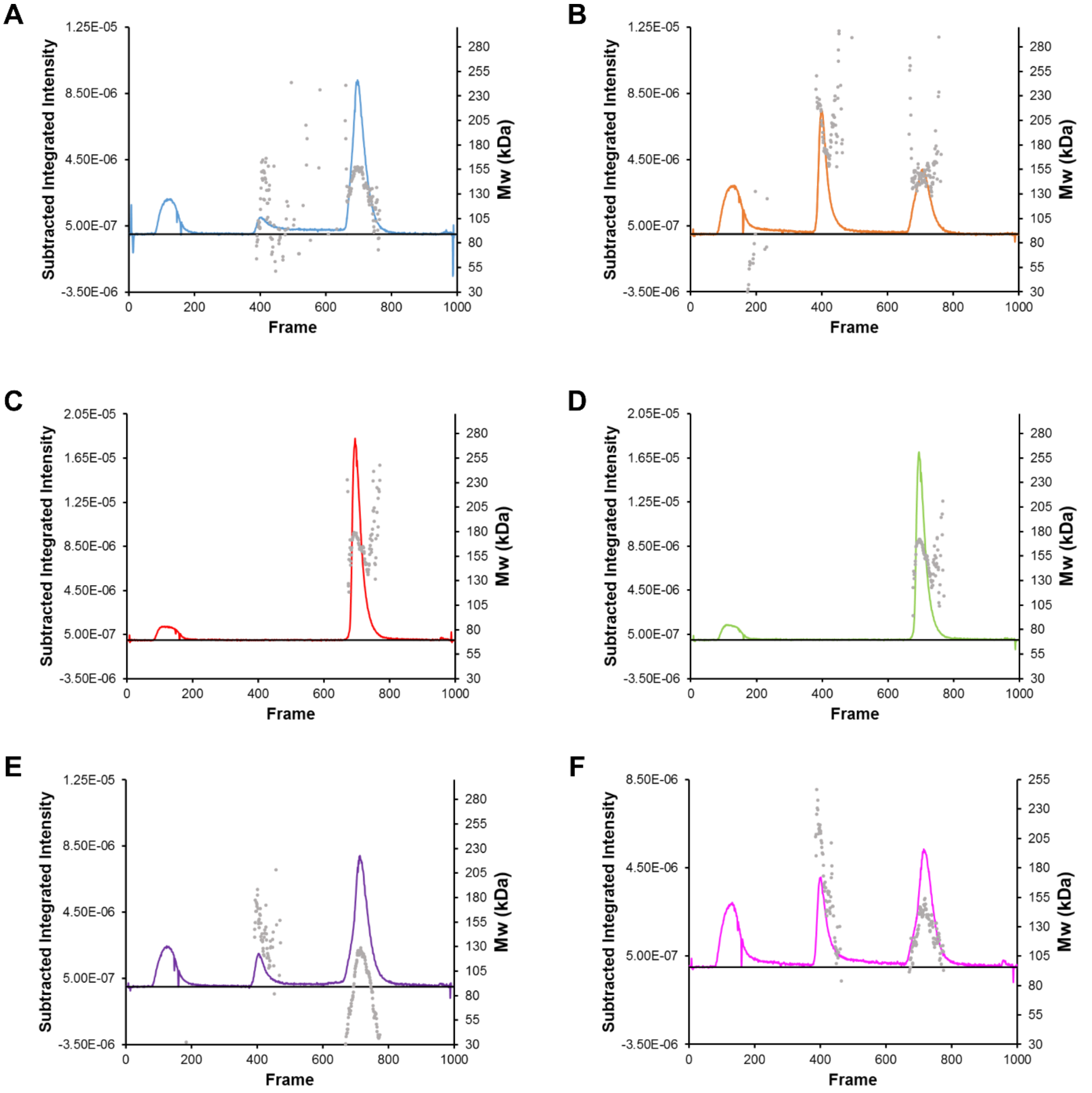

Figure IV.6 Subtracted integrated intensity versus frame featuring an automated molecular weight analysis. Mw is displayed in grey dots. (A) Wild-type. (B) Wild-type in the presence of L-cysteine. (C) R68L (D) R68L in the presence of L-cysteine (E) SHQ (F) SHQ in the presence of L-cysteine.

To circumvent this challenge, we used existing knowledge about our system to individually assign the species present and estimate their scattering parameters. To do this, we specifically isolated and averaged scattering curves based on minimal changes in Rg and reasonable signal to noise via manual inspection of the automated Rg assignments (Fig. IV.5). In most cases, the front side and back side of an elution peak was not evaluated as the radius of gyration and molecular weight appears to be changing too rapidly to isolate specific species. Therefore, we often analyzed the top of a peak and the tail ends of peaks which stabilized with respect to Rg change. Based on our previous work (Chapter III), we know that concentration dependent oligomerization occurs in $\mathrm{SDA_{ec}}$ samples. Samples with minimal concentration dependence by either analysis at low concentration or high ionic strength and, in the absence of substrate, appear to result in a Rg of approximately 37 Å and a D_{max} ranging from 112 to 122 Å.[233] We used this information to make assumptions about isolated, averaged scattering curves. In addition, we were unable to extract reliable information from peak 1 as it is mixture of sample buffer and buffer A, and in the case of L-cysteine addition, it is a mixture of sample buffer, buffer A, L-cysteine, and cysteine persulfides making buffer subtraction estimations impossible. Therefore, only peaks 2 and 3 of the elution phase were analyzed.

In wild-type peak 2, we identified a single species that is likely an apo form (substrate free) with a Rg of 40.08 Å, D_{max} of 116 Å, and estimated molecular weight of 139 kDa (Fig. IV.5A and Table IV.1). In peak 3, we identified two species: a larger form, likely a concentration dependent oligomer, and an apo form with SAXS parameters (Fig. IV.5A and Table IV.1) consistent with our previously determined SAXS parameters mentioned above. Upon addition of substrate, peak two now contained at least three species (Fig. IV.5B and Table IV.1). The first species appears to be a substrate bound oligomer. This assumption is made based on the analysis that integrated scattering intensity increases as protein concentration increases. The maximum peak intensity of peak 2 in the wild-type plus L-cysteine is less than that of the maximum peak intensity of peak 3 in the wild-type alone sample. Therefore, we would expect that any observed concentration dependent oligomer in peak 2 of the wild-type plus L-cysteine would have Rg and D_{max} parameters that are smaller than that of the concentration dependent oligomer observed in peak 3 of wild-type alone given that it would be present in a lower concentration, and a SAXS curve is a weighted average favoring larger species in a multi-component mixture. However, this is not the case. The scattering parameters of this species are much larger than that of any species observed in the wild-type alone sample. In addition, there is a large change in radius of gyration as a function of elution peak decay likely due to a mixture of a variety of species (Figure IV.5B and Table IV.1). The third species in this peak exhibited a Rg consistent with an apo species; however, the noise in the scattering curve made D_{max} and molecular weight difficult to estimate.

In both analyses of R68L in the absence and presence of L-cysteine, two species were observed in both peak 2 and 3 (Figure IV.5C,D and Table IV.1). These species were assigned as concentration dependent oligomer and apo. Consistent with the chromatographic behavior, R68L is incapable of generating the substrate bound species in peak 2, and this is clearly shown in the estimated SAXS parameters of isolated species as the same species observed in wild-type in the presence of L-cysteine is not observed.

In samples containing SHQ, we observed similar behavior to wild-type SDA_{ec} (Fig. 5E,F and Table IV.1). However, we did not identify an apo species in peak 2. This species could potentially be present at the back end tail of peak 2 but has a large variability in Rg in this region due to low signal to noise (Fig. IV.5F). Instead, we observed species consistent with the substrate bound oligomer observed in the wild-type, and an additional species with low population but a larger radius of gyration and observed molecular weight slightly larger than previously observed apo species. We preliminarily assigned this species as substrate bound (Table IV.1). In addition, we observed a mixture of the substrate bound oligomer and substrate bound species, but the large changes in Rg and molecular weight during the elution phase of this peak made it difficult to extract scattering parameters. In peak 3 we observed a mixture of concentration dependent oligomer and apo species which was assigned based on the larger D_{max} (150 Å) and molecular weight (157 kDa). Moreover, we also observed an apo species which had similar scattering parameters to other apo species that had been previously identified in this peak (Table IV.1).

Table IV.1 Extracted small-angle X-ray scattering parameters from manually isolated species.

Sample	Peak Number	Species Identified	Estimated SAXS Parameters				Preliminary Assignement	Additional Preprocessing
			Rg (Å)	Dmax (Å)	Rg (Å) from PD	Mw (kDa)		
WT	2	1	40.08 ± 0.46	116	39.22 ± 0.18	139	Apo	
WT	3	1	42.66 ± 0.11	161	43.40 ± 0.12	169	Concentration Dependent Oligomer	
		2	37.32 ± 0.33	128	37.68 ± 0.27	129	Apo	
WT + cys	2	1	52.48 ± 0.36	187	54.09 ± 0.31	242	Substrate Bound Oligomer	Linear Baseline Correction
		2	NA				Substrate Bound Oligomer Concentration Dependent Oligomer Substrate Bound	
		3*	40.49 ± 0.20	125	40.17 ± 0.17	170	Apo	
WT + cys	3	1	39.44 ± 0.12	124	39.32 ± 0.09	153	Concentration Dependent Oligomer	Linear Baseline Correction
		2	38.03 ± 0.29	125	38.03 ± 0.23	152	Apo	
R68L	3	1	46.59 ± 0.10	185	48.56 ± 0.13	195	Concentration Dependent Oligomer	
		2	38.35 ± 0.23	120	38.21 ± 0.14	157	Apo	
R68L + cys	3	1	45.85 ± 0.12	185	47.75 ± 0.16	189	Concentration Dependent Oligomer	
		2	37.37 ± 0.25	122	37.65 ± 0.18	145	Apo	
SHQ	2	1	46.52 ± 1.03	145	46.67 ± 0.49	184	Concentration Dependent Oligomer	
		2	39.26 ± 0.67	122	39.16 ± 0.41	150	Apo	
SHQ	3	1	41.11 ± 0.08	143	41.77 ± 0.09	151	Concentration Dependent Oligomer	
		2*	36.87 ± 0.34	119	37.15 ± 0.22	90	Apo	
SHQ + cys	2	1	58.68 ± 0.68	190	58.80 ± 0.40	286	Substrate Bound Oligomer	
		2	NA				Substrate Bound Oligomer Substrate Bound	
		3	45.96 ± 0.54	146	45.64 ± 0.37	172	Substrate Bound	
SHQ + cys	3	1	40.61 ± 0.13	150	41.08 ± 0.16	157	Concentration Dependent Oligomer/Apo	
		2	37.92 ± 0.23	124	38.08 ± 0.17	140	Apo	

*Noise in scattering profile made SAXS parameters difficult to estimate. Analysis such as D_{max} and molecular weight are likely unreliable.

While signal to noise is a challenge with these datasets, we isolated extracted scattering parameters for species identified (Table IV.1). Due to the noise of these scattering curves above 0.08 $Å^{-1}$, it was difficult to assess the fold of the isolated species via Kratky analysis (data not shown); however, based on our equilibrium experiments (Fig. IV.1) we expect the isolated species to be fully folded and functional. In wild-type samples containing substrate, the substrate bound oligomer identified features a distinctly different conformation in comparison to apo, and the identified concentration dependent oligomer. In fact it features a flatter scattering profile in the 0.03 to 0.06 $Å^{-1}$ q-range and a larger radius of gyration (Table IV.1 and Fig. IV.7A). In the SHQ sample, we were capable of isolating a species which appeared at lower concentrations within the elution peak but displayed elongated scattering parameters (Table IV.1). We compared this species to the SHQ apo species identified in peak 2 and the assigned substrate bound species which featured, again, a flatter scattering profile in the 0.03 to 0.06 $Å^{-1}$ q-range and a larger radius of gyration (Table IV.1 and Fig. IV.7B).

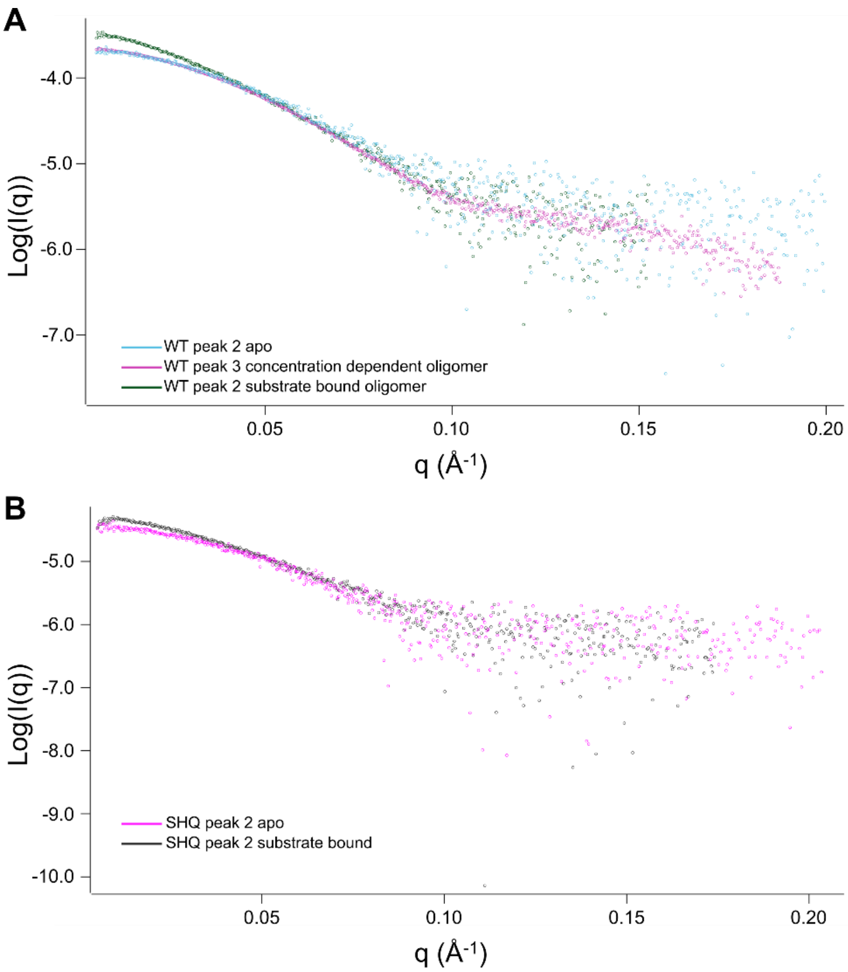

Figure IV.7 Comparison of substrate bound oligomer and substrate bound extracted small-angle X-ray scattering curves to concentration dependent oligomer and apo extracted scattering curves. (A) Scattering curves of apo, concentration dependent oligomer, and substrate bound oligomer in wild-type samples were scaled and compared in Scatter. (B) Scattering curves of apo and substrate bound were scaled and compared in Scatter.

Discussion

Given our previous establishment of a morpheein model for SDA_{ec} we attempted to analyze the effects of substrate on the complex. In our previous model, only adaptor protein binding influenced population distribution. However, in typical morpheein models, allosteric transitions are often driven by binding of a substrate or allosteric effector molecule. Here we utilized cation exchange chromatography, native ion-mobility mass spectrometry, and chromatography coupled SAXS to preliminarily characterize substrate driven transitions.

Using cation exchange chromatography, we were capable of observing chromatographic behavior changes of active species upon addition of substrate (Fig. IV.1 and Fig. IV.2). Interestingly, these species, regardless of substrate presence, appeared to be in equilibrium with one another (Fig. IV.1). In addition, the populations of species, presumably open and closed architectures, observed during elution corresponded well with ion mobility analysis of wild-type, R68L, and SHQ (Fig. IV.3). Interestingly, R68L is unaffected by substrate addition and features a single conformation in both the ion mobility spectra (Fig. IV.3C) and cation exchange experiments (Fig. IV.2B) indicating a non-productive conformation that is incapable of undergoing a conformation change required for substrate turnover.

Taken together, we were able to isolate and preliminarily characterize these species using chromatography coupled SAXS. In samples capable of substrate turnover, a larger species is always identified indicated by Rg, D_{max}, and molecular weight analysis (Table IV.1). These species have unique scattering curves (Figure IV.7), and this species is not identified in R68L samples (Table IV.1) consistent with the chromatographic analysis of this variant (Fig. IV.2B).

Unfortunately, as we have shown before, SAXS appears to be incapable of distinguishing open and closed architectures. Given the challenges associated with SDA_{ec} including concentration dependent oligomerization and the presence of multiple architectures, obtaining unique structural information with respect to independent species becomes difficult. However, this methodology of isolating individual species appears to be promising for further experiments attempting to characterize conformational changes of SDA_{ec} in the presence of substrate.

Some strategies which could improve this analysis would be the identification of variants which do not undergo concentration dependent oligomerization which has been done for other systems featuring challenging sample requirements.[290] Additionally, cation-exchange chromatography could be coupled to the ion mobility instrumentation to analyze the conformation populations with an additional degree of separation in a time resolved fashion.[291] Moreover, time-resolved cryoEM setups are currently being developed and may be particularly useful in this situation where individual particles featuring distinct conformational changes could be selected and analyzed to achieve high resolution structural information.[292]

Materials and Methods

Protein Expression and Purification

Site-directed mutagenesis using the QuickChange protocol (Agilent) was performed to generate Δ1-55NFS1(Q64S, P299H, L300Q). ISD11(R68L) was generated as previously described.[121] The NFS1(Δ1-55)-ISD11-ACP$_{ec}$ complex and the corresponding variants were co-expressed and co-purified as described previously.[121]

Cation-Exchange Chromatography

For un-treated samples, protein was thawed rapidly and diluted to 60 μM with 50 mM HEPES, 250 mM NaCl, 10 % glycerol, pH 7.5. The sample was diluted in half with Buffer A (50 mM HEPES, 20 mM NaCl, 2 % glycerol, pH 8.0) to a final concentration of 30 μM. For samples containing L-cysteine (Sigma-Aldrich), a 100 mM stock solution of L-cysteine was prepared by dilution of 12.1 mg of powder in 1 mL of Buffer A. A portion of this stock was used to dilute a 60 μM protein sample along with additional Buffer A to produce a sample containing 30 μM protein and 10 mM L-cysteine. The substrate treated sample was allowed to incubate for approximately 10 minutes prior to analysis.

Samples (1 mL) were injected onto a Mono S 5/50 GL (GE Healthcare) column using a BioRad Quest FPLC and eluted using a step gradient of Buffer B (50 mM Hepes, 1 M NaCl, 2 % glycerol, pH 8) with steps at 15 %, 30 %, and 100 %. For equilibrium experiments, the peak selected for isolation was concentrated to ~400 – 500 μL using a 100 kDa cutoff Vivaspin 500 (GE Healthcare) by centrifugation at 10,000 rcf. The remaining sample was diluted to 1 mL with Buffer A and reinjected and eluted using the same procedure. All experiments were performed at room temperature.

Cation-Exchange Coupled Small-Angle X-ray Scattering

Cation-exchange coupled SAXS was conducted at BioCAT (beamline 18ID at the Advanced Photon Source). Sample injections, runs, and gradients were conducted as previously described using an AKTA Pure FPLC (GE Healthcare Life Sciences). During elution, sample was passed through a UV-visible monitor and into a SAXS flow cell consisting of a 1.5 mm ID quartz capillary with 10 μm walls. Scattering intensity was measured using a Pilatus3 1M (Dectris) detector at a distance of 3.634 m from the sample providing a q-range of 0.0049 $Å^{-1}$ to 0.3166 $Å^{-1}$. Exposures of 0.5 seconds were recorded every 2 seconds during elution. Buffer A was used in the sheath with an inlet flow rate of 1.05 mL/min. SAXS data collection parameters can be found in Table IV.2.

Table IV.2 Small-angle X-ray scattering instrument and data collection parameters.

Instrument	BioCAT 18ID APS
Detector	Pilatus3 1M
Wavelength (Å)	1.033
Beam size (µm^2)	150 (h) x 35 (v)
Sample to Detector Distance (m)	3.634
q-range (Å^{-1})	0.0049 - 0.3166
Absolute scaling method	N/A
Basis for normalization to constant counts	To incident intensity, by ion chamber counting
Method for monitoring radiation damage	Automated frame-by-frame comparison of relevant regions
Exposure time, number of exposures	0.5 s exposure time with 2 s total exposure (0.5 s on, 1.5 s off)
Sample configuration	Cation-exchange coupled charge separation by AKTA Pure with a Mono S 5/50 GL column. SAXS data measured in a 1.5 mm ID quartz capillary.
Sample temperature (^{o}C)	20

Small-Angle X-ray Scattering Data Processing

All data was analyzed using RAW 1.6.0[252, 253] coupled with ATSAS 2.8.4.[236] Frame series for each sample were inspected in RAW along with the corresponding blank injections. For most runs, the blank before or after the run was used for buffer subtraction with exception of the use a different blank run for the subtraction of SHQ with 10 mM L-cysteine. Frame by frame buffer subtraction was achieved utilizing RAW and a custom python script. An additional linear baseline correction was applied to the dataset containing wild-type with 10 mM L-cysteine to correct for a small over subtraction. Automated radius of gyration and molecular weight analysis (V_c method)[234] was applied to the subtracted profiles to inspect the homogeneity of the elution peaks. Singular value decomposition and evolving factor analysis (EFA) was attempted in RAW. However, given the changes in radius of gyration as a function of frame due to concentration dependent oligomerization made EFA unstable and the deconvolution of individual species unreliable. Peaks were then manually inspected and regions with consistent radius of gyration were pursued for further analysis. Frames were extracted, scaled, and only similar scattering curves (evaluated by CorMap) were averaged in order to estimate scattering parameters. All scattering parameters were determined in RAW. Pair distribution functions were calculated using GNOM.[293]

Ion-Mobility Mass Spectrometry

Native ion-mobility mass spectrometry (Native IM-MS) was performed on a Synapt G2 instrument in a similar fashion as described in Chapter III with the following parameters: capillary voltage of 1.5 kV, source temperature (30 °C), sampling cone voltage of 20 V, extraction cone voltage of 1 V, trap and transfer collision energy off, and backing pressure (4.91 mbar), trap flow rate at 4 ml/min (2.95×10^{-2} mbar), He cell flow rate at 200 ml/min (1.38×10^{3} mbar), IMS flow rate at 50 ml/min (7.03 mbar). The T-wave settings for trap (310 ms^{-1}/6.0 V), IMS (250 ms^{-1}/9–12 V) and transfer (65 ms^{-1}/2 V), and trap bias (40 V). Sample preparation, data post-processing, and calibration were conducted as described in Chapter III.

Additional Software and Figure Generation

Plots were generated in Excel (Microsoft) or Scatter 3.1r (http://www.bioisis.net/tutorial/9). Artboards and high resolution figures were prepared using Inkscape (https://inkscape.org/) and GIMP (https://www.gimp.org/).

CHAPTER V

CONCLUSIONS AND FUTURE DIRECTIONS

Over the past thirty years, a significant effort has been made to find Fe-S cluster biosynthetic pathways and elucidate the cysteine desulfurase and Fe-S cluster synthesis mechanisms. Unfortunately, in humans, several diseases are linked to defects in Fe-S cluster biosynthetic pathway proteins.[232] The most prominent disease is Friedreich's ataxia which is caused either due to a GAA triplet repeat expansion or point mutations in the FXN gene.[158] Early studies on FXN showed its capability of activating the human cysteine desulfurase subcomplex consisting of NFS1-ISD11-ISCU2 (SDU).[118] Following reports showed that point mutations on FXN, which result in Friedreich's ataxia in patients carrying the mutation, compromise FXN binding to SDU and loss of activity stimulation proprerties.[172, 173] However, when FXN is utilized in the context of the 60 % identical cysteine desulfurase from *E. coli* (IscS) and homologous scaffold (IscU), FXN inhibits the Fe-S cluster assembly process on the scaffold.[87] Additionally, the structural homologue of FXN from *E. coli* (CyaY) was shown to be capable of activating the SDU complex.[87] These observations lead to the hypothesis that there are fundamental differences between the cysteine desulfurases in both human and *E. coli* ISC pathways. In fact, these results drove the need for structural information regarding the human Fe-S cluster assembly subcomplex.

In the past two years, substantial gains have been made in the structural biology of the human Fe-S cluster assembly complex. Here we showed the first crystal structure of the NFS1-ISD11-ACP$_{ec}$ complex.[121] This structure (5USR.pdb) showed a remarkable rearrangement of the cysteine desulfurase subunits with respect to one another when compared to the highly homologous IscS structure. This unique, open cysteine desulfurase architecture clearly demonstrated the essential natures of ISD11 and ACP_{ec} in stabilizing NFS1. Additionally, this was the first X-ray structure to capture the ACP-lipid-LYR motif at high resolution directly demonstrating how ACP provides additional support to the three helix bundle protein ISD11. In fact, just prior to the structure, studies showed that ACP was essential for eukaryotic Fe-S biosynthesis,[129] and the human NFS1-ISD11 complex co-purifies with *E. coli* ACP (ACP_{ec}) under recombinant conditions.[109] In combination with observations of ACP in complex with respiratory complex LYR proteins in similar orientations to the Fe-S cluster assembly subcomplex,[131, 133, 187] these structures opened up the possibility of an intertwined regulatory network governed by acyl-ACP and LYR proteins for the biogenesis of mitochondria and activation of oxidative phosphorylation through Fe-S cluster assembly and respiratory complex maturation. This model has recently been supported by demonstration that acetyl-CoA and acyl-ACP species are required for the activation and assembly of respiratory complexes in *S. cerevisiae*.[178]

Given the open architecture of SDA_{ec}, it was clear that the lack of an additional subunit providing a substrate tunnel was a likely explanation of the low activity of the SDA_{ec} and $SDA_{ec}U$ complexes. We proposed a model in which FXN acts as an activator by participating as the second half of the substrate tunnel in the open architecture. However, additional structures of SDA_{ec} (5WGB.pdb) and $SDA_{ec}U$ (5WLW.pdb and 5WKP.pdb)[122] were determined shortly after the open architecture structure of SDA_{ec} and featured a closed cysteine desulfurase architecture reminiscent of IscS and IscS-IscU.[85, [110, 193] While the closed architecture is to be expected for a cysteine desulfurase sharing such high homology to its prokaryotic counterpart, it did not fully explain the lack of activity in the human enzyme. Following these X-ray crystal structure determinations, a cryo-electron microscopy structure of $SDA_{ec}UF$ was determined which presented the cysteine desulfurase in a closed architecture, and the dimer interface of the cysteine desulfurase was stabilized by interactions with FXN.[143] While the authors proposed a model in which FXN activates the cysteine desulfurase by preventing the active site mobile loop cysteine from coordinating a zinc ion bound to ISCU2, this model directly contradicted their previous results where $SDA_{ec}U$ in which zinc had been removed from the complex still exhibited low activity.[294] Therefore, even though the structure of $SDA_{ec}UF$ had been determined, it still did not provide enough mechanistic information to reveal the structural basis of FXN-based activation. We hypothesized that FXN-based activation could possibly be due to the presence of two different subcomplex architectures and an equilibrium between low and high activity architectures that could be modulated by FXN.

To help provide a clearer picture of FXN-based activation, we investigated the architecture of SDA_{ec} in solution. We first showed that SDA_{ec} prepared by our lab displays the same activity properties and conformation, using SAXS, as other SDA_{ec} prepared by alternate labs. We followed this up by crystallizing different preparations of SDA_{ec} in both open and closed architecture crystallization conditions. Upon isolation of both open and closed architecture crystals, we were able to activate the cysteine desulfurase in both cases in the presence of ISCU2, FXN, and Fe^{2+}. This presented the possibility that either both architectures were capable of being activated, or there is an equilibrium between low and high activity architectures and that FXN drives the architecture equilibrium towards a high activity form. We were able to demonstrate this by native ion-mobility mass spectrometry and that this transition can occur through either SDA_{ec} dimer dissociation or through a tethered dimer transition using $^{15}N/^{14}N-SDA_{ec}$ dimer exchange kinetics. Here we observed two discrete conformations of SDA_{ec} which we assigned to open and closed architectures and upon binding ISCU2 both open and closed $SDA_{ec}U$ architectures could be identified. This observation is consistent with the low activity of SDA_{ec} and $SDA_{ec}U$.[121] However, upon binding of FXN, only a single architecture is observed which we preliminary assigned to a closed architecture based on the available chemical crosslinking, SAXS, and cryoEM models.[143, 233] These data allowed us to construct a morpheein model in which FXN drives an architecture transition to a closed, fully activated $SDA_{ec}UF$ species. This morpheein model is unique because a protein is used as an equilibrium effector instead of a small molecule.[245]

Based on our proposed morpheein model, we hypothesized that the substrate, L-cysteine, of the SDA_{ec} complex could also modulate conformational changes. We were able to isolate different conformations of SDA_{ec} on a cation exchange column using a step gradient method. Upon analysis of variants either designed to contain an enhancement in the population of the closed architecture or an inactive conformation, we were able to correlate population changes in our chromatography experiments with ion-mobility population changes. Upon treatment with substrate, we observed a chromatographic behavior change suggesting a conformational change within SDA_{ec}. Upon isolation of individual species eluting from the column, concentration, dilution, and re-injection, all species reappear in the cation-exchange chromatography experiment suggesting that all conformers are in equilibrium with one another. We attempted to characterize the species eluting from the cation-exchange column using an in-line SAXS setup. However, the presence of a concentration dependent oligomer made the isolation of scattering curves specific to individual species unreliable. In addition, based on our previous analysis, SAXS appears to not be a reliable technique for differentiating open and closed architectures in solution given the conformational diversity of SDA_{ec} in solution and the low resolution structural information achieved from SAXS measurements. However, we did identify a method for isolating specific conformations that could be parlayed into higher resolution structural methods or alternate biophysical techniques.

The SDA_{ec} subcomplex presents a unique challenge to the structural biology community where traditional solution structure techniques for evaluating protein conformations such as SAXS or NMR are limited by either resolution and experimental error or size of the complex respectively. There are still several questions to address about this system even though the structure of $SDA_{ec}UF$ has been determined. The structure of open $SDA_{ec}U$ is unknown, and the structural populations of the SDA_{ec} and $SDA_{ec}U$ need to be determined using a high resolution technique such as cryo-electron microscopy to corroborate our ion-mobility mass spectrometry experiments. In addition, the structural determination of $SDA_{ec}UF$ only utilized 20 % of the total identified particles which did not sufficiently rule out the presence of an open $SDA_{ec}UF$ structure.[143] We also believe that looking at architecture populations as a function of cell life cycle will help determine the reason for the presence of multiple architectures of the Fe-S cluster assembly subcomplex; however, these experiments will require advanced chemical probes and genetic manipulations which may leave the interpretation of *in vivo* results difficult. Moreover, the rates of architecture transitions *in vitro* could be measured using either carefully designed double electron electron resonance (DEER) or fluorescence resonant energy transfer (FRET) experiments in which real time measurements could be utilized to measure probe to probe distances that could be correlated to architectural transition events. The rate of transition between open and closed architecture should be equal to that of the FXN-based activation event in an activity assay. Lastly, it is possible that ion-mobility mass spectrometry could be used as an architecture screening method in drug discovery efforts. Addition of small molecules that drive the same conformation transition observed in our experiments could be used for further therapeutic development coupled with activity assays in order to find an appropriate treatment for Friedreich's ataxia.

Taken together, these results and the future experiments to be conducted on this system will provide insight into why multiple architectures of the Fe-S cluster assembly subcomplex exist, and how these architectures play a role in FXN-based activation. We believe that the presence of these architectures is an evolutionarily designed mechanism for controlling the activity of the Fe-S cluster biosynthetic system during the early stages of mitochondrial biogenesis when the requirement for the Fe-S clusters is low. However, during the later stages of development and respiratory complex maturation, the need for Fe-S clusters is high. Coupled with acyl-ACP based regulation and tied to respiratory complex maturation, FXN-based conformational transitions to a high activity Fe-S cluster assembly complex provide a tightly regulated system for mitochondrial biogenesis and activation of oxidative phosphorylation. However, the control of FXN expression levels as a function of mitochondrial life cycle will need to be thoroughly investigated to support this model.

REFERENCES

[1] Warburg, O. (1949) Heavy metal prosthetic groups and enzyme action., *Oxford: Clarendon Press*.

[2] Beinert, H. (2000) Iron-sulfur proteins: ancient structures, still full of surprises, *J. Biol. Inorg. Chem. 5*, 2-15.

[3] San Pietro, A., and Lang, H. M. (1958) Photosynthetic pyridine nucleotide reductase. I. Partial purification and properties of the enzyme from spinach, *J. Biol. Chem. 231*, 211-229.

[4] Tagawa, K., and Arnon, D. I. (1962) Ferredoxins as electron carriers in photosynthesis and in the biological production and consumption of hydrogen gas, *Nature 195*, 537-543.

[5] Mortenson, L. E., Valentine, R. C., and Carnahan, J. E. (1962) An electron transport factor from Clostridium pasteurianum, *Biochem. Biophys. Res. Commun. 7*, 448-452.

[6] Johnson, D. C., Dean, D. R., Smith, A. D., and Johnson, M. K. (2005) Structure, function, and formation of biological iron-sulfur clusters, *Annu. Rev. Biochem 74*, 247-281.

[7] Beinert, H., Holm, R. H., and Munck, E. (1997) Iron-sulfur clusters: nature's modular, multipurpose structures, *Science 277*, 653-659.

[8] Malkin, R., and Rabinowitz, J. C. (1966) The reconstitution of clostridial ferredoxin, *Biochem. Biophys. Res. Commun. 23*, 822-827.

[9] Freibert, S. A., Weiler, B. D., Bill, E., Pierik, A. J., Muhlenhoff, U., and Lill, R. (2018) Biochemical Reconstitution and Spectroscopic Analysis of Iron-Sulfur Proteins, *Methods Enzymol. 599*, 197-226.

[10] Fenton, H. J. H. (1894) LXXIII.—Oxidation of tartaric acid in presence of iron, *J. Chem. Soc., Trans. 65*, 899-910.

[11] Jiang, J., Chan, A., Ali, S., Saha, A., Haushalter, K. J., Lam, W. L., Glasheen, M., Parker, J., Brenner, M., Mahon, S. B., Patel, H. H., Ambasudhan, R., Lipton, S. A., Pilz, R. B., and Boss, G. R. (2016) Hydrogen Sulfide--Mechanisms of Toxicity and Development of an Antidote, *Sci Rep 6*, 20831.

[12] McLaughlin, M. I., Lanz, N. D., Goldman, P. J., Lee, K. H., Booker, S. J., and Drennan, C. L. (2016) Crystallographic snapshots of sulfur insertion by lipoyl synthase, *Proc. Natl. Acad. Sci. U.S.A. 113*, 9446-9450.

[13] Kondo, T., Nomata, J., Fujita, Y., and Itoh, S. (2011) EPR study of 1Asp-3Cys ligated 4Fe-4S iron-sulfur cluster in NB-protein (BchN-BchB) of a dark-operative protochlorophyllide reductase complex, *FEBS Lett. 585*, 214-218.

[14] Peters, J. W., Stowell, M. H., Soltis, S. M., Finnegan, M. G., Johnson, M. K., and Rees, D. C. (1997) Redox-dependent structural changes in the nitrogenase P-cluster, *Biochemistry 36*, 1181-1187.

[15] Ueno, Y., Matsumoto, T., Yamano, A., Imai, T., and Morimoto, Y. (2013) Increasing the electron-transfer ability of Cyanidioschyzon merolae ferredoxin by a one-point mutation--a high resolution and Fe-SAD phasing crystal structure analysis of the Asp58Asn mutant, *Biochem. Biophys. Res. Commun. 436*, 736-739.

[16] Friemann, R., Lee, K., Brown, E. N., Gibson, D. T., Eklund, H., and Ramaswamy, S. (2009) Structures of the multicomponent Rieske non-heme iron toluene 2,3-dioxygenase enzyme system, *Acta Crystallogr D Biol Crystallogr 65*, 24-33.

[17] Hirano, Y., Takeda, K., and Miki, K. (2016) Charge-density analysis of an iron-sulfur protein at an ultra-high resolution of 0.48 A, *Nature 534*, 281-284.

[18] Camba, R., Jung, Y. S., Hunsicker-Wang, L. M., Burgess, B. K., Stout, C. D., Hirst, J., and Armstrong, F. A. (2003) Mechanisms of redox-coupled proton transfer in proteins: role of the proximal proline in reactions of the [3Fe-4S] cluster in Azotobacter vinelandii ferredoxin I, *Biochemistry 42*, 10589-10599.

[19] Capozzi, F., Ciurli, S., and Luchinat, C. (1998) Coordination sphere versus protein environment as determinants of electronic and functional properties of iron-sulfur proteins, In *Metal Sites in Proteins and Models Redox Centres* (Hill, H. A. O., Sadler, P. J., and Thomson, A. J., Eds.), pp 127-160, Springer Berlin Heidelberg, Berlin, Heidelberg.

[20] Bak, D. W., and Elliott, S. J. (2014) Alternative FeS cluster ligands: tuning redox potentials and chemistry, *Curr. Opin. Chem. Biol. 19*, 50-58.

[21] Sheftel, A. D., Stehling, O., Pierik, A. J., Elsasser, H. P., Muhlenhoff, U., Webert, H., Hobler, A., Hannemann, F., Bernhardt, R., and Lill, R. (2010) Humans possess two mitochondrial ferredoxins, Fdx1 and Fdx2, with distinct roles in steroidogenesis, heme, and Fe/S cluster biosynthesis, *Proc. Natl. Acad. Sci. U.S.A. 107*, 11775-11780.

[22] Link, T. A., Hatzfeld, O. M., Unalkat, P., Shergill, J. K., Cammack, R., and Mason, J. R. (1996) Comparison of the "Rieske" [2Fe-2S] center in the bc1 complex and in bacterial dioxygenases by circular dichroism spectroscopy and cyclic voltammetry, *Biochemistry 35*, 7546-7552.

[23] Zhang, Z., Huang, L., Shulmeister, V. M., Chi, Y. I., Kim, K. K., Hung, L. W., Crofts, A. R., Berry, E. A., and Kim, S. H. (1998) Electron transfer by domain movement in cytochrome bc1, *Nature 392*, 677-684.

[24] Stephens, P. J., Jollie, D. R., and Warshel, A. (1996) Protein Control of Redox Potentials of Iron−Sulfur Proteins, *Chem. Rev. 96*, 2491-2514.

[25] Kaster, A. K., Moll, J., Parey, K., and Thauer, R. K. (2011) Coupling of ferredoxin and heterodisulfide reduction via electron bifurcation in hydrogenotrophic methanogenic archaea, *Proc. Natl. Acad. Sci. U.S.A. 108*, 2981-2986.

[26] Peters, J. W., Lanzilotta, W. N., Lemon, B. J., and Seefeldt, L. C. (1998) X-ray crystal structure of the Fe-only hydrogenase (CpI) from Clostridium pasteurianum to 1.8 angstrom resolution, *Science 282*, 1853-1858.

[27] Doukov, T. I., Iverson, T. M., Seravalli, J., Ragsdale, S. W., and Drennan, C. L. (2002) A Ni-Fe-Cu center in a bifunctional carbon monoxide dehydrogenase/acetyl-CoA synthase, *Science 298*, 567-572.

[28] Crane, B. R., Siegel, L. M., and Getzoff, E. D. (1995) Sulfite reductase structure at 1.6 A: evolution and catalysis for reduction of inorganic anions, *Science 270*, 59-67.

[29] Wu, M., Gu, J., Guo, R., Huang, Y., and Yang, M. (2016) Structure of Mammalian Respiratory Supercomplex I1III2IV1, *Cell 167*, 1598-1609 e1510.

[30] Robbins, A. H., and Stout, C. D. (1989) Structure of activated aconitase: formation of the [4Fe-4S] cluster in the crystal, *Proc. Natl. Acad. Sci. U.S.A. 86*, 3639-3643.

[31] Lauble, H., Kennedy, M. C., Beinert, H., and Stout, C. D. (1994) Crystal structures of aconitase with trans-aconitate and nitrocitrate bound, *J. Mol. Biol. 237*, 437-451.

[32] Haile, D. J., Rouault, T. A., Harford, J. B., Kennedy, M. C., Blondin, G. A., Beinert, H., and Klausner, R. D. (1992) Cellular regulation of the iron-responsive element binding protein: disassembly of the cubane iron-sulfur cluster results in high-affinity RNA binding, *Proc. Natl. Acad. Sci. U.S.A. 89*, 11735-11739.

[33] Broderick, J. B., Duffus, B. R., Duschene, K. S., and Shepard, E. M. (2014) Radical S-adenosylmethionine enzymes, *Chem. Rev. 114*, 4229-4317.

[34] Ugulava, N. B., Sacanell, C. J., and Jarrett, J. T. (2001) Spectroscopic changes during a single turnover of biotin synthase: destruction of a [2Fe-2S] cluster accompanies sulfur insertion, *Biochemistry 40*, 8352-8358.

[35] Gaudu, P., and Weiss, B. (1996) SoxR, a [2Fe-2S] transcription factor, is active only in its oxidized form, *Proc. Natl. Acad. Sci. U.S.A. 93*, 10094-10098.

[36] Wu, J., and Weiss, B. (1992) Two-stage induction of the soxRS (superoxide response) regulon of Escherichia coli, *J. Bacteriol. 174*, 3915-3920.

[37] Khoroshilova, N., Popescu, C., Munck, E., Beinert, H., and Kiley, P. J. (1997) Iron-sulfur cluster disassembly in the FNR protein of Escherichia coli by O2: [4Fe-4S] to [2Fe-2S] conversion with loss of biological activity, *Proc. Natl. Acad. Sci. U.S.A. 94*, 6087-6092.

[38] Crack, J., Green, J., and Thomson, A. J. (2004) Mechanism of oxygen sensing by the bacterial transcription factor fumarate-nitrate reduction (FNR), *J. Biol. Chem. 279,* 9278-9286.

[39] Reinhart, F., Achebach, S., Koch, T., and Unden, G. (2008) Reduced apo-fumarate nitrate reductase regulator (apoFNR) as the major form of FNR in aerobically growing Escherichia coli, *J. Bacteriol. 190*, 879-886.

[40] Fromme, J. C., and Verdine, G. L. (2003) Structure of a trapped endonuclease III-DNA covalent intermediate, *EMBO J. 22*, 3461-3471.

[41] Fromme, J. C., Banerjee, A., Huang, S. J., and Verdine, G. L. (2004) Structural basis for removal of adenine mispaired with 8-oxoguanine by MutY adenine DNA glycosylase, *Nature 427*, 652-656.

[42] Arnold, A. R., Grodick, M. A., and Barton, J. K. (2016) DNA Charge Transport: from Chemical Principles to the Cell, *Cell Chem Biol 23*, 183-197.

[43] Darnault, C., Volbeda, A., Kim, E. J., Legrand, P., Vernede, X., Lindahl, P. A., and Fontecilla-Camps, J. C. (2003) Ni-Zn-[Fe4-S4] and Ni-Ni-[Fe4-S4] clusters in closed and open subunits of acetyl-CoA synthase/carbon monoxide dehydrogenase, *Nat. Struct. Biol. 10*, 271-279.

[44] Svetlitchnyi, V., Dobbek, H., Meyer-Klaucke, W., Meins, T., Thiele, B., Romer, P., Huber, R., and Meyer, O. (2004) A functional Ni-Ni-[4Fe-4S] cluster in the monomeric acetyl-CoA synthase from Carboxydothermus hydrogenoformans, *Proc. Natl. Acad. Sci. U.S.A. 101*, 446-451.

[45] Jacobson, M. R., Brigle, K. E., Bennett, L. T., Setterquist, R. A., Wilson, M. S., Cash, V. L., Beynon, J., Newton, W. E., and Dean, D. R. (1989) Physical and genetic map of the major nif gene cluster from Azotobacter vinelandii, *J. Bacteriol. 171*, 1017-1027.

[46] Roberts, G. P., MacNeil, T., MacNeil, D., and Brill, W. J. (1978) Regulation and characterization of protein products coded by the nif (nitrogen fixation) genes of Klebsiella pneumoniae, *J. Bacteriol. 136*, 267-279.

[47] Jacobson, M. R., Cash, V. L., Weiss, M. C., Laird, N. F., Newton, W. E., and Dean, D. R. (1989) Biochemical and genetic analysis of the nifUSVWZM cluster from Azotobacter vinelandii, *Mol Gen Genet 219,* 49-57.

[48] Zheng, L., White, R. H., Cash, V. L., Jack, R. F., and Dean, D. R. (1993) Cysteine desulfurase activity indicates a role for NIFS in metallocluster biosynthesis, *Proc. Natl. Acad. Sci. U.S.A. 90*, 2754-2758.

[49] Zheng, L., White, R. H., Cash, V. L., and Dean, D. R. (1994) Mechanism for the desulfurization of L-cysteine catalyzed by the nifS gene product, *Biochemistry 33*, 4714-4720.

[50] Kaiser, J. T., Clausen, T., Bourenkow, G. P., Bartunik, H. D., Steinbacher, S., and Huber, R. (2000) Crystal structure of a NifS-like protein from Thermotoga maritima: implications for iron sulphur cluster assembly, *J. Mol. Biol. 297*, 451-464.

[51] Ugalde, R. A., Imperial, J., Shah, V. K., and Brill, W. J. (1984) Biosynthesis of iron-molybdenum cofactor in the absence of nitrogenase, *J. Bacteriol. 159*, 888-893.

[52] Dean, D. R., and Brigle, K. E. (1985) Azotobacter vinelandii nifD- and nifE-encoded polypeptides share structural homology, *Proc. Natl. Acad. Sci. U.S.A. 82*, 5720-5723.

[53] Fu, W., Jack, R. F., Morgan, T. V., Dean, D. R., and Johnson, M. K. (1994) nifU gene product from Azotobacter vinelandii is a homodimer that contains two identical [2Fe-2S] clusters, *Biochemistry 33,* 13455-13463.

[54] Agar, J. N., Yuvaniyama, P., JAck, R. F., Cash, V. L., Smith, A. D., Dean, D. R., and Johnson, M. K. (2000) Modular organization and identification of a mononuclear iron-binding site within the NifU protein, *J. Biol. Inorg. Chem. 5,* 167-177.

[55] Yuvaniyama, P., Agar, J. N., Cash, V. L., Johnson, M. K., and Dean, D. R. (2000) NifS-directed assembly of a transient [2Fe-2S] cluster within the NifU protein, *Proc. Natl. Acad. Sci. U.S.A. 97,* 599-604.

[56] Dos Santos, P. C., Smith, A. D., Frazzon, J., Cash, V. L., Johnson, M. K., and Dean, D. R. (2004) Iron-sulfur cluster assembly: NifU-directed activation of the nitrogenase Fe protein, *J. Biol. Chem. 279*, 19705-19711.

[57] Zheng, L., Cash, V. L., Flint, D. H., and Dean, D. R. (1998) Assembly of iron-sulfur clusters. Identification of an iscSUA-hscBA-fdx gene cluster from Azotobacter vinelandii, *J. Biol. Chem. 273*, 13264-13272.

[58] Blattner, F. R., Plunkett, G., 3rd, Bloch, C. A., Perna, N. T., Burland, V., Riley, M., Collado-Vides, J., Glasner, J. D., Rode, C. K., Mayhew, G. F., Gregor, J., Davis, N. W., Kirkpatrick, H. A., Goeden, M. A., Rose, D. J., Mau, B., and Shao, Y. (1997) The complete genome sequence of Escherichia coli K-12, *Science 277*, 1453-1462.

[59] Fleischmann, R. D., Adams, M. D., White, O., Clayton, R. A., Kirkness, E. F., Kerlavage, A. R., Bult, C. J., Tomb, J. F., Dougherty, B. A., Merrick, J. M., and et al. (1995) Whole-genome random sequencing and assembly of Haemophilus influenzae Rd, *Science 269*, 496-512.

[60] Oliver, S. G., van der Aart, Q. J., Agostoni-Carbone, M. L., Aigle, M., Alberghina, L., Alexandraki, D., Antoine, G., Anwar, R., Ballesta, J. P., Benit, P., and et al. (1992) The complete DNA sequence of yeast chromosome III, *Nature 357*, 38-46.

[61] Hwang, D. M., Dempsey, A., Tan, K. T., and Liew, C. C. (1996) A modular domain of NifU, a nitrogen fixation cluster protein, is highly conserved in evolution, *Journal of Molecular Evolution 43*, 536-540.

[62] Prischi, F., and Pastore, A. (2017) Hybrid Methods in Iron-Sulfur Cluster Biogenesis, *Front. Mol. Biosci. 4*, 12.

[63] Schwartz, C. J., Giel, J. L., Patschkowski, T., Luther, C., Ruzicka, F. J., Beinert, H., and Kiley, P. J. (2001) IscR, an Fe-S cluster-containing transcription factor, represses expression of Escherichia coli genes encoding Fe-S cluster assembly proteins, *Proc. Natl. Acad. Sci. U.S.A. 98*, 14895-14900.

[64] Giel, J. L., Rodionov, D., Liu, M., Blattner, F. R., and Kiley, P. J. (2006) IscR-dependent gene expression links iron-sulphur cluster assembly to the control of O2-regulated genes in Escherichia coli, *Mol. Microbiol. 60*, 1058-1075.

[65] Rajagopalan, S., Teter, S. J., Zwart, P. H., Brennan, R. G., Phillips, K. J., and Kiley, P. J. (2013) Studies of IscR reveal a unique mechanism for metal-dependent regulation of DNA binding specificity, *Nat. Struct. Mol. Biol. 20*, 740-747.

[66] Flint, D. H. (1996) Escherichia coli contains a protein that is homologous in function and N-terminal sequence to the protein encoded by the nifS gene of Azotobacter vinelandii and that can participate in the synthesis of the Fe-S cluster of dihydroxy-acid dehydratase, *J. Biol. Chem. 271*, 16068-16074.

[67] Mihara, H., and Esaki, N. (2002) Bacterial cysteine desulfurases: their function and mechanisms, *Appl. Microbiol. Biotechnol. 60*, 12-23.

[68] Urbina, H. D., Silberg, J. J., Hoff, K. G., and Vickery, L. E. (2001) Transfer of sulfur from IscS to IscU during Fe/S cluster assembly, *J. Biol. Chem. 276*, 44521-44526.

[69] Smith, A. D., Frazzon, J., Dean, D. R., and Johnson, M. K. (2005) Role of conserved cysteines in mediating sulfur transfer from IscS to IscU, *FEBS Lett. 579*, 5236-5240.

[70] Yan, R., Konarev, P. V., Iannuzzi, C., Adinolfi, S., Roche, B., Kelly, G., Simon, L., Martin, S. R., Py, B., Barras, F., Svergun, D. I., and Pastore, A. (2013) Ferredoxin competes with bacterial frataxin in binding to the desulfurase IscS, *J. Biol. Chem. 288*, 24777-24787.

[71] Kim, J. H., Frederick, R. O., Reinen, N. M., Troupis, A. T., and Markley, J. L. (2013) [2Fe-2S]-ferredoxin binds directly to cysteine desulfurase and supplies an electron for iron-sulfur cluster assembly but is displaced by the scaffold protein or bacterial frataxin, *J. Am. Chem. Soc. 135*, 8117-8120.

[72] Yan, R., Adinolfi, S., and Pastore, A. (2015) Ferredoxin, in conjunction with NADPH and ferredoxin-NADP reductase, transfers electrons to the IscS/IscU complex to promote iron-sulfur cluster assembly, *Biochim. Biophys. Acta 1854*, 1113-1117.

[73] Ding, H., Clark, R. J., and Ding, B. (2004) IscA mediates iron delivery for assembly of iron-sulfur clusters in IscU under the limited accessible free iron conditions, *J. Biol. Chem. 279,* 37499-37504.

[74] Ding, H., Yang, J., Coleman, L. C., and Yeung, S. (2007) Distinct iron binding property of two putative iron donors for the iron-sulfur cluster assembly: IscA and the bacterial frataxin ortholog CyaY under physiological and oxidative stress conditions, *J. Biol. Chem. 282,* 7997-8004.

[75] Ding, H., and Clark, R. J. (2004) Characterization of iron binding in IscA, an ancient iron-sulphur cluster assembly protein, *Biochem. J 379,* 433-440.

[76] Ollagnier-de-Choudens, S., Mattioli, T., Takahashi, Y., and Fontecave, M. (2001) Iron-sulfur cluster assembly: characterization of IscA and evidence for a specific and functional complex with ferredoxin, *J. Biol. Chem. 276*, 22604-22607.

[77] Krebs, C., Agar, J. N., Smith, A. D., Frazzon, J., Dean, D. R., Huynh, B. H., and Johnson, M. K. (2001) IscA, an alternate scaffold for Fe-S cluster biosynthesis, *Biochemistry 40*, 14069-14080.

[78] Cupp-Vickery, J. R., Silberg, J. J., Ta, D. T., and Vickery, L. E. (2004) Crystal structure of IscA, an iron-sulfur cluster assembly protein from Escherichia coli, *J. Mol. Biol. 338*, 127-137.

[79] Pastore, C., Adinolfi, S., Huynen, M. A., Rybin, V., Martin, S., Mayer, M., Bukau, B., and Pastore, A. (2006) YfhJ, a molecular adaptor in iron-sulfur cluster formation or a frataxin-like protein?, *Structure 14*, 857-867.

[80] Kim, J. H., Bothe, J. R., Frederick, R. O., Holder, J. C., and Markley, J. L. (2014) Role of IscX in iron-sulfur cluster biogenesis in Escherichia coli, *J. Am. Chem. Soc. 136*, 7933-7942.

[81] Hoff, K. G., Cupp-Vickery, J. R., and Vickery, L. E. (2003) Contributions of the LPPVK motif of the iron-sulfur template protein IscU to interactions with the Hsc66-Hsc20 chaperone system, *J. Biol. Chem. 278*, 37582-37589.

[82] Silberg, J. J., Tapley, T. L., Hoff, K. G., and Vickery, L. E. (2004) Regulation of the HscA ATPase reaction cycle by the co-chaperone HscB and the iron-sulfur cluster assembly protein IscU, *J. Biol. Chem. 279*, 53924-53931.

[83] Chandramouli, K., and Johnson, M. K. (2006) HscA and HscB stimulate [2Fe-2S] cluster transfer from IscU to apoferredoxin in an ATP-dependent reaction, *Biochemistry 45*, 11087-11095.

[84] Layer, G., Ollagnier-de Choudens, S., Sanakis, Y., and Fontecave, M. (2006) Iron-sulfur cluster biosynthesis: characterization of Escherichia coli CYaY as an iron donor for the assembly of [2Fe-2S] clusters in the scaffold IscU, *J. Biol. Chem. 281*, 16256-16263.

[85] Shi, R., Proteau, A., Villarroya, M., Moukadiri, I., Zhang, L., Trempe, J. F., Matte, A., Armengod, M. E., and Cygler, M. (2010) Structural basis for Fe-S cluster assembly and tRNA thiolation mediated by IscS protein-protein interactions, *PLoS Biol. 8*, e1000354.

[86] Adinolfi, S., Iannuzzi, C., Prischi, F., Pastore, C., Iametti, S., Martin, S. R., Bonomi, F., and Pastore, A. (2009) Bacterial frataxin CyaY is the gatekeeper of iron-sulfur cluster formation catalyzed by IscS, *Nat. Struct. Mol. Biol. 16*, 390-396.

[87] Bridwell-Rabb, J., Iannuzzi, C., Pastore, A., and Barondeau, D. P. (2012) Effector role reversal during evolution: the case of frataxin in Fe-S cluster biosynthesis, *Biochemistry 51*, 2506-2514.

[88] Patzer, S. I., and Hantke, K. (1999) SufS is a NifS-like protein, and SufD is necessary for stability of the [2Fe-2S] FhuF protein in Escherichia coli, *J. Bacteriol. 181*, 3307-3309.

[89] Tirupati, B., Vey, J. L., Drennan, C. L., and Bollinger, J. M., Jr. (2004) Kinetic and structural characterization of Slr0077/SufS, the essential cysteine desulfurase from Synechocystis sp. PCC 6803, *Biochemistry 43*, 12210-12219.

[90] Dunkle, J. A., Bruno, M. R., Outten, F. W., and Frantom, P. A. (2019) Structural Evidence for Dimer-Interface-Driven Regulation of the Type II Cysteine Desulfurase, SufS, *Biochemistry 58*, 687-696.

[91] Takahashi, Y., and Tokumoto, U. (2002) A third bacterial system for the assembly of iron-sulfur clusters with homologs in archaea and plastids, *J. Biol. Chem. 277*, 28380-28383.

[92] Yeo, W. S., Lee, J. H., Lee, K. C., and Roe, J. H. (2006) IscR acts as an activator in response to oxidative stress for the suf operon encoding Fe-S assembly proteins, *Mol. Microbiol. 61*, 206-218.

[93] Layer, G., Gaddam, S. A., Ayala-Castro, C. N., Ollagnier-de Choudens, S., Lascoux, D., Fontecave, M., and Outten, F. W. (2007) SufE transfers sulfur from SufS to SufB for iron-sulfur cluster assembly, *J. Biol. Chem. 282*, 13342-13350.

[94] Singh, H., Dai, Y., Outten, F. W., and Busenlehner, L. S. (2013) Escherichia coli SufE sulfur transfer protein modulates the SufS cysteine desulfurase through allosteric conformational dynamics, *J. Biol. Chem. 288*, 36189-36200.

[95] Wollers, S., Layer, G., Garcia-Serres, R., Signor, L., Clemancey, M., Latour, J. M., Fontecave, M., and Ollagnier de Choudens, S. (2010) Iron-sulfur (Fe-S) cluster assembly: the SufBCD complex is a new type of Fe-S scaffold with a flavin redox cofactor, *J. Biol. Chem. 285*, 23331-23341.

[96] Chahal, H. K., Dai, Y., Saini, A., Ayala-Castro, C., and Outten, F. W. (2009) The SufBCD Fe-S scaffold complex interacts with SufA for Fe-S cluster transfer, *Biochemistry 48*, 10644-10653.

[97] Strain, J., Lorenz, C. R., Bode, J., Garland, S., Smolen, G. A., Ta, D. T., Vickery, L. E., and Culotta, V. C. (1998) Suppressors of superoxide dismutase (SOD1) deficiency in Saccharomyces cerevisiae. Identification of proteins predicted to mediate iron-sulfur cluster assembly, *J. Biol. Chem. 273*, 31138-31144.

[98] Li, J., Kogan, M., Knight, S. A., Pain, D., and Dancis, A. (1999) Yeast mitochondrial protein, Nfs1p, coordinately regulates iron-sulfur cluster proteins, cellular iron uptake, and iron distribution, *J. Biol. Chem. 274*, 33025-33034.

[99] Kispal, G., Csere, P., Prohl, C., and Lill, R. (1999) The mitochondrial proteins Atm1p and Nfs1p are essential for biogenesis of cytosolic Fe/S proteins, *EMBO J. 18*, 3981-3989.

[100] Braymer, J. J., and Lill, R. (2017) Iron-sulfur cluster biogenesis and trafficking in mitochondria, *J. Biol. Chem. 292*, 12754-12763.

[101] Lill, R., and Kispal, G. (2000) Maturation of cellular Fe–S proteins: an essential function of mitochondria, *Trends Biochem. Sci 25*, 352-356.

[102] Sheftel, A. D., Wilbrecht, C., Stehling, O., Niggemeyer, B., Elsasser, H. P., Muhlenhoff, U., and Lill, R. (2012) The human mitochondrial ISCA1, ISCA2, and IBA57 proteins are required for [4Fe-4S] protein maturation, *Mol Biol Cell 23*, 1157-1166.

[103] Muhlenhoff, U., Richter, N., Pines, O., Pierik, A. J., and Lill, R. (2011) Specialized function of yeast Isa1 and Isa2 proteins in the maturation of mitochondrial [4Fe-4S] proteins, *J. Biol. Chem. 286*, 41205-41216.

[104] Land, T., and Rouault, T. A. (1998) Targeting of a human iron-sulfur cluster assembly enzyme, nifs, to different subcellular compartments is regulated through alternative AUG utilization, *Mol Cell 2*, 807-815.

[105] Biederbick, A., Stehling, O., Rosser, R., Niggemeyer, B., Nakai, Y., Elsasser, H. P., and Lill, R. (2006) Role of human mitochondrial Nfs1 in cytosolic iron-sulfur protein biogenesis and iron regulation, *Mol Cell Biol 26*, 5675-5687.

[106] Behshad, E., and Bollinger, J. M., Jr. (2009) Kinetic analysis of cysteine desulfurase CD0387 from Synechocystis sp. PCC 6803: formation of the persulfide intermediate, *Biochemistry 48*, 12014-12023.

[107] Behshad, E., Parkin, S. E., and Bollinger, J. M., Jr. (2004) Mechanism of cysteine desulfurase Slr0387 from Synechocystis sp. PCC 6803: kinetic analysis of cleavage of the persulfide intermediate by chemical reductants, *Biochemistry 43*, 12220-12226.

[108] Yan, R., Friemel, M., Aloisi, C., Huynen, M., Taylor, I. A., Leimkuhler, S., and Pastore, A. (2016) The Eukaryotic-Specific ISD11 Is a Complex-Orphan Protein with Ability to Bind the Prokaryotic IscS, *PLoS One 11*, e0157895.

[109] Cai, K., Frederick, R. O., Tonelli, M., and Markley, J. L. (2017) Mitochondrial Cysteine Desulfurase and ISD11 Coexpressed in Escherichia coli Yield Complex Containing Acyl Carrier Protein, *ACS Chem. Biol. 12*, 918-921.

[110] Cupp-Vickery, J. R., Urbina, H., and Vickery, L. E. (2003) Crystal structure of IscS, a cysteine desulfurase from Escherichia coli, *J. Mol. Biol. 330*, 1049-1059.

[111] Marelja, Z., Stocklein, W., Nimtz, M., and Leimkuhler, S. (2008) A novel role for human Nfs1 in the cytoplasm: Nfs1 acts as a sulfur donor for MOCS3, a protein involved in molybdenum cofactor biosynthesis, *J. Biol. Chem. 283*, 25178-25185.

[112] Adam, A. C., Bornhovd, C., Prokisch, H., Neupert, W., and Hell, K. (2006) The Nfs1 interacting protein Isd11 has an essential role in Fe/S cluster biogenesis in mitochondria, *EMBO J. 25*, 174-183.

[113] Lim, S. C., Friemel, M., Marum, J. E., Tucker, E. J., Bruno, D. L., Riley, L. G., Christodoulou, J., Kirk, E. P., Boneh, A., DeGennaro, C. M., Springer, M., Mootha, V. K., Rouault, T. A., Leimkuhler, S., Thorburn, D. R., and Compton, A. G. (2013) Mutations in LYRM4, encoding iron-sulfur cluster biogenesis factor ISD11, cause deficiency of multiple respiratory chain complexes, *Hum. Mol. Genet. 22*, 4460-4473.

[114] Friemel, M., Marelja, Z., Li, K., and Leimkuhler, S. (2017) The N-Terminus of Iron-Sulfur Cluster Assembly Factor ISD11 Is Crucial for Subcellular Targeting and Interaction with l-Cysteine Desulfurase NFS1, *Biochemistry 56*, 1797-1808.

[115] Richards, T. A., and van der Giezen, M. (2006) Evolution of the Isd11-IscS complex reveals a single alpha-proteobacterial endosymbiosis for all eukaryotes, *Mol Biol Evol 23*, 1341-1344.

[116] Shi, Y., Ghosh, M. C., Tong, W. H., and Rouault, T. A. (2009) Human ISD11 is essential for both iron-sulfur cluster assembly and maintenance of normal cellular iron homeostasis, *Hum. Mol. Genet. 18*, 3014-3025.

[117] Wiedemann, N., Urzica, E., Guiard, B., Muller, H., Lohaus, C., Meyer, H. E., Ryan, M. T., Meisinger, C., Muhlenhoff, U., Lill, R., and Pfanner, N. (2006)

Essential role of Isd11 in mitochondrial iron-sulfur cluster synthesis on Isu scaffold proteins, *EMBO J. 25*, 184-195.

[118] Tsai, C. L., and Barondeau, D. P. (2010) Human frataxin is an allosteric switch that activates the Fe-S cluster biosynthetic complex, *Biochemistry 49*, 9132-9139.

[119] Saha, P. P., Srivastava, S., Kumar, S. K. P., Sinha, D., and D'Silva, P. (2015) Mapping Key Residues of ISD11 Critical for NFS1-ISD11 Subcomplex Stability: Implications in the Development of Mitochondrial Disorder, COXPD19, *J. Biol. Chem. 290*, 25876-25890.

[120] Pandey, A., Golla, R., Yoon, H., Dancis, A., and Pain, D. (2012) Persulfide formation on mitochondrial cysteine desulfurase: enzyme activation by a eukaryote-specific interacting protein and Fe-S cluster synthesis, *Biochem. J 448*, 171-187.

[121] Cory, S. A., Van Vranken, J. G., Brignole, E. J., Patra, S., Winge, D. R., Drennan, C. L., Rutter, J., and Barondeau, D. P. (2017) Structure of human Fe-S assembly subcomplex reveals unexpected cysteine desulfurase architecture and acyl-ACP-ISD11 interactions, *Proc. Natl. Acad. Sci. U.S.A. 114*, E5325-E5334.

[122] Boniecki, M. T., Freibert, S. A., Muhlenhoff, U., Lill, R., and Cygler, M. (2017) Structure and functional dynamics of the mitochondrial Fe/S cluster synthesis complex, *Nat. Commun. 8*, 1287.

[123] Hiltunen, J. K., Autio, K. J., Schonauer, M. S., Kursu, V. A., Dieckmann, C. L., and Kastaniotis, A. J. (2010) Mitochondrial fatty acid synthesis and respiration, *Biochim. Biophys. Acta 1797*, 1195-1202.

[124] Brody, S., Oh, C. K., Hoja, U., and Schweizer, E. (1997) Mitochondrial acyl carrier protein is involved in lipoic acid synthesis in Saccharomyces cerevisiae, *FEBS Lett. 408*, 217-220.

[125] Feng, D., Witkowski, A., and Smith, S. (2009) Down-regulation of mitochondrial acyl carrier protein in mammalian cells compromises protein lipoylation and respiratory complex I and results in cell death, *J. Biol. Chem. 284*, 11436-11445.

[126] Majmudar, J. D., Feng, X., Fox, N. G., Nabhan, J. F., Towle, T., Ma, T., Gooch, R., Bulawa, C., Yue, W. W., and Martelli, A. (2019) 4'-Phosphopantetheine and long acyl chain-dependent interactions are integral to human mitochondrial acyl carrier protein function, *Medchemcomm 10*, 209-220.

[127] Zhang, L., Joshi, A. K., Hofmann, J., Schweizer, E., and Smith, S. (2005) Cloning, expression, and characterization of the human mitochondrial beta-ketoacyl synthase. Complementation of the yeast CEM1 knock-out strain, *J. Biol. Chem. 280*, 12422-12429.

[128] Kursu, V. A., Pietikainen, L. P., Fontanesi, F., Aaltonen, M. J., Suomi, F., Raghavan Nair, R., Schonauer, M. S., Dieckmann, C. L., Barrientos, A., Hiltunen, J. K., and Kastaniotis, A. J. (2013) Defects in mitochondrial fatty acid synthesis result in failure of multiple aspects of mitochondrial biogenesis in Saccharomyces cerevisiae, *Mol. Microbiol. 90*, 824-840.

[129] Van Vranken, J. G., Jeong, M. Y., Wei, P., Chen, Y. C., Gygi, S. P., Winge, D. R., and Rutter, J. (2016) The mitochondrial acyl carrier protein (ACP) coordinates mitochondrial fatty acid synthesis with iron sulfur cluster biogenesis, *Elife 5*.

[130] Angerer, H. (2015) Eukaryotic LYR Proteins Interact with Mitochondrial Protein Complexes, *Biology (Basel) 4*, 133-150.

[131] Zhu, J., King, M. S., Yu, M., Klipcan, L., Leslie, A. G., and Hirst, J. (2015) Structure of subcomplex Ibeta of mammalian respiratory complex I leads to new supernumerary subunit assignments, *Proc. Natl. Acad. Sci. U.S.A. 112*, 12087-12092.

[132] Angerer, H., Radermacher, M., Mankowska, M., Steger, M., Zwicker, K., Heide, H., Wittig, I., Brandt, U., and Zickermann, V. (2014) The LYR protein subunit NB4M/NDUFA6 of mitochondrial complex I anchors an acyl carrier protein and is essential for catalytic activity, *Proc. Natl. Acad. Sci. U.S.A. 111*, 5207-5212.

[133] Fiedorczuk, K., Letts, J. A., Degliesposti, G., Kaszuba, K., Skehel, M., and Sazanov, L. A. (2016) Atomic structure of the entire mammalian mitochondrial complex I, *Nature 538*, 406-410.

[134] Huttlin, E. L., Bruckner, R. J., Paulo, J. A., Cannon, J. R., Ting, L., Baltier, K., Colby, G., Gebreab, F., Gygi, M. P., Parzen, H., Szpyt, J., Tam, S., Zarraga, G., Pontano-Vaites, L., Swarup, S., White, A. E., Schweppe, D. K., Rad, R., Erickson, B. K., Obar, R. A., Guruharsha, K. G., Li, K., Artavanis-Tsakonas, S., Gygi, S. P., and Harper, J. W. (2017) Architecture of the human interactome defines protein communities and disease networks, *Nature 545*, 505-509.

[135] Floyd, B. J., Wilkerson, E. M., Veling, M. T., Minogue, C. E., Xia, C., Beebe, E. T., Wrobel, R. L., Cho, H., Kremer, L. S., Alston, C. L., Gromek, K. A., Dolan, B. K., Ulbrich, A., Stefely, J. A., Bohl, S. L., Werner, K. M., Jochem, A., Westphall, M. S., Rensvold, J. W., Taylor, R. W., Prokisch, H., Kim, J. P., Coon, J. J., and Pagliarini, D. J. (2016) Mitochondrial Protein Interaction Mapping Identifies Regulators of Respiratory Chain Function, *Mol Cell 63*, 621-632.

[136] Huttlin, E. L., Ting, L., Bruckner, R. J., Gebreab, F., Gygi, M. P., Szpyt, J., Tam, S., Zarraga, G., Colby, G., Baltier, K., Dong, R., Guarani, V., Vaites, L. P., Ordureau, A., Rad, R., Erickson, B. K., Wuhr, M., Chick, J., Zhai, B., Kolippakkam, D., Mintseris, J., Obar, R. A., Harris, T., Artavanis-Tsakonas, S., Sowa, M. E., De Camilli, P., Paulo, J. A., Harper, J. W., and Gygi, S. P. (2015) The BioPlex Network: A Systematic Exploration of the Human Interactome, *Cell 162*, 425-440.

[137] Brody, S., and Mikolajczyk, S. (1988) Neurospora mitochondria contain an acyl-carrier protein, *Eur. J. Biochem. 173*, 353-359.

[138] Carroll, J., Fearnley, I. M., Shannon, R. J., Hirst, J., and Walker, J. E. (2003) Analysis of the subunit composition of complex I from bovine heart mitochondria, *Mol Cell Proteomics 2*, 117-126.

[139] Angerer, H., Schonborn, S., Gorka, J., Bahr, U., Karas, M., Wittig, I., Heidler, J., Hoffmann, J., Morgner, N., and Zickermann, V. (2017) Acyl modification and binding of mitochondrial ACP to multiprotein complexes, *Biochim Biophys Acta Mol Cell Res 1864*, 1913-1920.

[140] Herrera, M. G., Pignataro, M. F., Noguera, M. E., Cruz, K. M., and Santos, J. (2018) Rescuing the Rescuer: On the Protein Complex between the Human Mitochondrial Acyl Carrier Protein and ISD11, *ACS Chem. Biol. 13*, 1455-1462.

[141] Gully, D., Moinier, D., Loiseau, L., and Bouveret, E. (2003) New partners of acyl carrier protein detected in Escherichia coli by tandem affinity purification, *FEBS Lett. 548*, 90-96.

[142] Song, J. Y., Marszalek, J., and Craig, E. A. (2012) Cysteine desulfurase Nfs1 and Pim1 protease control levels of Isu, the Fe-S cluster biogenesis scaffold, *Proc. Natl. Acad. Sci. U.S.A. 109*, 10370-10375.

[143] Fox, N. G., Yu, X., Feng, X., Bailey, H. J., Martelli, A., Nabhan, J. F., Strain-Damerell, C., Bulawa, C., Yue, W. W., and Han, S. (2019) Structure of the human frataxin-bound iron-sulfur cluster assembly complex provides insight into its activation mechanism, *Nat. Commun. 10*, 2210.

[144] Bridwell-Rabb, J., Fox, N. G., Tsai, C. L., Winn, A. M., and Barondeau, D. P. (2014) Human frataxin activates Fe-S cluster biosynthesis by facilitating sulfur transfer chemistry, *Biochemistry 53*, 4904-4913.

[145] Parent, A., Elduque, X., Cornu, D., Belot, L., Le Caer, J. P., Grandas, A., Toledano, M. B., and D'Autreaux, B. (2015) Mammalian frataxin directly enhances sulfur transfer of NFS1 persulfide to both ISCU and free thiols, *Nat. Commun. 6*.

[146] Kato, S., Mihara, H., Kurihara, T., Takahashi, Y., Tokumoto, U., Yoshimura, T., and Esaki, N. (2002) Cys-328 of IscS and Cys-63 of IscU are the sites of disulfide bridge formation in a covalently bound IscS/IscU complex: implications for the mechanism of iron-sulfur cluster assembly, *Proc. Natl. Acad. Sci. U.S.A. 99*, 5948-5952.

[147] Cook, J. D., Kondapalli, K. C., Rawat, S., Childs, W. C., Murugesan, Y., Dancis, A., and Stemmler, T. L. (2010) Molecular details of the yeast frataxin-Isu1 interaction during mitochondrial Fe-S cluster assembly, *Biochemistry 49*, 8756-8765.

[148] Fox, N. G., Das, D., Chakrabarti, M., Lindahl, P. A., and Barondeau, D. P. (2015) Frataxin Accelerates [2Fe-2S] Cluster Formation on the Human Fe-S Assembly Complex, *Biochemistry 54*, 3880-3889.

[149] Colin, F., Martelli, A., Clemancey, M., Latour, J. M., Gambarelli, S., Zeppieri, L., Birck, C., Page, A., Puccio, H., and Ollagnier de Choudens, S. (2013) Mammalian frataxin controls sulfur production and iron entry during de novo Fe4S4 cluster assembly*, J. Am. Chem. Soc. 135*, 733-740.

[150] Fox, N. G., Chakrabarti, M., McCormick, S. P., Lindahl, P. A., and Barondeau, D. P. (2015) The Human Iron-Sulfur Assembly Complex Catalyzes the Synthesis of [2Fe-2S] Clusters on ISCU2 That Can Be Transferred to Acceptor Molecules, *Biochemistry 54*, 3871-3879.

[151] Shi, Y., Ghosh, M., Kovtunovych, G., Crooks, D. R., and Rouault, T. A. (2012) Both human ferredoxins 1 and 2 and ferredoxin reductase are important for iron-sulfur cluster biogenesis, *Biochim. Biophys. Acta 1823*, 484-492.

[152] Cai, K., Tonelli, M., Frederick, R. O., and Markley, J. L. (2017) Human Mitochondrial Ferredoxin 1 (FDX1) and Ferredoxin 2 (FDX2) Both Bind Cysteine Desulfurase and Donate Electrons for Iron-Sulfur Cluster Biosynthesis, *Biochemistry 56*, 487-499.

[153] Tsvetkov, P., Detappe, A., Cai, K., Keys, H. R., Brune, Z., Ying, W., Thiru, P., Reidy, M., Kugener, G., Rossen, J., Kocak, M., Kory, N., Tsherniak, A., Santagata, S., Whitesell, L., Ghobrial, I. M., Markley, J. L., Lindquist, S., and Golub, T. R. (2019) Mitochondrial metabolism promotes adaptation to proteotoxic stress, *Nat. Chem. Biol. 15*, 681-689.

[154] Webert, H., Freibert, S. A., Gallo, A., Heidenreich, T., Linne, U., Amlacher, S., Hurt, E., Muhlenhoff, U., Banci, L., and Lill, R. (2014) Functional reconstitution of mitochondrial Fe/S cluster synthesis on Isu1 reveals the involvement of ferredoxin, *Nat. Commun. 5*, 5013.

[155] Cai, K., Frederick, R. O., Tonelli, M., and Markley, J. L. (2018) ISCU(M108I) and ISCU(D39V) Differ from Wild-Type ISCU in Their Failure To Form Cysteine Desulfurase Complexes Containing Both Frataxin and Ferredoxin, *Biochemistry 57*, 1491-1500.

[156] Priller, J., Scherzer, C. R., Faber, P. W., MacDonald, M. E., and Young, A. B. (1997) Frataxin gene of Friedreich's ataxia is targeted to mitochondria, *Ann Neurol 42*, 265-269.

[157] Babcock, M., de Silva, D., Oaks, R., Davis-Kaplan, S., Jiralerspong, S., Montermini, L., Pandolfo, M., and Kaplan, J. (1997) Regulation of mitochondrial iron accumulation by Yfh1p, a putative homolog of frataxin, *Science 276*, 1709-1712.

[158] Campuzano, V., Montermini, L., Molto, M. D., Pianese, L., Cossee, M., Cavalcanti, F., Monros, E., Rodius, F., Duclos, F., Monticelli, A., Zara, F., Canizares, J., Koutnikova, H., Bidichandani, S. I., Gellera, C., Brice, A., Trouillas, P., De Michele, G., Filla, A., De Frutos, R., Palau, F., Patel, P. I., Di Donato, S., Mandel, J. L., Cocozza, S., Koenig, M., and Pandolfo, M. (1996) Friedreich's ataxia: autosomal recessive disease caused by an intronic GAA triplet repeat expansion, *Science 271*, 1423-1427.

[159] Schmucker, S., and Puccio, H. (2010) Understanding the molecular mechanisms of Friedreich's ataxia to develop therapeutic approaches, *Hum. Mol. Genet. 19*, R103-110.

[160] Seguin, A., Sutak, R., Bulteau, A. L., Garcia-Serres, R., Oddou, J. L., Lefevre, S., Santos, R., Dancis, A., Camadro, J. M., Latour, J. M., and Lesuisse, E. (2010) Evidence that yeast frataxin is not an iron storage protein in vivo, *Biochim. Biophys. Acta 1802*, 531-538.

[161] Cavadini, P., Adamec, J., Taroni, F., Gakh, O., and Isaya, G. (2000) Two-step processing of human frataxin by mitochondrial processing peptidase. Precursor and intermediate forms are cleaved at different rates, *J. Biol. Chem. 275*, 41469-41475.

[162] Schmucker, S., Argentini, M., Carelle-Calmels, N., Martelli, A., and Puccio, H. (2008) The in vivo mitochondrial two-step maturation of human frataxin, *Hum. Mol. Genet. 17*, 3521-3531.

[163] Schmucker, S., Martelli, A., Colin, F., Page, A., Wattenhofer-Donze, M., Reutenauer, L., and Puccio, H. (2011) Mammalian frataxin: an essential function for cellular viability through an interaction with a preformed ISCU/NFS1/ISD11 iron-sulfur assembly complex, *PLoS One 6*, e16199.

[164] Yoon, T., and Cowan, J. A. (2003) Iron-sulfur cluster biosynthesis. Characterization of frataxin as an iron donor for assembly of [2Fe-2S] clusters in ISU-type proteins, *J. Am. Chem. Soc. 125*, 6078-6084.

[165] Ahlgren, E. C., Fekry, M., Wiemann, M., Soderberg, C. A., Bernfur, K., Gakh, O., Rasmussen, M., Hojrup, P., Emanuelsson, C., Isaya, G., and Al-Karadaghi, S. (2017) Iron-induced oligomerization of human FXN81-210 and bacterial CyaY frataxin and the effect of iron chelators, *PLoS One 12*, e0188937.

[166] Manicki, M., Majewska, J., Ciesielski, S., Schilke, B., Blenska, A., Kominek, J., Marszalek, J., Craig, E. A., and Dutkiewicz, R. (2014) Overlapping binding sites of the frataxin homologue assembly factor and the heat shock protein 70 transfer factor on the Isu iron-sulfur cluster scaffold protein, *J. Biol. Chem. 289*, 30268-30278.

[167] Muhlenhoff, U., Richhardt, N., Ristow, M., Kispal, G., and Lill, R. (2002) The yeast frataxin homolog Yfh1p plays a specific role in the maturation of cellular Fe/S proteins, *Hum. Mol. Genet. 11*, 2025-2036.

[168] Stehling, O., Elsasser, H. P., Bruckel, B., Muhlenhoff, U., and Lill, R. (2004) Iron-sulfur protein maturation in human cells: evidence for a function of frataxin, *Hum. Mol. Genet. 13*, 3007-3015.

[169] Pandey, A., Gordon, D. M., Pain, J., Stemmler, T. L., Dancis, A., and Pain, D. (2013) Frataxin directly stimulates mitochondrial cysteine desulfurase by exposing substrate-binding sites, and a mutant Fe-S cluster scaffold protein with frataxin-bypassing ability acts similarly, *J. Biol. Chem. 288*, 36773-36786.

[170] Turowski, V. R., Busi, M. V., and Gomez-Casati, D. F. (2012) Structural and functional studies of the mitochondrial cysteine desulfurase from Arabidopsis thaliana, *Mol Plant 5*, 1001-1010.

[171] Das, D., Patra, S., Bridwell-Rabb, J., and Barondeau, D. P. (2019) Mechanism of frataxin "bypass" in human iron-sulfur cluster biosynthesis with implications for Friedreich's ataxia, *J. Biol. Chem. 294*, 9276-9284.

[172] Bridwell-Rabb, J., Winn, A. M., and Barondeau, D. P. (2011) Structure-function analysis of Friedreich's ataxia mutants reveals determinants of frataxin binding and activation of the Fe-S assembly complex, *Biochemistry 50*, 7265-7274.

[173] Tsai, C. L., Bridwell-Rabb, J., and Barondeau, D. P. (2011) Friedreich's ataxia variants I154F and W155R diminish frataxin-based activation of the iron-sulfur cluster assembly complex, *Biochemistry 50*, 6478-6487.

[174] Kim, K. S., Maio, N., Singh, A., and Rouault, T. A. (2018) Cytosolic HSC20 integrates de novo iron-sulfur cluster biogenesis with the CIAO1-mediated transfer to recipients, *Hum. Mol. Genet. 27*, 837-852.

[175] Pandey, A., Pain, J., Dziuba, N., Pandey, A. K., Dancis, A., Lindahl, P. A., and Pain, D. (2018) Mitochondria Export Sulfur Species Required for Cytosolic tRNA Thiolation, *Cell Chem Biol 25*, 738-748 e733.

[176] Pandey, A. K., Pain, J., Dancis, A., and Pain, D. (2019) Mitochondria export iron-sulfur and sulfur intermediates to the cytoplasm for iron-sulfur cluster assembly and tRNA thiolation in yeast, *J. Biol. Chem. 294*, 9489-9502.

[177] Sharma, A. K., Pallesen, L. J., Spang, R. J., and Walden, W. E. (2010) Cytosolic iron-sulfur cluster assembly (CIA) system: factors, mechanism, and relevance to cellular iron regulation, *J. Biol. Chem. 285*, 26745-26751.

[178] Van Vranken, J. G., Nowinski, S. M., Clowers, K. J., Jeong, M. Y., Ouyang, Y., Berg, J. A., Gygi, J. P., Gygi, S. P., Winge, D. R., and Rutter, J. (2018) ACP Acylation Is an Acetyl-CoA-Dependent Modification Required for Electron Transport Chain Assembly, *Mol Cell 71*, 567-580 e564.

[179] Rocha, A. G., Knight, S. A. B., Pandey, A., Yoon, H., Pain, J., Pain, D., and Dancis, A. (2018) Cysteine desulfurase is regulated by phosphorylation of Nfs1 in yeast mitochondria, *Mitochondrion 40*, 29-41.

[180] Roche, B., Aussel, L., Ezraty, B., Mandin, P., Py, B., and Barras, F. (2013) Iron/sulfur proteins biogenesis in prokaryotes: formation, regulation and diversity, *Biochim. Biophys. Acta 1827*, 455-469.

[181] Terali, K., Beavil, R. L., Pickersgill, R. W., and van der Giezen, M. (2013) The effect of the adaptor protein Isd11 on the quaternary structure of the eukaryotic cysteine desulphurase Nfs1, *Biochem. Biophys. Res. Commun. 440*, 235-240.

[182] Maio, N., Singh, A., Uhrigshardt, H., Saxena, N., Tong, W. H., and Rouault, T. A. (2014) Cochaperone binding to LYR motifs confers specificity of iron sulfur cluster delivery, *Cell Metab 19*, 445-457.

[183] Krogan, N. J., Cagney, G., Yu, H., Zhong, G., Guo, X., Ignatchenko, A., Li, J., Pu, S., Datta, N., Tikuisis, A. P., Punna, T., Peregrin-Alvarez, J. M., Shales, M., Zhang, X., Davey, M., Robinson, M. D., Paccanaro, A., Bray, J. E., Sheung, A., Beattie, B., Richards, D. P., Canadien, V., Lalev, A., Mena, F., Wong, P., Starostine, A., Canete, M. M., Vlasblom, J., Wu, S., Orsi, C., Collins, S. R., Chandran, S., Haw, R., Rilstone, J. J., Gandi, K., Thompson, N. J., Musso, G., St Onge, P., Ghanny, S., Lam, M. H., Butland, G., Altaf-Ul, A. M., Kanaya, S., Shilatifard, A., O'Shea, E., Weissman, J. S., Ingles, C. J., Hughes, T. R., Parkinson, J., Gerstein, M., Wodak, S. J., Emili, A., and Greenblatt, J. F. (2006) Global landscape of protein complexes in the yeast Saccharomyces cerevisiae, *Nature 440*, 637-643.

[184] Hiltunen, J. K., Schonauer, M. S., Autio, K. J., Mittelmeier, T. M., Kastaniotis, A. J., and Dieckmann, C. L. (2009) Mitochondrial fatty acid synthesis type II: more than just fatty acids, *J. Biol. Chem. 284*, 9011-9015.

[185] Runswick, M. J., Fearnley, I. M., Skehel, J. M., and Walker, J. E. (1991) Presence of an acyl carrier protein in NADH:ubiquinone oxidoreductase from bovine heart mitochondria, *FEBS Lett. 286*, 121-124.

[186] Sackmann, U., Zensen, R., Rohlen, D., Jahnke, U., and Weiss, H. (1991) The acyl-carrier protein in Neurospora crassa mitochondria is a subunit of NADH:ubiquinone reductase (complex I), *Eur. J. Biochem. 200*, 463-469.

[187] Vinothkumar, K. R., Zhu, J., and Hirst, J. (2014) Architecture of mammalian respiratory complex I, *Nature 515*, 80-84.

[188] Lill, R., and Muhlenhoff, U. (2008) Maturation of iron-sulfur proteins in eukaryotes: mechanisms, connected processes, and diseases, *Annu. Rev. Biochem 77*, 669-700.

[189] Rouault, T. A. (2015) Mammalian iron-sulphur proteins: novel insights into biogenesis and function, *Nat Rev Mol Cell Biol 16*, 45-55.

[190] Nakai, Y., Umeda, N., Suzuki, T., Nakai, M., Hayashi, H., Watanabe, K., and Kagamiyama, H. (2004) Yeast Nfs1p is involved in thio-modification of both mitochondrial and cytoplasmic tRNAs, *J. Biol. Chem. 279*, 12363-12368.

[191] Farhan, S. M., Wang, J., Robinson, J. F., Lahiry, P., Siu, V. M., Prasad, C., Kronick, J. B., Ramsay, D. A., Rupar, C. A., and Hegele, R. A. (2014) Exome sequencing identifies NFS1 deficiency in a novel Fe-S cluster disease, infantile mitochondrial complex II/III deficiency, *Mol Genet Genomic Med 2*, 73-80.

[192] Olsson, A., Lind, L., Thornell, L. E., and Holmberg, M. (2008) Myopathy with lactic acidosis is linked to chromosome 12q23.3-24.11 and caused by an intron mutation in the ISCU gene resulting in a splicing defect, *Hum. Mol. Genet. 17*, 1666-1672.

[193] Marinoni, E. N., de Oliveira, J. S., Nicolet, Y., Raulfs, E. C., Amara, P., Dean, D. R., and Fontecilla-Camps, J. C. (2012) (IscS-IscU)2 complex structures provide insights into Fe2S2 biogenesis and transfer, *Angew. Chem. Int. Ed. Engl. 51*, 5439-5442.

[194] Qiu, X., and Janson, C. A. (2004) Structure of apo acyl carrier protein and a proposal to engineer protein crystallization through metal ions, *Acta Crystallogr D Biol Crystallogr 60*, 1545-1554.

[195] Byers, D. M., and Gong, H. (2007) Acyl carrier protein: structure-function relationships in a conserved multifunctional protein family, *Biochem. Cell Biol. 85*, 649-662.

[196] Agar, J. N., Krebs, C., Frazzon, J., Huynh, B. H., Dean, D. R., and Johnson, M. K. (2000) IscU as a scaffold for iron-sulfur cluster biosynthesis: sequential assembly of [2Fe-2S] and [4Fe-4S] clusters in IscU, *Biochemistry 39*, 7856-7862.

[197] Ghaemmaghami, S., Huh, W. K., Bower, K., Howson, R. W., Belle, A., Dephoure, N., O'Shea, E. K., and Weissman, J. S. (2003) Global analysis of protein expression in yeast, *Nature 425*, 737-741.

[198] Kulak, N. A., Pichler, G., Paron, I., Nagaraj, N., and Mann, M. (2014) Minimal, encapsulated proteomic-sample processing applied to copy-number estimation in eukaryotic cells, *Nat Methods 11*, 319-324.

[199] Hudder, B. N., Morales, J. G., Stubna, A., Munck, E., Hendrich, M. P., and Lindahl, P. A. (2007) Electron paramagnetic resonance and Mossbauer spectroscopy of intact mitochondria from respiring Saccharomyces cerevisiae, *J. Biol. Inorg. Chem. 12*, 1029-1053.

[200] Gakh, O., Ranatunga, W., Smith, D. Y. t., Ahlgren, E. C., Al-Karadaghi, S., Thompson, J. R., and Isaya, G. (2016) Architecture of the Human Mitochondrial Iron-Sulfur Cluster Assembly Machinery, *J. Biol. Chem. 291*, 21296-21321.

[201] Wu, H. Y., Chen, S. F., Hsieh, J. Y., Chou, F., Wang, Y. H., Lin, W. T., Lee, P. Y., Yu, Y. J., Lin, L. Y., Lin, T. S., Lin, C. L., Liu, G. Y., Tzeng, S. R., Hung, H. C., and Chan, N. L. (2015) Structural basis of antizyme-mediated regulation of polyamine homeostasis, *Proc. Natl. Acad. Sci. U.S.A. 112*, 11229-11234.

[202] Na, U., Yu, W., Cox, J., Bricker, D. K., Brockmann, K., Rutter, J., Thummel, C. S., and Winge, D. R. (2014) The LYR factors SDHAF1 and SDHAF3 mediate maturation of the iron-sulfur subunit of succinate dehydrogenase, *Cell Metab 20*, 253-266.

[203] Atkinson, A., Smith, P., Fox, J. L., Cui, T. Z., Khalimonchuk, O., and Winge, D. R. (2011) The LYR protein Mzm1 functions in the insertion of the Rieske Fe/S protein in yeast mitochondria, *Mol Cell Biol 31*, 3988-3996.

[204] Lefebvre-Legendre, L., Vaillier, J., Benabdelhak, H., Velours, J., Slonimski, P. P., and di Rago, J. P. (2001) Identification of a nuclear gene (FMC1) required for the assembly/stability of yeast mitochondrial F(1)-ATPase in heat stress conditions, *J. Biol. Chem. 276*, 6789-6796.

[205] Maio, N., Kim, K. S., Singh, A., and Rouault, T. A. (2017) A Single Adaptable Cochaperone-Scaffold Complex Delivers Nascent Iron-Sulfur Clusters to Mammalian Respiratory Chain Complexes I-III, *Cell Metab 25*, 945-953 e946.

[206] Schonauer, M. S., Kastaniotis, A. J., Hiltunen, J. K., and Dieckmann, C. L. (2008) Intersection of RNA processing and the type II fatty acid synthesis pathway in yeast mitochondria, *Mol Cell Biol 28*, 6646-6657.

[207] Gerhard, D. S., Wagner, L., Feingold, E. A., Shenmen, C. M., Grouse, L. H., Schuler, G., Klein, S. L., Old, S., Rasooly, R., Good, P., Guyer, M., Peck, A. M.,

Derge, J. G., Lipman, D., Collins, F. S., Jang, W., Sherry, S., Feolo, M., Misquitta, L., Lee, E., Rotmistrovsky, K., Greenhut, S. F., Schaefer, C. F., Buetow, K., Bonner, T. I., Haussler, D., Kent, J., Kiekhaus, M., Furey, T., Brent, M., Prange, C., Schreiber, K., Shapiro, N., Bhat, N. K., Hopkins, R. F., Hsie, F., Driscoll, T., Soares, M. B., Casavant, T. L., Scheetz, T. E., Brown-stein, M. J., Usdin, T. B., Toshiyuki, S., Carninci, P., Piao, Y., Dudekula, D. B., Ko, M. S., Kawakami, K., Suzuki, Y., Sugano, S., Gruber, C. E., Smith, M. R., Simmons, B., Moore, T., Waterman, R., Johnson, S. L., Ruan, Y., Wei, C. L., Mathavan, S., Gunaratne, P. H., Wu, J., Garcia, A. M., Hulyk, S. W., Fuh, E., Yuan, Y., Sneed, A., Kowis, C., Hodgson, A., Muzny, D. M., McPherson, J., Gibbs, R. A., Fahey, J., Helton, E., Ketteman, M., Madan, A., Rodrigues, S., Sanchez, A., Whiting, M., Madari, A., Young, A. C., Wetherby, K. D., Granite, S. J., Kwong, P. N., Brinkley, C. P., Pearson, R. L., Bouffard, G. G., Blakesly, R. W., Green, E. D., Dickson, M. C., Rodriguez, A. C., Grimwood, J., Schmutz, J., Myers, R. M., Butterfield, Y. S., Griffith, M., Griffith, O. L., Krzywinski, M. I., Liao, N., Morin, R., Palmquist, D., Petrescu, A. S., Skalska, U., Smailus, D. E., Stott, J. M., Schnerch, A., Schein, J. E., Jones, S. J., Holt, R. A., Baross, A., Marra, M. A., Clifton, S., Makowski, K. A., Bosak, S., Malek, J., and Team, M. G. C. P. (2004) The status, quality, and expansion of the NIH full-length cDNA project: the Mammalian Gene Collection (MGC), *Genome Res 14*, 2121-2127.

[208] Studier, F. W. (2005) Protein production by auto-induction in high density shaking cultures, *Protein Expr Purif 41*, 207-234.

[209] Otwinowski, Z., and Minor, W. (1997) Processing of X-ray diffraction data collected in oscillation mode, *Methods Enzymol. 276*, 307-326.

[210] McCoy, A. J., Grosse-Kunstleve, R. W., Adams, P. D., Winn, M. D., Storoni, L. C., and Read, R. J. (2007) Phaser crystallographic software, *J. Appl. Crystallogr. 40*, 658-674.

[211] Adams, P. D., Afonine, P. V., Bunkoczi, G., Chen, V. B., Davis, I. W., Echols, N., Headd, J. J., Hung, L. W., Kapral, G. J., Grosse-Kunstleve, R. W., McCoy, A. J., Moriarty, N. W., Oeffner, R., Read, R. J., Richardson, D. C., Richardson, J. S., Terwilliger, T. C., and Zwart, P. H. (2010) PHENIX: a comprehensive Python-based system for macromolecular structure solution, *Acta Crystallogr D Biol Crystallogr 66*, 213-221.

[212] Terwilliger, T. (2004) SOLVE and RESOLVE: automated structure solution, density modification and model building, *J Synchrotron Radiat 11*, 49-52.

[213] Afonine, P. V., Grosse-Kunstleve, R. W., Echols, N., Headd, J. J., Moriarty, N. W., Mustyakimov, M., Terwilliger, T. C., Urzhumtsev, A., Zwart, P. H., and Adams, P. D. (2012) Towards automated crystallographic structure refinement with phenix.refine, *Acta Crystallogr D Biol Crystallogr 68*, 352-367.

[214] Headd, J. J., Echols, N., Afonine, P. V., Grosse-Kunstleve, R. W., Chen, V. B., Moriarty, N. W., Richardson, D. C., Richardson, J. S., and Adams, P. D. (2012) Use of knowledge-based restraints in phenix.refine to improve macromolecular refinement at low resolution, *Acta Crystallogr D Biol Crystallogr 68*, 381-390.

[215] Emsley, P., Lohkamp, B., Scott, W. G., and Cowtan, K. (2010) Features and development of Coot, *Acta Crystallogr D Biol Crystallogr 66*, 486-501.

[216] Lebedev, A. A., Young, P., Isupov, M. N., Moroz, O. V., Vagin, A. A., and Murshudov, G. N. (2012) JLigand: a graphical tool for the CCP4 template-restraint library, *Acta Crystallogr D Biol Crystallogr 68*, 431-440.

[217] Moriarty, N. W., Grosse-Kunstleve, R. W., and Adams, P. D. (2009) electronic Ligand Builder and Optimization Workbench (eLBOW): a tool for ligand coordinate and restraint generation, *Acta Crystallogr D Biol Crystallogr 65*, 1074-1080.

[218] Brunger, A. T. (1993) Assessment of phase accuracy by cross validation: the free R value. Methods and applications, *Acta Crystallogr D Biol Crystallogr 49*, 24-36.

[219] The PyMOL Molecular Graphics System, Version 1.3 Schrödinger, LLC.

[220] Davis, I. W., Leaver-Fay, A., Chen, V. B., Block, J. N., Kapral, G. J., Wang, X., Murray, L. W., Arendall, W. B., 3rd, Snoeyink, J., Richardson, J. S., and Richardson, D. C. (2007) MolProbity: all-atom contacts and structure validation for proteins and nucleic acids, *Nucleic Acids Res. 35*, W375-383.

[221] Christie, W. W. (1993) Preparation of ester derivatives of fatty acids for chromatographic analysis, In *Advances in Lipid Methodology - Two* (Christie, W. W., Ed.), pp 69-111, Oily Press, Dundee, Scotland.

[222] Wittig, I., Braun, H. P., and Schagger, H. (2006) Blue native PAGE, *Nat Protoc 1*, 418-428.

[223] Mastronarde, D. N. (2005) Automated electron microscope tomography using robust prediction of specimen movements, *J Struct Biol 152*, 36-51.

[224] Rohou, A., and Grigorieff, N. (2015) CTFFIND4: Fast and accurate defocus estimation from electron micrographs, *J Struct Biol 192*, 216-221.

[225] Scheres, S. H. (2012) RELION: implementation of a Bayesian approach to cryo-EM structure determination, *J Struct Biol 180*, 519-530.

[226] Scheres, S. H. (2015) Semi-automated selection of cryo-EM particles in RELION-1.3, *J Struct Biol 189*, 114-122.

[227] Tang, G., Peng, L., Baldwin, P. R., Mann, D. S., Jiang, W., Rees, I., and Ludtke, S. J. (2007) EMAN2: an extensible image processing suite for electron microscopy, *J Struct Biol 157*, 38-46.

[228] Goddard, T. D., Huang, C. C., and Ferrin, T. E. (2007) Visualizing density maps with UCSF Chimera, *J Struct Biol 157*, 281-287.

[229] Sievers, F., Wilm, A., Dineen, D., Gibson, T. J., Karplus, K., Li, W., Lopez, R., McWilliam, H., Remmert, M., Soding, J., Thompson, J. D., and Higgins, D. G. (2011) Fast, scalable generation of high-quality protein multiple sequence alignments using Clustal Omega, *Mol Syst Biol 7*, 539.

[230] Tamura, K., Stecher, G., Peterson, D., Filipski, A., and Kumar, S. (2013) MEGA6: Molecular Evolutionary Genetics Analysis version 6.0, *Mol Biol Evol 30*, 2725-2729.

[231] Armon, A., Graur, D., and Ben-Tal, N. (2001) ConSurf: an algorithmic tool for the identification of functional regions in proteins by surface mapping of phylogenetic information, *J. Mol. Biol. 307*, 447-463.

[232] Rouault, T. A., and Tong, W. H. (2008) Iron-sulfur cluster biogenesis and human disease, *Trends Genet. 24*, 398-407.

[233] Cai, K., Frederick, R. O., Dashti, H., and Markley, J. L. (2018) Architectural Features of Human Mitochondrial Cysteine Desulfurase Complexes from Crosslinking Mass Spectrometry and Small-Angle X-Ray Scattering, *Structure 26*, 1127-1136 e1124.

[234] Rambo, R. P., and Tainer, J. A. (2013) Accurate assessment of mass, models and resolution by small-angle scattering, *Nature 496*, 477-481.

[235] Valentini, E., Kikhney, A. G., Previtali, G., Jeffries, C. M., and Svergun, D. I. (2015) SASBDB, a repository for biological small-angle scattering data, *Nucleic Acids Res. 43*, D357-363.

[236] Franke, D., Petoukhov, M. V., Konarev, P. V., Panjkovich, A., Tuukkanen, A., Mertens, H. D. T., Kikhney, A. G., Hajizadeh, N. R., Franklin, J. M., Jeffries, C. M., and Svergun, D. I. (2017) ATSAS 2.8: a comprehensive data analysis suite for small-angle scattering from macromolecular solutions, *J. Appl. Crystallogr. 50*, 1212-1225.

[237] Schneidman-Duhovny, D., Hammel, M., and Sali, A. (2010) FoXS: a web server for rapid computation and fitting of SAXS profiles, *Nucleic Acids Res. 38*, W540-544.

[238] Petoukhov, M. V., and Svergun, D. I. (2015) Ambiguity assessment of small-angle scattering curves from monodisperse systems, *Acta Crystallogr D Biol Crystallogr 71*, 1051-1058.

[239] Franke, D., and Svergun, D. I. (2009) DAMMIF, a program for rapid ab-initio shape determination in small-angle scattering, *J. Appl. Crystallogr. 42*, 342-346.

[240] Volkov, V. V., and Svergun, D. I. (2003) Uniqueness of ab initio shape determination in small-angle scattering, *J. Appl. Crystallogr. 36*, 860-864.

[241] Svergun, D. I. (1999) Restoring low resolution structure of biological macromolecules from solution scattering using simulated annealing, *Biophys. J. 76*, 2879-2886.

[242] Petoukhov, M. V., Franke, D., Shkumatov, A. V., Tria, G., Kikhney, A. G., Gajda, M., Gorba, C., Mertens, H. D., Konarev, P. V., and Svergun, D. I. (2012) New developments in the ATSAS program package for small-angle scattering data analysis, *J. Appl. Crystallogr. 45*, 342-350.

[243] Weinkam, P., Pons, J., and Sali, A. (2012) Structure-based model of allostery predicts coupling between distant sites, *Proc. Natl. Acad. Sci. U.S.A. 109*, 4875-4880.

[244] Eswar, N., Webb, B., Marti-Renom, M. A., Madhusudhan, M. S., Eramian, D., Shen, M. Y., Pieper, U., and Sali, A. (2006) Comparative protein structure modeling using Modeller, *Curr Protoc Bioinformatics Chapter 5*, Unit-5 6.

[245] Jaffe, E. K., and Lawrence, S. H. (2012) The morpheein model of allostery: evaluating proteins as potential morpheeins, *Methods Mol Biol 796*, 217-231.

[246] Jaffe, E. K., Stith, L., Lawrence, S. H., Andrake, M., and Dunbrack, R. L., Jr. (2013) A new model for allosteric regulation of phenylalanine hydroxylase: implications for disease and therapeutics, *Arch. Biochem. Biophys. 530*, 73-82.

[247] Jaffe, E. K., and Lawrence, S. H. (2012) Allostery and the dynamic oligomerization of porphobilinogen synthase, *Arch. Biochem. Biophys. 519*, 144-153.

[248] Sen, S., and Banerjee, R. (2007) A pathogenic linked mutation in the catalytic core of human cystathionine beta-synthase disrupts allosteric regulation and allows kinetic characterization of a full-length dimer, *Biochemistry 46*, 4110-4116.

[249] Tang, L., Breinig, S., Stith, L., Mischel, A., Tannir, J., Kokona, B., Fairman, R., and Jaffe, E. K. (2006) Single amino acid mutations alter the distribution of human porphobilinogen synthase quaternary structure isoforms (morpheeins), *J. Biol. Chem. 281*, 6682-6690.

[250] Miyazaki, K. (2011) MEGAWHOP cloning: a method of creating random mutagenesis libraries via megaprimer PCR of whole plasmids, *Methods Enzymol. 498,* 399-406.

[251] Wilkins, M. R., Gasteiger, E., Bairoch, A., Sanchez, J. C., Williams, K. L., Appel, R. D., and Hochstrasser, D. F. (1999) Protein identification and analysis tools in the ExPASy server, *Methods Mol Biol 112*, 531-552.

[252] Nielsen, S. S., Toft, K. N., Snakenborg, D., Jeppesen, M. G., Jacobsen, J. K., Vestergaard, B., Kutter, J. P., and Arleth, L. (2009) BioXTAS RAW, a software program for high-throughput automated small-angle X-ray scattering data reduction and preliminary analysis, *J. Appl. Crystallogr. 42*, 959-964.

[253] Hopkins, J. B., Gillilan, R. E., and Skou, S. (2017) BioXTAS RAW: improvements to a free open-source program for small-angle X-ray scattering data reduction and analysis, *J. Appl. Crystallogr. 50*, 1545-1553.

[254] Battye, T. G., Kontogiannis, L., Johnson, O., Powell, H. R., and Leslie, A. G. (2011) iMOSFLM: a new graphical interface for diffraction-image processing with MOSFLM, *Acta Crystallogr D Biol Crystallogr 67*, 271-281.

[255] Winn, M. D., Ballard, C. C., Cowtan, K. D., Dodson, E. J., Emsley, P., Evans, P. R., Keegan, R. M., Krissinel, E. B., Leslie, A. G., McCoy, A., McNicholas, S. J., Murshudov, G. N., Pannu, N. S., Potterton, E. A., Powell, H. R., Read, R. J., Vagin, A., and Wilson, K. S. (2011) Overview of the CCP4 suite and current developments, *Acta Crystallogr D Biol Crystallogr 67*, 235-242.

[256] Laganowsky, A., Reading, E., Allison, T. M., Ulmschneider, M. B., Degiacomi, M. T., Baldwin, A. J., and Robinson, C. V. (2014) Membrane proteins bind lipids selectively to modulate their structure and function, *Nature 510*, 172-175.

[257] Marty, M. T., Baldwin, A. J., Marklund, E. G., Hochberg, G. K., Benesch, J. L., and Robinson, C. V. (2015) Bayesian deconvolution of mass and ion mobility spectra: from binary interactions to polydisperse ensembles, *Anal. Chem. 87*, 4370-4376.

[258] Allison, T. M., Reading, E., Liko, I., Baldwin, A. J., Laganowsky, A., and Robinson, C. V. (2015) Quantifying the stabilizing effects of protein-ligand interactions in the gas phase, *Nat. Commun. 6*, 8551.

[259] Ruotolo, B. T., Benesch, J. L., Sandercock, A. M., Hyung, S. J., and Robinson, C. V. (2008) Ion mobility-mass spectrometry analysis of large protein complexes, *Nat Protoc 3*, 1139-1152.

[260] Bush, M. F., Hall, Z., Giles, K., Hoyes, J., Robinson, C. V., and Ruotolo, B. T. (2010) Collision cross sections of proteins and their complexes: a calibration framework and database for gas-phase structural biology, *Anal. Chem. 82*, 9557-9565.

[261] Bleiholder, C., Wyttenbach, T., and Bowers, M. T. (2011) A novel projection approximation algorithm for the fast and accurate computation of molecular collision cross sections (I). Method, *Int. J. Mass Spectrom. 308*, 1-10.

[262] Anderson, S. E., Bleiholder, C., Brocker, E. R., Stang, P. J., and Bowers, M. T. (2012) A novel projection approximation algorithm for the fast and accurate computation of molecular collision cross sections (III): Application to supramolecular coordination-driven assemblies with complex shapes, *Int. J. Mass Spectrom. 330*, 78-84.

[263] Bleiholder, C., Contreras, S., Do, T. D., and Bowers, M. T. (2013) A novel projection approximation algorithm for the fast and accurate computation of molecular collision cross sections (II). Model parameterization and definition of empirical shape factors for proteins, *Int. J. Mass Spectrom. 345*, 89-96.

[264] Pettersen, E. F., Goddard, T. D., Huang, C. C., Couch, G. S., Greenblatt, D. M., Meng, E. C., and Ferrin, T. E. (2004) UCSF Chimera--a visualization system for exploratory research and analysis, *J. Comput. Chem. 25*, 1605-1612.

[265] Lawrence, S. H., and Jaffe, E. K. (2008) Expanding the Concepts in Protein Structure-Function Relationships and Enzyme Kinetics: Teaching using Morpheeins, *Biochem Mol Biol Educ 36*, 274-283.

[266] Kery, V., Poneleit, L., and Kraus, J. P. (1998) Trypsin cleavage of human cystathionine beta-synthase into an evolutionarily conserved active core: structural and functional consequences, *Arch. Biochem. Biophys. 355*, 222-232.

[267] Shan, X., and Kruger, W. D. (1998) Correction of disease-causing CBS mutations in yeast, *Nat Genet 19*, 91-93.

[268] Frank, N., Kery, V., Maclean, K. N., and Kraus, J. P. (2006) Solvent-accessible cysteines in human cystathionine beta-synthase: crucial role of cysteine 431 in S-adenosyl-L-methionine binding, *Biochemistry 45*, 11021-11029.

[269] Kavanagh, K. L., Dunford, J. E., Bunkoczi, G., Russell, R. G., and Oppermann, U. (2006) The crystal structure of human geranylgeranyl pyrophosphate synthase reveals a novel hexameric arrangement and inhibitory product binding, *J. Biol. Chem. 281*, 22004-22012.

[270] Miyagi, Y., Matsumura, Y., and Sagami, H. (2007) Human geranylgeranyl diphosphate synthase is an octamer in solution, *J. Biochem. 142*, 377-381.

[271] Yang, Z., Lanks, C. W., and Tong, L. (2002) Molecular mechanism for the regulation of human mitochondrial NAD(P)+-dependent malic enzyme by ATP and fumarate, *Structure 10*, 951-960.

[272] Hsieh, J. Y., Chen, S. H., and Hung, H. C. (2009) Functional roles of the tetramer organization of malic enzyme, *J. Biol. Chem. 284*, 18096-18105.

[273] Phillips, R. S., Parniak, M. A., and Kaufman, S. (1984) Spectroscopic investigation of ligand interaction with hepatic phenylalanine hydroxylase: evidence for a conformational change associated with activation, *Biochemistry 23*, 3836-3842.

[274] Martinez, A., Knappskog, P. M., Olafsdottir, S., Doskeland, A. P., Eiken, H. G., Svebak, R. M., Bozzini, M., Apold, J., and Flatmark, T. (1995) Expression of recombinant human phenylalanine hydroxylase as fusion protein in Escherichia coli circumvents proteolytic degradation by host cell proteases. Isolation and characterization of the wild-type enzyme, *Biochem. J 306 (Pt 2)*, 589-597.

[275] Knappskog, P. M., Flatmark, T., Aarden, J. M., Haavik, J., and Martinez, A. (1996) Structure/function relationships in human phenylalanine hydroxylase. Effect of terminal deletions on the oligomerization, activation and cooperativity of substrate binding to the enzyme, *Eur. J. Biochem. 242*, 813-821.

[276] Fusetti, F., Erlandsen, H., Flatmark, T., and Stevens, R. C. (1998) Structure of tetrameric human phenylalanine hydroxylase and its implications for phenylketonuria, *J. Biol. Chem. 273*, 16962-16967.

[277] Bjorgo, E., de Carvalho, R. M., and Flatmark, T. (2001) A comparison of kinetic and regulatory properties of the tetrameric and dimeric forms of wild-type and Thr427-->Pro mutant human phenylalanine hydroxylase: contribution of the flexible hinge region Asp425-Gln429 to the tetramerization and cooperative substrate binding, *Eur. J. Biochem. 268*, 997-1005.

[278] Meisburger, S. P., Taylor, A. B., Khan, C. A., Zhang, S., Fitzpatrick, P. F., and Ando, N. (2016) Domain Movements upon Activation of Phenylalanine Hydroxylase Characterized by Crystallography and Chromatography-Coupled Small-Angle X-ray Scattering, *J. Am. Chem. Soc. 138*, 6506-6516.

[279] Arturo, E. C., Gupta, K., Hansen, M. R., Borne, E., and Jaffe, E. K. (2019) Biophysical characterization of full-length human phenylalanine hydroxylase provides a deeper understanding of its quaternary structure equilibrium, *J. Biol. Chem. 294*, 10131-10145.

[280] Arturo, E. C., Gupta, K., Heroux, A., Stith, L., Cross, P. J., Parker, E. J., Loll, P. J., and Jaffe, E. K. (2016) First structure of full-length mammalian phenylalanine hydroxylase reveals the architecture of an autoinhibited tetramer, *Proc. Natl. Acad. Sci. U.S.A. 113*, 2394-2399.

[281] Ibsen, K. H., Schiller, K. W., and Haas, T. A. (1971) Interconvertible kinetic and physical forms of human erythrocyte pyruvate kinase, *J. Biol. Chem. 246*, 1233-1240.

[282] Schulz, J., Sparmann, G., and Hofmann, E. (1975) Alanine-mediated reversible inactivation of tumour pyruvate kinase caused by a tetramer-dimer transition, *FEBS Lett. 50*, 346-350.

[283] Kozik, A., Potempa, J., and Travis, J. (1998) Spontaneous inactivation of human lung tryptase as probed by size-exclusion chromatography and chemical cross-linking: dissociation of active tetrameric enzyme into inactive monomers is the primary event of the entire process, *Biochim. Biophys. Acta 1385*, 139-148.

[284] Hlodan, R., and Pain, R. H. (1995) The folding and assembly pathway of tumour necrosis factor TNF alpha, a globular trimeric protein, *Eur. J. Biochem. 231*, 381-387.

[285] Tang, L., Stith, L., and Jaffe, E. K. (2005) Substrate-induced interconversion of protein quaternary structure isoforms, *J. Biol. Chem. 280*, 15786-15793.

[286] Jaffe, E. K., and Stith, L. (2007) ALAD porphyria is a conformational disease, *Am J Hum Genet 80*, 329-337.

[287] Selwood, T., Tang, L., Lawrence, S. H., Anokhina, Y., and Jaffe, E. K. (2008) Kinetics and thermodynamics of the interchange of the morpheein forms of human porphobilinogen synthase, *Biochemistry 47*, 3245-3257.

[288] Breinig, S., Kervinen, J., Stith, L., Wasson, A. S., Fairman, R., Wlodawer, A., Zdanov, A., and Jaffe, E. K. (2003) Control of tetrapyrrole biosynthesis by alternate quaternary forms of porphobilinogen synthase, *Nat. Struct. Biol. 10*, 757-763.

[289] Hutin, S., Brennich, M., Maillot, B., and Round, A. (2016) Online ion-exchange chromatography for small-angle X-ray scattering, *Acta Crystallogr D Struct Biol 72*, 1090-1099.

[290] Scholz, R., Suter, M., Weimann, T., Polge, C., Konarev, P. V., Thali, R. F., Tuerk, R. D., Viollet, B., Wallimann, T., Schlattner, U., and Neumann, D. (2009) Homo-oligomerization and activation of AMP-activated protein kinase are mediated by the kinase domain alphaG-helix, *J. Biol. Chem. 284*, 27425-27437.

[291] Leblanc, Y., Bihoreau, N., and Chevreux, G. (2018) Characterization of Human Serum Albumin isoforms by ion exchange chromatography coupled on-line to native mass spectrometry, *J Chromatogr B Analyt Technol Biomed Life Sci 1095*, 87-93.

[292] Frank, J. (2017) Time-resolved cryo-electron microscopy: Recent progress, *J Struct Biol 200*, 303-306.

[293] Svergun, D. I. (1992) Determination of the Regularization Parameter in Indirect-Transform Methods Using Perceptual Criteria, *J. Appl. Crystallogr. 25*, 495-503.

[294] Fox, N. G., Martelli, A., Nabhan, J. F., Janz, J., Borkowska, O., Bulawa, C., and Yue, W. W. (2018) Zinc(II) binding on human wild-type ISCU and Met140 variants modulates NFS1 desulfurase activity, *Biochimie 152*, 211-218.